Seismicity and regional tectonics of the Estremadura, Southwestern Portugal

João F.B. Duarte Fonseca

Seismicity and Regional Tectonics of the Estremadura, Southwestern Portugal

by

João F. B. Duarte Fonseca

A Thesis submitted in partial fulfilment
of the requirements for the degree of
Doctor of Philosophy

The Graduate Society Department of Geological Sciences

The University of Durham
1989

Abstract

The RESTE Project was an integrated geophysical-geological study of the Estremadura, southwestern Portugal. The core of the programme consisted of the acquisition and analysis of microearthquake data. This was complemented by an investigation of the structural evolution of the sedimentary basins of the Estremadura.

The geological evolution of the Lusitanian Basin was strongly marked by the reactivation of Palaeozoic basement faults, in response to a sequence of tectonic events: opening of the Central Atlantic, opening of the North Atlantic and Alpine convergence between Africa and Eurasia. The current tectonics are regarded as a subdued continuation of the Miocene deformation (Betic Orogeny), and the "tectonic memory" revealed by the Lusitanian and Lower Tagus Basins is explored to characterize the current tectonic processes. Strike-slip tectonics are identified as a dominant feature of several stages of the evolution of the basins, with particular relevance during the Miocene.

The technique of "backstripping" is applied to well data, to constrain the history of vertical movement in the basins. This analysis highlighted the premature truncation, in the Late Jurassic, of a normal passive-margin evolution. Tectonic unstability caused the structural inversion of areas within the basins, and seems to have inhibited the predictable thermal subsidence. The rifting process, initially taking place at the Lusitanian Basin, jumped westwards in the Late Jurassic. Crustal underplating and the activity of transfer faults are invoked as possible explanations for the subsequent deformation of the aborted rift. An upper-plate margin configuration is in good agreement with several observations. The tendency for structural inversion continued throughout the Cretaceous, and with the onset of the Alpine convergence in the Turonian the

control of the tectonic activity seems to have switched from the Atlantic to the Mediterranean. This reinforced the tectonic unstability, marked by magmatic activity and by a regional upwarp that was to last until the Eocene. Of particular interest was the behaviour, during the Late Cretaceous, of the Setúbal Peninsula sub-basin, which seems to have tilted towards the NW as a block, with a hinge line along the present Lower Tagus Valley. When sedimentation was resumed in the Eocene, a pattern of differential vertical movement was established, with some areas continuing to undergo inversion while nearby areas subsided. This pattern characterized the Cainozoic evolution of the basins, and probably still applies to the neotectonic deformation. The activity of strike-slip basement faults, reactivated under the compressive regime caused by the Afro-Eurasian convergence, is proposed as the best explanation for the Miocene deformation, with particular relevance for the Lower Tagus Valley.

The RESTE Microearthquake Survey is described, and the data acquired with the RESTE network are analysed. The local earthquakes are accurately located, and focal mechanism solutions are obtained for some of them. This information is used to discuss a neotectonic model for the Lower Tagus Valley. In view of their small magnitudes ($1.1 < M_L < 3.8$), the focal mechanisms of these events cannot be interpreted directly in terms of the current tectonics. Such small events are usually local readjustments to previous episodes of deformation. However, such features as the along-strike reversal of the polarity of vertical motion or the coexistence at the same region of different types of source mechanism are diagnostic of strike-slip deformation. This model was supported by the occurrence of a macroearthquake (M_D=3.8) with an interpreted source mechanism of sinistral strike-slip. The alignment of four hypocentres along the direction of the Lower Tagus Valley, with a compatible orientation of the interpreted nodal planes, supports the existence of a crustal fracture associated with the Valley. The hypocentral depths of the recorded events reach 20 km, showing that the basement faults responsible for the seismicity affect at least the entire upper crust. Since the limited existing data suggest a high level of heat flow in the Lusitanian Basin, the depths reached by the microearthquakes may indicate an abnormally thick seismogenic layer. An investigation of the broad velocity structure of the lithosphere underneath the RESTE Network using the technique of teleseismic tomographic inversion suggested a correlation between

Moho undulations and the inversion of areas of the Lusitanian Basin, and this may indicate that the controlling faults cut the entire crust.

In order to provide a *rationale* for the intraplate seismicity of western Portugal, the neotectonics of Iberia are discussed, and a new kinematic model, centred on the idea of continental extrusion, is proposed. According to the model, a continental block formed by Iberia and northern Morocco is being pushed westwards by the convergence between Africa and Eurasia. The resistance offered by the oceanic parts of the plates varies across the East Azores Transform, leading to dextral shear in the Betic Range. The regional stress field induced by the continental convergence can explain the reactivation, in a simple-shear regime, of basement faults of Hercynian orientation, in particular that proposed for the Lower Tagus Valley.

Contents

Acknowledgements

The RESTE Project was a joint effort of the Department of Geological Sciences of the University of Durham and the Instituto Nacional de Meteorologia e Geofísica, Lisbon (INMG), with the cooperation of the Laboratório Nacional de Engenharia Civil, Lisbon (LNEC). I wish to thank the following individuals and institutions, from whom I received support and guidance throughout the course of the RESTE Project:

- Dr Roger Long, my supervisor, for his advice and contagious enthusiasm, and for his valuable criticisms to a previous manuscript of this thesis; Prof Martin Bott and Prof Roger Searle, for the use of the departmental facilities;

- Dr Victor Moreira (INMG) and Eng. J. Moura Esteves (LNEC), for their support to the RESTE Project;

- Dr Donny Hutton and Dr Rob Gawthorpe (Durham Univ.), for their guidance in the fields of structural geology and seismic stratigraphy; Dr Gomes Coelho (LNEC), for his valuable indications concerning the tectonics of the Lower Tagus Valley;

- Dr Manuela Costa (GPEP, Lisbon), for her guidance through the wealth of commercial seismic data under her command;

- J. Costa Nunes (INMG), for his interest and cooperation, and V. Neves (INMG, Lisbon), for superintending the technical operations of the RESTE Network;

- Dave Stevenson (Durham Univ.), for his computational guidance, and Dr Gillian Foulger, for many useful seismological hints, and for being a source of inspiration for young geophysicists;

- my colleagues Tracey, Mike, Sam, Stuart, Gordon, and many others, for making my stay at the Department a pleasant one; Tracey, Stuart, Mike and Dr Chris Roberts for proverea, sorry, proofreading parts of this thesis; Simon Day for his advice on magmatism;

- Rui Almeida and A. Goulão (LNEC) and A. Latas (INMG), for their efficient field work;

- Mr D. Asbery, for his permanent willingness to help in a variety of ways; Mr G. Ruth (Durham Univ.) and Mr A. Haston (NERC, Edinburgh), for their assistance to the electronic equipment; Mrs Karen Atkinson, for drawing most of the diagrams in this thesis;

- Dr C. Wilson, Prof P. Talwani, Dr A. Mauffret, Dr L. Osete, Prof N. Kusznir and João Cabral, for providing me with pre-print copies of their publications.

The Gabinete de Pesquiza e Exploração de Petróleo, Lisbon, provided me with access to, and copies of, large quantities of commercial geophysical data, without which the reach of the RESTE Project would be severely limited. Many institutions helped running individual seismic stations. The Council of Almeirim, the Companhia das Lezírias, the Rádio Renascença (Muge) and the Serviços Florestais, as well as a long list of farmers and land owners, allowed the intalation of RESTE stations within their premises, and bore with me during many a visit. The Força Aérea Portuguesa was particularly helpful, and I am indebted to the Commanding Officer of the Esquadra 11 (Montejunto) and to Asp. Brum and the remaining staff of the Radar Station, and to the Meteo officers of the Base Aérea 6 (Montijo). Mr Manuel Vicente, from the Misericórdia de Benavente, and his staff gave a contribution of special meaning. I am also indebted to Cor. Cunha Lima and to Ten. Cor. Conceição Santos, from the Transmissions Division of Polícia de Segurança Pública, Lisbon, for clearing last-minute complications with the availability of radio frequencies. Mr Joaquim Parracho, from the Museu de Benavente, shared with me his vast knowledge of the history and sociology of that "earthquake town".

My stay at Durham was made financially possible by a grant from the Gulbenkian Foundation, Lisbon, and by a remunerated leave from the Instituto Su-

perior Técnico, Lisbon. Field work expenses were partially covered by JNICT, Lisbon. The field equipment was loaned from the NERC Equipment Pool, Edinburgh.

I thank the Pricipal and the staff of the Graduate Society, Durham University, to whom I owe so many attentions, and the same acknowledgement goes to Miss Maria Antónia da Silva and the staff of the Portuguese Affairs Department of the Gulbenkian Foundation, London. My wife Paula and my son Pedro, at Durham, my Mother and the rest of my family, in Lisbon, took up some of the strain, and kept me going.

To all, my sincere *Obrigado*.

...ils marchèrent vers Lisbonne; ... A peine ont-ils mis le pied dans la ville ... qu'ils sentent la terre trembler sous leurs pas; la mer s'élève en bouillonant dans le port, et brise les vaisseaux qui sont à l'ancre. Des tourbillons de flamme et de ceindres courent les rues et les places publiques; les maisons s'écroulent, les toits sont renversés sur les fondements, et les fondements se dispersent; trinte mille habitants de tout âge et de tout sexe sont écrasés sous les ruines ...

Quelques éclats de pierre avaient blessé Candide; il était étendu dans la rue et couvert de débris. Il disait à Pangloss: "Hélas! procure-moi un peu de vin et d'huile; je me meurs. - Ce tremblement de terre n'est pas une chose nouvelle, répondit Pangloss; la ville de Lima éprouva les mêmes secousses en Amerique l'année passée; mêmes causes, mêmes effects; il y a certainement une trainée de souphre sous terre depuis Lima jusqu'á Lisbonne. - Rien n'est plus probable, dit Candide; mais pour Dieu, un peu d'huile et de vin.

In *Voltaire's* Candide ou l'Optimisme.

To my Family,

and to the Memory of my Father,

I dedicate this work.

J.F.

Preface

The RESTE Project (*Rede de Estações Sísmicas Temporárias da Estremadura* / Temporary Seismic Network of Estremadura) was initiated in April 1987, when the Department of Geological Sciences of the University of Durham and the Instituto Nacional de Meteorologia e Geofisica, Lisbon, decided to join efforts to collect accurate seismographic data in the Portuguese Estremadura, the area surrounding Lisbon. For a period of eleven months, starting in June 1987, a microearthquake network was used to provide data for hypocentral locations and focal mechanism estimates, in an area where moderate to strong seismicity has been responsible for extensive losses of human lives in the past.

The study of the seismicity (chapter 4) is but a part of the RESTE programme. After a critical overview of the bibliography on the geological evolution of Iberia through the major tectonic events that shaped its present characteristics (Hercynian Orogeny, openning of the Central Atlantic, openning of the North Atlantic, Alpine Orogeny; chapter 1), the structural style and evolution of the Estremadura are investigated (chapters 2 and 3), with the help of commercial geophysical data (seismic maps and sections, well data and gravity map). A new geodynamic model to explain the neotectonics of Iberia is derived through the integration of seismological and geological data (chapter 5). Finally, teleseismic data recorded at the RESTE stations are used to explore what can be learned about the deep structure of the lithosphere underneath the network, using tomographic inversion (chapter 6).

The approach followed throughout this thesis stems from the fundamental assumption that intraplate neotectonics cannot be understood with seismological data alone (Blenkinsop et al.,1986; Long, 1988). The intrinsic scarsity and the diffuse nature of earthquake data in the plate interiors create a challenge for the geophysicist, which can only be met through an effort to bring toghether the contributions of seismology, structural geology, sedimentology and basin analysis, side by side with the methods of geophysical exploration. From this interdisciplinary standpoint, and with a criterial application of the ideas developed during the plate tectonics revolution (and more recently during the continental deformation revolution), some light may be shed on the grey area of the processes

taking place away from the boundaries of the plates.

It is widely accepted today, eleven years after the classic work of L. Sykes, that the active tectonics of most intraplate regions under compression are controlled by the distribution of crustal weaknesses inherited from the youngest orogenic event in which the area was directly involved. Although the deformation of the interior of the continents can still be seen, like its interplate conterpart, as the search for a minimum-energy stable crustal configuration compatible with a particular set of boundary conditions, the "energy budget" involved is not adequate to provide the disruption of homogeneous crust. Relatively fresh fault zones, not welded by extensive volcanism or metamorphic processes, can nevertheless be reactivated and used as strain guides, allowing the continental crust to adjust to the ever changing (in a geological time scale) conditions at the plate margins.

The western margin of the Iberian Peninsula provides a prime example of the type of "tectonic memory" described above. It is therefore adequate to start the discussion of the current tectonic activity back in the times of the Hercynian Orogeny, when most of the structural background that can be observed today had its origins. This will be covered in the first chapter, which starts with a discription of the main structural divisions that are usually considered in the western Peninsula; detailed accounts may be found in Julivert et al.(1974) and Ribeiro et al.(1980).

Chapter I

Geology and Tectonic Setting of Portugal

1.1 Structural provinces of Iberia.

The regional geology of Iberia (Figure 1.1) is dominated by a large block of granitic basement of Hercynian age, the Hesperic Massif. To the W lie two Meso-Cainozoic depressions to which particular attention will be devoted throughout this thesis: the Lusitanian Basin and the Lower Tagus and Sado Basin. To the S the Algarve Basin, formed during the Mesozoic, gives way westwards to the Guadalquivir Basin, blanketed by Tertiary sediments, which separates the Hesperic Massif from the Betic Cordillera. Three other important basins cover a considerable part of the eastern half of Iberia: the Douro Basin and the Tagus Basin, occupying symmetrical positions around the Central Cordillera, a major structural feature of the basement, and the Ebro Basin to the NE, separated from the previous two by the Iberian Cordillera. The Pyrenees and the Cantabric Chain occupy the NE extreme of the Peninsula.

According to the way in which they were affected by the Hercynian Orogeny several zones may be considered, forming a pattern characterized by a tightly arcuate shape, the Ibero-Armorican Arc (Figure 1.2). The axis of the Orogen corresponds to the Centro-Iberian Zone, dominated by syn-orogenic granites, which give place to the SW, accross the Coimbra-Cordoba Shear Zone, to the metamorphic rocks of the Ossa-Morena Zone, characterized by abundant Precambrian outcrops. The northwestern part of the contact is a first order structural discontinuity, the Porto-Abrantes Fault, whereas to the SE the Ferreira Thrust, dipping towards the SW, puts the deformed Precambrian rocks on top of the Hercynian granites. The next structural unit to be found to the SW and S is the South Portuguese Zone, which comes into contact with the Ossa Morena Zone at the Ficalho Thrust, in this case dipping towards the NE.

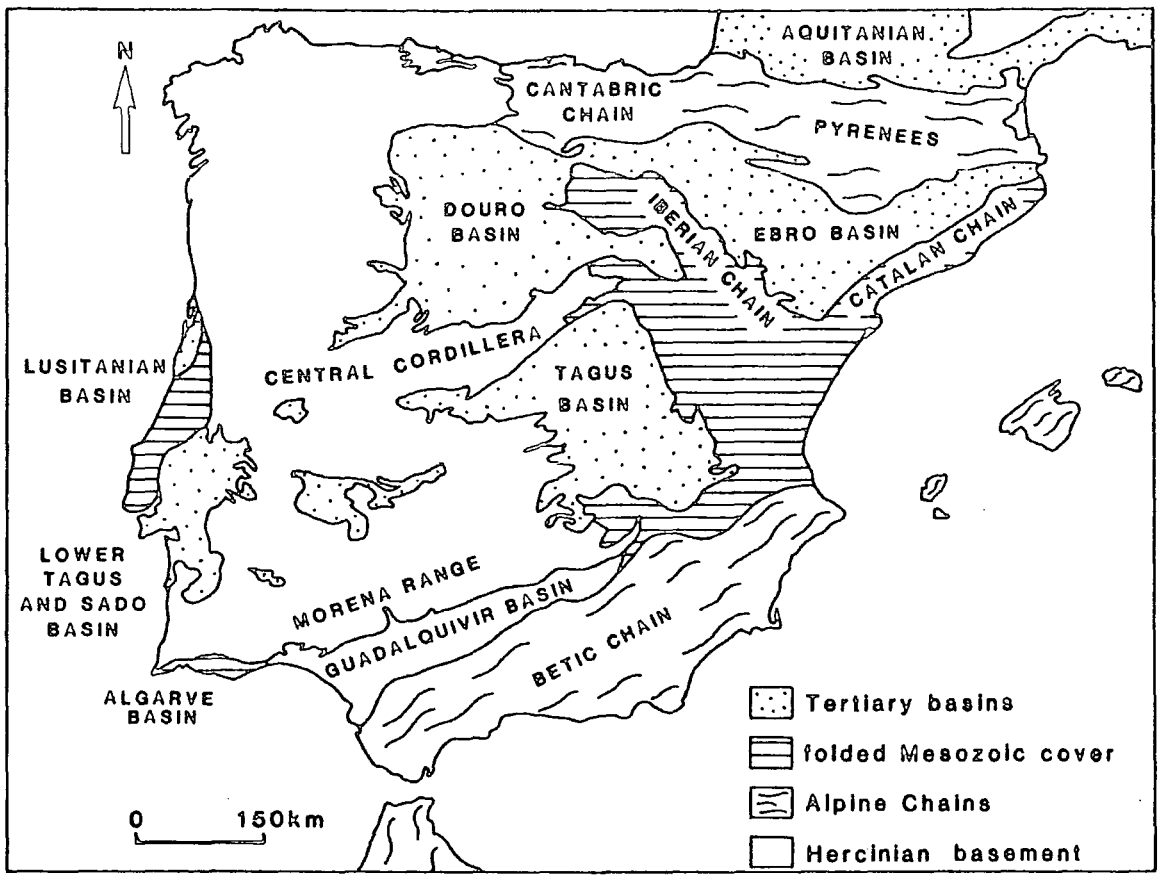

Fig. 1.1 - Regional geology of Iberia. After Julivert et al. (1974) and Ribeiro et al. (1980).

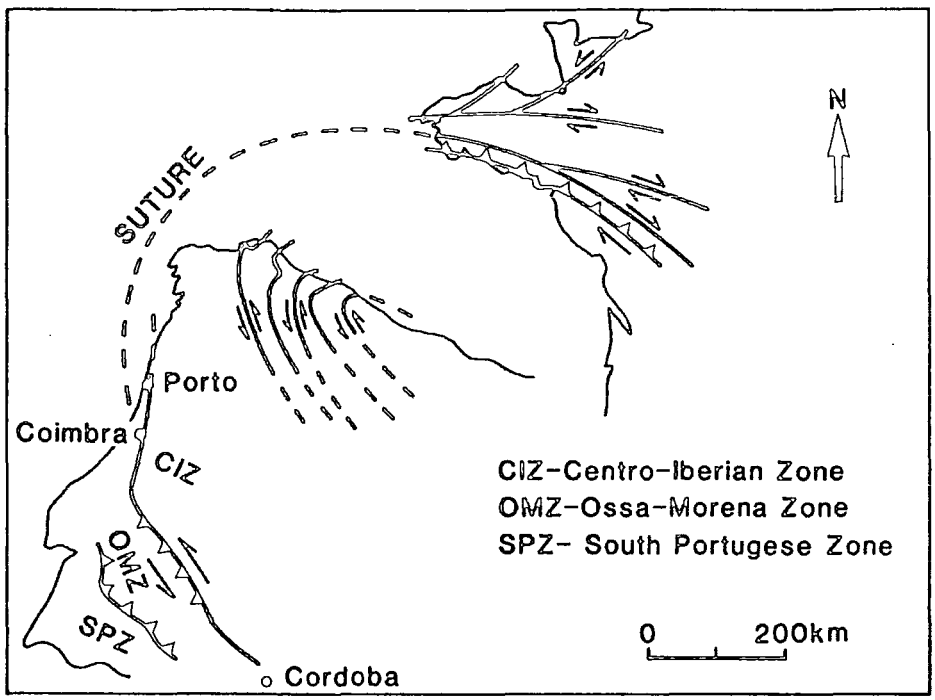

Fig. 1.2 - The Ibero-Armorican Arc. After Burg et al. (1981).

Whilst the basement geology of SW Iberia may have been affected by the Carboniferous scenario of subduction at the southern margin of Laurasia, it was however the subsequent continent-continent collision that determined the structural grain of the Peninsula as we see it today. The fundamentals of the diastrophism that affected most of Europe and Northern Africa in the Late Palaeozoic will now be described, as it had a bearing on the subsequent evolution of Iberia throughout the Mesozoic and Cainozoic times.

1.2 The Hercynian heritage.

After the final closure of the Iapetus Ocean in the Mid Devonian, the tectonic setting of western Europe was dominated by the northerly subduction of the Proto- Tethys Ocean under the southern border of the Laurasian Megacontinent (Ziegler, 1982). Several microcontinents (Austro-Alpine, Avalon, Iberia), were sequentially accreted at the plate boundary, causing a step by step southward migration of the subduction zone. Iberia collided with Laurasia during the late Early Carboniferous, and a zone of N-S sinistral shear (NNW-SSE in present coordinates) probably linked two offset zones of subduction during the latest stages of the northward displacement (Figure 1.3). This led to the complex shape of the Iberian part of the Hercynian fold belt. Carboniferous troughs (Douro-Beira, Santa Suzana, Buçaco) ranging in age from Late Westphalian to Late Stephanian (Teixeira, 1981) developed along major strike-slip basement faults (Ribeiro et al., 1980). In cross section, the reverse faults of the Ossa Morena Zone diverge upwards across a belt some 100km wide (Julivert et al., 1974, their Figure 6), in a pattern that is possibly evocative of the importance of transpression during the Hercynian Orogeny.

The consolidation of the Hercynian fold belt was not synchronous along its length; by the end of the Carboniferous the mountain building process was already dormant in western and central Europe, but crustal shortening continued to the W (Apalachians) and to the E (Urals) until the end of Early Permian times (Ziegler, 1982). This was achieved by the development of a dextral "Megashear" zone, 10000 km long and 1000 km wide, connecting the two active belts through most of the recently consolidated section of the orogen (Arthaud and Matte, 1977). The main strike-slip faults had an E-W orientation, forming angles of 20

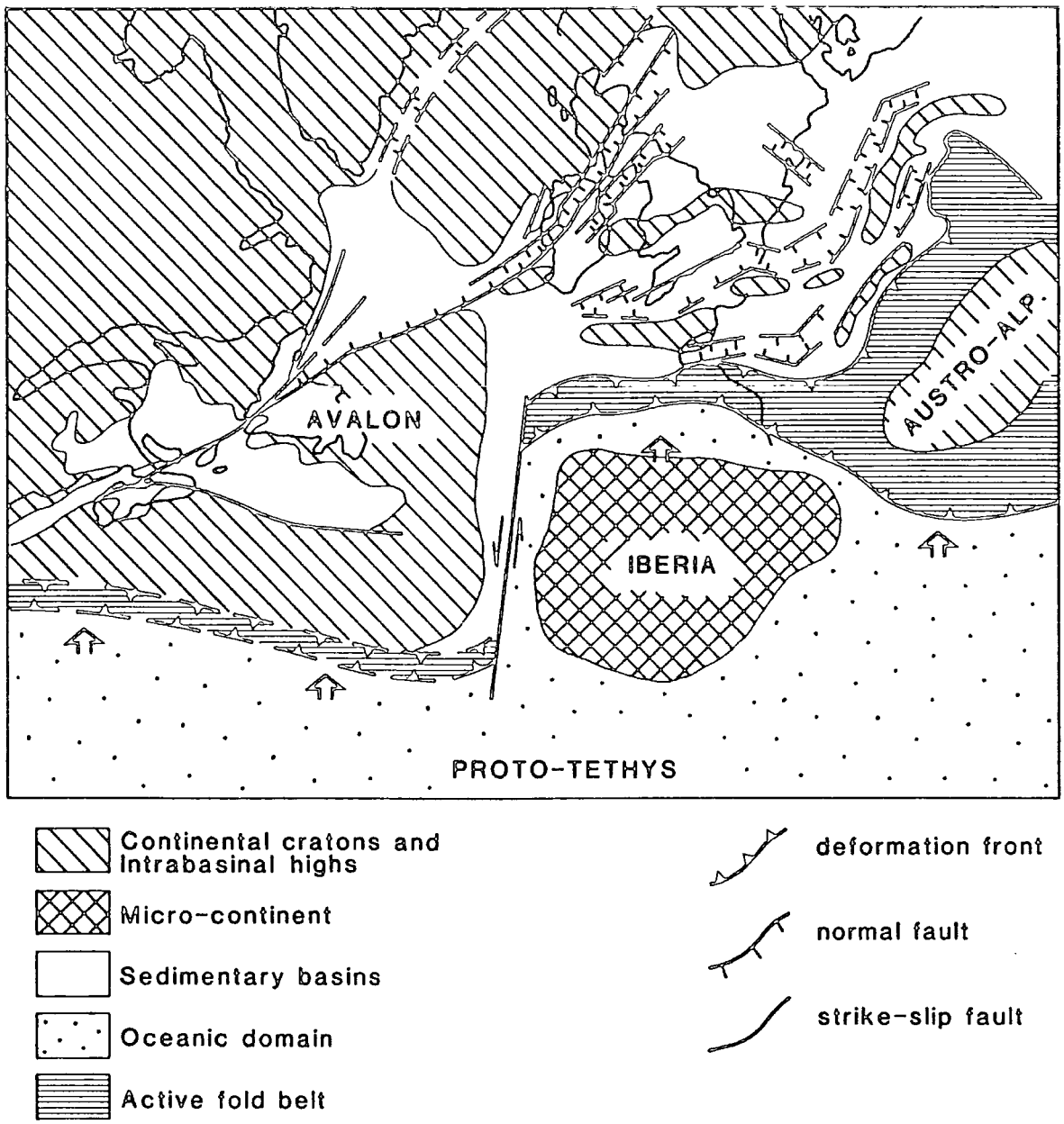

Fig. 1.3 - Carboniferous emplacement of Iberia. After Ziegler (1982).

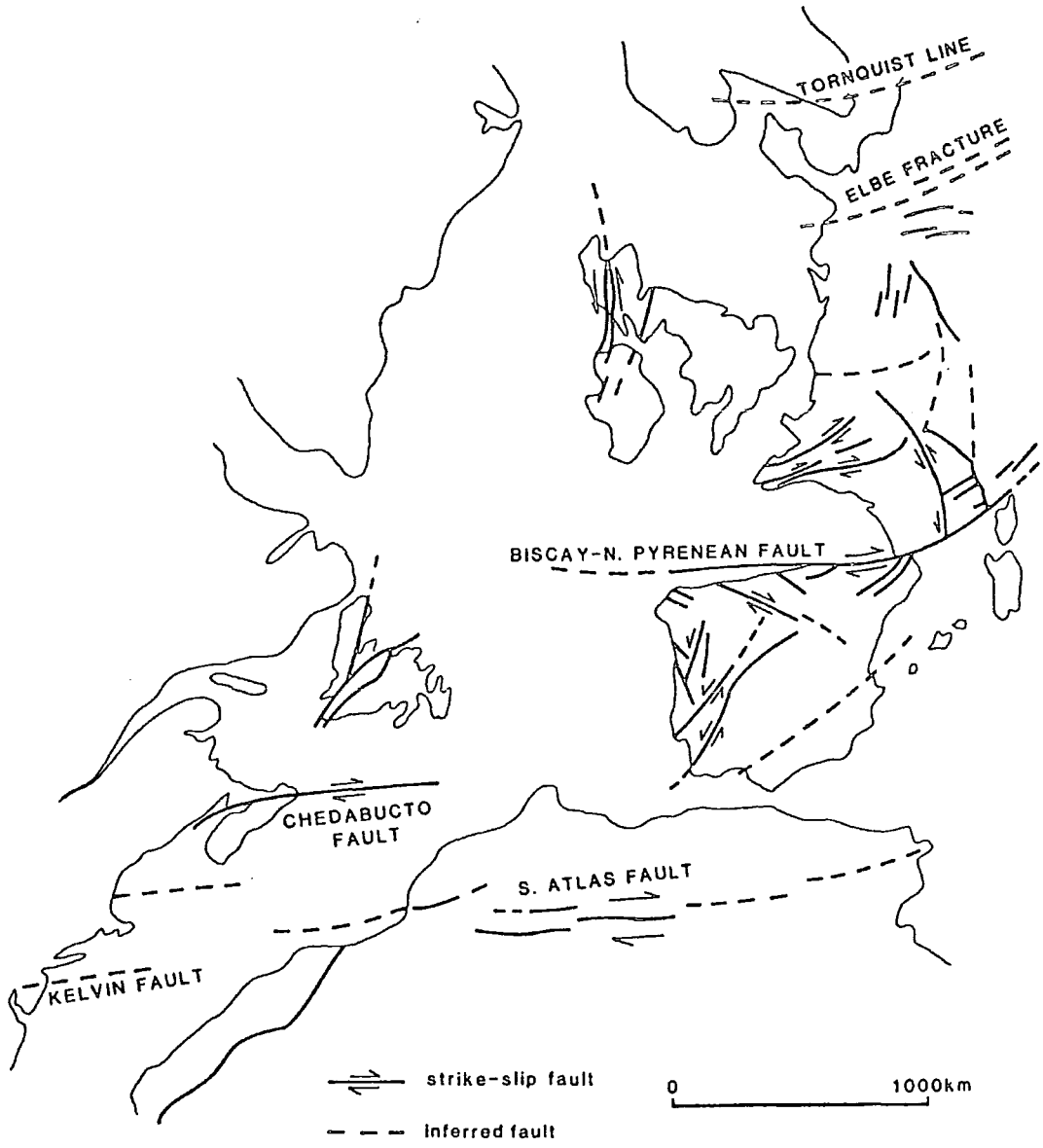

Fig. 1.4a) - Late Hercynian "megashear" zone of southwestern Europe and northwestern Africa. After Arthaud and Matte (1975, 1977).

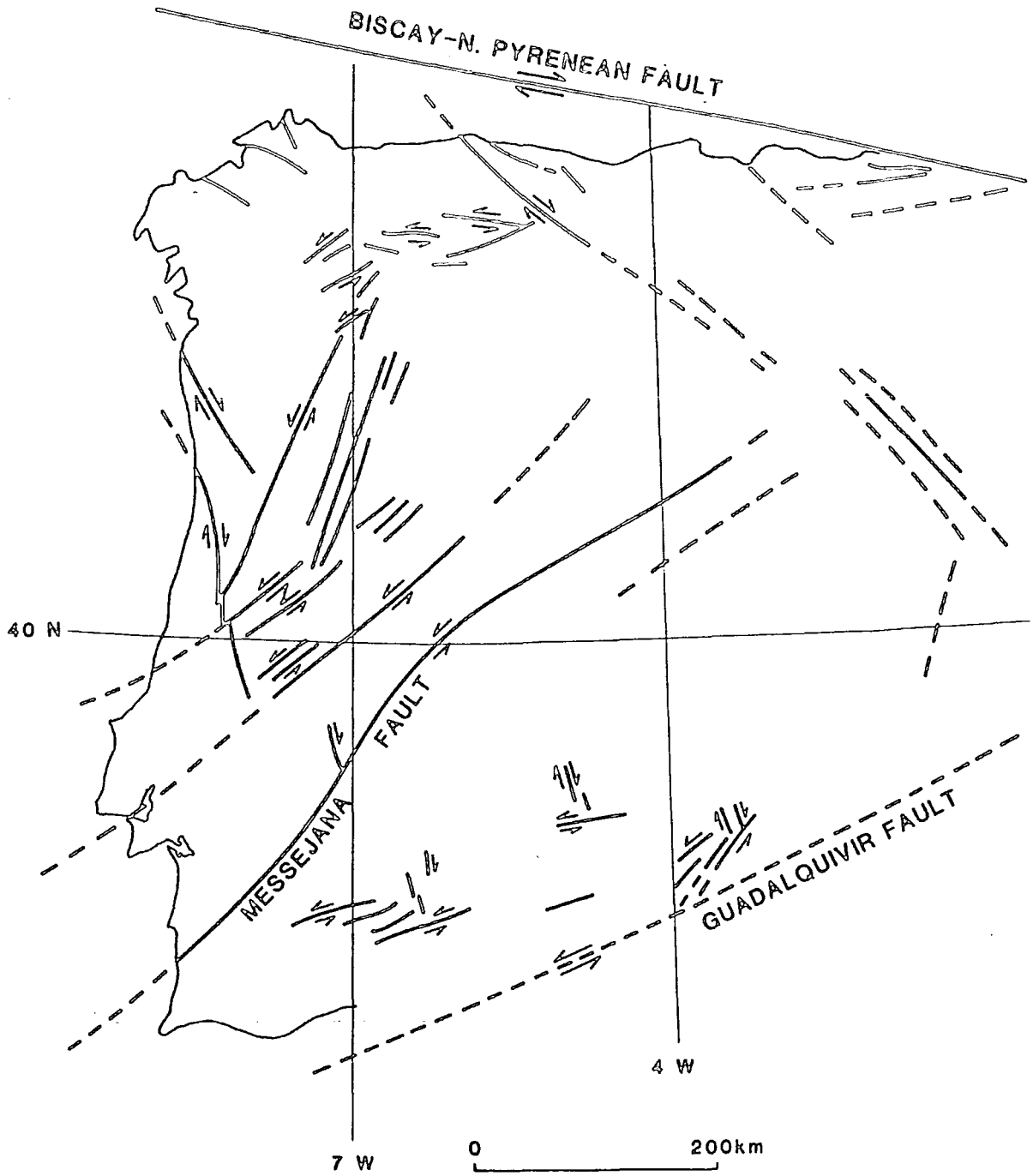

Fig. 1.4b) - Late Hercynian faults of Iberia. After Arthaud and Matte (1975, 1977).

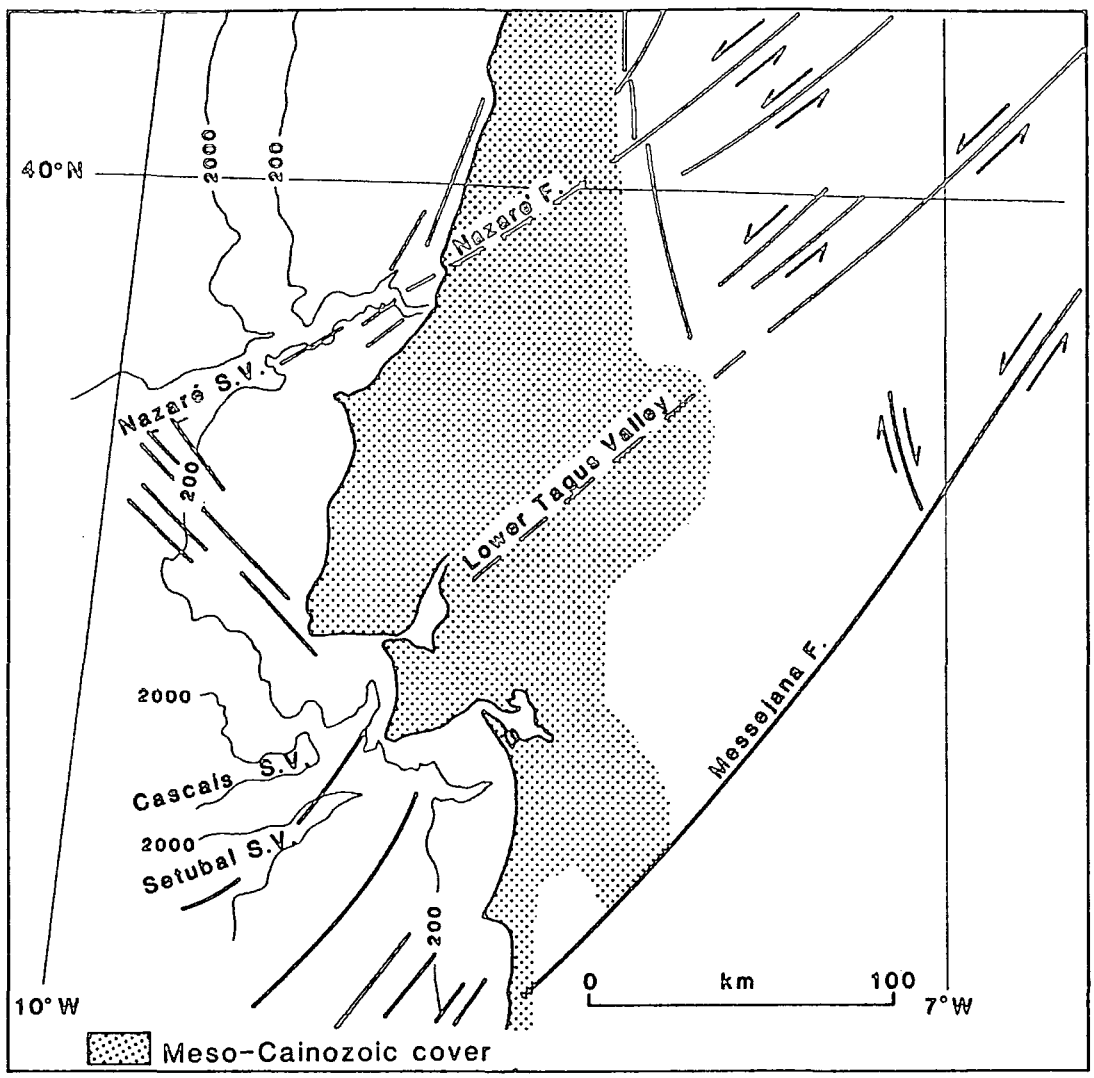

Fig. 1.4c) - Correlation between the Late Hercynian basement faults of western Portugal and the structures of the continental shelf. Based on Arthaud and Matte (1975, 1977) and Vanney and Mougenot (1981).

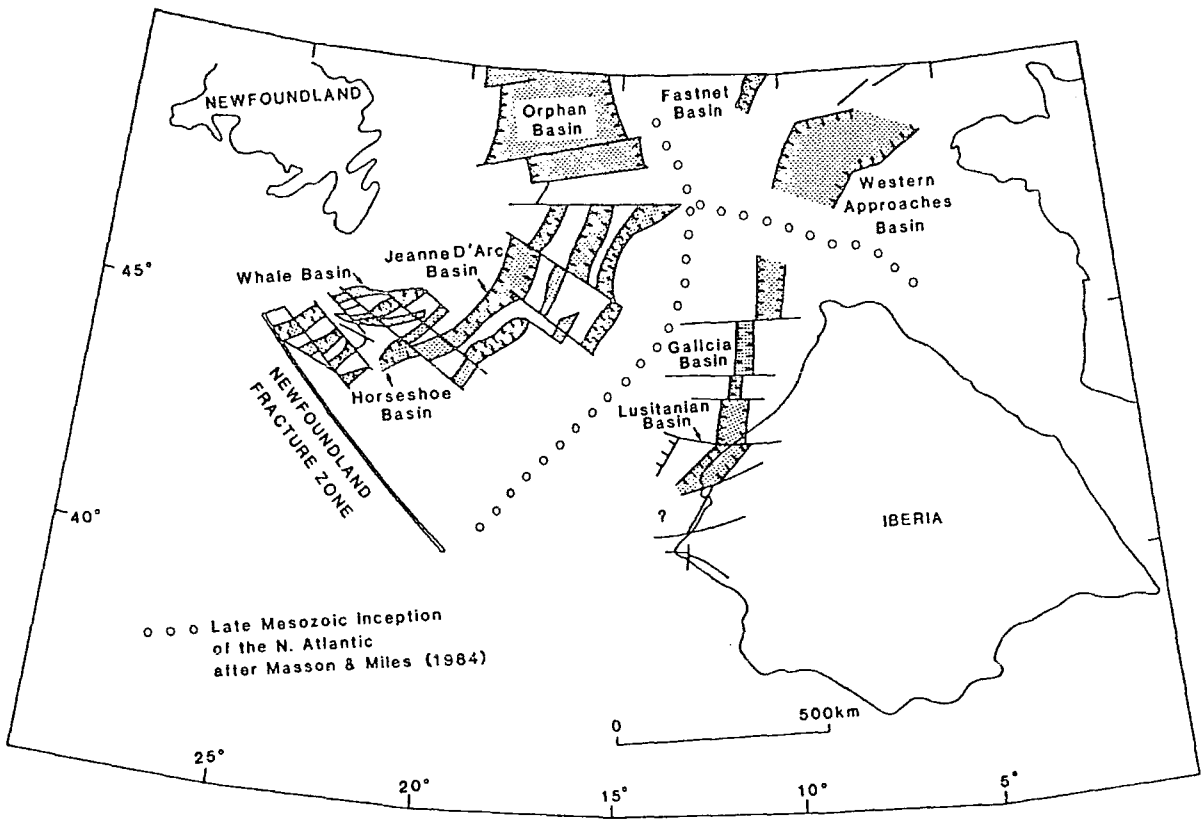

Fig. 1.5 - Early Jurassic rift basins of the North Atlantic margins. Based on Masson and Miles (1984, 1986), Tankard and Welsink (1986) and Guery at al. (1986). Atlantic closure after Masson and Miles (1984).

to 30 degrees with the strike of the shear zone. They measure several hundred kilometres in length and show tens of kilometres of offset. The best preserved examples are the South Atlas Fault of Morocco and the Biscay-North Pyrenean Fault (Figure 1.4a). The Chedabucto Fault to the S of Newfoundland may have had a continuation through Gibraltar, although no positive evidence can be found due to the Alpine tectonic overprint. In western Iberia, a set of left lateral strike-slip faults were particularly well developed (Figure 1.4b), with dominant directions of 030^o and 015^o. Several dextral faults with directions close to 310^o also originated in this period.

When the transpressional setting of the Late Carboniferous-Early Permian gave way to the tensional regime that was to dominate during the Mesozoic, a vast network of strike-slip faults criss-crossed the Hercynian basement of western Europe. These structures were to dominate the mechanical behaviour of the crust throughout the next 250 million years (Le Pichon et al., 1977).

1.3 Early Mesozoic evolution.

Extension and rifting were the dominant processes taking place in western Europe during the Early Mesozoic, and the weak lithosphere inherited from the Hercynian Orogeny was probably instrumental in allocating to the western margin of Iberia part of the future passive margin of the North Atlantic.

At the bottom of the sedimentary fill of the Lusitanian and Algarve Basins, the Upper Triassic siliciclastic formation "Gres de Silves" rests unconformably on top of Palaeozoic and Precambrian basement (Palain, 1979; Ribeiro et al., 1980). This gap (the Permian and Early Triassic being almost entirely absent in Portugal) marks a stage of erosion of the Hercynian mountains, and corresponds to the transition from the compressive tectonics of the Late Palaeozoic to the Mesozoic desintegration of Pangea (Dewey et al., 1973; Manspeizer, 1981).

In the Central and North Atlantic, the breakup of Pangea was not synchronous, the onset of sea floor spreading ranging from Middle Jurassic between North America and Africa to Early Palaeocene in the Norwegian Sea and Baffin Bay (Bally, 1981). When the northward propagating rift reached the zone between the Canary Islands and southern Iberia, it interfered with the tectonic

activity in the Tethys Ocean (Dewey et al., 1973; Stetz and Wurster, 1982). In fact, to the N of the South Atlas Fault the African continent was no longer a stable craton, having been dissected by the Late Hercynian Megashear Zone. This provided a zone of crustal weakness that was reactivated under the new extensional regime, creating seaways for the westward transgression of the Tethys Ocean. The South Atlas Trough separated Africa from the small continental fragments of the Oran and Moroccan Mesetas, themselves separated by the Middle Atlas Trough (Dewey et al., 1973). Faunal evidence for this Atlantic-Tethys connection is clear in Morocco (Manspeizer et al., 1978) and Portugal (Mouterde et al., 1979). At the same time (Early Jurassic), deep water sediments were deposited and alkaline volcanics were erupted along the troughs of northwestern Africa (Dewey et al., 1973). In Portugal, the Algarve Basin was sharing the volcanic activity and sediment facies of the Moroccan province (Aires-Barros, 1979; Ribeiro et al., 1980). In Spain, clastic deposition and alkaline volcanism were taking place in the Betic and Iberian Cordilleras. Along the Pyrenees-Biscay Trough, another seaway connected the Tethys Ocean to the basins of northwestern Europe (Ziegler, 1982; Gaeley, 1988).

The Lusitanian Basin, whose first stages of subsidence date from Late Triassic to Middle Jurassic, has a clear genetic relation with the early episodes of rifting described above. However, it is different from most Early Jurassic troughs of Iberia and NW Africa in that it does not show significant volcanic activity associated with its early evolution. In Portugal only the Algarve Basin shows important basic magmatism during this period (Aires-Barros, 1979). It is therefore difficult to relate in a direct manner the origin of the Lusitanian Basin to a thermal event of the type invoked by Wilson (1974) to explain rifting further north offshore Northwest Iberia and by Manspeizer (1978,1981) to explain the Morrocan rifts. This illustrates the more general difficulty of assessing the dominance of either thermal or mechanical factors as the origin of the complex and somewhat obscure process by which continents split to give birth to oceans (Burke, 1976, 1980; Bott, 1980; Keen and de Voogt, 1988). Such variations on rifting style along the same margin may be indicative of the validity of the model of detachment-controlled assymetric rifting (Wernicke and Burchfield, 1982; Lister et al., 1986), which accounts for the development of several different tectonic provinces separated by first order transfer faults (Gibbs, 1984). This model has

been proposed for the Portuguese margin by Wilson et al. (in press), and will be further discussed in section 3.4.

1.4 Late Mesozoic evolution.

1.4.1 The opening of the North Atlantic.

One of the challenges of studying the tectonic evolution of Iberia is the determination of the boundary between continental and oceanic crust, i.e., the line along which the successful onset of sea floor spreading took place. All pre-split reconstructions of the North Atlantic are dependent on some ad-hoc assumption regarding this boundary (Dewey et al., 1973; Le Pichon et al., 1977; Kristofferson, 1978; Masson and Miles, 1984; Srivastara and Tapscott, 1986). This uncertainty notwithstanding, it is clear that the location of the Lusitanian Basin has little connection with the inception of the ocean. Several reasons support the assumption that the successful rifting between Iberia and the Grand Banks of Newfoundland was accomplished after a jump of the rifting axis towards the W, to the place where the true ocean-continent boundary is presently located. The main argument is the existence offshore Portugal and W of the Lusitanian Basin of a block of shallow granitic basement, presently outcroping at two small islands, Berlengas and Farilhões. This positive block is not due to the later Alpine evolution of the area, as can be established by the analysis of the stratigraphic record: Vanney and Mougenot (1981) and Guery (1984) recognize this basement block as a westerly source of clasts to the Lusitanian Basin throughout the Jurassic and Cretaceous and during the Oligocene, and considered it a permanent feature of the Mesozoic palaeogeography.

Figure 1.5 shows the configuration of the set of Early Jurassic rift basins on both sides of the Atlantic. In the Grand Banks, a large number of small elongated rift basins can be found which to the S of Flemish Cap are oriented NE-SW and are offset by NW-SE transform faults (Figure 1.5) ; to the N of that point the pattern is reversed: the basins now trend NW-SE, and the transform faults strike NE-SW. Although the geometry of the offshore extension of the Lusitanian Basin is not well known, it seems to reproduce a similar pattern: to the S of latitude 40°N, the basin cuts the shoreline at an oblique angle, striking NNE-

SSW; it reaches inland as far as the Porto-Abrantes Fault and then (probably) swings to the W, crossing the shoreline again and defining, with the offshore Porto and Inner Galicia Basins, a NNW-SSE trend. There was an interval of 40 million years between the end of the Early Jurassic rifting pulse that shaped the Lusitanian Basin and the rifting episode that was to evolve successfully into the opening of the ocean (Tankard and Welsink, 1987; Hubbard, 1988). This was a period of major tectonic modifications taking place in the vicinity of Iberia. With the northward propagation of sea floor spreading in the Central Atlantic, the Moroccan block to the N of the South Atlas Fault started to move to the E even faster than the African craton, reversing the polarity of strike-slip in that fracture and partially closing the High Atlas Trough (Dewey et al., 1973). The changes in stress regime at the latitude of the Lusitanian Basin were probably important enough for its geometry to become obsolete. This may have favoured the westward jump of the rifting axis to its final position, now striking N-S and offset by NW-SE transforms only (Figure 1.6).

Once sea floor spreading started to the N of the Azores-Gibraltar Transform in the Barremian (Masson and Miles, 1984), a new element was introduced which recorded the tectonic evolution of Iberia: sea floor magnetic lineations. Unfortunately, most of the initial stages of drifting took place during the Cretaceous Magnetic Quiet Period, and only at anomaly 33 time (80 Ma) did a clear pattern start to be imprinted. Between the inception of sea floor immediately to the N of the Azores-Gibraltar Transform and the Late Aptian (118 Ma; anomaly M0) when drifting started offshore Galicia and in the Bay of Biscay (Groupe Galice, 1979; Montadert et al., 1979; Boillot et al., 1987), an additional complication was introduced by the fact that the rift-drift transition was diachronous along the western Iberian Margin (Masson and Miles, 1984). Also, the Alpine deformation was important offshore SW Iberia, making the identification of magnetic lineations even more problematic. Nevertheless, the wavelength character of the anomalies can be considered even when particular lineations cannot be identified, and this will be done for the interval between the Barremian and anomaly 34. Figure 1.6 shows the magnetic anomaly chart of Verhoef et al. (1985) as background to the following discussion.

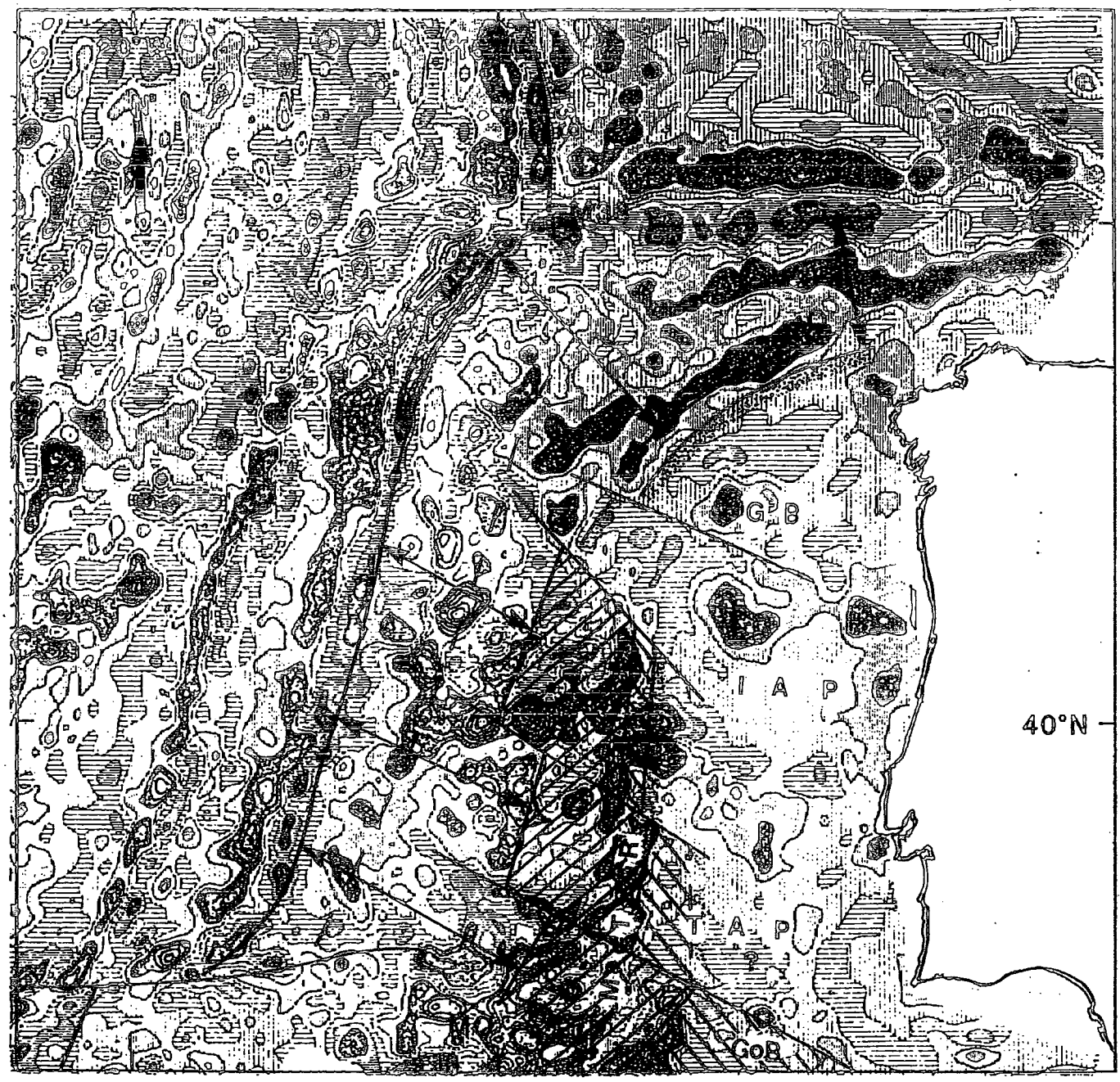

negative magnetic anomaly

positive magnetic anomaly

oceanic crust older than anomaly MO

oceanic crust contemporaneous of the opening of the Bay of Biscay

GB - Galicia Bank
IAP - Iberian Abyssal Plain
MTR - Madeira-Tore Rise
TAP - Tagus Abyssal Plain
GoB - Gorringe Bank

Fig. 1.6 - Tentative model for pre-anomaly 33 sea floor spreading offshore Portugal. Magnetic anomalies after Verhoef et al. (1986).

The Deep Sea Drilling Project showed that the Gorringe Bank, 110 km off the SW corner of Portugal (Cape São Vicente), is a slab of uplifted oceanic crust (Ryan and Hsu, 1973). To the N, offshore Galicia, the ocean-continent boundary is further W, surrounding the seaward protuberance of the Galicia Bank (Groupe Galice, 1978). In between lies an area of deep water, with the Iberian Abyssal Plain to the N and the Tagus Abyssal Plain to the S, where the boundary cannot be located in a conclusive manner. The first strong magnetic anomaly borders the western margin of the Tagus Abyssal Plain, in clear association with the structural high of the Madeira-Tore Rise, and was identified by Masson and Miles (1984) and Srivastara and Tapscott (1986) as anomaly M0. This anomaly corresponds to the continent-ocean boundary W of the Galicia Bank and in the Bay of Biscay (Verhoef et al.,1985), but considerable amounts of older oceanic crust (Valangian-Aptian) are likely to exist to the S. In fact, the transition from magnetically quiet to magnetically noisy crust, trending N-S between 37°N and 41°N, steps towards the W with increasing latitude, indicating the existence of NW-SE transform faults that were active during the early stages of sea floor formation (Figure 1.6). These transforms allowed for the differential spreading rates implied by a northward propagating rift, and the control they imposed on the sedimentation in marginal basins is documented offshore Newfoundland (Tankard and Welsink, 1987) and in the European continental shelf (Masson and Miles, 1986). As a consequence of their role, oceanic crust of increasingly older age should be found with decreasing latitude, offshore Portugal.

The nature and age of the crust underlying the Tagus Abyssal Plain, which is key to the issue under discussion, has been the subject of different interpretations. Le Pichon et al. (1977) pointed out that a large gap would result in the fit of the continents if the area were floored by Mesozoic oceanic crust, and suggested that a Palaeozoic oceanic or continental crustal character for this area would overcome the difficulty. Mason and Miles (1984) also rule out, on geometric grounds, Mesozoic sea floor spreading in the abyssal plain, and propose that it is floored by Palaeozoic continental crust. Mauffret et al. (in press) prefer a continent-ocean boundary much closer to the shoreline, and introduce a Late Jurassic spreading episode, abandoned in the Early Cretaceous by a westward jump of the spreading axis, to justify the presence of oceanic crust in the area.

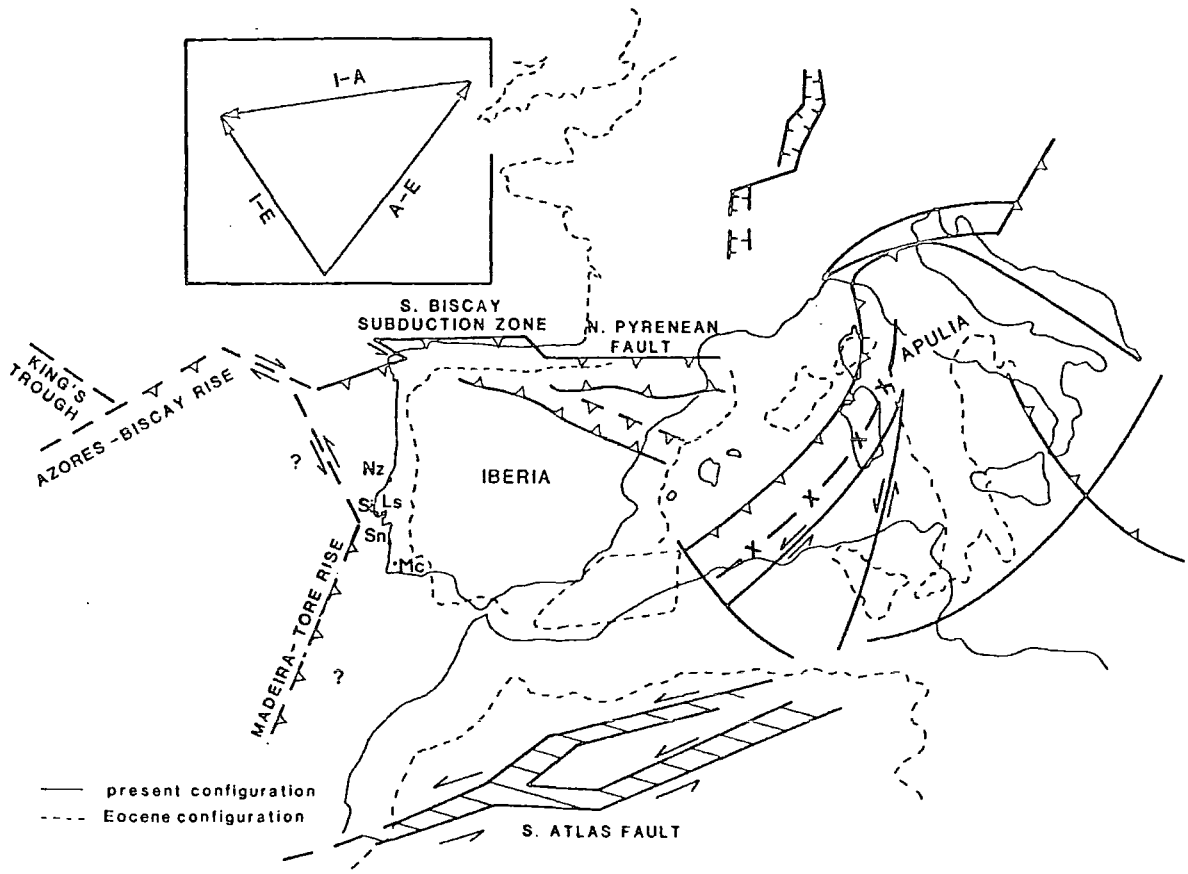

Fig. 1.7 - Early Cainozoic tectonic setting of the western Mediterranean and eastern North Atlantic. After Gealey (1988) and Grimaud et al. (1982), modified. The dots show the locus of magmatic activity in southwestern Portugal at the end of the Cretaceous, after Aires-Barros (1979): St - Sintra; Sn - Sines; Mc - Monchique; Nz - Nazaré; Ls - Lisbon. The inset shows the Early Cainozoic kinematic model proposed in chapter 5 : I - Iberia; E - Eurasia; A - stable Africa.

The nature of the crust underneath the Tagus Abyssal Plain is the object of research currently underway (L.M. Pinheiro, pers. comm.), and with the evidence available to date it is not possible to exclude a possible continental character, nor is it possible to confirm it. This hypothesis, leading to a 250 km wide zone of continental crust offshore Portugal, is consistent with recent results of deep seismic reflection studies that indicate less extension of continental crust than usually assumed offshore Newfoundland (Keen and deVoogd, 1988).

Besides the location of the ocean-continent transition, another outstanding problem of the tectonic evolution of Iberia is its time-varying links with either Africa or Eurasia. After the Late Hercynian fracturing of the Hercynian Belt and the extensional tectonics of the Early Mesozoic, Iberia was a fragment of continental crust with little continuity towards the N (Biscay-Pyrenees Trough) or S (Algarve-Guadalquivir Trough and High Atlas Trough). Based on sea floor spreading data, Klitgord and Shouten (1986) conclude that Iberia was part of the African Plate from the beginning of drifting to anomaly 10 time (30 Ma), well into the Cainozoic. The reconstruction of Masson and Miles (1984), in an attempt to solve the pre-drift overlap of the Galicia Bank and the Flemish Cap, implies some degree of relative motion between Iberia and Africa during the early stages of spreading (Srivastara and Tapscott, 1986).

The discussion of the geodynamics of Iberia (chapter 5) will show that the ambiguity of its movements was to persist throughout the Cainozoic and into the present. But before proceeding to this, the evidence and discussions on the rotation of the Iberian Peninsula will now be reviewed.

1.4.2 The rotation of Iberia.

The classic works of Van der Voo (1969) and Van der Voo and Zijderweld (1971) established from palaeomagnetic evidence that Iberia rotated 35 degrees conterclockwise between the Triassic and the Late Cretaceous. This framework was taken into account in all the later continental reconstructions. The mechanism of rotation, however, remains a focus of controversy. Bullard et al. (1965) "closed" the Bay of Biscay by rotating Iberia around an eulerian pole located on the axis of the Pyrenees, and thereby improved the geometrical fit of the continents. Le Pichon and Sibuet (1971 a,b), based on onshore structural data, ar-

gued in favour of a pole of rotation near Paris, implying large amounts of dextral strike-slip along the Pyrenees during the opening of the Bay of Biscay. Masson and Miles (1984) claim that the pre-anomaly 34 evolution is best explained as a single rotation, and exclude major transcurrent movement in the Pyrenees during the Early Cretaceous. Schott and Peres (1988) argue again in favour of the transcurrent model, based on palaeomagnetic data from the Pyrenees.

Galdeano et al. (1989), based on palaeomagnetic data collected to the W of Lisbon, propose that the post-Aptian opening of the Bay of Biscay was due to transcurrent movement of Iberia without rotation, and introduce an earlier Late Jurassic simple rotation as a radical solution to the problem of the rotation of Iberia. In view of the tectonic setting of Western Iberia during the Late Jurassic, discussed in the previous section, palaeomagnetic data pertinent to this stage of evolution ought to be considered with great caution, since localized block rotations associated with the northward propagation of the rift may have occurred, and these would produce results undistinguishable from those of a rigid-body rotation of the Peninsula. The more conservative view that the rotation of Iberia and the opening of the Bay of Biscay took place at the same time and after the Late Aptian (as indicated by sea floor spreading) is therefore prefered.

1.4.3 Late Cretaceous reorganization.

Simultaneously with the rotation of Iberia, the first stages of continental collision were taking place in the Eastern Mediterranean, following the consumption of the Tethys Ocean (e.g., Gealey, 1988). On the Canadian margin, the stratigraphy indicates a steady period of post-rift thermal subsidence outpacing sediment supply and leading to the deposition of a thick transgressive megasequence between the Cenomanian and the Mid Oligocene (Tankard and Welsink, 1986; Hubbard, 1988). This is in sharp contrast with the evolution of the Lusitanian Basin, were a Cenomanian transgression was followed by a period of uplift and erosion starting at the Turonian and lasting through the remaining Cretaceous and Early Palaeogene (Berthou and Lauverjat, 1979). The Nazaré Fault had an important role in this phase of tectonic instability, marking the northern limit of the uplifted area, and was the locus of basaltic extrusions (Figure 1.7) during the Late Cretaceous (Aires-Barros, 1979).

It seems that the end of the Cenomanian transgression marks a turning point when most of the control on the tectonics of the Portuguese margin shifted from the Atlantic to the Mediterranean, thereby truncating prematurely a passive margin type of evolution. To the S, the High Atlas Trough of Morocco was also evolving from transgressive deposition in the Cenomanian (Wurster and Stetz, 1982) to structural inversion from the Turonian onwards (Stetz and Wurster, 1982). In the Alps, Dewey et al. (in press) assign to the Cenomanian-Turonian boundary the onset of northeasterly directed convergence between Africa and Europe. With the "tightening of the grip" between the two plates, tectonism was likely to propagate well into the continents. In southwestern Portugal, the emplacement of alkaline intrusives in Sintra, Sines and Monchique (Figure 1.7) during the Late Cretaceous (Aires-Barros, 1979) may indicate the switch to the new tectonic regime, which was to reach its greatest intensity during the Eocene and during the Miocene.

1.5 Cainozoic evolution of Iberia.

1.5.1 Collision with Europe.

The Early Cainozoic collision between Iberia and Europe is well recorded in the Pyrenean Chain. However, no agreement has been reached about the direction of the convergence leading to the collision. Le Pichon and Sibuet (1971) assumed that the continental collision was caused by the movement of Iberia towards the NE at the end of the Cretaceous. But Grimaud et al. (1982), using the vast amounts of seismic reflection and magnetic data acquired during the 1970's, identified an E-W Early Cainozoic active margin to the N of Iberia offset by NW-SE transform faults (Figure 1.7), and favoured therefore a NW-SE direction of convergence. Schott and Peres (1988) described palaeomagnetic evidence for clockwise block rotations of up to 102° in the Pyrenees which they attributed to Early Cainozoic compression and dextral shear along the Pyrenean fold belt, which is in good agreement with the model of Grimaud et al. (1982).

Whether Iberia is considered a promontory of Africa or an independent microplate during the Early Cainozoic, the outstanding problem that remains to be solved is the westward continuation of its northern boundary, i.e., the offshore

accommodation of the relative movements. Le Pichon and Sibuet (1971) first addressed this problem, extrapolating the Pyrenees-Biscay trend into the ocean along the Azores-Biscay Rise and the King's Trough (Figure 1.7). As a result of their assumed SW-NE motion of Iberia, a compressive origin was attributed to the King's Trough. Grimaud et al. (1982) proposed a model with similar geometry but different motions, the King's Trough now being predominantly transcurrent. However, the clear evidence put forward by Kidd et al. (1982) for the extensional origin of that structure sheds doubt on the validity of both interpretations, as does the continuation of the Azores-Biscay Rise towards the SW past the King's Trough. Also, the chart of magnetic anomalies of Verhoef et al. (1986) shows clearly that the Mesozoic anomalies 34 to 31 cut obliquely across the Azores-Biscay Rise without distortion, weighing therefore against an Early Cainozoic plate boundary in the area.

By the end of the Eocene the plate tectonic setting changed drastically (e.g., Rona and Richardson, 1978): the movement of Africa with respect to Eurasia was re-oriented to a northwesterly direction, with a pole of rotation near the Canary Islands (Dewey et al., in press). An E-W plate boundary was established to the E of the Azores Triple Junction, showing extension at its eastern end and pure dextral strike-slip along the 700 km long Gloria Fault, passing into a zone of NW-SE convergence near the 16°E meridian. This is essentially the situation that prevails today (Figure 1.8), as indicated by the seismic activity (Purdy, 1975; Moreira, 1985; Grimison and Chen, 1986; Buforn et al., 1988). For this reason the Miocene deformation of Iberia will be discussed in some detail.

1.5.2 Collision with Africa.

With the new direction of convergence between Africa and Eurasia, characterized by an E-W component of movement of the former relative to the latter, the tectonic setting of Iberia changed from continental collision to the NE to continental collision to the SE. The peak of tectonic activity that caused the uplift of the Pyrenees in the Eocene was followed in the Mid Miocene by the tectonism recorded in the Betic Chain of Southeast Spain and in the Rif Chain of Northern Morocco (Julivert et al., 1974; de Smet, 1984).

Contrasting with the Pyrenean Orogeny, the Miocene continental collision caused widespread deformation throughout Iberia. From this period dates one of the main structural features of Spain, the Central Cordillera (Figure 1.1), the origin and structure of which are poorly understood. It is composed of several mountain ranges striking NE-SW (Somosierra, Guadarrama, Gredos, Gata, Peña de Francia), and can also be traced across Portugal along the Estrela, Aire, Candeeiros and Montejunto Ranges, totalling more then 500 km in length. It consists of uplifted and tilted basement blocks, in places vertically offset as much as 3000 meters with respect to the basement underneath the flanking basins (Julivert et al., 1974). Another important structure of Miocene age is the Iberian Cordillera, this time striking in a NW-SE direction.

In Portugal, the Montejunto and Candeeiros Ranges (Figure 2.1), corresponding to the western termination of the Central Cordillera, were the scope of a preliminary structural investigation under the aegis of the RESTE Project (Hutton and Gawthorpe, 1988). Here, a wealth of diagnostic features indicate the dominance of sinistral strike-slip during the Miocene deformation, and the offset, but probably linked, Arrábida Range (Figure 2.1) was also interpreted as a sinistral transpressive structure (Fonseca et al., 1988; Hutton and Gawthorpe, 1988; and also Montenat et al., 1988). The more localized study of Guery (1984) also identified sinistral strike-slip as the origin of the deformation of the Montejunto Range.

Regarding the offshore, the multichannel seismic reflection data of Maufret et al. (in press) shed unprecedented light on the tectonic structure of the Portuguese continental margin. The authors discribe with particular detail the Miocene tectonic event and reveal the presence of important NNE-SSW strike-slip faults with transpressive structures and probable sinistral movement, particularly important to the S of latitude 38 °N. The westernmost and most important of such faults runs along the strike of the Montejunto-Candeeiros lineament. "Pull-apart" basins and compressive ridges associated with the strike-slip faults are also described.

1.5.3 Active tectonics.

The structural and seismotectonic complexity of the Euro-African plate bound-

ary between longitude 16° W and the Strait of Gibraltar have been the subject of numerous studies. Minster and Jordan's (1978) RM2 model of relative plate motions positioned the African pole of rotation at latitude 25.23±4.23 N and longitude 21.19±0.98 W, with a rate of anticlockwise rotation of 0.104±0.036 °/Ma. Searle (1980) mapped the tectonic elements of the Azores triple junction, and concluded that they are in good agreement with this pole position. Buforn et al. (1988) used a selection of the source mechanisms between the Azores and Gibraltar to propose a slightly different position of the pole, at 28.2° N and 21.1° W. Whatever result is prefered, it will still explain the main characteristics of the contact between the plates along its 4500 km of length, namely crustal accretion at the Azores triple junction (Terceira Rift) passing into pure dextral strike-slip along the Gloria Fault or East Azores Transform and then into ocean-ocean oblique convergence and continental collision.

Purdy (1975) conducted what was probably the first detailed and integrated geological-geophysical investigation of the eastern end of the "Azores-Gibraltar Transform". He concluded that the mechanical behaviour of the lithosphere was atypical of areas of lithospheric consumption, in view of the absence of a clear Benniof Zone; perhaps for the first time, the inadequacy of Plate Tectonics to explain small-scale complexities in convergent boundaries was clearly stated.

Udias et al. (1976) argued in favour of the continuation of the linear plate boundary towards the E as far as Gibraltar, and supported an earlier suggestion that the Alboran Basin (westernmost Mediterranean) might correspond to an independent microplate, explaining in this manner the more diffuse seismicity to the east of the Strait of Gibraltar. The existence of very deep (~650 km) earthquakes showing E-W compression in the Granada region (SE Spain) was attributed by these authors to a detached piece of lithosphere subducted eastwards at a palaeo-subduction zone at the Gibraltar Arc.

More recently, Grimison and Chen (1986) revised some earlier hypocentre parametres for events E of longitude 18° W, and concluded in favour of a wide (100 to 300 km) zone of distributed deformation, rather than any particular linear trend identifiable as a plate boundary. Although the authors recognized the consistency of the orientation of the P-axes of the source mechanisms, giv-

ing NNW-SSE horizontal compression, they observed that the slip vectors were widely scattered around the directions predicted by the broadly accepted African pole of rotation (Minster and Jordan, 1978). The absence of a single plate boundary in the region was partly attributed to limited lateral offset of the two plates, causing two pieces of mechanically and thermally similar oceanic lithosphere to collide (Karner et al., 1985). The seismicity of the zone of continental collision west of Gibraltar was very poorly reported in this study.

Buforn et al. (1988a, b) also revised previous results regarding focal mechanisms, including the area to the S of Portugal and Spain, and contended that the observations are better explained in terms of a subduction zone between Africa and Iberia, with lithospheric material being pushed under Iberia in a northwesterly direction. The deeper (650 km) earthquakes were still attributed to a relic slab, its subduction being independent of the current tectonic processes.

In the interior of Iberia, the active tectonics become more intense towards the Mediterranean, and are particularly significant in the Betic Chain, in the Catalan Chain and in the Pyrenees (Julivert et al., 1974). In the hinterland, most of the fracture tectonics of the Miocene (Central Cordillera, Iberian Chain) seem to have terminated at the end of that period, although some isolated places (Montes de Toledo, Campo de Calatrava) display clear neotectonic deformation, sometimes accompanied by alkaline volcanism (ibid.).

Close to the western margin of Iberia the neotectonics have clear expression again. From the extreme N (Galicia) to the extreme S (Algarve), the coastal region shows a dense network of faults with signs of activity during the Quaternary, extending farther inland in the northern region of Portugal (Julivert et al., 1974; Cabral, 1986). According to the indications of the seismicity, the current faulting in the Portuguese territory is more intense in the region between the Nazaré Fault and the Arrábida Range (Estremadura), in the Algarve and in the Northeast of the country (Moreira, 1985). Besides faulting, the neotectonics of Portugal are also characterized by regional uplift, more important in the North, where it reached 450 m during the Quaternary, than in the South, where it was of the order of 250 m during the same period (Cabral, 1986).

In chapter 5 the problem of the current geodynamics of Iberia will be adressed again, and an alternative model will then be proposed. In the next chapter, the discussion will be focused on the evolution of the Lusitanian and Lower Tagus Basins throughout the tectonic episodes that have been described till now.

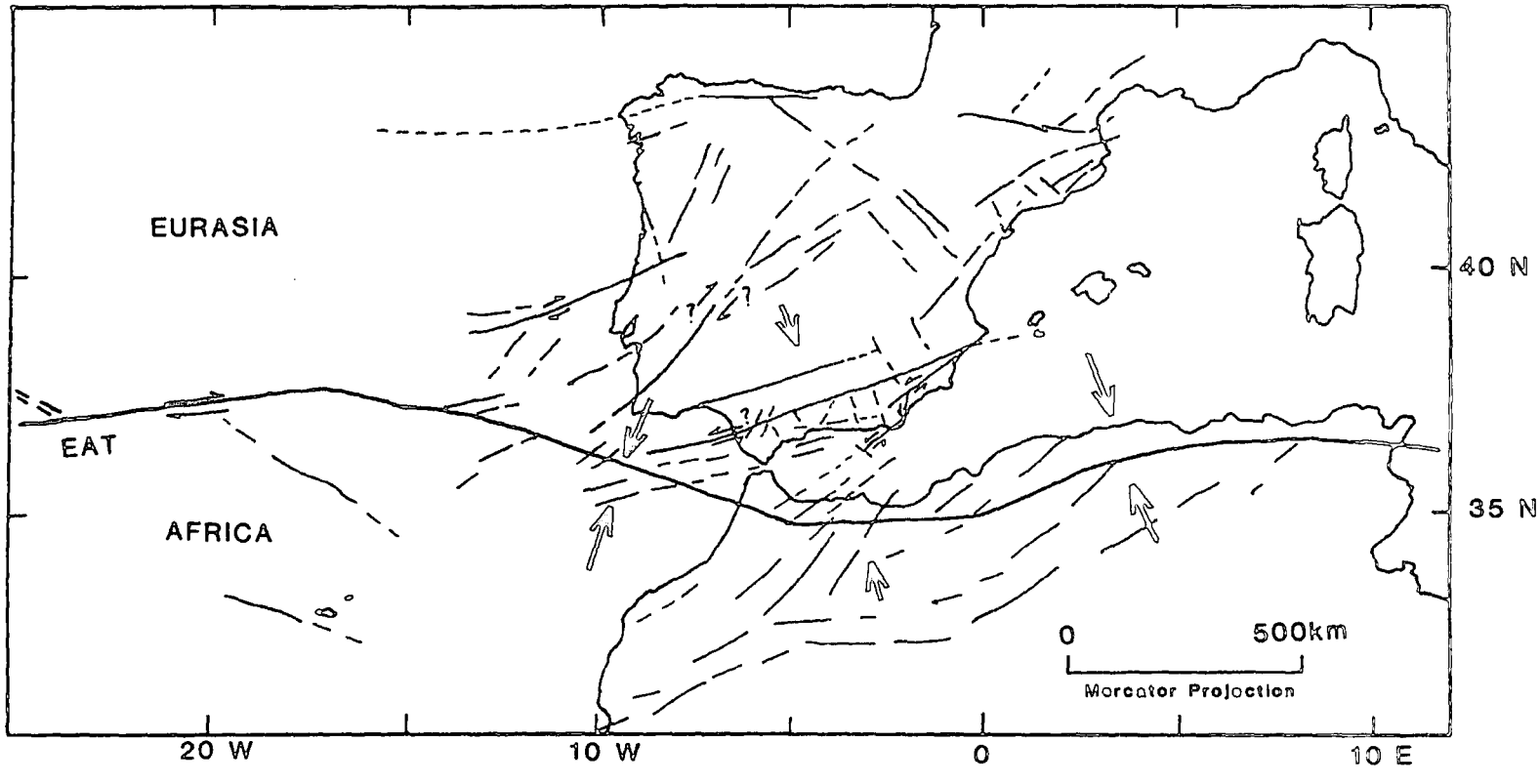

Fig. 1.8 - Neotectonic setting of Iberia, after Udias et al. (1986). The arrows show the proposed orientation of the regional maximum compressive stress.

Chapter II

Analysis of the Meso-Cainozoic Lusitanian and Lower Tagus Basins

2.1 Broad structure of the basins.

The Meso-Cainozoic cover of western Portugal may be divided into three main zones (Figure 2.1): the Lusitanian Basin *sensu stricto*, characterized by the outcrop of Mesozoic sediments; the Lower Tagus (and Sado) Basin, to the SE of the former, with Tertiary and Quaternary cover; and the Monte Real Basin to the NW, also covered by Cainozoic sediments. The Mesozoic is also present in the flanking basins ; however, drastic changes in the sedimentary columns (Figure 2.2) reflect the existence of major tectonic boundaries between the different regions.

The boundary between the Monte Real and the Lusitanian Basins is the Nazaré Fault, a major tectonic structure associated with the Nazaré Submarine Valley on the continental shelf and separating areas with different structural style (Vanney and Mougenot, 1981; Wilson et al., in press). Between the Lusitanian and the Lower Tagus basins the boundary is more complex (Figure 2.1): to the N of Lisbon it follows the NNE-SSW Vila-Franca Fault for 25 km, to inflect along a less defined N-S trending fault towards the Montejunto Range; here it regains the NNE-SSW trend, this time with a complex geometry due to the presence of large rotated blocks (Hutton and Gawthorpe, 1988), and is truncated near Tomar by the Porto-Abrantes Fault. In the vicinity of Lisbon, the boundary between the Mesozoic and Cainozoic sediments is lost within the Lisbon Volcanics, emplaced near the transition to the Cainozoic (Aires-Barros, 1979; Telles-Antunes, 1979).

Taking into account the tectonic boundaries and differences in the sediment record, further divisions may be considered within the Lusitanian Basin: to the N of the Torres Vedras-Montejunto Fault, the Bombarral Sub-basin, where maximum basement subsidence occurred during the Jurassic ; to the S of that

fault and to the W of the Sobral Fault, the Turcifal Sub-basin; and to the E of the Sobral Fault, the Arruda Sub-basin.

The Lower Tagus Basin (ignoring its southward continuation, the Sado Basin, with which it is usually merged to form one single unit) shows two distinct depocentres, which can be called the Setúbal Peninsula Sub-basin and the Ribatejo Sub-basin. Both of these are very clear on the Bouguer anomaly pattern (Figure 2.3a) and are separated by the N-S trending Alcochete Fault Zone (unpublished data, GPEP; Fonseca et al., 1988).

2.2 Subsurface structure.

Published studies of the subsurface geology of the Lusitanian Basin are rare, and the exceptions are mostly concerned with sedimentological aspects (Guery, 1984; Guery et al., 1986; Montenat et al., 1988; Wilson,1988; Wilson et al., in press). For the Lower Tagus Basin, such studies are nonexistent. At an early stage of the RESTE Project it was felt that the investigation of the structural characteristics of the two basins was needed to provide a framework for the understanding of the active tectonics. Such study was carried out using unpublished commercial data (seismic sections, two-way traveltime maps, well and gravity data) kindly made available by G.P.E.P., Lisbon, and also with field work.

Crustal studies in the area of the Lusitanian Basin were carried out in the late seventies (Moreira et al., 1980; Mendes-Victor et al., 1980). The Nazaré-Cabo Raso refraction profile (Figure 2.4), parallel to the dominant structural trend, yielded a crustal thickness of 31 km (Moreira et al., 1980). The Peniche-Montemor o Novo refraction profile, prependicular to the structural trend (Figure 2.4), gave contrasting results concerning layer thicknesses and interface depths and tilts for the two margins of the Tagus River (Mendes-Victor et al., 1980). Figure 2.4 synthesizes the main results of the refraction studies. The crustal structure for the southeastern extreme of the section is extrapolated from the Ferreira-Évora profile of Caetano (1984).

The Bouguer gravity anomaly profiles of Figure 2.3b) show a proeminent regional increase towards the W (approx. 0.5 mgal km^{-1}). A seaward increase in gravity is common in Atlantic margins, and reflects the gradual thinning of the

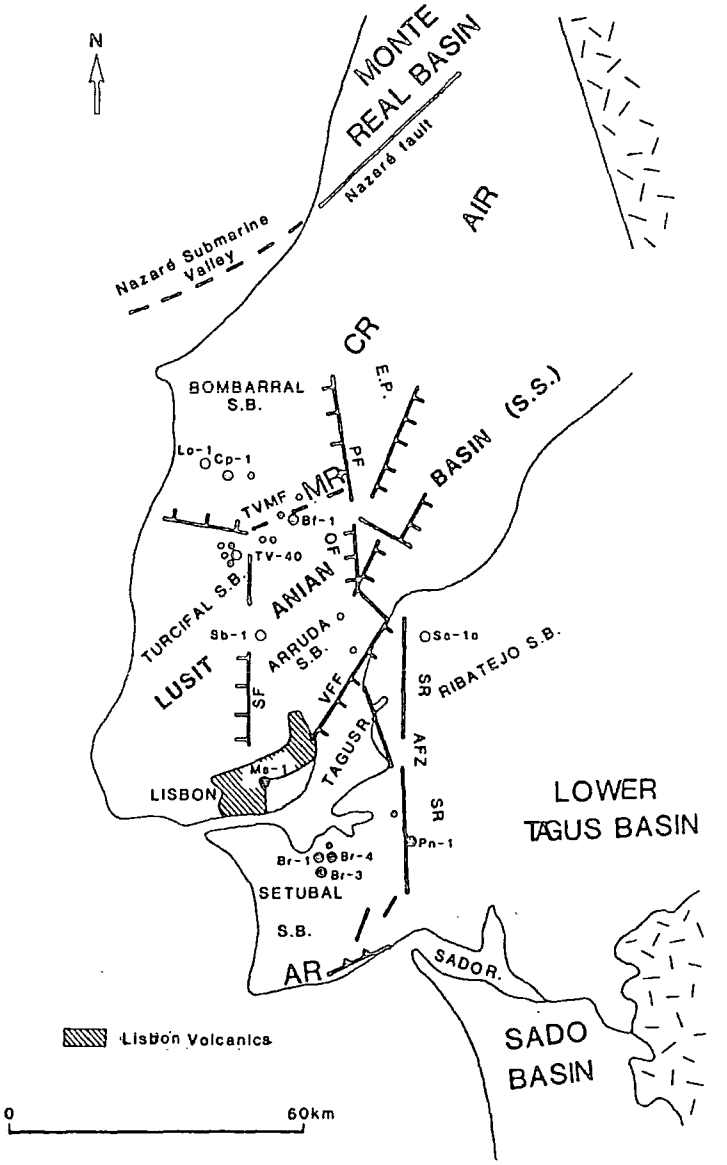

Fig. 2.1 - Main divisions and structural features of the Meso-Cainozoic cover of western Portugal. Based on Montenat et al. (1988) and Wilson et al. (1988). AIR - Aire Range; CR - Candeeiros Range; MR - Montejunto Range; AR - Arrábida Range; EP - Espigão Platform; TVMF - Torres Vedras-Montejunto Fault; PF - Pragança Fault; SR - Samora Ridge; OF - Ota Fault; SF - Sobral Fault; VFF - Vila Franca Fault; AFZ - Alcochete Fault Zone. S.B. - sub-basin. Dots indicate the location of commercial wells, larger dots with code names indicate wells used in this study.

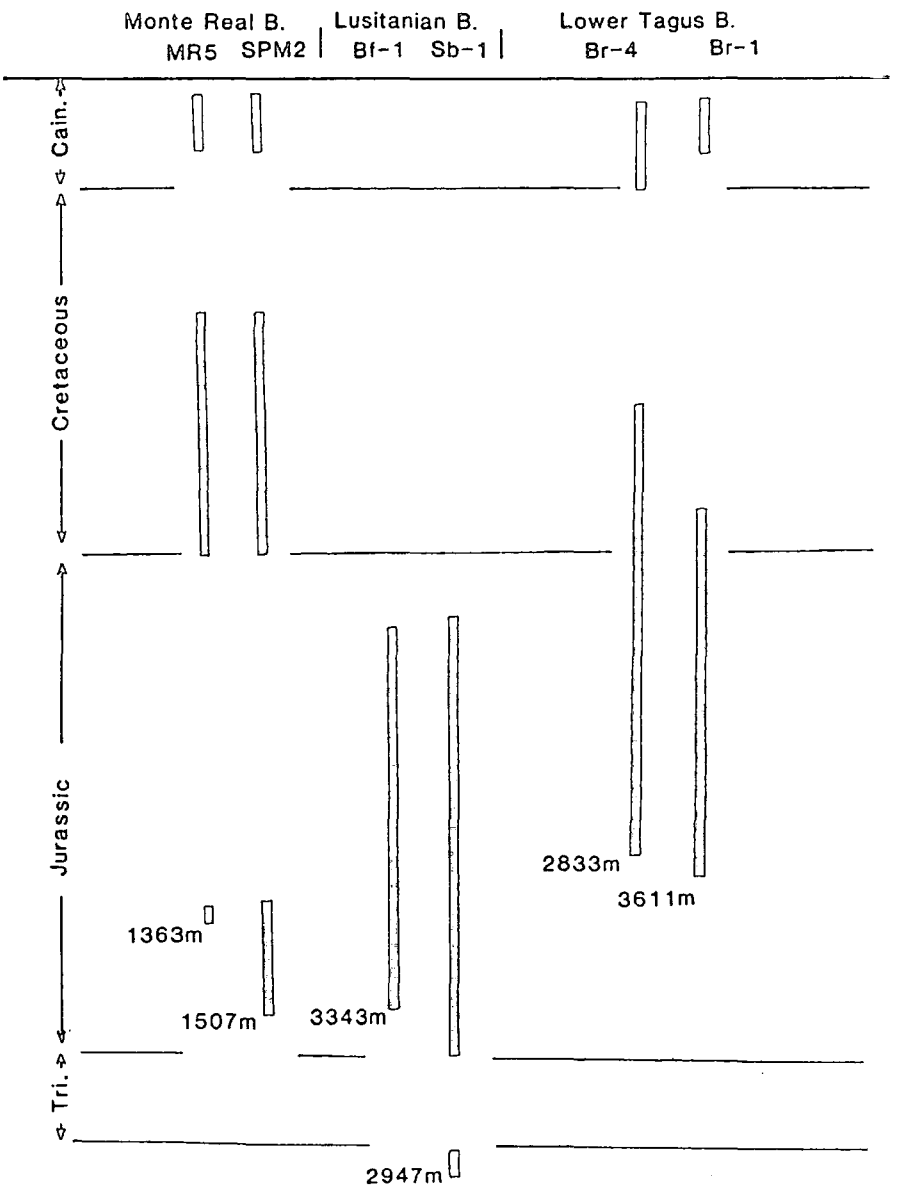

Fig. 2.2 - Typical sedimentary collumns of the Monte Real, Lusitanian and Lower Tagus Basins. Based on data made available by GPEP, Lisbon.

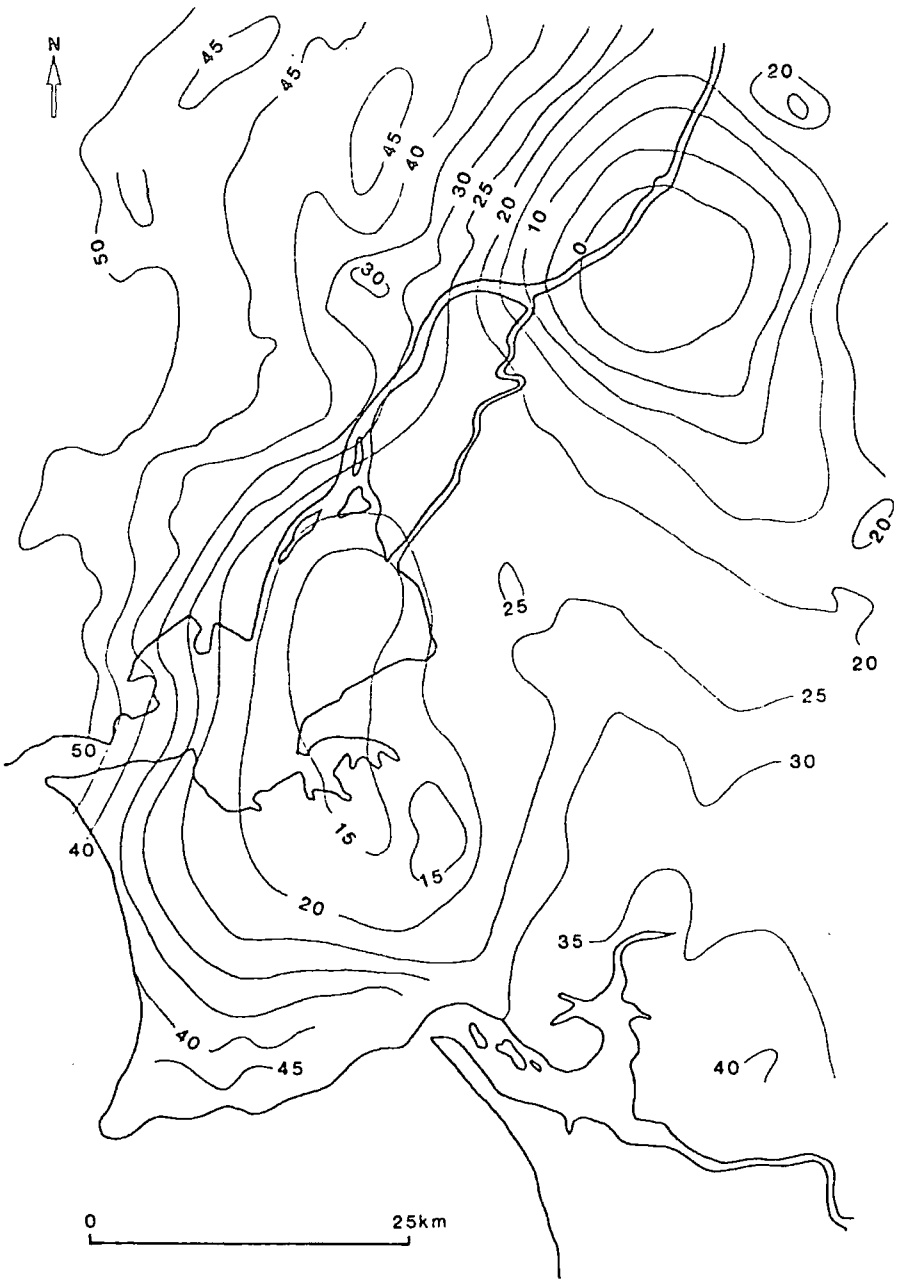

Fig. 2.3a - Bouguer gravity anomalies, in mgal, on the Lower Tagus Basin. Contour interval is 5 mgal.

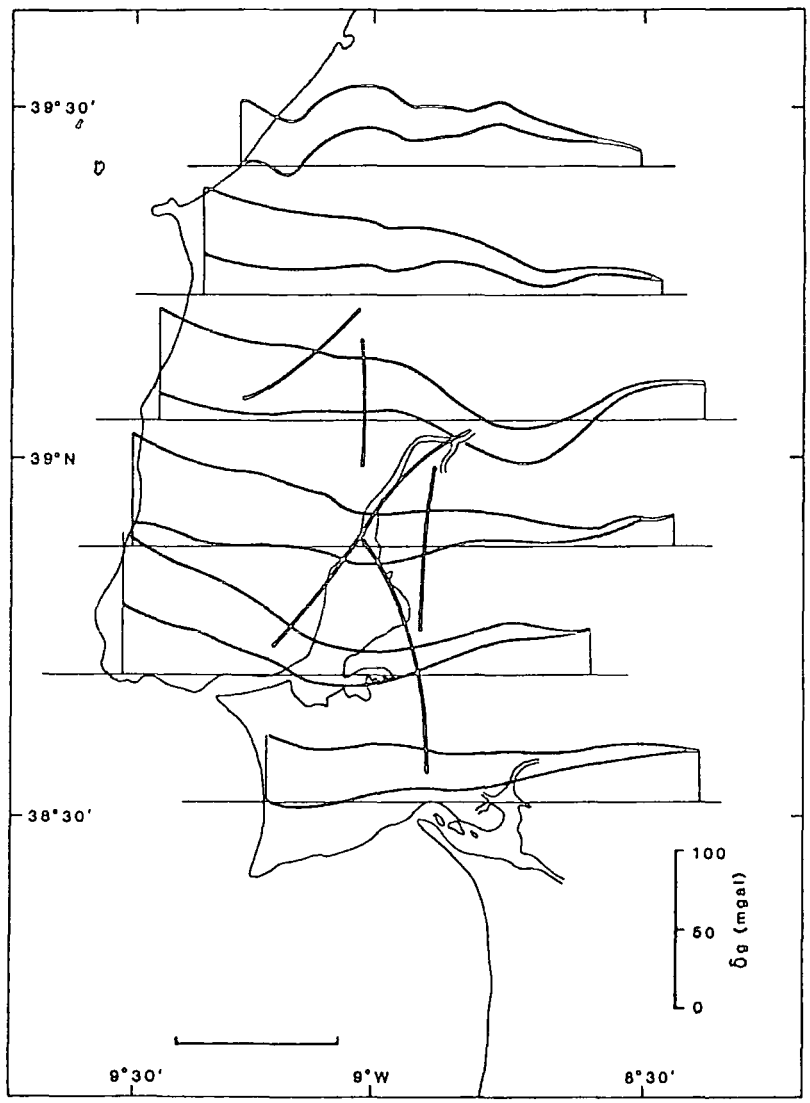

Fig. 2.3b - E-W profiles of Bouguer gravity anomaly, drawn after the map reproduced in a), with and without the subtraction of the regional gradient (0.48 mgal km^{-1}). The scale for all profiles is given in the lower right corner of the figure. Main intrabasinal faults are shown as thick lines Based on data made available by GPEP, Lisbon.

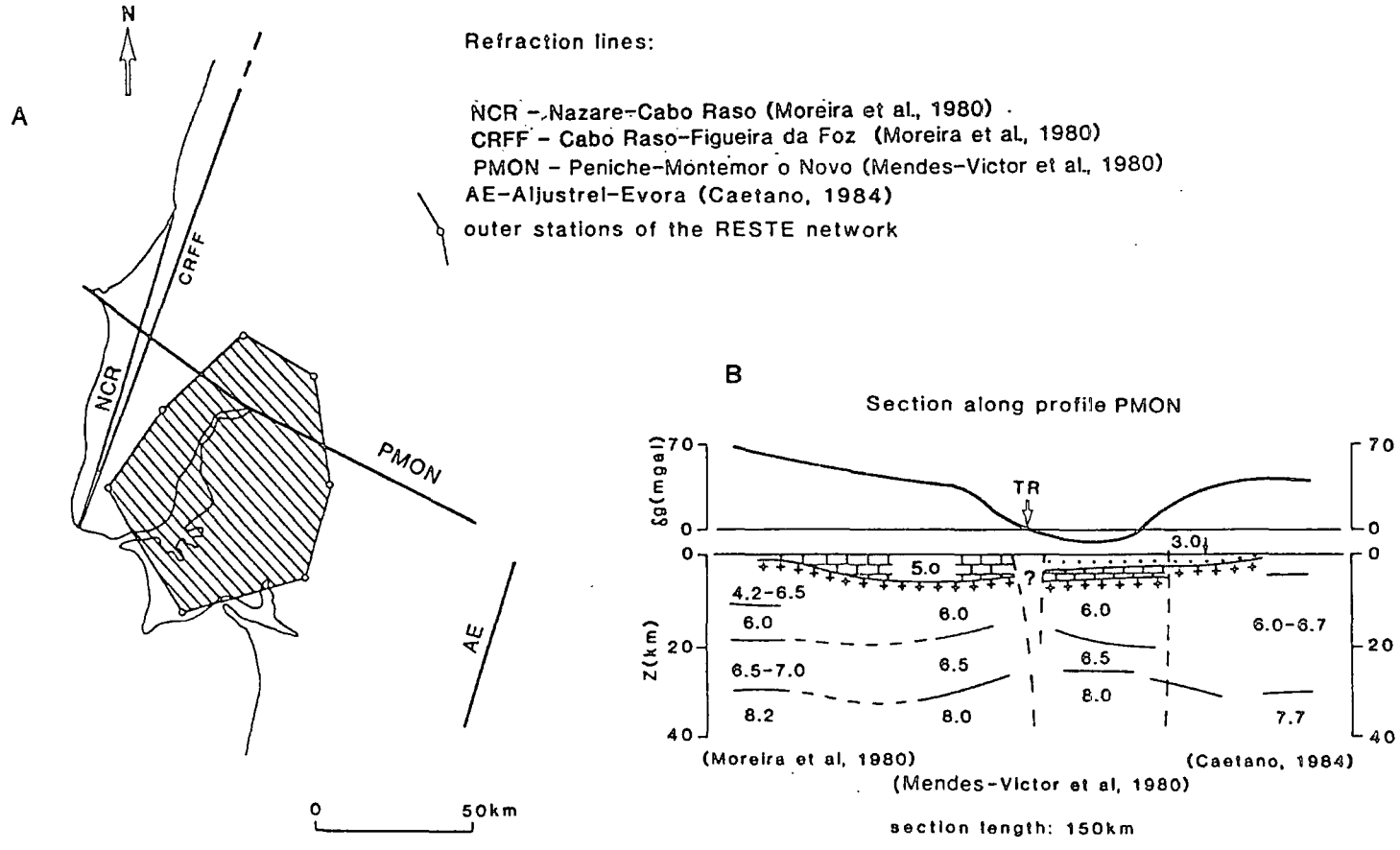

Fig. 2.4 - A) Location of the refraction profiles mentioned in the text. The area covered by the RESTE Network is outlined; B) Synthesis of the results of the refraction surveys. Seismic velocities in km s^{-1}. Based on Moreira et al. (1980), Mendes-Victor et al. (1980) and Caetano (1984).

continental crust in the direction of the ocean-continent boundary (Grow, 1981; Keen, 1982). However, according to Figure 2.4b) no such thinning is observed underneath the Lusitanian Basin. The conspicuously thin crust to the E of the Tagus River reported by Mendes-Victor et al. (1980) is only a local perturbation, since the crust then thickens again towards the W. This observations will be discussed in section 3.3. The short wavelength gravity lows correspond to the location of Cainozoic depocentres, described in the previous section.

The continental shelf offshore Portugal has been intensively surveyed by single channel reflection profiling, and its shallow structure is well known (Mougenot, 1976; Mougenot et al., 1979; Vanney and Mougenot, 1981). Figure 1.4c) shows the pattern of faulting of the shelf, after Vanney and Mougenot (1981). Although the faults were only observed in shallow sediments, they are likely to correspond to the reactivation of deeper structures, and probably provide a broad picture of the tectonic framework of the shelf.

2.3 Evolution of the basins.

2.3.1 Aborted rift stage of evolution.

According to Wilson et al. (in press), the sedimentary fill of the Lusitanian Basin consists of four megasequences separated by basinwide unconformities. The first megasequence ranges from Late Triassic to Mid Jurassic, and corresponds to the first rifting pulse of the Portuguese margin (section 1.3). At this early stage the Lusitanian Basin did not show yet the differentiation into sub-basins. With a structure of tilted blocks controlled by the NNE-SSW basement faults, it accumulated thick layers of evaporites on several 10 km scale half-graben, and reached a width of about 100 km, between the crystalline basement block of Berlengas to the W and the Hercynian granites of the Hesperic Massif to the E (Guery, 1984). During the Early and Mid Jurassic, this evaporitic complex was blanketed by open water marine sediments, in turn deformed by the remobilization of the evaporites, which migrated upwards along the block-bounding NNE-SSW faults (Montenat et al., 1988).

2.3.2 Successful rift stage.

The absence of latest Calovian-Early Oxfordian sediments constitutes the first megasequence boundary (Wilson et al., in press), and marks the beginning of a new tectonic setting related to the early stages of opening of the North Atlantic. The nature of this relation will be discussed later, bearing in mind that rifting was taking place at a considerable (and unknown) distance to the W (section 1.4.1). During the Late Oxfordian and Kimmeridgian, the Berlengas Block was rejuvenated and sourced clasts to a deep and elongated trough that developed to its E. The coming into play of a number of N-S trending faults, for the first time not clearly related to the basement structure (Sobral Fault, Alcochete Fault Zone), is a characteristic of this extensional episode (Montenat et al., 1988) The extension was responsible for the subdivision of the trough into the compartments already mentioned (Turcifal, Bombarral and Arruda Sub-basins). The Torres Vedras-Montejunto Fault marks the southern limit of the area of maximum subsidence (the Bombarral Sub-basin), where in places more than 3 km of Late Jurassic sediments accumulated. To the E the trough was confronted with a platform-type region of subdued subsidence: the Espigão Platform to the N of Montejunto, the Ota Horst between Montejunto and the Tagus Valley (Montenat et al., 1988), and the Samora Ridge between the Tagus River and the vicinity of Setúbal (Figure 2.1). The eastern boundary of the trough trends NNW-SSE along the Pragança Fault to the N of Montejunto (Montenat et al., 1988), and N-S to NNW-SSE between Montejunto and Setúbal, along the Ota Fault and the Alcochete Fault Zone. Simultaneously with the deepening of the trough, the eastern marginal platform was cut by NNE-SSW and NW-SE reactivated faults (Montenat et al., 1988). At the Oxfordian-Kimmeridgian transition the Montejunto Range was uplifted and eroded, sourcing carbonate clasts to the deeper parts of the trough (Wilson, 1988). Similar rejuvenation was probably taking place in the western border of the Hesperic Massif, since the entire basin received siliciclastic sediments, which are particularly important in the Arruda Sub-basin, where the subsidence rate accelerated (ibid.). Wilson et al. (in press) suggested a "pull-apart" mechanism to explain this fast and localized subsidence.

The latest Jurassic (Portlandian) saw the emersion of most of the Lusitanian Basin, and the erosion was important in the NE (Espigão Platform) and extreme

S (Arrábida), sourcing the deposition of a continental formation (Grés Superior) to the S of the Tagus River (Montenat et al., 1988). Hutton and Gawthorpe (1988) assign to this period the beginning of the structural inversion of the central area of the basin, a process which was to be dominant until the Late Miocene, and considered it to be induced by strike-slip deformation.

The scarcity of sediments from the Berriasian-Valangian interval, mostly confined to the Lower Tagus Basin and in outcrop to the W of Lisbon, marks the second megasequence boundary. It is probably a breakup unconformity, since it preceeded sea-floor spreading offshore Portugal (section 1.4.1).

2.3.3 Passive margin stage.

The third and fourth megasequences of Mesozoic sediments range from Valangian to Turonian, and are separated by an intra-Aptian unconformity (Wilson et al., in press). The most remarkable characteristic of this period is the reduced importance of the post-rift sediments (Wilson, 1988; Montenat et al., 1988), indicating that very little thermal subsidence actually took place in the Lusitanian Basin. Distribution of facies was controlled by the variable degree of incursion of the sea. The marine environment never reached the area of the eastern platform, where discontinuous terrigenous sedimentation occurred throughout the Cretaceous (Montenat et al., 1988), indicating spasmodic episodes of structural inversion. Inside the trough, the intra-Aptian boundary and a subsequent Late Albian unconformity were caused by episodes of uplift and erosion (Rey, 1979). The palaeomagnetic data of Galdeano et al. (1989) may indicate that this was followed by block rotations to the W of Lisbon (Hauterrivian-Barremian), in agreement with the idea that the structural inversion was caused by strike-slip tectonics.

Finally, the Cenomanian was a time of widespread transgression in the Lusitanian Basin, with the sea reaching as far E as the Porto-Abrantes Fault.

Sea-floor spreading in the Bay of Biscay and the rotation of Iberia were important tectonic events of the late Early and early Late Cretaceous, but the uncertainties regarding its mechanism (section 1.4.2) make it difficult to assess its impact on the evolution of the Portuguese basins.

2.3.4 Early Alpine stage.

In contrast with the important Cenomanian transgression, during the Turonian the entire area between the Nazaré and Arrábida Faults emerged, and the marine environment was restricted to the N of the former. This scenario was to last through the remainder of the Cretaceous: none of the exploration wells of the Lusitanian and Lower Tagus Basins show deposits from the latest Cretaceous, nor can they be observed in outcrop, with only two exceptions of reduced expression to the N of the Nazaré Fault (Berthou and Lauverjat, 1979). The late stages of the Mesozoic evolution point in fact to a phase of important unstability (Telles-Antunes, 1979). This is underlined by the emplacement of the Sintra intrusive and the extrusion of the Nazaré Basalt (Aires-Barros, 1979) and, according to Telles-Antunes (1979), the Basaltic Complex of Lisbon.

The importance of the Late Cretaceous erosional episode in the Lower Tagus Basin is variable (Figure 2.5), and can be used to investigate the tectonic evolution of the area to the S of the Tagus River. The well Ms-1 (unpublished data, GPEP), sampled 337 metres of Upper Cretaceous sediments, but in Br-2, on the south margin of the river, Eocene sandstones (Benfica Formation) rest unconformably on top of late Early Cretaceous rocks. Further E, in Mj-1, the same Eocene formation lies now on top of Kimmeridgian limestones. To the NE of that point and across the Alcochete Fault Zone, in the well Sa-1A, the contact is with Mid Jurassic deposits, whereas in PN-1 the transition is between the Miocene and the evaporitic series at the base of the Mesozoic. Although this pattern may be in part due to the absence of deposition, it suggests the tilting towards the NW of a block defined by the Arrabida Range, the Alcochete Fault Zone and the Lisbon-Sintra trend, followed by the erosion of the uplifted edge. The magmatic ascent in Lisbon and Sintra at the end of the Cretaceous suggests localized extension, and is compatible with this model.

When sedimentation was resumed in the Eocene, the distribution of subsidence and uplift was reversed with respect to the Late Cretaceous, leading to the deposition of a thick series of Neogene clasts to the S of the Tagus River increasing in importance towards the Alcochete Fault Zone. This reversal in polarity of vertical movement may be diagnostic of strike-slip induced tectonism

(e.g., Rodgers, 1980), and will be further discussed in section 3.3.

2.3.5 Palaeogene: the Benfica Formation.

The Palaeogene in the Lower Tagus Basin is of continental facies and outcrops mostly near Lisbon under the name of "Benfica Formation" as a blanket of arkosic sandstones. Correlatable deposits also occur along a narrow stripe following the contact with the Lusitanian Basin (Carvalho, 1968). Traditionally dated as Oligocene, this formation was attributed mainly to the (Late?) Eocene by Telles-Antunes (1979). It marks the end of the period of regional uplift described in the previous section, and the onset of a regime of differential vertical movement between the Lusitanian Basin and the Lower Tagus Basin, with the former continuing to undergo structural inversion and the latter receiving the products of erosion. This regime was to characterize the remainder of the Cainozoic.

The Benfica Formation was cut at all the exploration wells to the S of the Tagus River (with one exception, PN-1) with thicknesses varying from 120 m to 320 m. The earlier clasts originate from the erosion of Hercynian granites (Carvalho, 1968), and this makes their provenance problematic due to the distance between source area and depocentres. Telles-Antunes (1979) allocates the source area for the earlier stages of deposition to the Central Cordillera, some 200 km to the NE. Alternatively, the erosion of an uplifted basement ridge to the E of the Alcochete Fault Zone is a possible explanation for the provenance of the clasts that should not be disregarded, as it is supported by the geometry of the Late Cretaceous unconformity (previous section). In fact, the N-S structure suggested by the Bouguer anomaly map (Figure 2.3a) may correspond to the remainder of such basement outcrop, now covered by later sedimentation.

During the earliest Oligocene, the clasts of the Benfica Formation became calcareous in nature, indicating that the source shifted towards the Mesozoic sediments. An important tectonic pulse with rejuvenation of the Lusitanian Basin was recorded within the Benfica Formation by the deposition during the Oligocene of conglomerates containing large blocks of sandstone and limestone (Telles-Antunes, 1979).

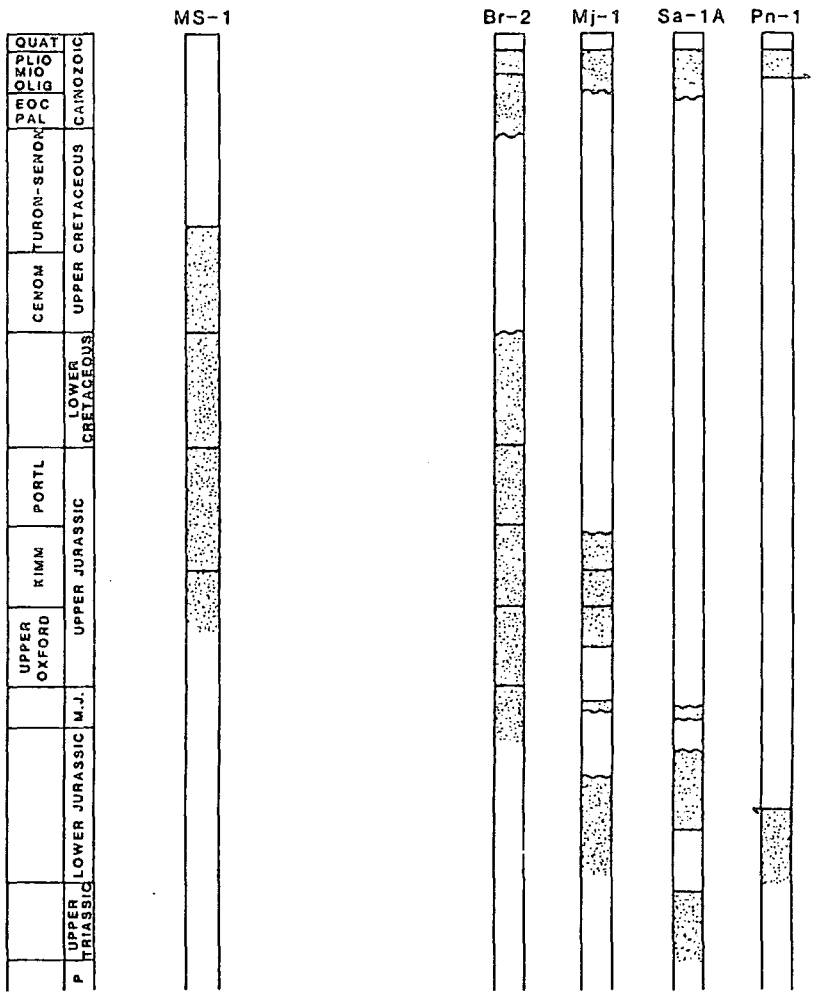

Fig. 2.5 - Sediment collums showing the variable importance of the unconformity at the base of the Cainozoic, in the Lower Tagus Basin. Based on data made available by GPEP, Lisbon.

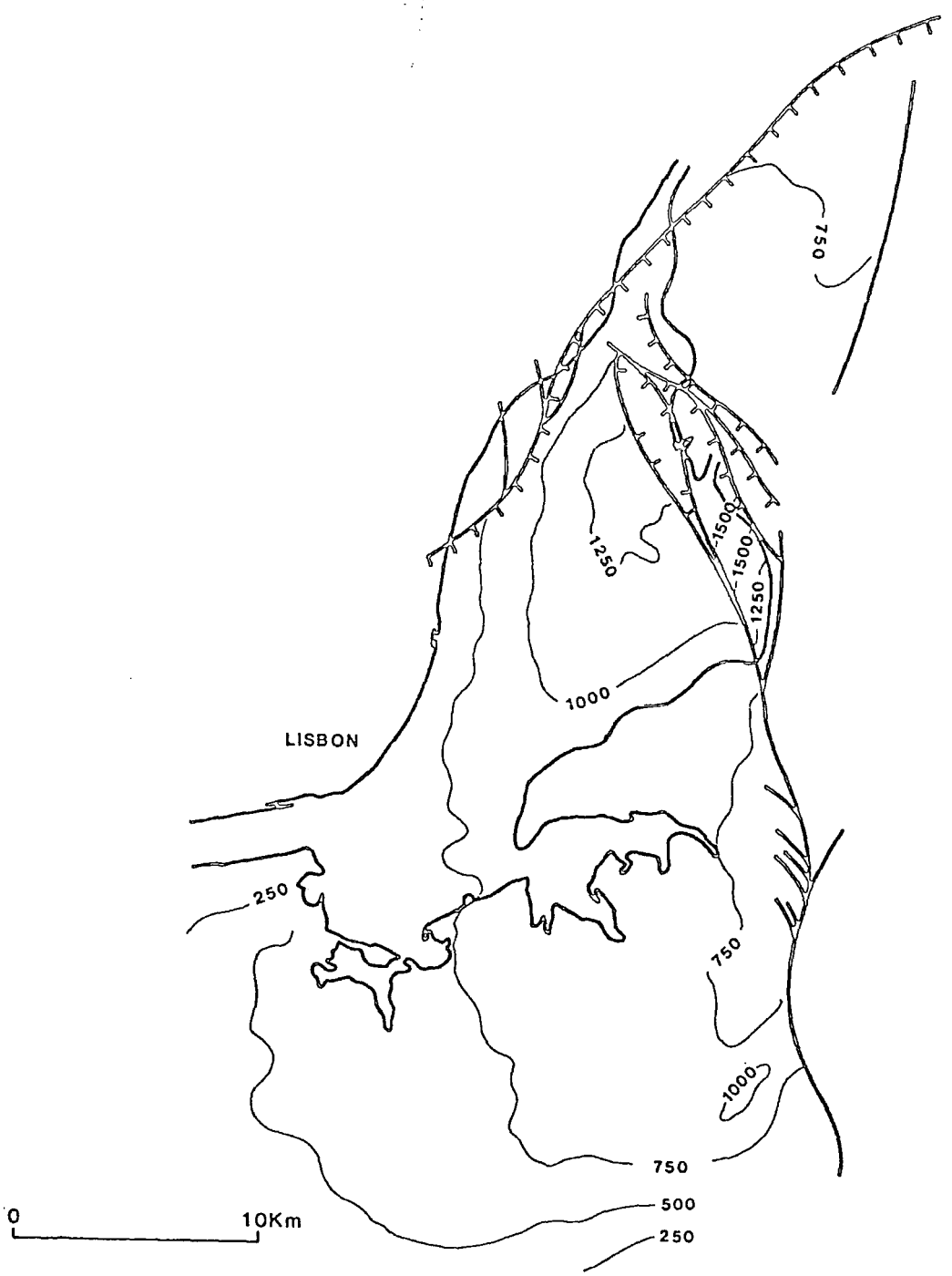

Fig 2.6 - Top Oligocene two-way traveltime map of the Lower Tagus Basin (Setúbal Peninsula Sub-basin). Traveltimes in milliseconds. Redrawn after material made available by GPEP, Lisbon.

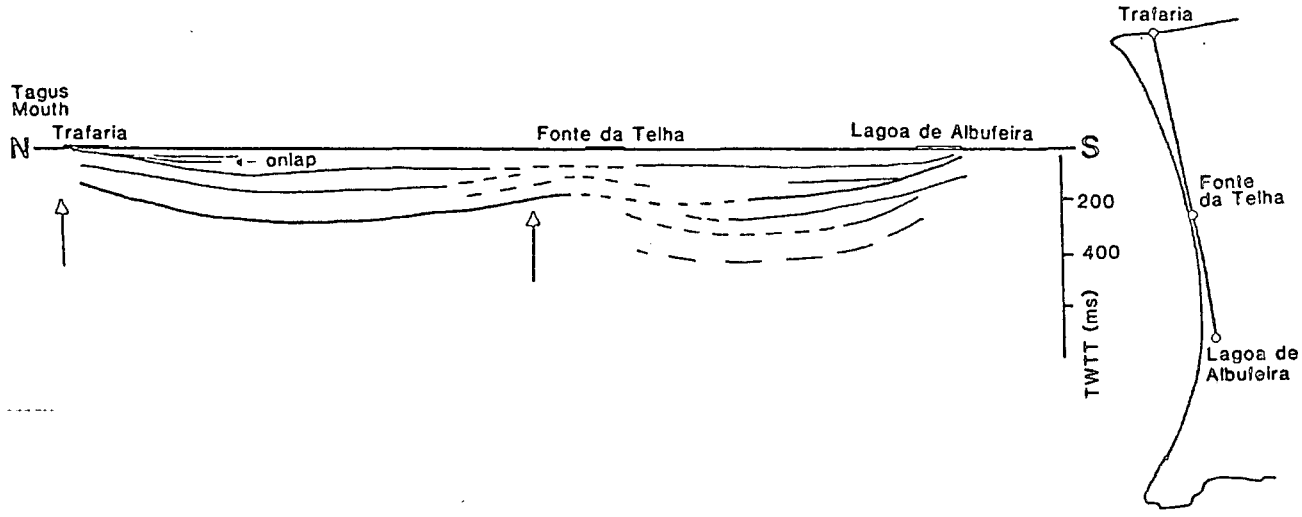

Fig 2.7 - Sketch of the geometry of the post-Oligocene sediments in section Ca1/81, along the coastal area of the Setúbal Peninsula Sub-basin. The arrows show the zones that were uplifted after the mid Miocene. Based on data made available by GPEP, Lisbon.

The reason why the Lower Tagus Valley became a site of deposition probably lies in the geometry and kinematics of the faults associated with it. Although this relationship is obscure during the Palaeogene, it becomes clearer in the Miocene, which was a period of intense tectonic activity in the Lusitanian and Lower Tagus Basins.

2.3.6 Miocene tectonics.

During the Miocene the stress regime in Portugal changed as a consequence of the continental collision between Iberia and Africa, which now were converging in a NW-SE direction (section 1.5.2). The most important result of this was a major phase of structural inversion of the Lusitanian Basin, with the uplift of the Montejunto, Candeeiros and Aire Ranges, along the NNE-SSW Hercynian trend (Figure 2.1). To the S of the Setúbal Peninsula sub-basin (Lower Tagus Basin), the Arrábida Range was also the scene of intense tectonism, which peaked during the Late Miocene (Ribeiro et al., 1980). Here, the mountains reach heights of 400 to 500 m, and trend on a ESE-WNW direction. The southern flank is a major thrust fault, with Miocene sandstones in the foot wall and Jurassic limestones in the hanging wall. This fault is cut by several en echelon ENE-WSW sinistral strike-slip faults. To the NE, the Arrábida Range passes into a zone of folds, to be truncated by the N-S trend of the Alcochete Fault Zone (Figure 2.1).

Between the Arrábida Range and the Tagus River, sedimentation was taking place throughout the Miocene. Figure 2.6, based on the Neogene isopachyte map (unpublished data, GPEP), depicts the distribution of post-Oligocene deposits in the Setúbal Peninsula sub-basin. It shows a triangular depocentre, with maximum thicknesses towards the NE, where the Alcochete Fault Zone diverges from the Vila Franca Fault. The control of the subsidence by the activity of these faults is very clear. The good agreement between the shape of the 1000 ms contour line and the border of the floodplain of the Tagus River (NE sector) suggests that the relationship still persists to the present.

Between the Alcochete Fault Zone and the coast, the Setúbal Peninsula sub-basin is mostly a featureless syncline. However, one of the seismic sections reveals the existence of a buried ridge of small amplitude, which was uplifted during the deposition of post-Mid Miocene sediments (Figure 2.7). In chapter 4 the possible

relationship between this structure and the seismotectonics of the Lower Tagus Valley will be discussed.

There is no seismic data to the E of the Alcochete Fault Zone. But the gravity map (Figure 2.3a) shows the existence of a second depocentre to the NE of the Setúbal Peninsula. This has already been referred to as the Ribatejo Sub-basin.

2.3.7 Neotectonics.

In the area of this study, the identification of active basement structures is hindered by the sedimentary cover, probably detached from the basement by the thick evaporitic layer. Cabral et al. (1984) observed small-scale reverse faulting in the coastal cliffs on the western flank of the Setúbal Peninsula Sub-basin, and this is the only satisfactory geological evidence of neotectonic deformation in the region. In the Lusitanian Basin, the scarcity of Cainozoic sediments makes it difficult to determine whether or not the Miocene deformation continued into the Quaternary. The seismicity, nevertheless, indicates that some degree of activity is still taking place at present.

Besides the seismicity, the clearest indication of neotectonic activity in the Lower Tagus Valley may be the configuration of the of the Tagus Mouth (Figure 2.1). The termination of the river seems to have been further to the S until recent geological times, near the axis of the Setúbal Peninsula syncline. Carvalho (1968) described Plio-Pleistocene sands containing clasts from the igneous rocks of the northern margin of the Tagus, and concluded that the present configuration must be of Quaternary age.

The reason for the shift in the position of the Tagus Mouth has remained obscure. The neotectonic map of Cabral (1986; draft version) associates the narrow bar that presently connects the river to the ocean with an active fault. The geologic map of Lisbon (Moutinho-Almeida, 1986) in fact reveals the presence of a fault along the trajectory of the river. However, the youngest stratigraphic level cut by the fault, directly below the alluvial deposits, dates from the earliest Miocene. On the other hand, the northwestern corner of the broad internal mass of water (Mar da Palha) is clearly fault-controlled (Figure 2.6), suggesting some degree of tectonic control. The present configuration also suggests that

the broad internal mass of water (Mar da Palha) is clearly fault-controlled (Figure 2.6), suggesting some degree of tectonic control. The present configuration also suggests that the drainage towards the W, either fault-controlled or due to erosion, resulted from the recent elevation of a topographic barrier striking approximately E-W and laying to the S of the water mass. This is not in agreement with the classic interpretation of the Setúbal Peninsula Sub-basin as a featureless syncline. On the other hand, it is in very good agreement with the evidence put forward in Figure 2.7 for the uplift of an E-W ridge close to the axis of the basin, at some time after the Mid Miocene.

Most of the discussion of the neotectonics of the Estremadura has been centred on the possible existence of a major basement fracture with seismogenic activity, oriented along the Lower Tagus Valley and associated with the contact between the Lusitanian Basin and the Lower Tagus Basin. The identification of a surface lineament on satellite imagery has been the main support for this model (e.g., Cabral, 1986), although the significance of these data have been questioned (Coelho, 1986), since no geological evidence was found at the surface that could be linked to the proposed lineaments. This aspect, which is fulcral to the problem of seismic hazard assessment in the Lisbon area, will be addressed again in chapter 4, where new data will be presented and discussed.

Chapter III

Quantitative Analysis of the Lusitanian and Lower Tagus Basins

3.1 Models of basin evolution. "Backstripping".

So far the evolution of the Lusitanian and Lower Tagus Basins have been described in a qualitative manner. The alternative approach of using the well data to model and quantify the tectonic factors which controlled the subsidence will now be taken. First, some concepts of basin dynamics will be briefly reviewed.

After lithospheric cooling was applied successfully to explain the bathymetric profile across mid-ocean ridges, the same principle was used by Sleep (1971) to explain the subsidence at passive continental margins following rifting. In this early model, upwelling of hot asthenospheric magma heats and expands the lithosphere, increasing the buoyancy of the crust, which is then uplifted. This is followed by erosion and, as the lithosphere returns to thermal equilibrium by vertical heat flow, the free surface sinks below sea level due to the absence of the eroded material. The main shortcoming of this model is that realistic amounts of erosion fall short of explaining sediment thicknesses larger than 4 km (Bott, 1982, p. 208); also, an erosional unconformity should follow rifting, but this is not always the case (Bott, 1980). However, since crustal thinning at continental margins is widely documented, it retains an important role in most models of shelf subsidence, and its causes were the subject of intense research. Bott (1971,1980) proposed that crustal thinning takes place at passive margins due to the oceanward flow of material from the ductile lower crust, in response to horizontal deviatoric stresses induced by the juxtaposition of differing types of crust (Bott and Dean, 1972). An alternative explanation involves the upward migration of the Moho caused by a phase transition at the bottom of the crust.

McKenzie (1978) modelled crustal thinning by pure shear lithospheric extension, and explored the subsequent heating and cooling of the lithosphere to explain the evolution of sedimentary basins. Airy isostatic equilibrium is assumed

throughout, and the temperature is kept constant at the surface and at a depth equal to the initial lithospheric thickness. If this thickness is reduced instantaneously by a factor of $1/\beta$ (Figure 3.1), the passive upwelling of asthenosphere will heat and expand the lithosphere, having as a combined effect an isostatic readjustment given by the subsidence

$$S_i = \frac{a[(\rho_o - \rho_c)\frac{t_c}{a}(1 - \alpha T_1 \frac{t_c}{a}) - \frac{\alpha T_1 \rho_o}{2}](1 - 1/\beta)}{\rho_0(1 - \alpha T_1) - \rho_w} \tag{3.1}$$

(McKenzie, 1978), where the constants have the meaning given in Table 3.1. Depending on the thickness of the crust t_c, uplift may occur at this stage ($S_i < 0$). With the initial conditions of Figure 3.1, the solution of the heat equation

$$\frac{\partial T}{\partial t} = k \frac{\partial^2 T}{\partial^2 z} \tag{3.2}$$

(k being the thermal conductivity) is

$$\frac{T}{T_1} = 1 + \frac{z}{a} + \frac{2}{\pi} \sum_{n=1}^{\infty} \frac{(-1)^{n+1}}{n} [\frac{\beta}{n\pi} sin\frac{n\pi}{\beta}] exp(-\frac{n^2 t}{\tau}) sin\frac{n\pi z}{a} \qquad (\tau = \frac{a^2}{\pi^2 k}). \tag{3.3}$$

The condition of isostatic equilibrium implies a subsidence given by

$$S(t) = S_i + S'(t) \tag{3.4}$$

with

$$S'(t) = e(0) - e(t) \tag{3.5}$$

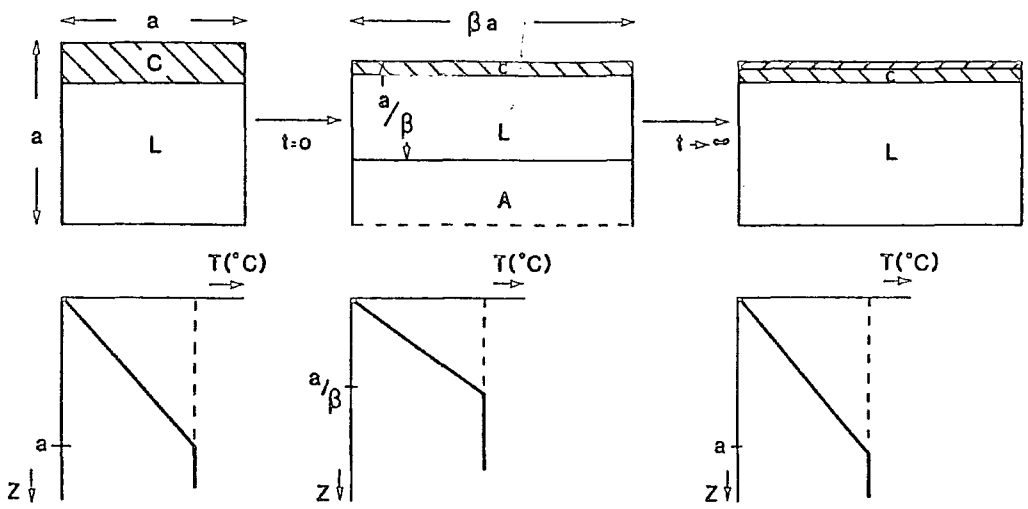

Fig. 3.1 - McKenzie's (1978) model of pure-shear lithospheric extension. C is the crust, L is the lithospheric mantle and A is asthenosphere. The percentage increase in surface is β. Redrawn after McKenzie (1978).

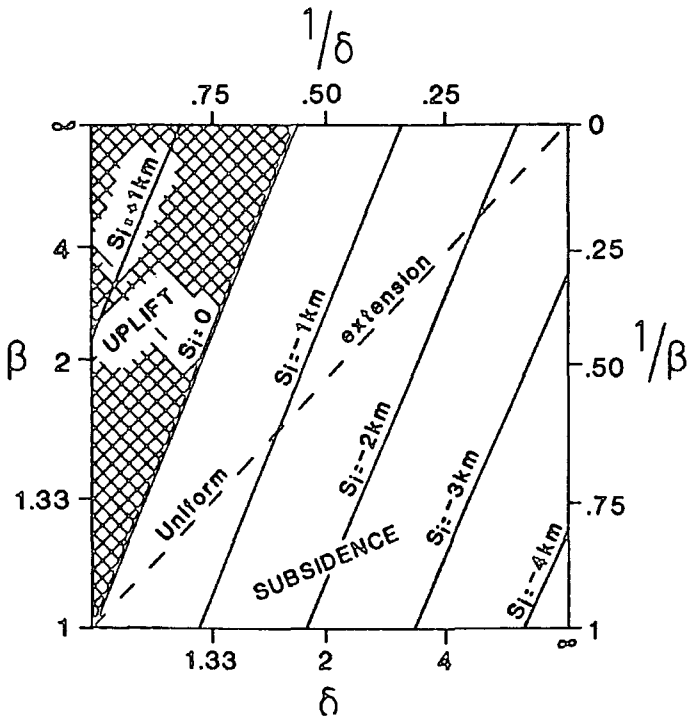

Fig. 3.2 - Initial subsidence (or uplift) due to rifting, as a function of the stretching factors β and δ, for a detachment depth of 35 km. Redrawn after Royden and Keen (1980).

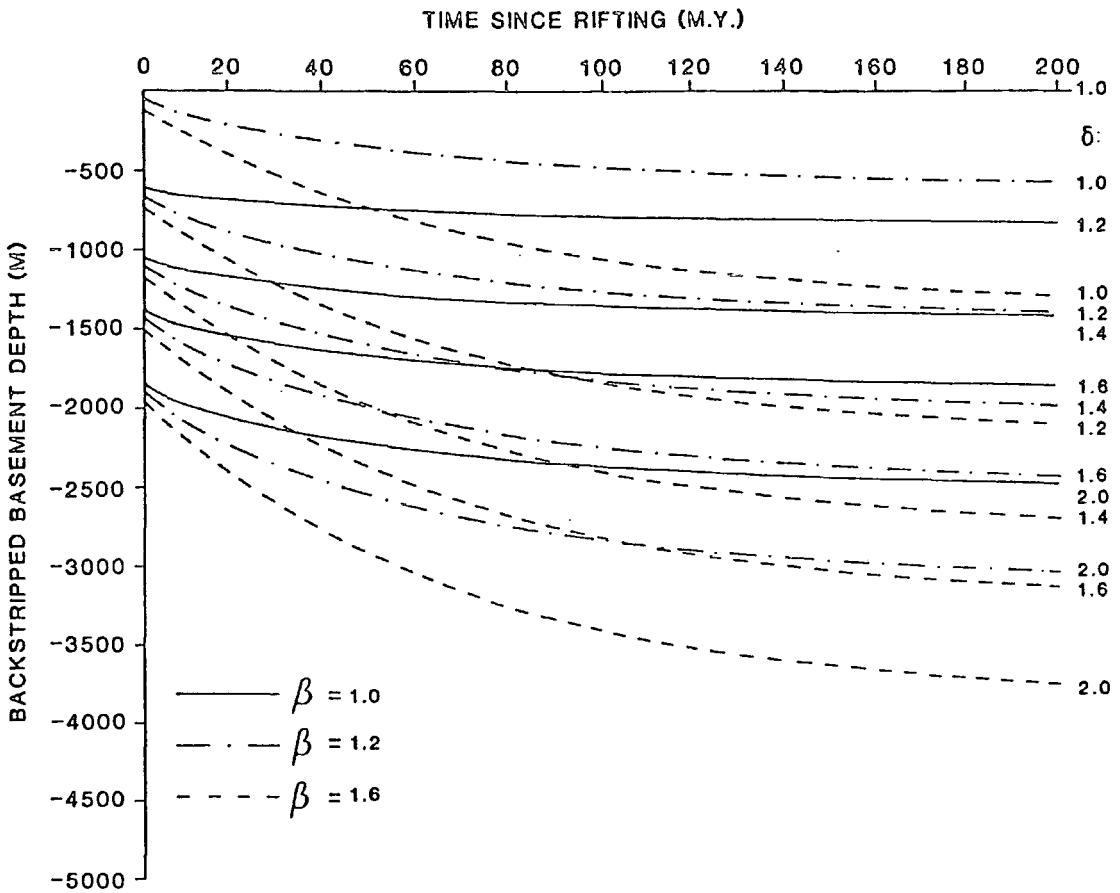

Fig. 3.3 - Theoretical subsidence curves predicted by the modified McKenzie model, for various values of stretching factors β and δ. Detachment depth 35 km. Curves computed with program BACKSTRIP (see text for references).

Table 3.1

a	thickness of the lithosphere
ρ_o	density of the mantle
ρ_c	density of the crust
ρ_w	density of the water
t_c	initial crustal thickness
$alpha$	thermal expansion coefficient
T_1	temperature of the asthenosphere

where

(3.6)

$$e(t) = \frac{a\rho_o\alpha T_1}{\rho_o - \rho_w}\left[\frac{4}{n^2}\sum_{m=0}^{\infty}\left[\frac{1}{(2m+1)^2}\left[\frac{\beta}{(2m+1)\pi}sin\frac{(2m+1)\pi}{\beta}\right]exp\left[-(2m+1)^2\frac{t}{\tau}\right]\right]\right.$$

(ibid.).

The model described above was used by Sclater and Christie (1980) to explain some of the features of the subsidence in the Central North Sea Basin. For more widespread application, however, some of its simplistic assumptions had to be dropped. Sclater et al. (1980) and Royden and Keen (1980) took into account the changes in rehology with depth by allowing for a horizontal detachment separating two zones with different stretching factors, β (below the detachment) and δ (above the detachment). Convenient combinations of the two parameters yield either uplift or subsidence at the initial stage, independently of the crustal thickness (Figure 3.2). Royden and Keen (1980) used this approach to model the rifting at the continental margin of eastern Canada, in Nova Scotia and off Labrador. Pitman and Andrews (1985) incorporated lateral heat flow into McKenzie's model to adapt it to narrow troughs, and allowed for a finite duration of the stretching process and for syn-rift heat loss. With these refinements, they modelled the formation and thermal history of "pull-apart" basins associated with high slip-rate strike-slip faults (e.g., the San Andreas Fault), characterized by very rapid subsidence, initial starvation and reduced post-rift thermal subsidence. Kusznir and Egan (in press) developed a mathematical model for the extensional deformation of the lithosphere incorporating simple shear (faulting) deformation in the upper crust and pure shear in the ductile lower crust and mantle, as well as flexural deformation, and used it to model the evolution of the Jeanne D'Arc Basin, Grand Banks of Newfoundland.

Figure 3.3 shows the tectonic subsidence curves predicted by McKenzie's theory, modified to include a detachment level, for a detachment depth of 35 km and for various values of the parameters β and δ. The expression "tectonic subsidence", introduced by Keen (1982), refers to that part of the actual subsidence which can be attributed to independent tectonic processes. In fact, before well

data can be used to quantify the amount of extension of the lithosphere, they must be corrected for the "positive feedback" effect of sediment loading, which strongly enhances the subsidence of the basement by isostatic response to the weight of the sediments. This adjustment may be estimated assuming either Airy or flexural isostasy (Watts, 1982), the former being preferable when subsidence is fault-controlled. This process requires also the estimate of the original thickness and density of each formation prior to compaction.

A technique to perform the corrections mentioned above was developed by Steckler and Watts (1978) under the term "backstripping". To "backstrip" a column of sediments, it is divided into a number of segments whose boundaries correspond to known geologic ages. The segment at the top is removed, and those below it are transported upwards: the depths to the boundaries are computed by bringing the top remaining segment to the relevant palaeobathymetric level and adjusting each density and thickness to verify the conservation of mass. This last step requires the use of a porosity profile. The bottom of the lowest segment is equated to the depth z of the basement at a time corresponding to the bottom of the segment removed. At this stage the average density $\bar{\rho}$ of the decompacted stratigraphic column is computed, and the "backstripped" basement depth z_b is obtained by replacing the sediment load with a water load and assuming isostatic equilibrium. For the Airy isostasy model, the relation between the two depths is

$$\frac{z_b}{z} = \frac{\rho_m - \bar{\rho}}{\rho_m - \rho_w}. \tag{3.7}$$

Repeated for each segment of the stratigraphic column, this procedure yields two sequences of basement depths versus time, which can be interpolated to estimate the subsidence curves. The "backstripped" depth should account for tectonically induced subsidence only, and can therefore be compared with the theoretical curves predicted by the different models.

One of the delicate aspects of "backstripping" is the need to select a porosity profile for the well. Porosity can be estimated from well logging data, but accuracy requires that a sonic log, a neutron log and a gamma-gamma log be used

in conjunction, since they respond differently to sources of error (Schlumberger Limited, 1972). In ideal conditions, one single log would be sufficient; the sonic log, for instance, may be used to compute the porosity ϕ from Wyllie's formula,

$$\phi = \frac{s - s_m}{s_f - s_m} \tag{3.8}$$

where s is the reciprocal of acoustic velocity, given by the log, and s_m and s_f are the corresponding values for the matrix of the sedimentary rocks and for the pore fluid (Telford et al., 1976).

3.2 Application to the Lusitanian and Lower Tagus Basins.

The sedimentary columns of eleven wells where "backstripped" according to the technique described above. Five wells are located in the Lusitanian Basin (Cp-1, Mt-1, Sb-1, TV-4 and Bf-1) and six in the Lower Tagus Basin (Ms-1, Br-1, Br-3, Br-4, Sa-1A and PN-1); strictly speaking, the well Ms-1 lies on the boundary between the two basins. The locations of the wells are shown in Figure 2.1. The selected wells are those which penetrate deeper into the basins, but in several cases the thicknesses of the lowest Jurassic and Upper Triassic sediments had to be extrapolated laterally, since only Sb-1 and Mt-1 probe the Palaeozoic basement. In Ms-1 the pre-Kimmeridgian section was arbitrarily made equal to that of Br-3.

Sonic logs were the only data available from the wells and so Wyllie's formula was used to estimate the porosity. This method gave extremely low (virtually zero) porosities for carbonates at depths of the order of 2 km and below (Figure 3.4). Published studies show that carbonates usually preserve porosities near 10% at depths of the order of 4 km (e.g., Schmoker and Halley, 1982). To explain the values obtained with Wyllie's formula, post-burial uplift of the order of 4 km would be required. Although some degree of basin inversion occurred, it is unlikely that such a thickness of sediments were ever eroded. Even if the porosity estimates were correct, causes other than compaction could explain the loss of porosity, such as cementation or pressure solution (Tucker, 1981). Rather

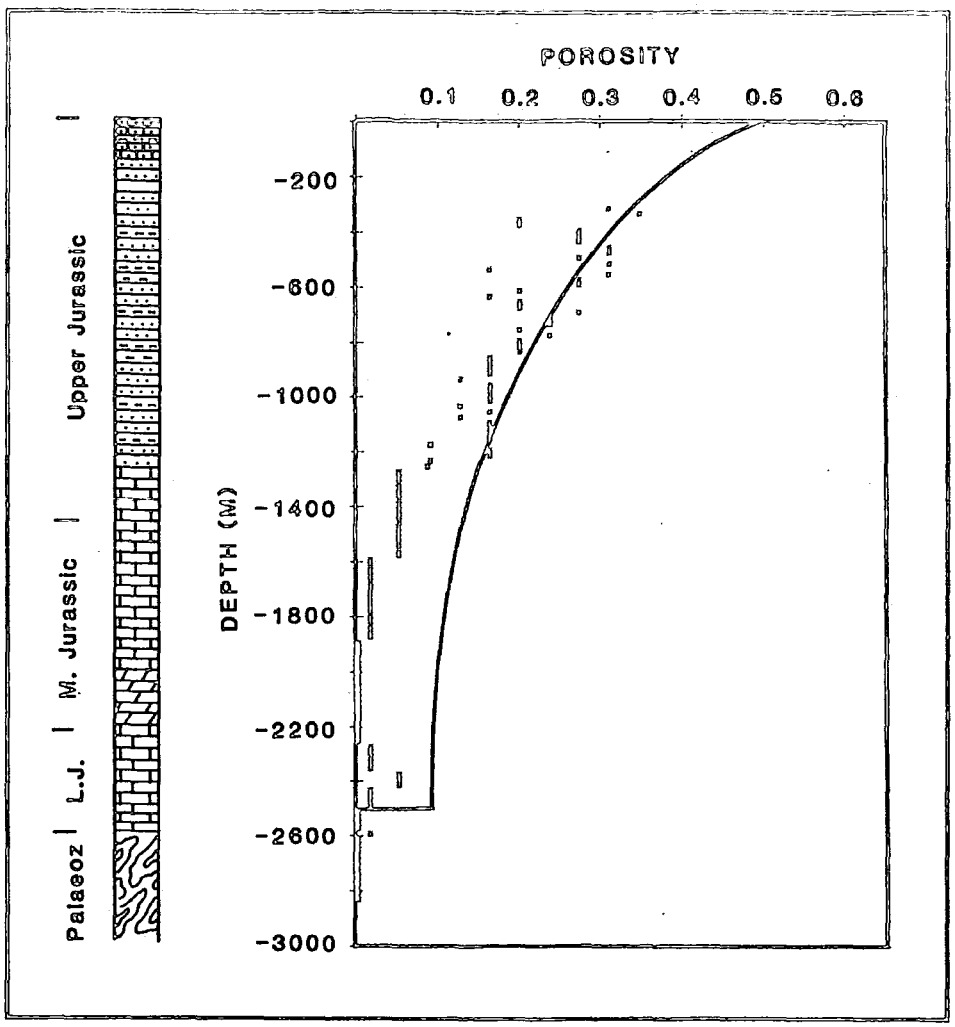

Fig. 3.4 - Comparison between the porosity values computed with Wyllie's formula for a typical well of the Lusitanian Basin (dots) and the porosity profile of Baldwin and Butler (1985) for the same lithology (shale and limestone) (solid line).

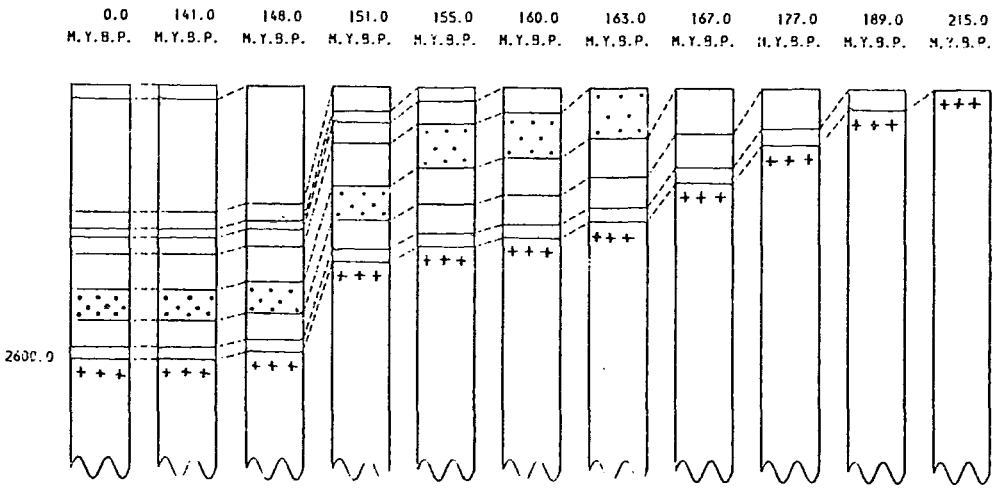

Fig. 3.5 - Graphical ilustration of "backstripping".

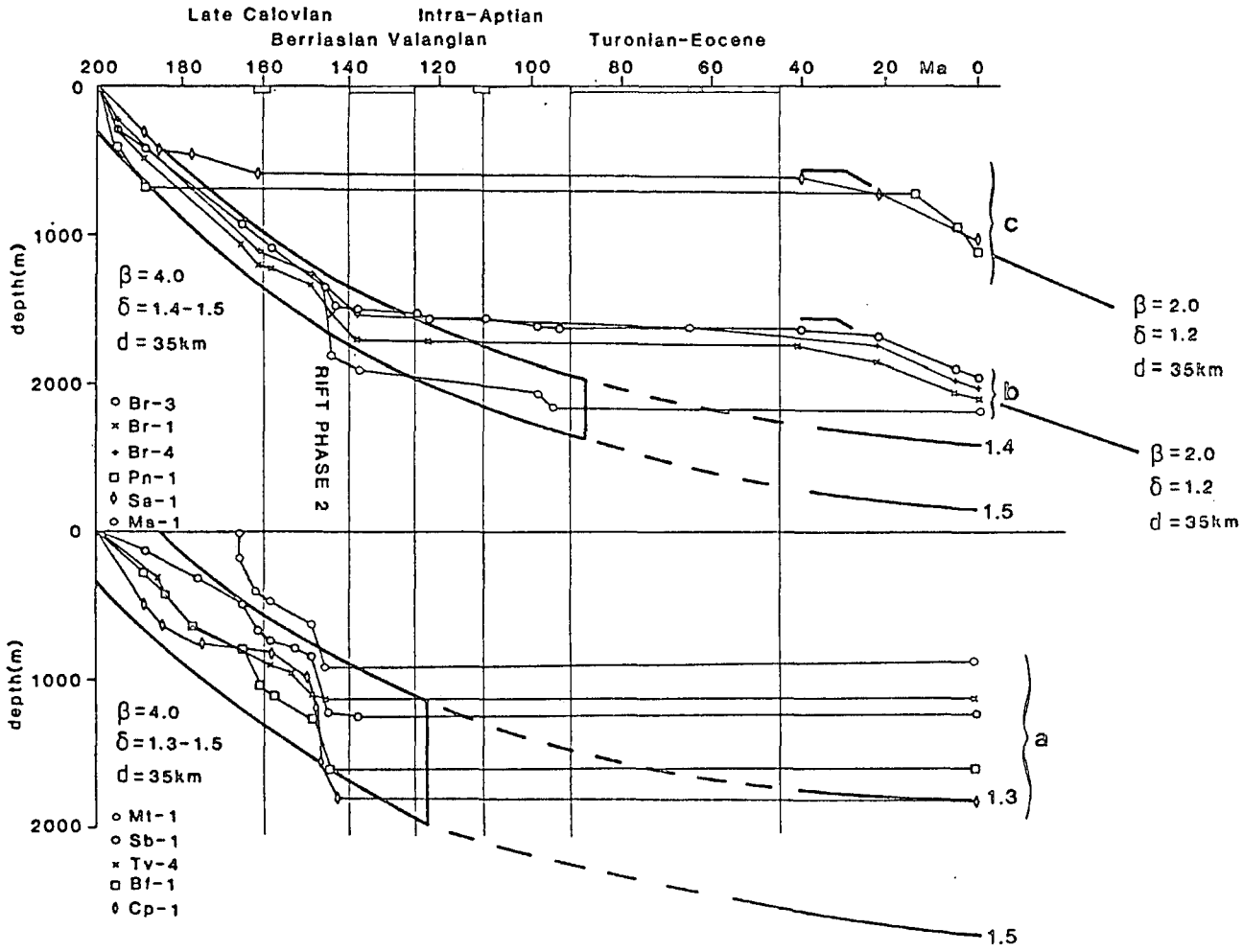

Fig. 3.6 - "Backstripped" basement depths as functions of geological time for eleven wells of the Lusitanian and Lower Tagus Basins, after isostatic correction. The bars on the horizontal axis indicate the megasequence boundaries proposed by Wilson et al. (in press).

than establishing the overcompaction of the sediments on such weak grounds, the indications of the sonic log were ignored and published standard curves of variation of porosity with depth for different lithologies (Sclater and Christie, 1980; Baldwin and Butler, 1985) were employed instead.

The program BACKSTRIP, written by M.S. Steckler and improved by G.D. Karner and W. Mohriak, was modified (Appendix B) to use a lithology-dependent porosity profile, obtained by combining standard curves according to the lithological variations with depth. The program follows the procedure described in the previous section to correct for compaction and isostatic response, each segment of the column being "moved" upwards along the porosity-depth law that applies to its composition. The numerical computation of the integral of solidity (1 - porosity) has to be carried out along the relevant sections of the column, when balancing the masses prior to and after decompaction. This was not required in the previous versions of the program, where a porosity function defined analytically was used for the entire column. Figure 3.5 illustrates graphically the "backstripping" sequence.

Sea level variations were not taken into account in this analysis: they correspond to second order effects (less than 100 m) and its quantitative estimates are prone to errors. Another source of innacuracy resulted from the lack of reliable palaeo-bathymetric data: the sediments were decompacted as if they had been deposited at sea-level. This approximation is reasonable for most of the history of the basins, characterized (with the exception of the Late Oxfordian-Kimmeridgian) by shallow-marine or continental facies (Wilson et al., in press).

Figure 3.6 shows the results obtained with the program BACKSTRIP using as input the well data from the Lusitanian and Lower Tagus Basins. Basement depths at several points in time were plotted after isostatic correction. Periods of uplift and erosion have the effect of removing from the record those amounts of subsidence during which the eroded sediments were deposited: both the deposition of the (subsequently) eroded sediments and the uplift are represented by flat sections of the curves.

Three categories of wells may be considered in Figure 3.6:

a) wells from the Oxfordian-Kimmeridgian Trough, N of the Tagus River (Cp-1, TV-4, Sb-1, Bf-1 and Mt-1);

b) wells from the Oxfordian-Kimmeridgian Trough, S of the Tagus River (Br-1, Br-3 and Br-4);

c) wells from the eastern platform, S of the Tagus River (PN-1 and Sa-1A).

Although the well Ms-1 is actually on the northern margin of the Tagus River, it will be included in group b), for reasons that will be explained later.

In group a), the initial dispersion of the curves (200 to 170 Ma) may be attributed to errors in the assumed thicknesses of the Hettangian evaporites, which are poorly constrained since the wells usually terminate within this formation, and are likely to vary significantly within distances of the order of 10 km (section 2.3.1). The thicker evaporites at the well Cp-1 (Bombarral Sub-basin) are in agreement with the observations of Wilson (1988).

The discrepancy of the early section of the Mt-1 curve is due to later deformation: this well is on the eastern border of the trough, where it has a reverse fault contact with the Cainozoic Lower Tagus Basin at the Vila Franca Fault. Apart from this perturbation, the well Mt-1 parallels very closely the Sb-1 and Bf-1 curves, documenting the evolution of the Arruda Sub-basin, to which they all belong: moderate subsidence rates until the Mid Jurassic (~170 Ma), a pulse of fast subsidence in the Calovian (165 to 160 Ma), moderate subsidence during the Oxfordian (160 to 152 Ma) followed by fast subsidence in the Kimmeridgian (152 to 146 Ma), very moderate subsidence in the Portlandian (146 to 141 Ma) followed by a period of uplift and erosion starting at the Berriasian (141 Ma).

The well TV-4, in the northeastern corner of the Turcifal Sub-basin, follows the evolution of the Arruda Sub-basin untill the Mid Jurassic (~170 Ma). Then it becomes independent and has only limited subsidence during the Late Oxfordian and Kimmeridgian (154 to 146 Ma). The latter period in particular shows great contrast of subsidence rates, indicating intense differential vertical movements. To the NE, the Montejunto Range was uplifted during the Kimmeridgian (section 2.2.3), with the formation of an elongated anticlinal structure with a NE-SW axial direction, probably continuing through the eastern platform. The importance of

this Torres Vedras-Montejunto Anticline as a structural boundary during the Jurassic is further documented by well Cp-1: sedimentation was faster to the N of the anticline during the latest Triassic and Early Lias (200 to 176 Ma), much slower during the Dogger (176 to 170 Ma; a mere 170 m of the Mid Jurassic Brenha Formation in Cp-1 as opposed to 850 m in TV-4 and 1040 m in Bf-1) and again much faster in the Malm (160 to 141 Ma; 2770 m of Late Oxfordian-Kimmeridgian carbonates in Cp-1 as opposed to 780 m in TV-4 and 1580 m in Bf-1).

Whatever sedimentation may have occurred in the wells of group a) after the end of the Jurassic (141 Ma) was removed during the Late Cretaceous-Early Tertiary inversion of the trough.

The wells in group b) were selected to provide some control on the evolution of the Lower Tagus Valley. For this reason the well Ms-1 was included in this group, despite being located to the N of the Tagus River. Before the end of the Oxfordian (152 Ma) this well cannot be used, since it was extrapolated from Br-3 across the river. During the Kimmeridgian (152 to 146 Ma), a sharp contrast can be observed, with well Ms-1 following the levels of subsidence of the Arruda Sub-basin and the Br wells having a gentler evolution: the Early Kimmeridgian Abadia Formation has in Ms-1 a thickness of 1250 m, whereas in the Br wells it averages 440 m. After this pulse, no significant deviation can be observed until the earliest Late Cretaceous (95 Ma), when the Cacém Formation was deposited to the N of the River (337 m). To the S it was either not deposited or eroded on the subsequent episode of uplift. From Turonian to Eocene (94 to 38 Ma) no subsidence is recorded on any of the wells. After the end of the Eocene (38 Ma) the subsidence was significant to the S of the river and absent in Ms-1. During the Early Miocene (22.5 to 15 Ma) the contrast was increased by the reinforcement of the subsidence in the Br wells.

The wells in group c) represent the evolution of the southern part of the eastern platform. They show an initial phase of subsidence, corresponding to the regional downwarp of the Late Triassic-Mid Jurassic (section 2.2.2), but no significant subsidence during the Late Jurassic (160 to 141 Ma). The differences between PN-1 and the Br wells illustrate the importance of the Alcochete Fault

Zone as the eastern boundary of the Oxfordian-Kimmeridgian Trough (section 2.2.3), although it is not clear how such differences should be distributed between different levels of sedimentation and different levels of erosion in the Late Cretaceous (section 2.2.5). After the end of the Eocene (38 Ma) the role of the fault zone changed, since both sides show subsidence at moderate rates, with, if any, limited differential vertical movement.

Figure 3.6 shows the comparison between the "backstripped" basement depth curves and the best-fitting curves predicted by McKenzie's model (with vertically variable rehology). The parameters were selected to fit the first 60 million years of basin formation, for an instantaneous lithospheric extension 200 million years ago (Mid Upper Triassic). The pre-Kimmeridgian evolution can be modelled with considerable accuracy for the wells of group b) with $\beta = 4.0$ and $\delta = 1.4$ to 1.5 and a Moho-depth detachment at 35 km (before stretching). For group a), satisfactory modelling can be obtained with $\beta = 4.0$ and $\delta = 1.3$ to 1.5, the larger scatter reflecting the structural complexity of the area.

The main result from Figure 3.6 is that the Oxfordian-Kimmeridgian event seems to mark the beginning of a period during which the thermal subsidence predicted by the theoretical curves was inhibited rather than enhanced. This leads to a discrepancy of the order of 1 km between predicted and observed total tectonic subsidence. This is particularly clear for the Ms-1 and Br wells, were a complete Lower Cretaceous sequence documents the inflection in the subsidence curves. Also, the present crustal thickness of 31 km below the Lusitanian Basin (Moreira et al., 1980) exceeds the predictions of the model: for an initial thickness of 35 km and $\delta = 1.4$, the crust should be 25 km thick after stretching, and thin even further by thermal contraction. An initial thickness larger than 35 km is unlikely, since refraction profiles inland from the basins observed a crustal thickness of 30 km (Caetano, 1984). This evidence suggests that the crust underneath the Lusitanian Basin was thickened by about 20% during the Late Jurassic and Cretaceous. A possible explanation for this result will be advanced in the next section.

Although the Cainozoic subsidence observed to the S of the Tagus River is probably unrelated to the evolution of the Atlantic Ocean (section 1.4.3), it can

still be modelled as the result of crustal extension and thinning, and in view of the subdued Cretaceous subsidence the thermal effects of previous extensional episodes can be ignored. Figure 2.4b) shows that the crustal thickness underneath the Lower Tagus Basin is about 25 km (Mendes-Victor et al., 1980). Assuming that before the formation of the Tertiary basin the crust was 31 km thick as underneath the Lusitanian Basin, a stretching factor $\delta = 1.2$ results. Combined with a subcrustal stretching of $\beta = 2.0$, this value provides a satisfactory modelling of the subsidence in the Lower Tagus Basin during the Tertiary (Figure 3.6), for a pulse of instantaneous extension in the Late Eocene (40 Ma). Naturally, this quantitative modelling has to be simplistic, since the Tertiary tectonic activity was distributed in time rather than "instantaneous".

In modelling the Tertiary subsidence of the Lower Tagus Basin with McKenzie's theory no implicit assumption is being made about the direction of extension. In fact, the model assumes infinite horizontal dimensions of the basin, and is therefore insensitive to the direction along which the extension occurs.

3.3 Discussion.

The quantitative analysis of the evolution of the Lusitanian and Lower Tagus Basins, toghether with the qualitative description of the previous chapter, raise the following questions:

a) What was the mechanism of rifting between Iberia and the Grand Banks of Newfoundland in the Late Triassic-Mid Jurassic?

b) What was the nature of the Late Oxfordian-Kimmeridgian tectonic event in the Lusitanian Basin?

c) What was the cause of the structural inversion of the basins during the Cretaceous and the Cainozoic?

d) Which tectonic style explains the post-Eocene subsidence of the Lower Tagus Basin, concomitant to the uplift of parts of the Lusitanian Basin?

Question a) was adressed by Wilson et al. (in press), regarding the Portuguese margin, and Tankard and Welsink (1987) and Kusznir and Egan (in

press), regarding the Canadian margin. The first two studies identified a marked asymmetry between the conjugate margins, and proposed that the separation between Iberia and the Grand Banks took place along a low angle listric detachment, in line with the model of extensional tectonics developed by Wernicke and Burchfield (1982) and applied to passive margins by Lister et al. (1986). The mathematical modelling of Kusznir and Egan (in press) favoured the control of the extension by a planar, rather than listric, fault.

Changes in rifting style were also identified along each margin: the evolution of the Lusitanian Basin differs significantly from that recorded by the sediments deposited offshore West Galicia (Montenat et al., 1988; Wilson et al., in press); the Grand Banks can be divided into three provinces with different styles (Tankard and Welsink, 1987). Such geometry of areas under extension was first described by Gibbs (1984), who identified the boundaries between the different deformation styles as a special type of strike-slip fault, designated by "transfer fault", which he considered to be a part of the extensional system. Wilson et al. (in press) suggest that the Nazaré Fault may be a transfer fault, separating an eastward dipping low angle detachment to the S from a westward dipping detachment to the N. The continental margin to the W of the Lusitanian Basin would therefore be an upper-plate margin (i.e., margin above the detachment), according to the terminology of Lister et al. (1986). Figure 3.7 illustrates the main characteristics of upper-plate and lower-plate margins.

Several aspects of the quantitative analysis of section 2.3.2 are in good agreement with the upper-plate model. The detachment level at 35 km of depth separating a zone of reduced (40%) extension above from a zone of high (400%) extension below depicts such a model with considerable accuracy. Although McKenzie's theory, strictly speaking, applies only to pure-shear extension, the inclusion of a detachment level should allow the modelling of "Wernicke-type" extension to a first approximation. The lack of significant Cretaceous subsidence to the S of the Nazaré Fault also suggests an upper-plate setting, and this point will be further developed in connection with question b).

A more detailed study of the evolution of the Lusitanian Basin during the Late Jurassic should provide important elements for an answer to question a).

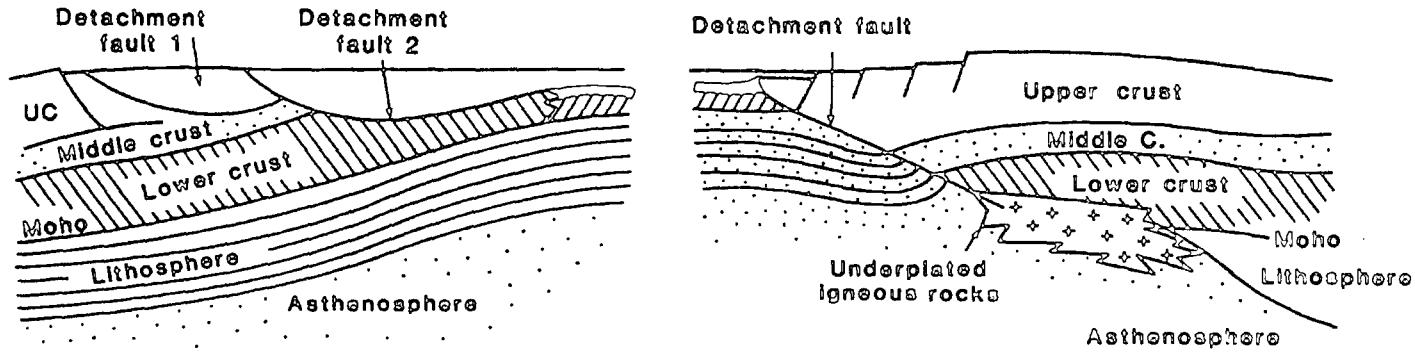

Fig. 3.7 - Main characteristics of upper-plate and lower-plate continental margins. Redrawn after Lister et al. (1987).

The lack of deep (crustal scale) reflection data on the Portuguese coast, in contrast to the conjugate margin (Keen and deVoogd, 1988), is a major hindrance to this objective.

During the Late Jurassic a second episode of rifting took place which evolved into sea-floor spreading in the Early Cretaceous. In section 1.4.1 it was discussed how this was accomplished after a westward jump of the rifting axis, an event which was then tentatively related to the evolution of the regional tectonic setting. The model of asymmetric rifting described above provides a visualization of the process of rift jump, which can be interpreted as the switching of the detachment fault to a deeper level, a possibility noted by Lister et al. (1986). Gibbs (1984) discussed this type of detachment switching, and considered the lock-up of the initial fault system after extension by a factor of 1.5 as a possible cause.

The fact that the second episode of rifting seems to have inhibited the thermal subsidence associated with the earlier event may perhaps be related to crustal underplating (Cox, 1980). This phenomenon, whereby basaltic magma sourced by partial melting in the upper mantle crystallizes underneath the lower crust, has been associated with lithospheric extension in intracratonic basins and passive margins (Furlong and Fountain, 1986; McKenzie and Bickle, 1988). An eastward dipping detachment would favour underplating to the E of the active rift (Lister et al., 1986), perhaps coinciding with the de-activated rift, leading to a regional upwarp of the Late Jurassic Lusitanian Basin which would compensate the tendency for subsidence due to thermal cooling. This hypothesis is also supported by the fact that the Jurassic-Cretaceous transition was marked by important magmatic activity, with many dolerite dykes being emplaced in the Lusitanian Basin (Aires-Barros, 1979).

The activity of transfer faults during the second episode of rifting can be invoked to explain the formation of the Torres Vedras-Montejunto Anticline. The rejuvenation of the Arrábida Range during the Late Jurassic (Montenat et al., 1988) could be another consequence of that activity. The idea of a simple fault separating the different extensional compartments is an oversimplification, and zones of complex and distributed shear deformation are likely to occur (Gibbs,

1985). Secondary compression parallel to the margin would cause the transpressive style associated with the transverse faults. The interference of extensional faults parallel to the margin with a system of transverse transfer faults of variable importance probably occurred during the early history of the Lusitanian Basin in the Late Oxfordian-Kimmeridgian, as described in section 2.2.3.

Very little is known about the answer to question c). Field evidence shows that the inversion was related to the activity of a complex network of faults (Hutton and Gawthorpe, 1988), but the tectonic overprint of the Miocene obscures the record of the Cretaceous evolution, which is poorly understood. Wilson et al. (in press) assign the structural inversion to the Cainozoic, and allow for 1 km of Tertiary sediments to have been deposited over the Lusitanian Basin before uplift and erosion. There are, however, indications of inversion during the Mesozoic, such as the uplift of the Torres Vedras-Montejunto Anticline in the Late Jurassic and the Alcochete Fault Zone in the Late Cretaceous. This is in agreement with the observations of Hutton and Gawthorpe (1988), who attribute the uplift of the Lusitanian Basin to continuing distributed sinistral strike-slip between the Late Jurassic and the Late Miocene.

Salt tectonics (Jaritz, 1987; Davis and Engelder, 1987) have been invoked to explain localized structural inversion in the Lusitanian Basin, in classic (e.g., Zbyszewski et al., 1966) as well as in modern studies (Wilson, 1988). The configuration and distribution of evaporitic outcrops, elongated and coinciding with major basement faults, suggest however that the rising of the salt was tectonically driven (Fonseca et al., 1988), in which case it cannot be considered the ultimate cause of the associated deformation. The main role of the evaporitic layer and associated salt walls was probably to provide a detachment between sediment cover and basement (and between blocks of sediment cover), thereby controlling the structural style of the inversional deformation.

The best answer to question d) seems to be strike-slip tectonics. The structural characteristics of the Lower Tagus Basin are indicative of deformation under the sinistral strike-slip regime of the Miocene (section 1.5.2). The clearest diagnostic feature is the coexistence in time and the vicinity in space of compressional (Arrábida) and extensional (Setúbal Peninsula) styles. The meandering, splay-

ing and anastomosing geometry of the Alcochete Fault Zone and the Vila Franca Fault are also typical of strike-slip faults (e.g., Rodgers, 1980). Also, the important depocentre near the zone where the two faults diverge (Figure 2.7), with a maximum thickness of post-Oligocene sediments of the order of 2 km, seems a clear example of what Crowell (1974) designated by "fault wedge basin", caused by the divergence of strike-slip faults.

On a broader scale, the faults of the Lower Tagus Basin can be regarded as a releasing bend (during the Miocene) on a sinistral shear zone, the strain being transfered southwards from the Vila Franca Fault to the Arrábida Thrust along the Alcochete Fault Zone (Figure 3.8). Under the contemporaneous stress field, transpression prevailed in Arrábida whereas transtension caused subsidence along the Lower Tagus Valley. To the NE, the Vila Franca Fault is another example of a transpressive structure, with the Mesozoic rocks of the Lusitanian Basin overthrusting in places the Tertiary sediments. The shallow basement drilled at the Mt-1 well (1705 m) may indicate the existence of a flower structure (e.g., Biddle and Christie-Blick, 1985) associated with this stretch of the contact between the two basins. This geometry is in fact suggested by the seismic reflection data (Figure 3.9). The intense thinning of the lower crust underneath the Lower Tagus Valley indicated by the refraction survey of Mendes-Victor et al. (1980) and shown in Figure 2.4b) may have taken place at this stage, as a consequence of the pulling-apart of the crust at the releasing bend.

A dextral sense of motion in the system of faults of the Lower Tagus Basin during the latest Cretaceous, under which it would behave as a restraining bend, could be the explanation for the intense uplift on both sides of the Alcochete Fault Zone during that period; the reversal of the sense of motion on the same system of faults would lead to the reversal of the pattern of uplift and deposition at the end of the Eocene, described in section 2.3.4. This type of reversal of the polarities of vertical motion is in fact a diagnostic feature of strike-slip tectonics (e.g., Rodgers, 1980).

Further evidence for strike-slip deformation during the Miocene may be found in the Montejunto Range, on the northern limit of the Arruda Sub-basin. Here, the microstructural survey of Guery (1984) links the rejuvenation of the moun-

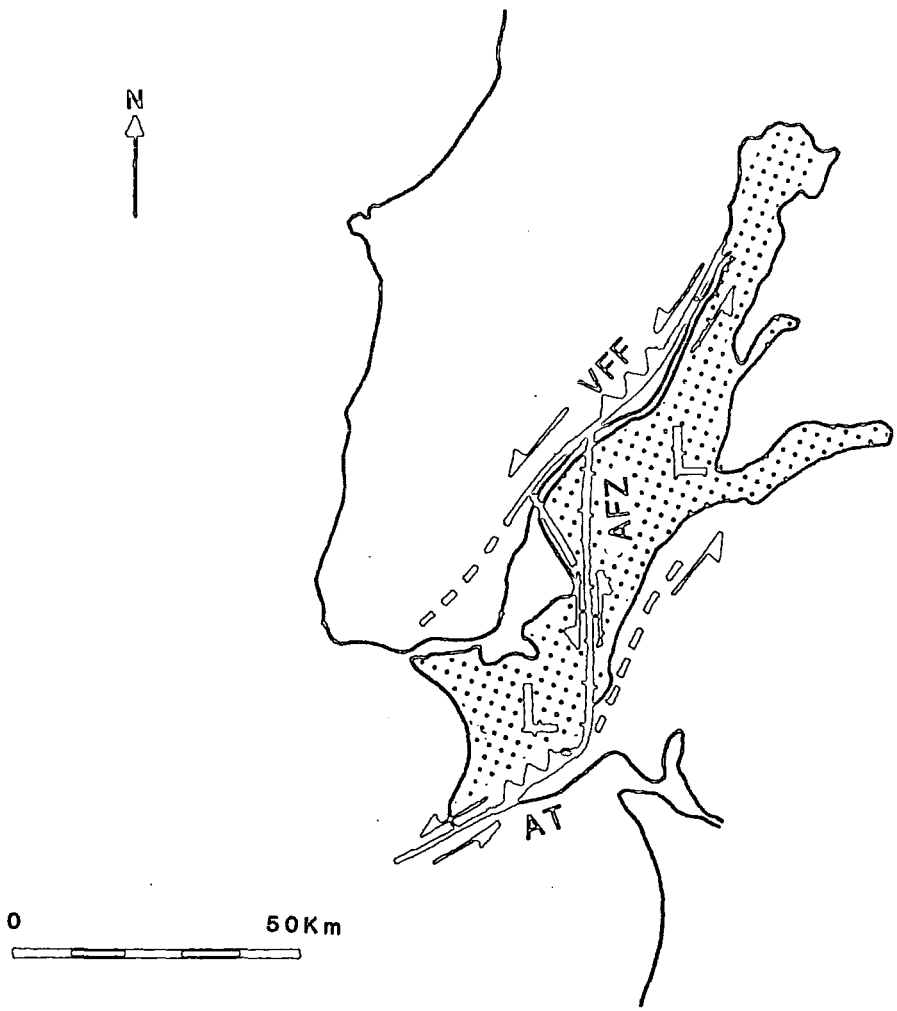

Fig. 3.8 - Tectonic model for the Lower Tagus Basin during the Miocene. AT - Arrábida Thrust; AFZ - Alcochete Fault Zone; VFF - Vila Franca Fault. Gravity lows, interpreted as Cainozoic depocentres, are indicated by L. The dotted area corresponds to the Quaternary cover, suggesting that the same setting controlled the neotectonic evolution of the Lower Tagus Valley.

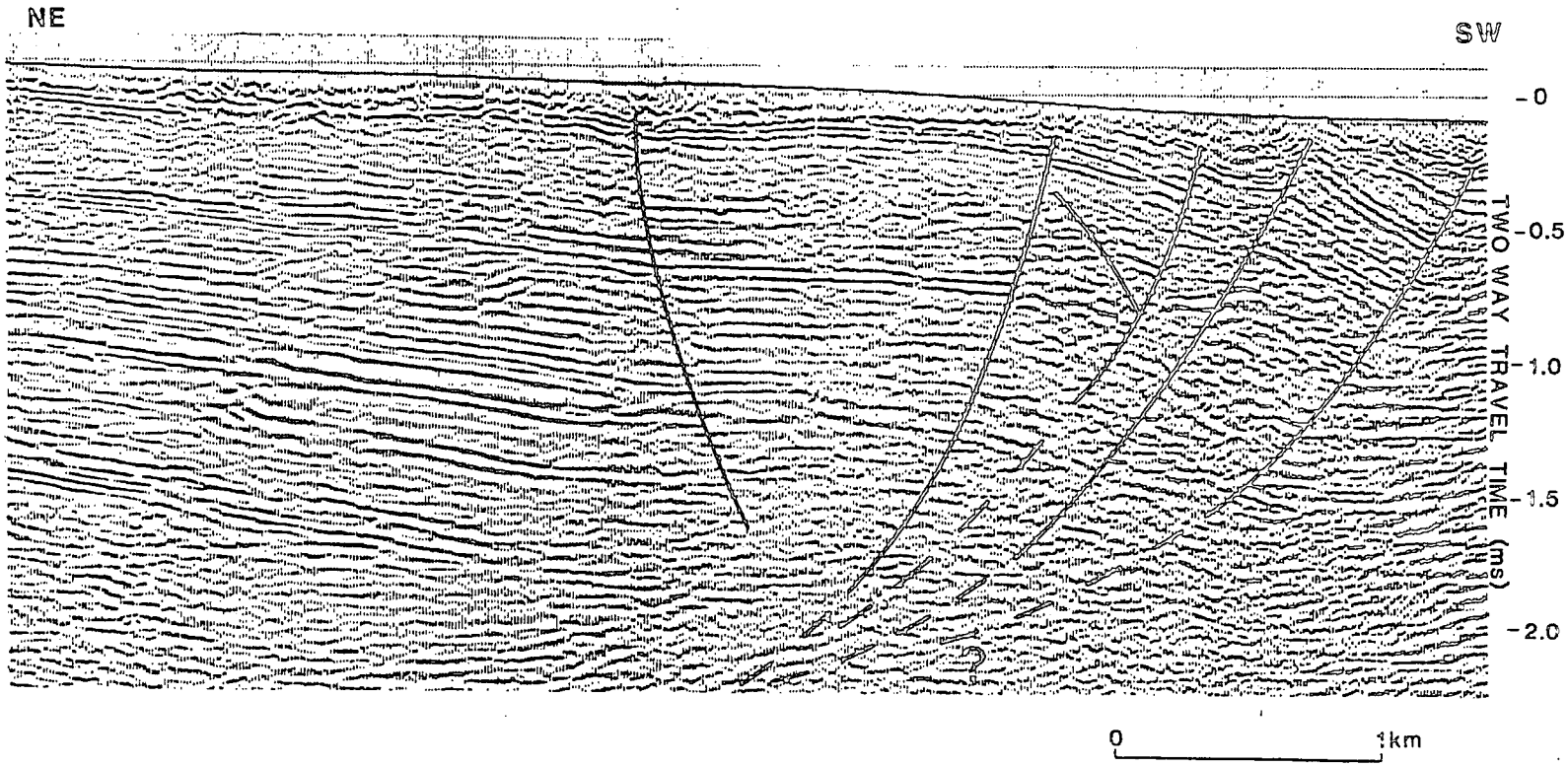

Fig. 3.9 - Seismic section accross the Vila Franca Fault, with interpretation. Data made available by GPEP, Lisbon.

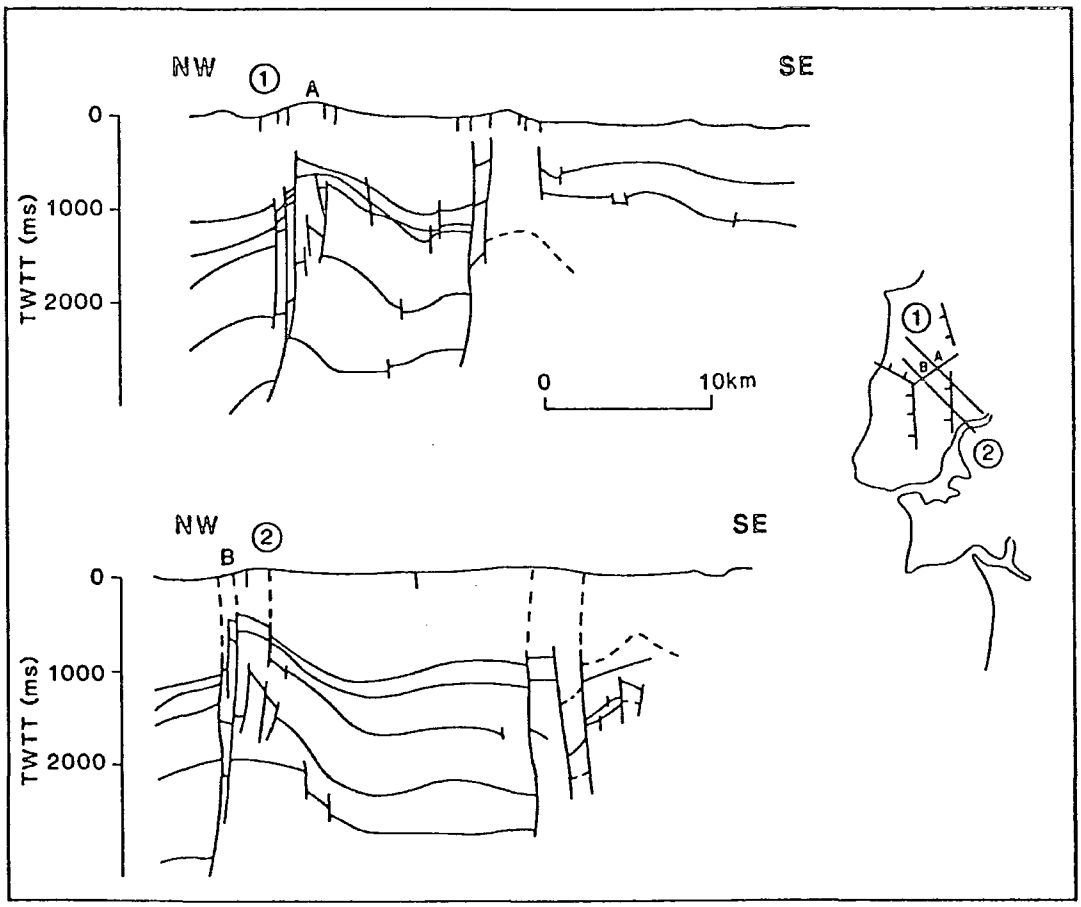

Fig 3.10 - Re-interpretation of the structure of the Torres Vedras-Montejunto Anticline (towards the left of the section), suggesting the existence of a transpressive flower structure. Based on interpreted two-way traveltime maps,made available by GPEP, Lisbon.

tains, reaching a maximum height of 666 m, to the strike-slip reactivation of the easternmost section of the Torres Vedras-Montejunto Fault (Figure 2.1). This author describes the Montejunto Range as a fold associated with the termination of a strike-slip fault to the NE of it, but the analysis of the seismic reflection data shows that strike-slip was also important further to the SW, on the western sector of the Torres Vedras-Montejunto Fault (Figure 3.10).

Areas of transpression are usually difficult to interpret objectively from seismic reflection data, since they are characterized by structural complexity at shallow depth, hampering the penetration of energy. On a seismic section, the materials squeezed upwards between the diverging faults of a flower structure are usually undistinguishable from salt diapirs, and in basins bearing evaporites the ambiguity and controversy are likely to emerge (e.g., the North Sea Basin). The structure of the Torres Vedras-Montejunto Fault was reinterpreted (Figure 3.10) starting with the two-way traveltime contour maps for five horizons (unpublished data, GPEP). This maps were produced from a dense network of seismic sections, and incorporate already the more subjective stage of identifying the reflections in those areas where they are not particularly clear. The structural pattern associated with the fault resembles very closely what has been described for other well established transpressive flower structures (e.g., Harding, 1985; Harding and Tuminas, 1988; Sylvester, 1988).

Montenat et al. (1988) presented recently an independent interpretation of the structure of the Torres Vedras-Montejunto Fault which also invokes Cainozoic transpressional deformation.

Evidence for Miocene strike-slip tectonics is also important further N, in the Candeeiros Range (Hutton and Gawthorpe, 1988). This area still lacks, however, a detailed survey, and lies to the N of the zone covered by this study.

Chapter IV

Seismicity of the Estremadura, and tectonic implications

4.1 Introduction. Historical seismicity.

The RESTE Project had as its central objective the acquisition of earthquake data to enable the computation of accurate (within 2 km) hypocentral locations and focal mechanisms. Previous studies had recognized the importance of a microearthquake survey in the Estremadura, the region surrounding the Lower Tagus Valley (Ribeiro et al., 1980; Mendes-Victor et al., 1980; Cabral,1986), but such work had not been attempted.

The data from the Portuguese National Seismographic Network does not allow reliable computations of focal mechanisms for small local earthquakes. Furthermore, focal depths cannot be obtained with acceptable accuracy, and large uncertainties (typically of about 20 km) are associated with the epicentral locations. This leads to a scattered picture of the seismicity pattern, and under these circumstances neotectonic studies have relied exclusively on the surface geology (Cabral et al., 1984; Cabral, 1986). However, in other intraplate areas where microearthquake networks where deployed, it has been possible to define the active structures and to characterize the ongoing deformation by the associated seismicity (e.g., Talwani, 1989). Although the patterns of seismic activity in the interior of the plates are intrinsically more complex than at the plate boundaries, the diffuse nature frequently described is likely to result in part from the inadequacy of the data.

Moreira (1984) gives a modern account of the historical seismicity of Portugal. Oliveira (1986) provides a compilation of historical data, and includes estimates of magnitudes (M_L?) which will be quoted throughout this section, although large uncertainties must be associated with these values.

The most destructive earthquakes that affected Portugal in the past were interplate events related to the convergence between Africa and Eurasia. The

Gorringe Bank, ca. 330 km SSW of Lisbon, is usually believed to be the epicentral region of the 1755 Lisbon Earthquake, which ruined most of the Portuguese capital. This is in general agreement with the distribution of damage, which was also very significant in Southern Portugal and Morocco. The occurrence of a large ($M_L = 7.5$) earthquake at the Gorringe Bank in February 1969, causing considerable shaking in Lisbon, reinforced this widespread belief. Moreira (1984) attributes also to this seismic area the historical event of 1356, felt in Portugal with similar intensity to that of 1755.

Superimposed on this series of interplate earthquakes, a less well known history of intraplate events, some of catastrophic proportions, characterizes the area surrounding the Lower Tagus Valley. The best studied example is the Benavente Earthquake of 1909 ($M_L = 6.7$), ca. 40 km to the NNE of Lisbon, which caused the loss of 30 human lives and was felt in most of the Iberian Peninsula (Choffat and Bensaúde, 1912). Similar events in 1344 and 1531 ($M_L = 7.0$) seem to have originated in the same region (Moreira, 1984). The Setúbal Earthquake of 1858 ($M_L = 7.2$), ca. 30 km S of Lisbon, was also responsible for important destructions and the loss of human lives.

Figure 4.1 shows the spatial distribution of the historical seismicity in the Estremadura, along with macroseismic locations for 20th century events and instrumental locations for the period 1980-87 (INMG, unpublished data). It shows clusters of seismic activity near the Nazaré Fault and to the N of the Tagus River.

The time distribution of the main historic events is shown in Figure 4.2. Only the events responsible for damage of buildings were included, and they are grouped according to the area were the damage was reported. The important fact that becomes apparent is that the 20th century, and in particular the last 50 years, correspond to a period of atypically low seismic activity, which can be compared to similar periods in the 15th and 17th centuries. For this reason, instrumental data on its own will provide a crude underestimate of the levels of seismicity that are characteristic of longer periods of time.

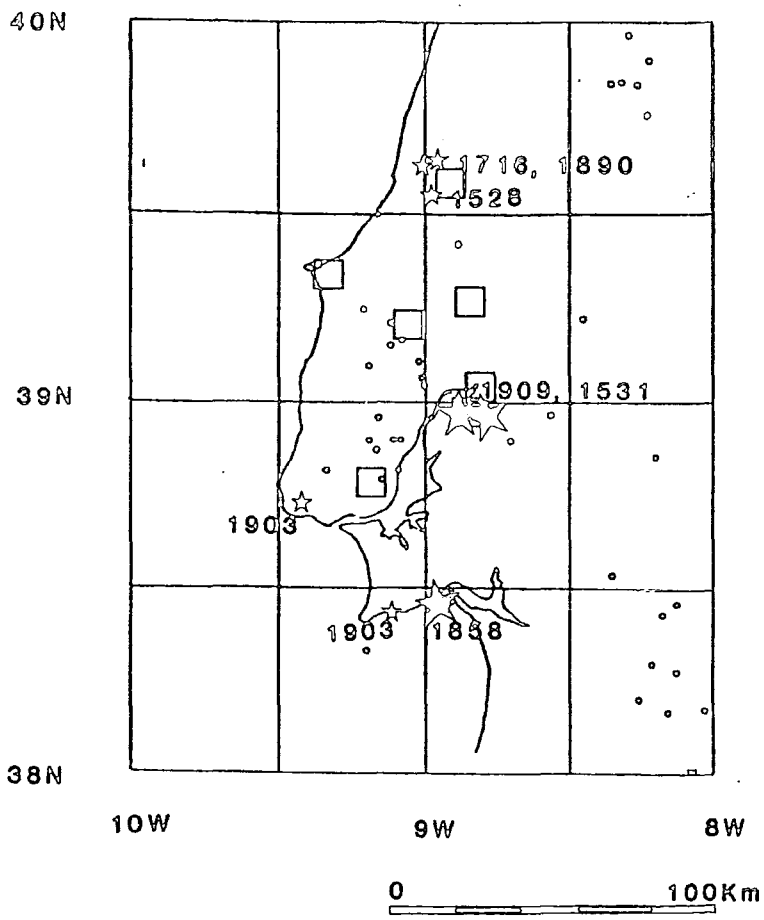

Fig. 4.1 - Spatial distribution of the seismicity in the Estremadura. Large stars are very damaging historical earthquakes, small stars are events that caused minor damage. The squares indicate macroseismic locations of 20th century macroearthquakes, and the dots are instrumental locations for the period 1980-87 (errors may be as large as 20 km). Historical seismicity after Moreira (1984); 20th century seismicity after INMG (unpublished data).

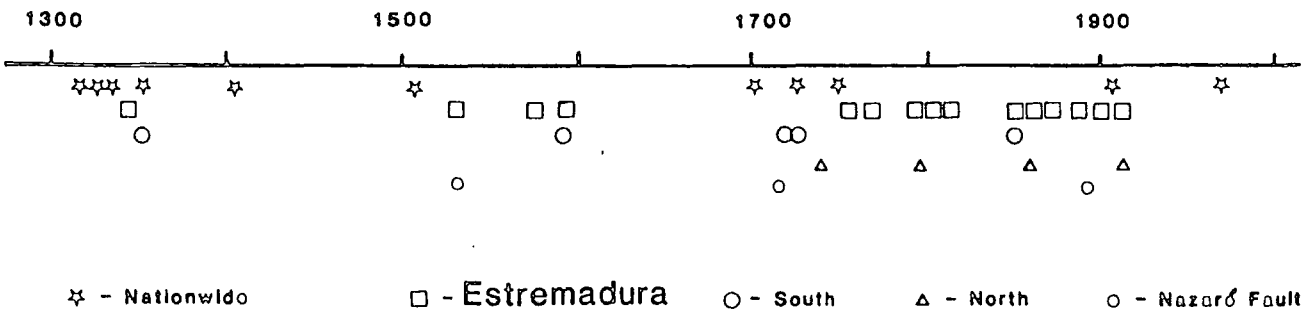

Fig. 4.2 - Time distribution of the main historical earthquakes of Portugal, grouped according to the region where the damage was reported. Based on Moreira (1984).

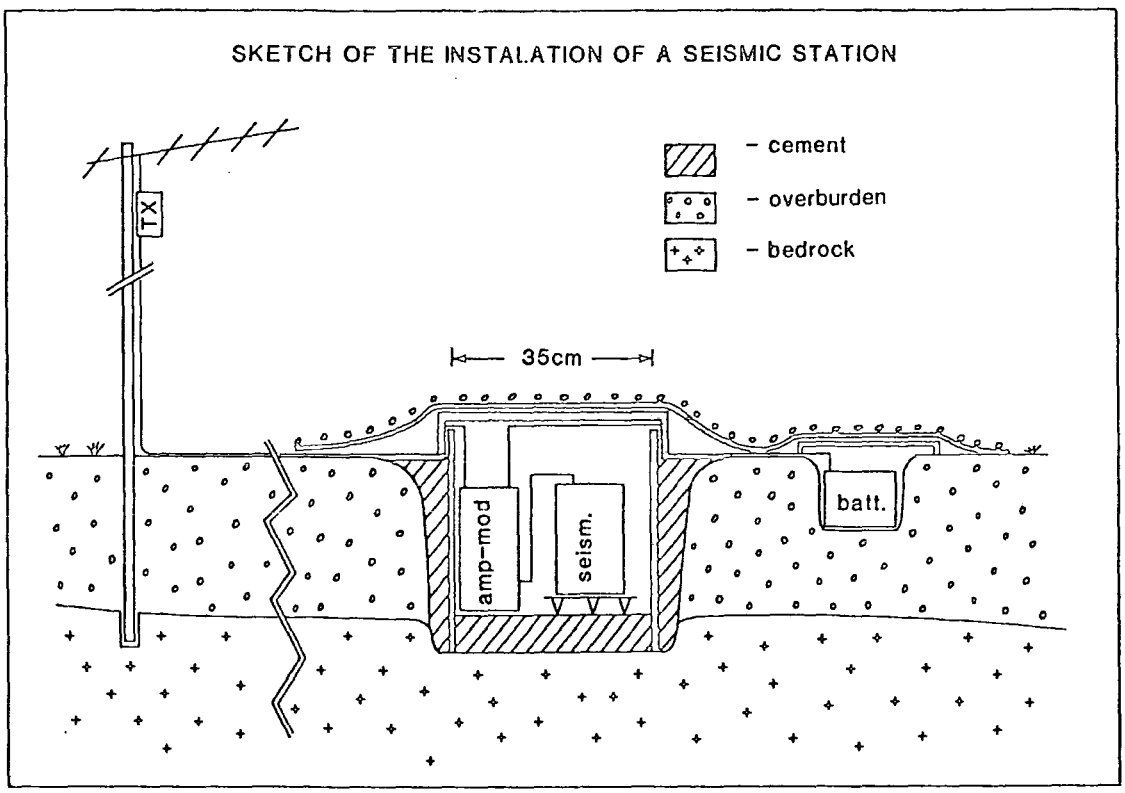

Fig. 4.3 - Layout of a RESTE seismic station.

4.2 The RESTE Microearthquake Survey.

4.2.1 Logistics and instrumentation.

In April 87, formal contacts were initiated with the Instituto Nacional de Meteorologia e Geofísica, Lisbon (INMG) and the Laboratório Nacional de Engenharia Civil, Lisbon (LNEC) towards the instalation of a temporary microearthquake network in the area surrounding the Lower Tagus Valley. It was agreed that the INMG would provide logistic support (vehicle and staff) to build and maintain the network, with the cooperation of the LNEC. The equipment was loaned from the NERC Seismic Equipment Pool, Edinburgh, through the University of Durham. The experiment was named RESTE (Rede de Estações Sismográficas Temporárias da Estremadura/ Temporary Seismographic Network of Estremadura).

No.	Description
24	vertical component seismometer Wilmore MKIII, resonant frquency 1 Hz
24	FM amplifier-modulator, manufactured by Earth Data Ltd (9690 Data Acquisition System), with central frequency 676 Hz and frequency deviation ±40%
24	radio transmitter/receiver (9690 Data Acquisition System), with carrier frequencies in the range 458-459 MHz, typical output power of 100 mW and range of 50 to 100 km
2	MSF (Rugby, U.K.) time code radio-receiver
48	Yagi aerial, with 12, 8, 6 or 3 elements
2	Geo-store field recorder, manufactured by RACAL Ltd, with eleven data input channels and internal VELA time code generator

Table 4.1

Table 4.1 gives a list of the equipment used in the experiment. The data were recorded continuously onto magnetic tape (analog record), at a selected speed of 15/160 inches per second, alongside FM modulated VELA and external MSF time codes and a reference frequency to be used as a servo-control during playout.

Figure 4.3 shows the layout of a RESTE seismic station. A concrete pipe (35 cm in diameter; 50 to 100 cm long) was placed in a hole through the overburden, reaching the bedrock whenever possible, and cemented at the bottom to provide coupling with the solid rock. The seismometer was placed inside the pipe, with the amplifier-modulator. The pit was then covered with a especially moulded concrete lid. The electrical connections between the amplifier-modulator, the transmitter and the battery were made through a small hole in the side of the concrete pipe, slightly above ground level. The lid and surrounding area were covered with plastic and the hole for the wiring was protected with vaseline. The site was then disguised with soil and vegetation. The transmitter and the aerial were mounted on a 4 metre high mast, about 10 metres away from the seismometer pit to reduce the seismic noise generated by the action of the wind. The battery was wraped in plastic and buried in a nearby pit.

The layout of the network consisted of two groups of seismic stations (9+10), each group radio-linked to a central station where one of the recorders was installed (Figure 4.4). The requirement of line of sight for the FM radio-transmition restricted the possible locations of the central stations: one (LISBOA) was sited at the INMG headquarters in NE Lisbon, on top of an eight storey building; the other (MONTEJUNTO) was installed in premises of the 11th Air Base of the Portuguese Air Force, at an elevation of 660 m, 50 km to the N of Lisbon. Table 4.2 lists the coordinates and elevations of the 19 seismic stations.

Major constraints on the location of the seismic stations were imposed by the topography, the use of the land and the geology, and in some cases a compromise had to be reached in order to safegard the geometry of the network. In the Lower Tagus Basin, geological conditions were less favourable, with total absence of well consolidated outcrops; this notwithstanding, sites which were located in quiet areas far from human activity proved to have very good signal-to-noise ratios.

Table 4.2

#	STAT	LATITUDE DG MIN	LONGITUDE DEG MIN	ELEV m
1	ABV	38N58.93	8W50.92	20.
2	AMG	38N58.88	8W39.13	50.
3	ASN	38N47.27	9W23.21	530.
4	AVL	38N53.64	9W 6.50	300.
5	ACA	38N49.39	8W48.10	50.
6	AST	38N50.18	8W31.40	130.
7	AMJ	38N42.04	9W 2.49	5.
8	ASZ	38N27.53	9W 5.44	200.
9	AMT	38N35.00	8W36.11	50.
10	BMM	39N15.56	8W50.82	100.
11	BMJ	39N17.17	9W 2.86	660.
12	BPT	39N 9.92	8W50.82	90.
13	BOT	39N 5.87	8W58.84	50.
14	BAL	39N 8.36	8W35.05	170.
15	BSM	39N 2.40	9W 8.53	260.
16	BCR	38N59.18	8W59.59	200.
17	BMU	39N 4.61	8W40.99	30.
18	BPA	38N53.62	8W53.35	5.
19	BSE	38N53.26	8W46.62	25.

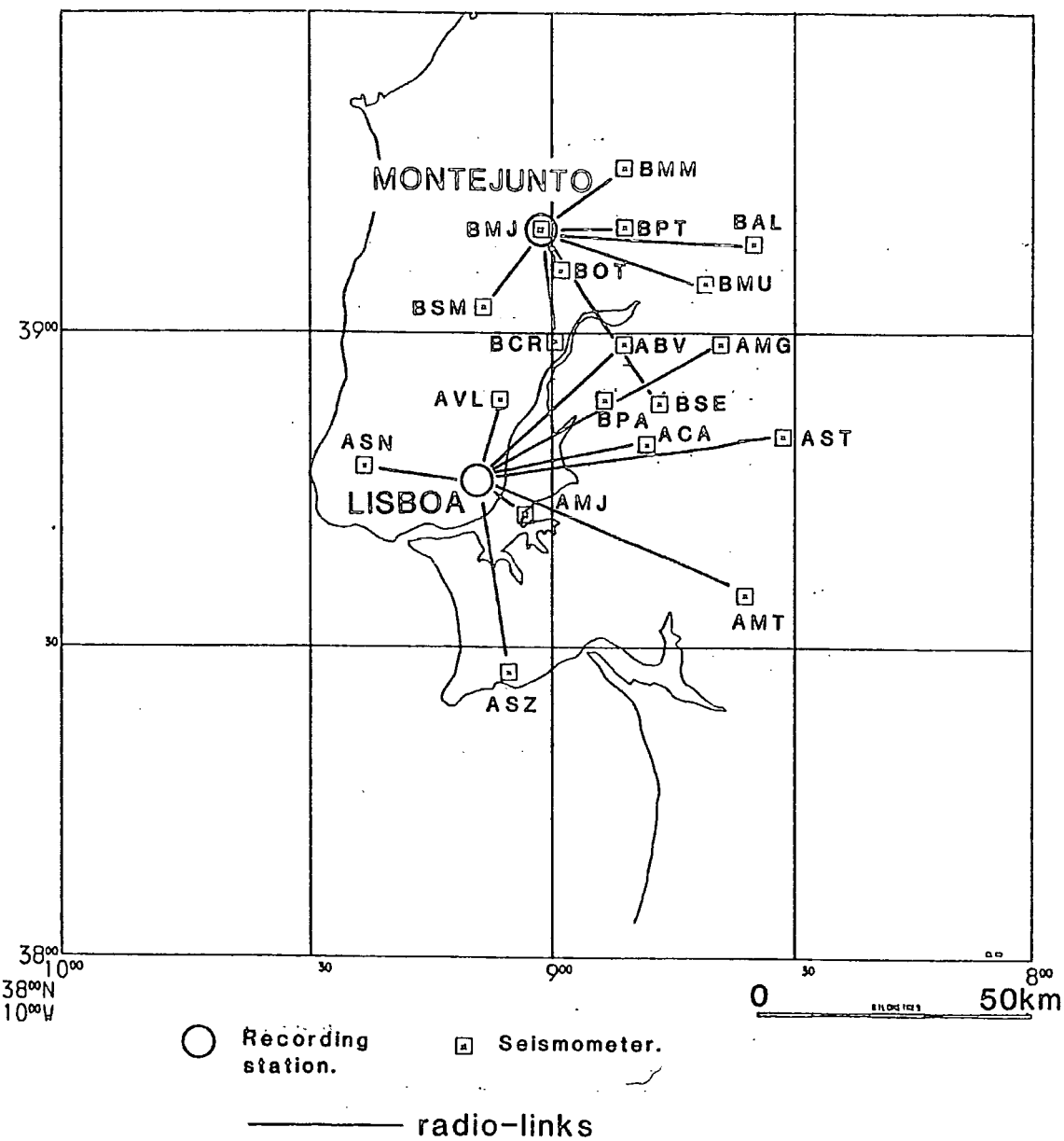

Fig. 4.4 - Layout of the RESTE Network.

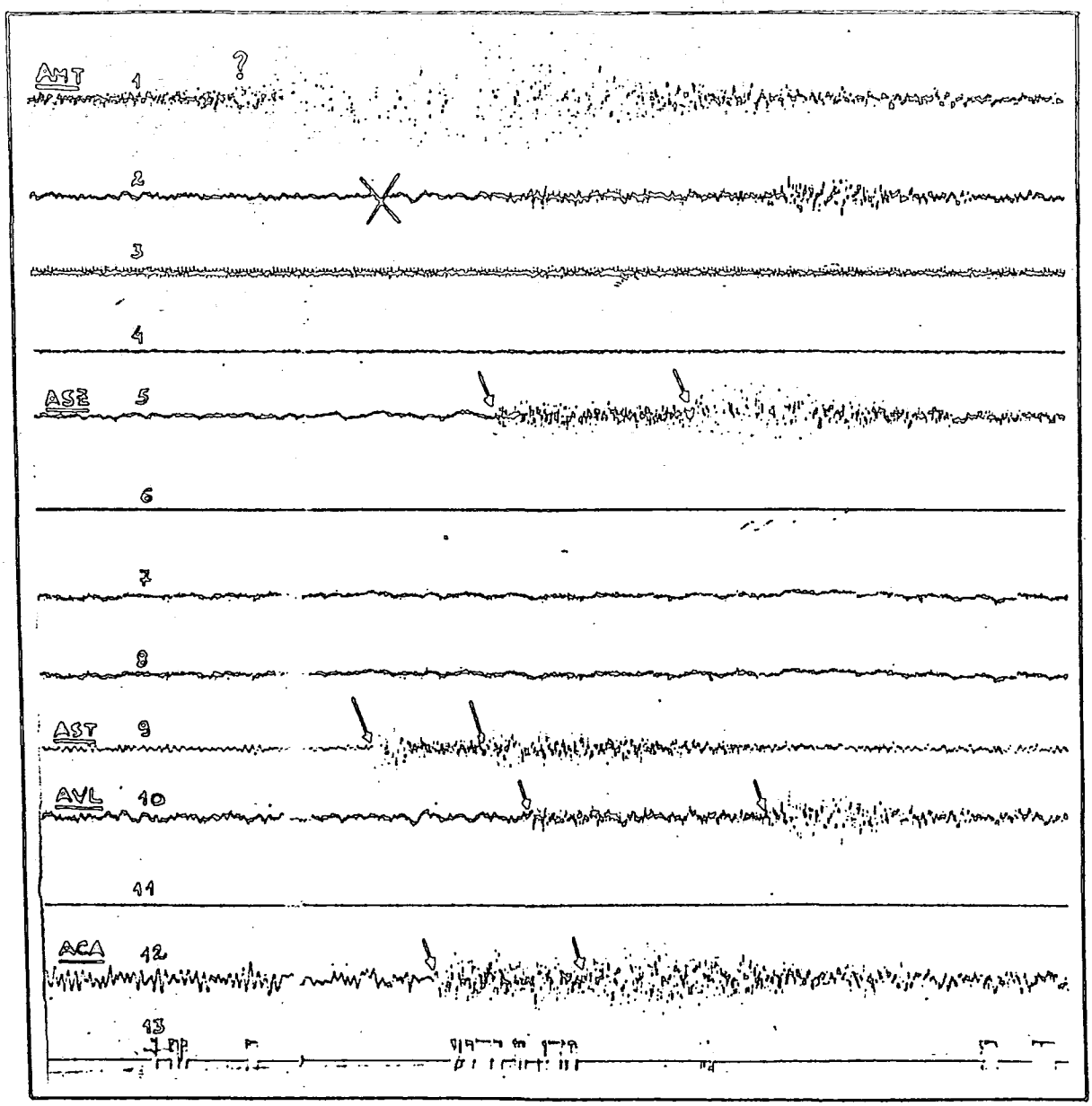

Fig. 4.5 - Jet-pen multi-channel record of event EL06.

In the Lusitanian Basin, the abundant outcrops of Mesozoic limestones allowed better coupling of the seismometers, but the population density is higher and the industrial activity more intense. Combined with the rugged topography, these factors made the selection of quiet sites more problematic there.

With good logistic support and fair weather, the building of the seismic stations could be achieved at a rate of three stations per working day, and the ideal number of people involved in the operation is probably three. In the RESTE experiment, the latter number was usually exceeded and the former was seldom reached, with very high temperatures initially, and heavy rain later, affecting considerably the efficiency of the works.

Figure 4.5 reproduces the jet-pen record of a small earthquake that occurred on October 25/26, 1987, code-named EL06. An extreme concentration of disfavourable conditions makes this event the natural choice to exemplify the difficulties that can be encountered when operating a microearthquake network. An electronic fault had disrupted temporarily the recording of the VELA time code (trace 13), and the conditions of radio-reception did not allow the recording of the MSF code (trace 11). However, the relative timing of the arrivals was still possible, because the standard frequency generated inside the recorder by a crystal oscillator was recorded on trace 6. Only 9 stations had been installed at this stage, and due to temporary logistic difficulties only 6 were operating normally at the time of the event. Due to an anomaly in the radio-reception, trace 2 is reproducing trace 10 with the additional loss of one station. Finally, a burst of radio-noise obscured the record of the event on trace 1.

4.2.2 Data preparation.

The magnetic tapes recorded at the RESTE central stations were dispatched to Durham and processed with the facilities of the Seismic Processing System (Stevenson, 1986), running on a PDP-11 workstation. The first step consisted of scanning systematically the tapes: the seismic trace from a selected channel was displayed as a series of raster lines on a Techtronics 619 VDU for visual inspection, at a rate of about 2.2 hours of data per screen, arranged in 40 lines. This allowed the identification of seismic events in a highly effective way, with two different channels from each tape (recording time of ca. 3.5 days) scanned in

under one hour. The combined use of a multi-channel high-frequency jet-pen in parallel with the scanning system allowed the quick check of any suspected event, to rule out bursts of local noise in the channel being scanned. After approval, each event was classified as local, regional or teleseismic, according to whether it seemed to originate within or close to the network, within a radius of 500 km or further away. This preliminary classification was done by inspection of such features as event duration and separation between the p- and s-wave arrivals.

Automatic facilities were available to read the time of a particular event by picking its position on the screen with a stylus, and to position the magnetic tape accordingly. After a seismic event had been approved and classified, a user-defined length of tape including the event (usually two minutes of recording time) was re-read and the data in the several channels was digitized, multiplexed and stored in a disc file, for further processing. A sampling rate of 100 Hz was used for local events and 50 Hz was used for regional and teleseismic events. Adequate anti-aliasing analog filters were automatically selected by the digitizing software.

The operation of the RESTE Network generated 144 analog magnetic tapes, 95 from the central station LISBOA and 49 from the central station MONTEJUNTO. A total of 87 events were identified and selected, from which 28 were classified as local, 24 as regional and 35 as teleseismic. Of the 28 local events 16 were found to be quarry blasts and the remaining 12 were genuine earthquakes. Figure 4.6 shows examples of the different types of records. After digitization, these data were stored on one single 2400" magnetic tape.

After the digitizing procedure, the processing of the data was carried out on the MTS mainframe (Amdahl 470 system) of the Durham University Computer Centre, still using the software of the Seismic Processing System. For each event, the digital time-series corresponding to the different stations were displayed graphically on screen and enlarged to a convenient scale, and the p (and when possible the s) arrivals were identified and picked with the stylus. The polarities of the p-wave first motions were picked using the analog jet-pen seismograms (Figure 4.7), to minimize the amount of processing, thus avoiding possible modifications of the waveforms.

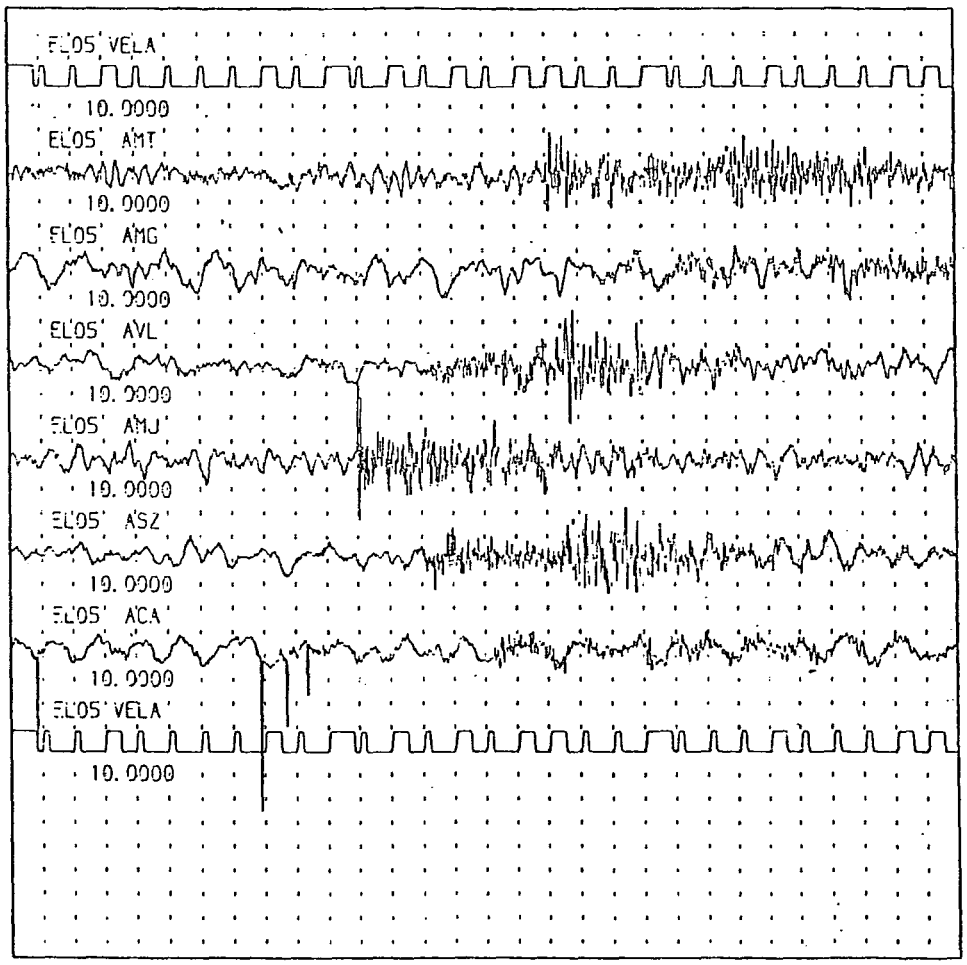

Fig. 4.6a - Digital seismogram of a local microearthquake.

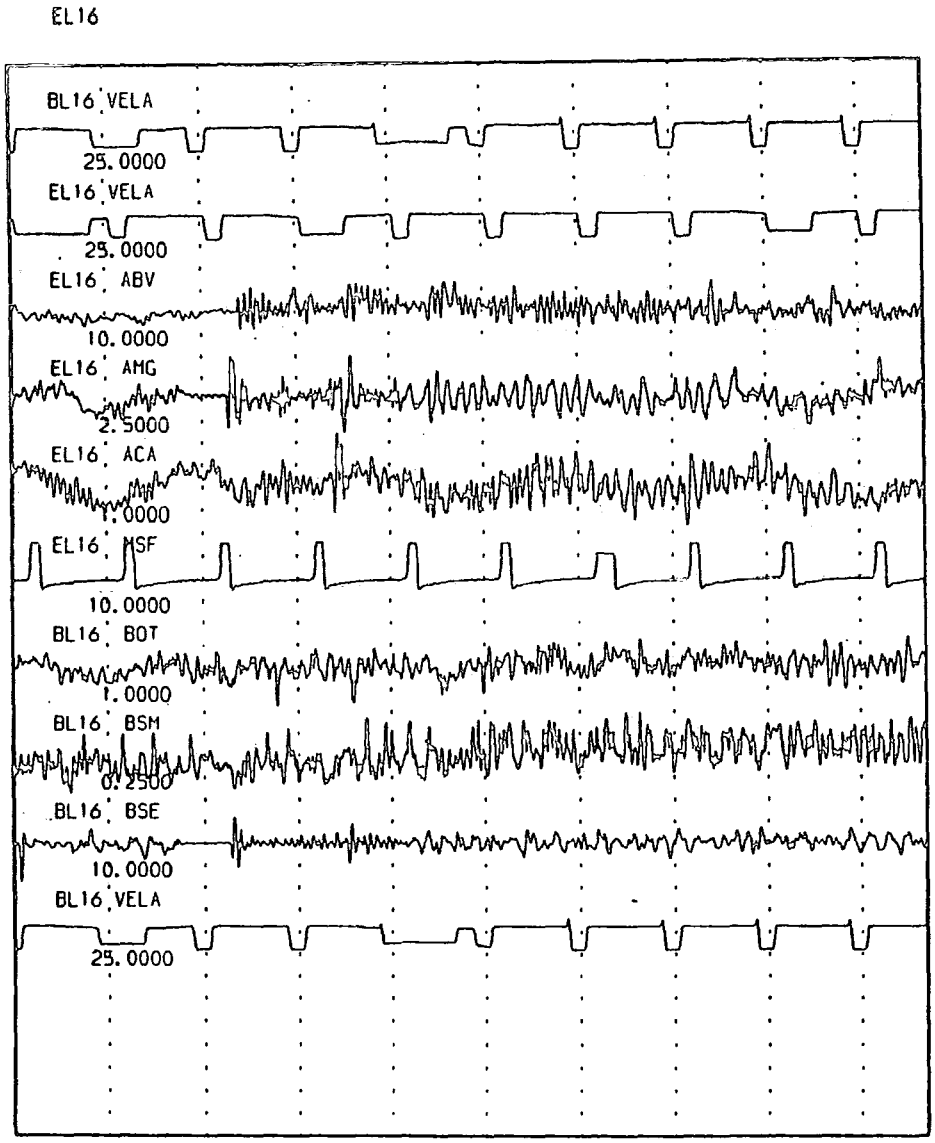

Fig. 4.6b - Digital seismogram of a quarry blast. Some first motions are dilatational, despite the explosive nature of the source.

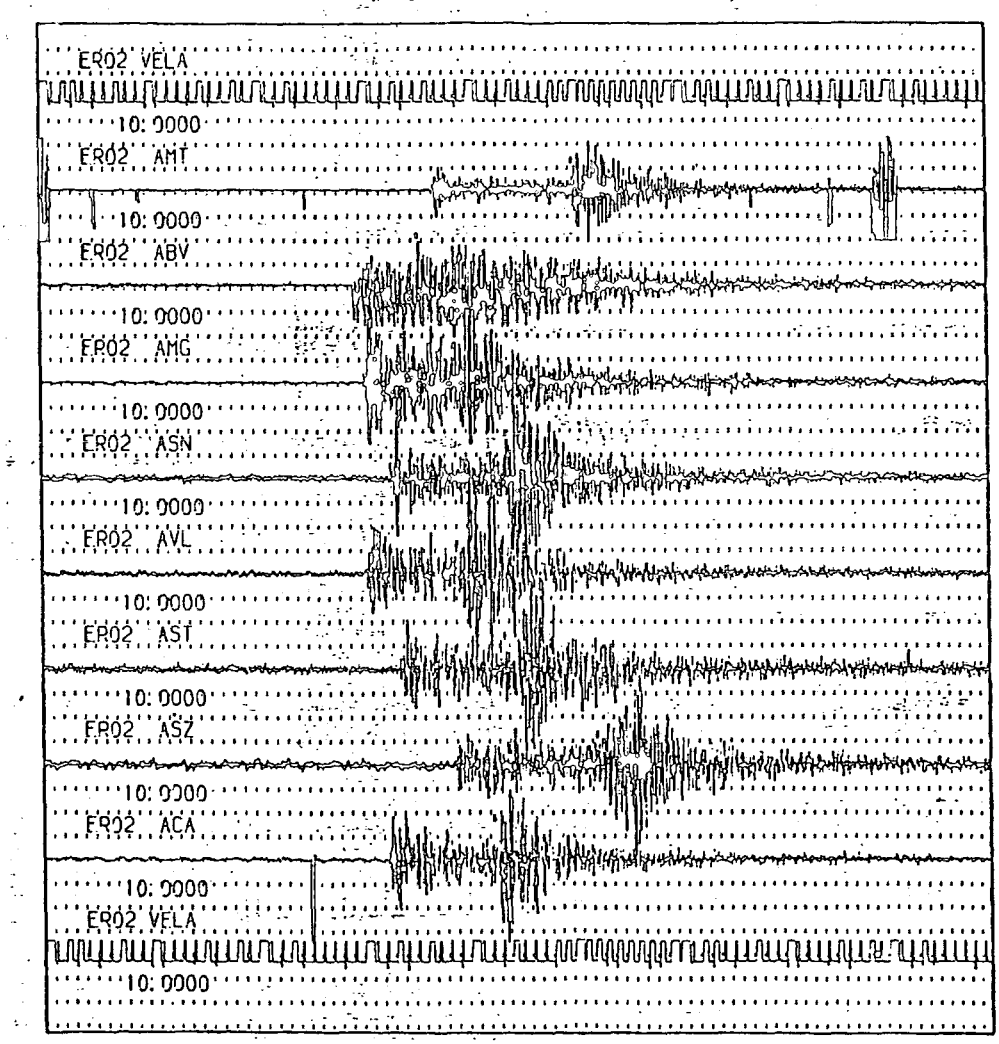

Fig. 4.6c - Digital seismogram of an earthquake close to the network.

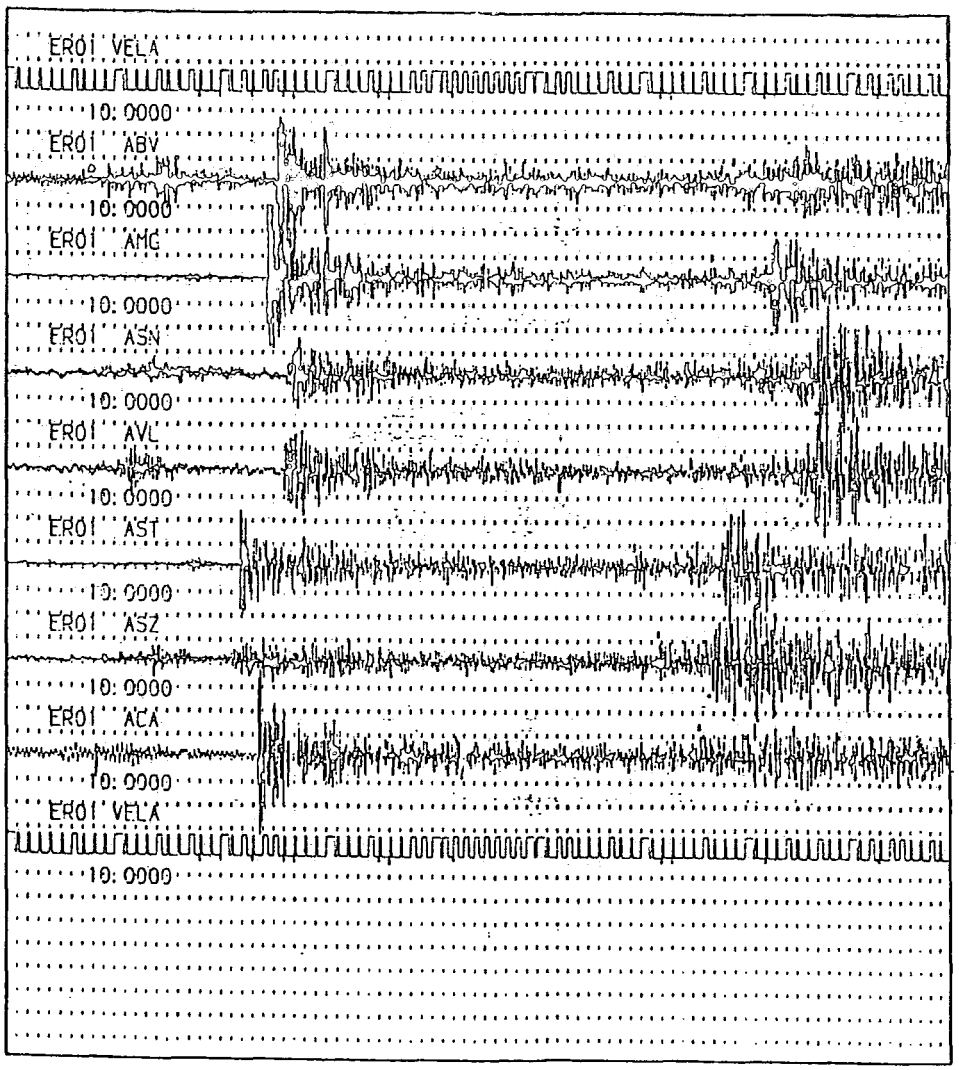

Fig. 4.6d - Digital seismogram of a regional earthquake (Gulf of Cadiz), preceeded shortly by a local microearthquake.

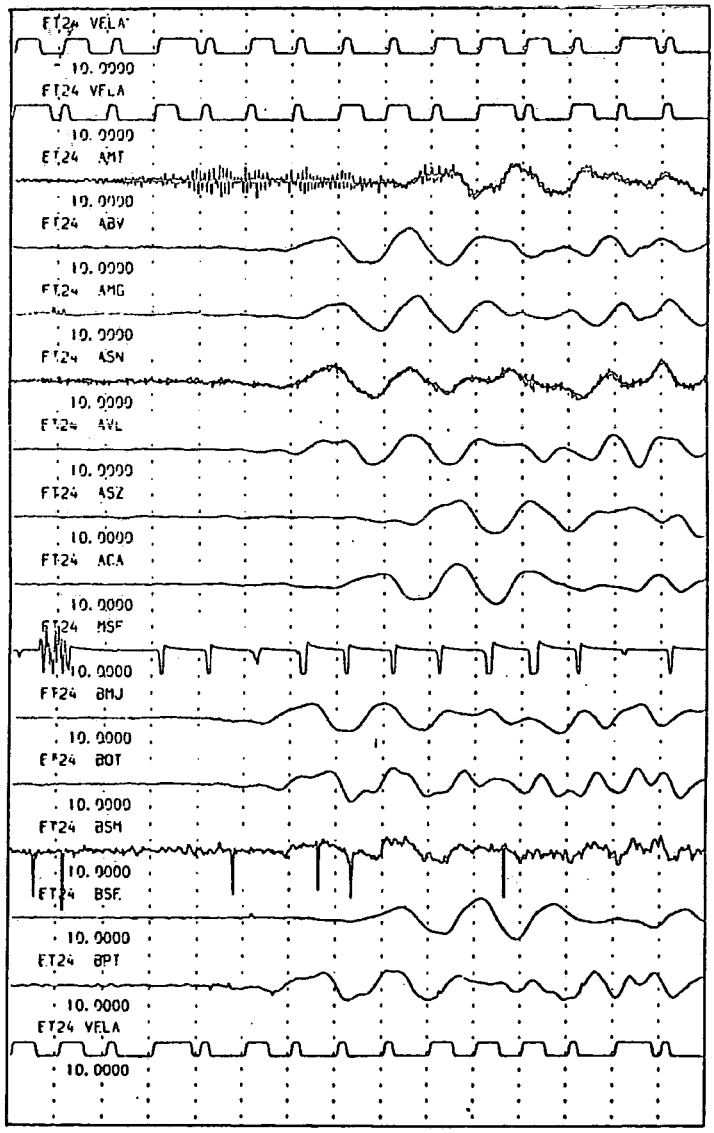

Fig. 4.6e - Digital seismogram of a teleseism (06MAR88, 22:36 GMT, 57 27' N, 142 79' W, Alaska, $m_s = 7.6$).

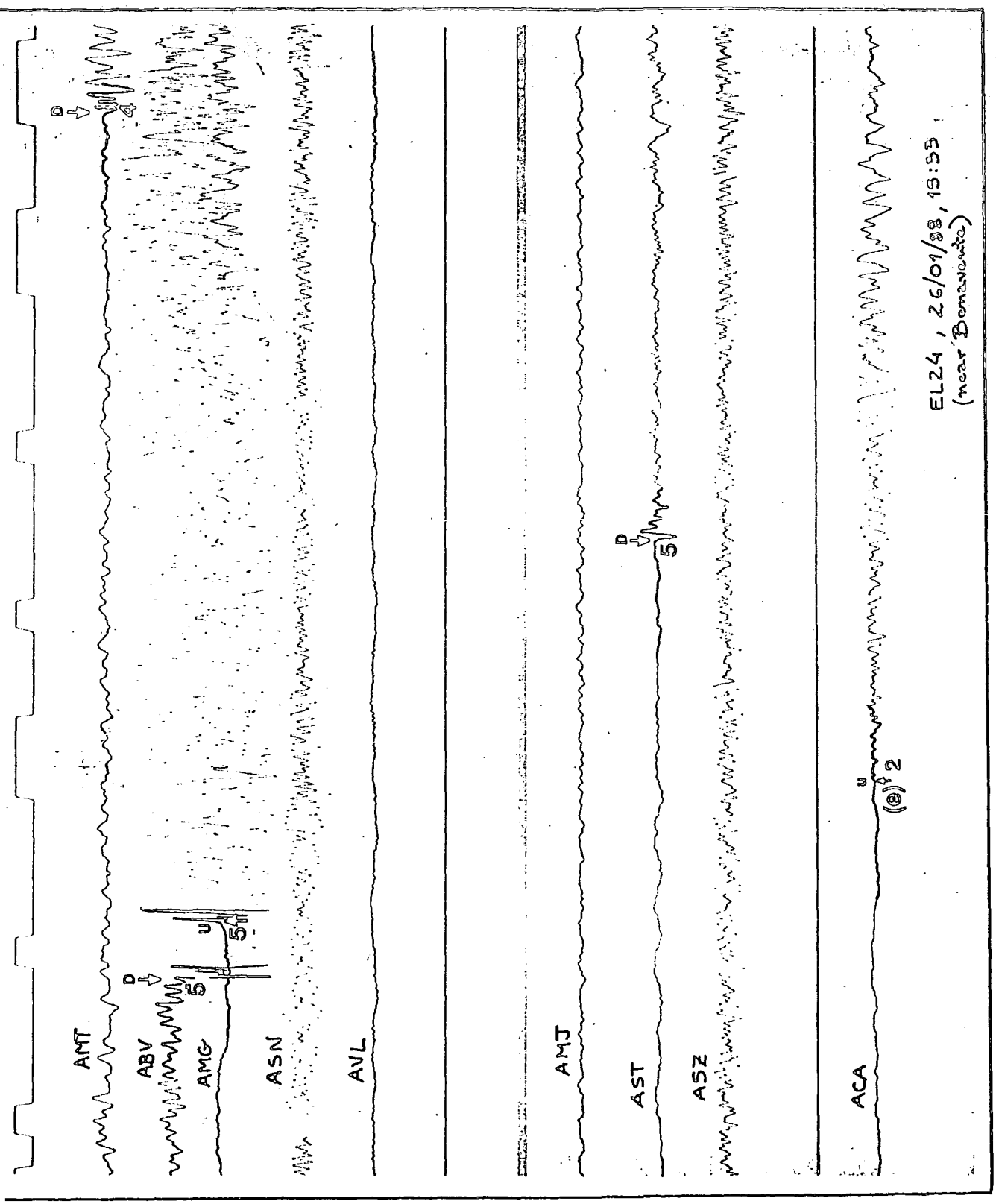

Fig. 4.7 - Jet-pen seismogram of a RESTE microearthquake, with analysis of p-wave first motions.

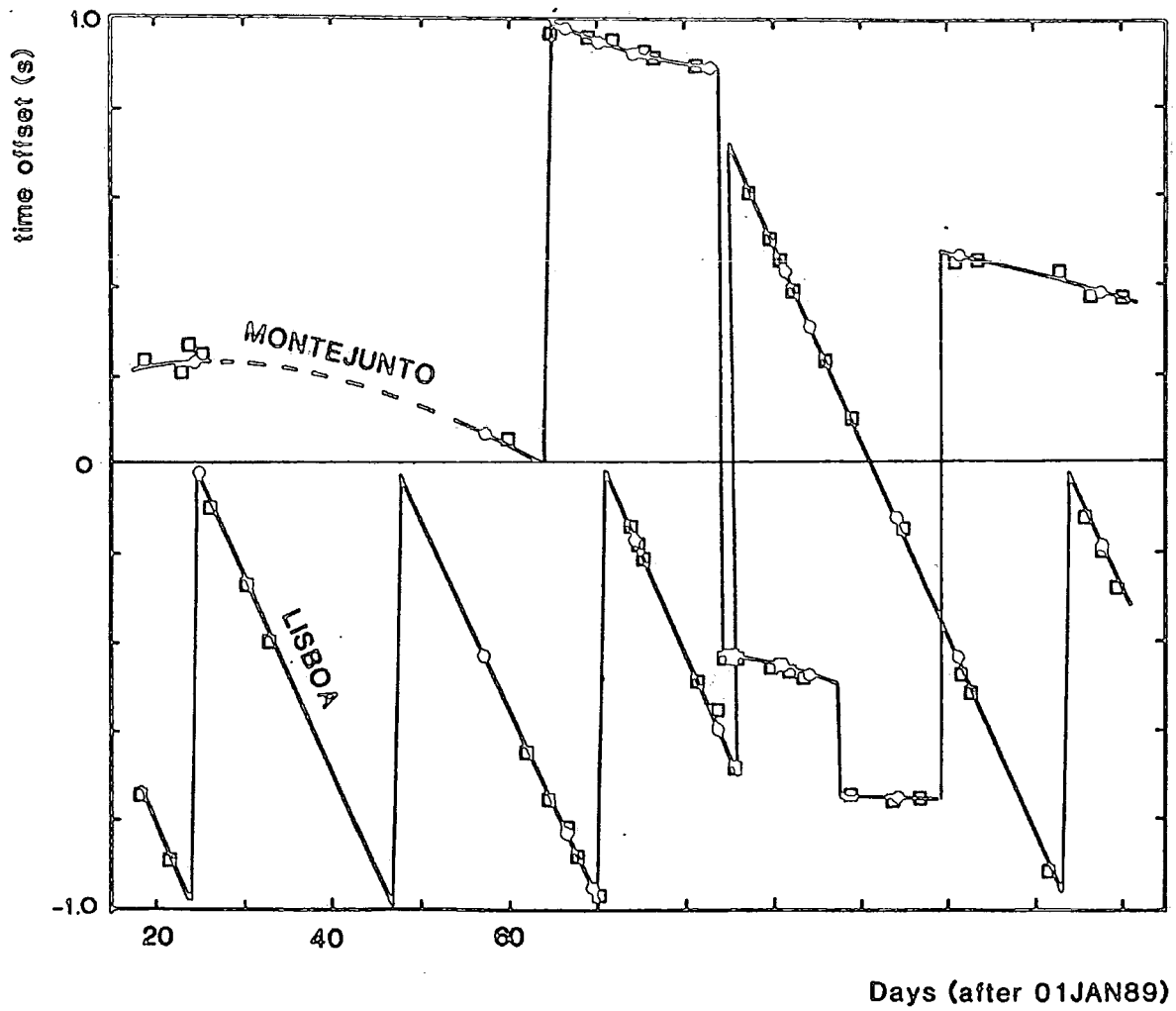

Fig. 4.8 - Drift curves for the VELA time code generators of the two Geo-store recorders. MSF time was used as standard. Only the non-integer parts of the drifts are represented. The curves correspond to the interval 16JAN88-14MAY88.

The arrival times of the picked phases were calculated automatically from the corresponding VELA time code channel, and stored in a disc file. The main contribution to timing error at this stage is due to the subjectivity inherent to the identification of the onset of a noise-contaminated signal. This uncertainty was typically not large than ± 5 ms, but could reach the double of this value in adverse noise conditions.

Before using the arrival times obtained by the procedure described above, they were corrected for the drift of the internal time code generator in each Geostore recorder. This was done by comparing the VELA time code with the MSF time code recorded alongside. The offset was measured repeatedly at different points along the record, allowing the estimate of a standard error of ±7 ms associated with the correction. This error was mostly due to the distortion of the MSF time code signal, which on a fast jet-pen playout differs significantly from a square wave.

The recording of MSF time-code was not continuous, due to problems with its radio-reception in the area of the survey. It was nevertheless possible to obtain calibration points spaced by intervals of the order of two or three days and to interpolate in between. This procedure was satisfactory because both recorders were installed inside acclimatized buildings with virtually no temperature oscillations, and under these conditions the clock drifts can be expected to be almost linear, within the manufacturer's specification of less than 1 second per week. At any rate, the need to interpolate corresponds to a loss of accuracy that will be accounted for by doubling the error associated with the conversion between VELA and MSF times. This results in a global conversion error of ±14 ms, which combined geometrically with the average picking error of ±5 ms yelds an overall timing error of ±15 ms. Hence, a value of 0.02 s will be adopted for the error in the timing of first arrivals.

Figure 4.8 shows the drifts of both internal clocks with respect to MSF time for a period of four months, obtained by fitting the calibration points with a polynomial. For the less stable clock the drift was of the order of 0.3 second per week. The discontinuities of the drift curve were caused by re-setting the clocks after maintenance operations.

Once corrected arrival times were obtained, the hypocentres of the local earthquakes were located using DUEDROPS, a software package developed at Durham University (Smith and Foulger, 1987) which uses the FORTRAN program HYPOINVERSE (Klein, 1978). Before discussing the results, the next section will deal with several theoretical aspects of hypocentral location.

4.3 Hypocentral locations.

4.3.1 Nonlinear optimization. Location pitfalls.

Hypocentral location is a problem of non-linear optimization, since the observable quantities (arrival times) are non-linear functions of the unknowns (focal coordinates and origin time) that are to be estimated (Lee and Stewart, 1981). The "objective function" to be minimized is the sum of the squares of the traveltime residuals (for a trial solution), and any implementation involves an algorithm to search iteratively for a minimum of this quantity. Although some attempts have been made to use full non-linear methods such as the SIMPLEX algorithm (Rabinowitz and Kulhanek, 1988) or Newton's algorithm (Thurber, 1985), most well-tested computer programs involve the linearization of the dependence between traveltime and source coordinates, through a procedure known as Geiger's method (Lee and Stewart, 1981).

Denoting by $\mathbf{r}$ a nx1 array of traveltime residuals (n being the number of stations) corresponding to a trial solution $\mathbf{x}$ (source coordinates and origin time), the objective function becomes

$$F(\mathbf{x}) = \mathbf{r}^T.\mathbf{r} \tag{4.1}$$

and can be expanded as a Taylor series around $\mathbf{r}$ according to

$$\delta F = F(\mathbf{x} + \delta\mathbf{x}) - F(\mathbf{x}) = \tag{4.2}$$

$$= \mathrm{g}^T.\delta\mathrm{x} + \frac{1}{2}\delta\mathrm{x}.(H\delta\mathrm{x}) + \textit{higher order terms},$$

where g is the gradient of F and the "Hessian matrix" H is composed of the second partial derivatives of F. The direction along which the variation of F is faster can be found by applying the standard extremum criteria to (4.2), and is given by

(4.3) $$\delta\mathrm{x} = -H^{-1}\mathrm{g}$$

(Lee and Stewart, 1981).

Geiger's method of hypocentral location uses the iterative scheme suggested by (4.3), after introducing two approximations. The first consists of linearizing the relation between the traveltime residuals and the errors δx_j in the source parameters through

(A4) $$r_i = \frac{\partial T_i}{\partial x_j}\Delta x_j, \qquad or \qquad \mathrm{r} = B\ \Delta\mathrm{x}$$

where $B_{ij} = \frac{\partial T_i}{\partial x_j}$ is the derivative of the traveltime to station i with respect to the source parametre x_j. With this notation, the gradient of F and the Hessian matrix can be re-written as

(4.5) $$\mathrm{g} = -2B^T\mathrm{r}$$

and

(4.6) $$H = 2(B^TB - (gradB^T)\mathrm{r}).$$

The second approximation in Geiger's method consists of ignoring the dyad of non-linear terms on the right-hand side of (4.6). In this way, (4.3) becomes

$$\delta\mathbb{x} = A^{-1}\mathbb{r}, \qquad with \qquad A^{-1} = (B^T B)^{-1} B^T. \tag{4.7}$$

This result, formally equivalent to the least-squares solution for linear problems, is known as the Gauss-Newton iterative method of non-linear optimization.

Different algorithms have been proposed to solve the system of linear equations (4.7), which is liable to diverge from the true solution whenever the approximations inherent to the method cease to be valid. In particular, the success of the iterative process depends critically on the geometry of the seismic network and on the degree of "excentricity" of the epicentre with respect to the distribution of the stations. This aspect will be further pursued later in this section.

The program HYPOINVERSE solves the system of equations (4.7) with the method of generalized inversion with eigenvalue truncation, the fundamentals of which will be discussed in section 6.2.3. To deter divergence associated with non-linearity, the program applies a damping factor to the length (in space) of each iteration step, and applies a larger damping factor whenever an increase in the objective function is detected. The iteration process stops when the spacial adjustment becomes smaller than a user-defined value, when the improvement in the RMS residual traveltime falls below a certain threshold or when the number of iterations reaches a specified limit.

The first step towards the location of hypocentres is the choice of a suitable seismic velocity model. The version of HYPOINVERSE that was used calculates traveltimes and take-off angles at the source by interpolating from a traveltime table, previously computed with a user-defined velocity model. The table consists of a grid of values of source-depth and epicentral distance with corresponding values of traveltime, generated with the program TTGEN (Klein, 1978). This program traces rays from each specified source-depth z_s at constant increments of the function Q defined by

(4.8) $$Q = (z_s + 0.5)\, tan\frac{\phi}{2},$$

where ϕ is the take-off angle. A curve of traveltime versus distance is thus obtained for each value of depth. This curve is interpolated at specified distance intervals and the resulting values are entered on the traveltime table. The program then proceeds to a different depth, with an increment defined by the user. Two values of increment are used, both for z_s and Q, to provide a better distribution of the rays. The traveltime derivatives used in Geiger's method (equation 4.4) are estimated directly from the traveltime tables using finite differences.

Once a solution of the location problem is obtained, the errors affecting the hypocentral parameters are computed using the covariance matrix. (The details of this methodology will be discussed in section 6.2.3.) This matrix reflects the degree of stability in the solution of the system (4.7), which controls the "propagation" of errors from the data to the solution, and is scaled by the variance of the input data (equation 6.17). In practical applications, the covariance matrix is also made to depend on the RMS traveltime residual for the solution, as a means of incorporating the limitations of the velocity model into the error estimates.

The program HYPOINVERSE equates the error in origin time to the square-root of the corresponding diagonal element of the covariance matrix. In doing this, it neglects the contribution of the position errors to the error in origin time, a practice validated by Fermat's Principle and by the more pragmatic reason that accuracy in origin time is seldom required. To obtain the errors in position, the row and column of the covariance matrix associated with the origin time are removed, and the resulting sub-array is diagonallized by an appropriate rotation of the reference frame. (This is always possible since the covariance matrix is symmetric by construction.) The principal direction associated with the largest (smallest) covariance eigenvalue corresponds to the direction along which the position of the source is worst (best) constrained.

The uncertainty of the position of the epicentre varies radially, and it can be depicted by an ellipsoid, centred at the solution and with principal axes oriented

along the principal directions of the covariance matrix. The semi-axes are made equal to the covariance eigenvalues. The projection of this ellipsoid onto the horizontal plane is an ellipse, whose large semi-axis is a measure of the horizontal error in the hypocentral location. The vertical error is obtained by a similar procedure. For a well-conditioned problem and assuming that the errors in the input data are gaussian, the covariance ellipsoid is a reliable indicator of the quality of the location: enlarged by a factor of 2.4, it has a probability of 95% of containing the real hypocentre (Klein, 1978).

If both p- and s-waves can be used, the location problem becomes better conditioned (the condition number of the matrix inversion, defined below, becomes smaller). This is particularly significant if the network-event geometry is not favourable, as is the case when the epicentre is outside the network. In addition, the combined use of the two types of wave allows a straightforward estimate of the epicentral position, which can be used for a preliminary inspection.

If τ is the difference in seconds between the arrival times of the p-wave and the s-wave at a particular station, α is the (uniform) p-wave velocity in km s^{-1}, and a constant ratio of 1.8 between the p-wave and the s-wave velocities is assumed, it is straightforward to establish that the distance between the station and the epicentre is given by

$$d = [(1.25\ \alpha\ \tau)^2 - h^2]^{1/2} \qquad (km), \tag{4.9}$$

where h is the hypocentral depth in km. If this estimate is made for several stations using a trial value for h, an approximate epicentre can be obtained by plotting the stations on a map and drawing circles with radii corresponding to the different distances and centred at the stations. If the rough assumption about the velocities is valid and a reasonable guess for the depth h can be made, the intersection of these circles should define a small region containing the epicentre.

Hypocentres are located with respect to a conceptual velocity model, and any errors in that model will also lead to location errors. This effect is investigated in Figure 4.9. It is assumed that the true hypocentre is located underneath

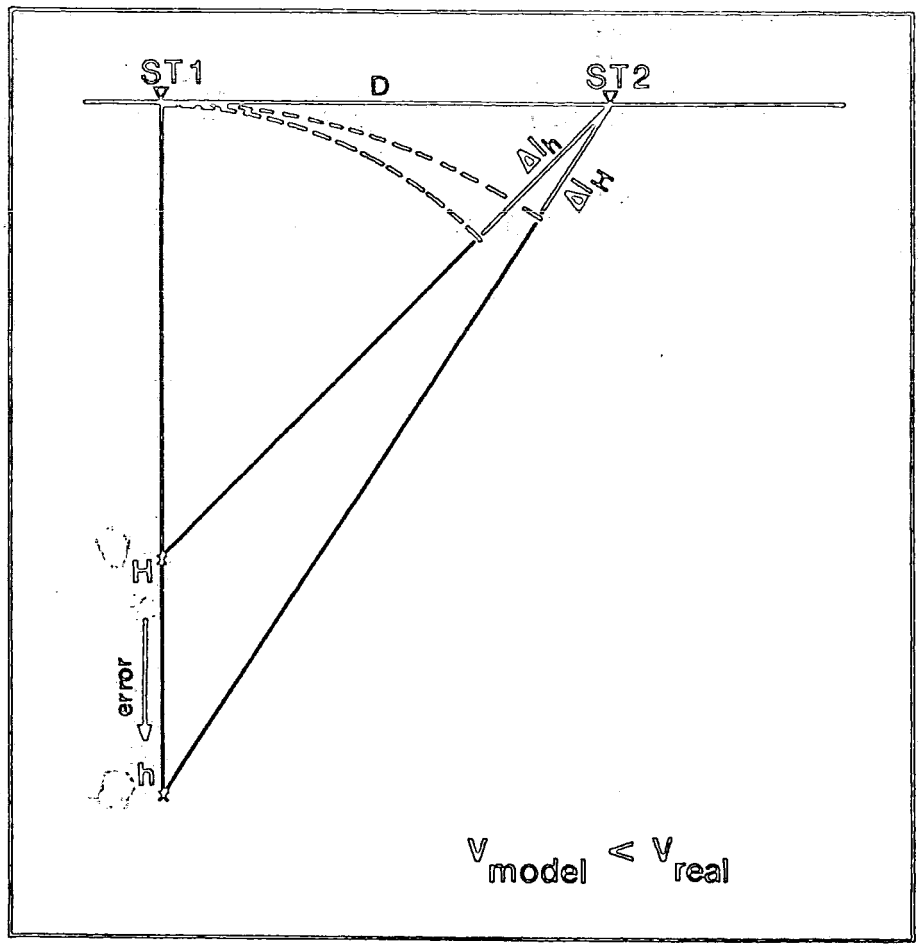

Fig. 4.9 - Effect of using a slow velocity model for the estimate of hypocentral depth, when p-wave data only are used. H is the true position of the source, h is the estimated depth.

station ST1, at a depth h. The p-wave arrivals are observed at station ST1 at some instant, and at station ST2 an interval Δt later. If s-wave arrival times are not available, the origin time is poorly constrained, since all the information consists of differences between p-wave arrival times at pairs of stations such as (ST1,ST2). If the velocity model is slow, the same (observable) Δt for a pair of stations will imply a shorter difference in the length of the two raypaths. This can be achieved by moving the source to a depth H>h. With the appropriate changes, the same reasoning applies to a fast model. If both p- and s-wave arrival times are available for at least a few stations, the estimate of origin time becomes more accurate, and its error can no longer absorb the effects of the wrong velocity model. The error for this situation is in agreement with common intuition, i.e., a slow model leads to a shallower source, and vice-versa.

In conclusion, the effect of a wrong average velocity on the estimate of focal depths seems to be as follows:

- If the model is too slow, using both p- and s-wave data results in a deficit in the depth estimate, whereas using only p-wave arrival times will lead to an overestimate in the depth.

- If the model is too fast, the depth will be over- or under-estimated, depending on whether both types of data are used or only p-wave data are used.

Before s-wave traveltimes are used for hypocentral location, the picks may be checked for incorrect identifications. To do this, the s-p traveltime differences are plotted against the p-wave arrival times. The two quantities are related (assuming constant velocities) by

$$t_s - t_p = (\rho - 1)t_p - (\rho - 1)t_o, \tag{4.10}$$

where ρ is the ratio between the p and s velocities and t_o is the origin time. The ratio ρ, which depends exclusively on the Poisson ratio, usually takes values in the range 1.75 to 1.80. Accordingly, the slope of a straight line fitting the

points in the plot should be in the range 0.75 to 0.80. Picks that deviate significantly from this line probably correspond to misidentified phases, and should be neglected.

The most common pitfalls of earthquake location could not be avoided even with error-free data and a perfect velocity model. They result from the invalidity of the approximations inherent to Geiger's method, occurring in situations of strong non-linearity, or from numerical instability associated with the quasi-singularity of the matrix A in (4.7), or from both. In the case of an unstable system of linear equations, the solution is highly sensitive to errors in the values of the matrix coefficients, and the finite-difference estimate of traveltime derivatives from the traveltime table may not be accurate enough to prevent disparate results. This aspect can be quantified with the introduction of the "condition number", characteristic of the matrix of a system of linear equations.

If $\mathbf{x}_1$ is the solution of the linear system of equations $A\mathbf{x} = \mathbf{t}$, with A non-singular, and $\mathbf{x}' = \mathbf{x}_1 + \delta\mathbf{x}$ is the solution of $(A + \delta A)\mathbf{x} = \mathbf{t}$, it can be shown (e.g., Ortega, 1972) that to a first order of approximation

$$\frac{\|\delta\mathbf{x}\|^2}{\|\mathbf{x}\|^2} \leq k_2(A)\frac{\|\delta A\|^2}{\|A\|^2}, \tag{4.11}$$

with

$$k_2(A) = \|A\|^2\|A^{-1}\|^2, \tag{4.12}$$

where $\|\cdot\|$ indicates the L2 norm (e.g., Ralston and Rabinowitz, 1978). The number k_2(A) is called the "spectral condition number" of A, and for a symmetric matrix it is given by

$$k_2 = \frac{|\lambda_i|_{max}}{|\lambda_i|_{min}} \tag{4.13}$$

where the λ_i are the eigenvalues of A (Ortega, 1972). Equation (4.11) shows that if the matrix A has a very large condition number, a small fluctuation in the value of its coefficients may imply a large relative variation of the solution. For this reason, matrices (or linear problems) with large condition numbers are said to be "ill-conditioned".

In the case of hypocentral locations, the condition number depends critically on the geometry of the network, and on the position of the iteration point with respect to the set of stations. Unfavourable geometries are those that cause two or more columns of A to become nearly proportional in the region containing the source. This situation tends to occur when the epicentre is outside the network and far from its periphery. This is the reason why the use of s-waves is crucial in this situation, since the corresponding traveltime derivatives are different from those of the p-waves. Figure 4.10 (after Buland, 1976), depicts the spatial distribution of the condition number for a network of four stations (p-waves only), showing that variations of up to four orders of magnitude may take place within distances from the periphery of the network that are comparable to its diameter. Based on experience, Klein (1978) considers a condition number of $\sim$200 to be the upper limit for stable hypocentral location.

When the traveltime dependence on distance is strongly non-linear, as can be expected when the iteration point crosses a sharp horizontal velocity variation, convergence of the iteration scheme can still be achieved provided that the matrix A is well-conditioned, especially if damping of the adjustment length is introduced. When strong non-linearity occurs in association with an ill-conditioned matrix the iteration is most likely to diverge.

The solution of an ill-conditioned system of equations may be very far from the true solution and still produce very small residuals (e.g., Ortega, 1972, Example 2.2.3). For this reason, the RMS traveltime residual for a particular hypocentral location cannot always be used as a guide to the quality of the location. It was already pointed out that this is best done by considering instead the covariance matrix. This matrix is sensitive to the size of the eigenvalues of the matrix being inverted, and thus to the condition of the problem.

4.3.2 Velocity modelling and HYPOINVERSE performance tests.

Information on the velocity structure of the crust was obtained from the published refraction surveys of Moreira et al. (1980) and Mendes-Victor et al. (1980), and from Caetano (1984). These studies apply to different regions underneath or around the area of the network (Figure 2.4): the profiles of Moreira et al. (1980) run on a NNE-SSW direction along its western border; the section of Mendes-Victor et al. (1980) crosses the area centrally in a NW-SE direction; and the Ferreira-Évora profile of Caetano (1984) characterizes the sediment-free area to the SW. Figure 4.11 shows the differences between the proposed models, due in part to subjective interpretation but mainly to the geological contrasts of the region.

The velocity model used to generate the traveltime table is defined by assigning velocity values to specified depths and assuming constant vertical gradients of velocity in between, without discontinuities. The selected model is shown in Figure 4.11, and corresponds to a compromise between the different results of the published refraction surveys.

Figure 4.12 shows the theoretical traveltime curve predicted by the adopted velocity model for a source at the surface, and a sample of first-arrival picks from some of the published refraction profiles pertaining to the area of the network. The agreement between the prediction and the observations should not be expected to be good, since the majority of the picks in the figure correspond to head-waves, which cannot be predicted by the velocity model due to the absence of velocity discontinuities. This is not a hindrance when the source is at a depth that is not small compared to the epicentral distances of the stations, because in this case the rays travel upwards from the source and the first arrival is a direct wave. The interest of Figure 4.12 is that it allows an estimate of the lateral variations in the delays due to shallow low-velocity structures, responsible for most of the scatter between the different profiles. These should also be expected to cause important contributions to the location errors, since with program TTGEN the choice is restricted to velocity models with horizontally homogeneous layers. This will be further discussed in the next section.

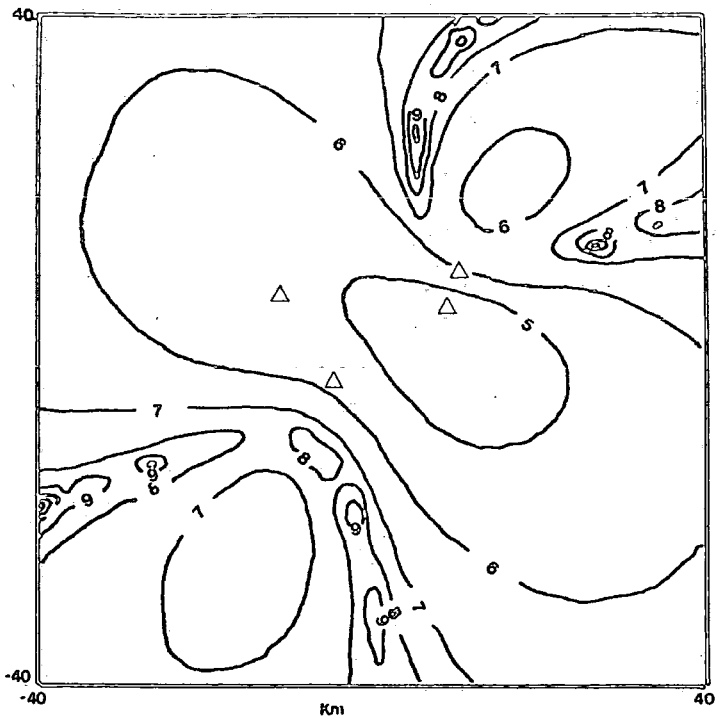

Fig. 4.10 - Spatial variation of the base 10 logarithm of the condition number for Geiger's method of earthquake location, for a network of four seismic stations. Redrawn after Buland (1976).

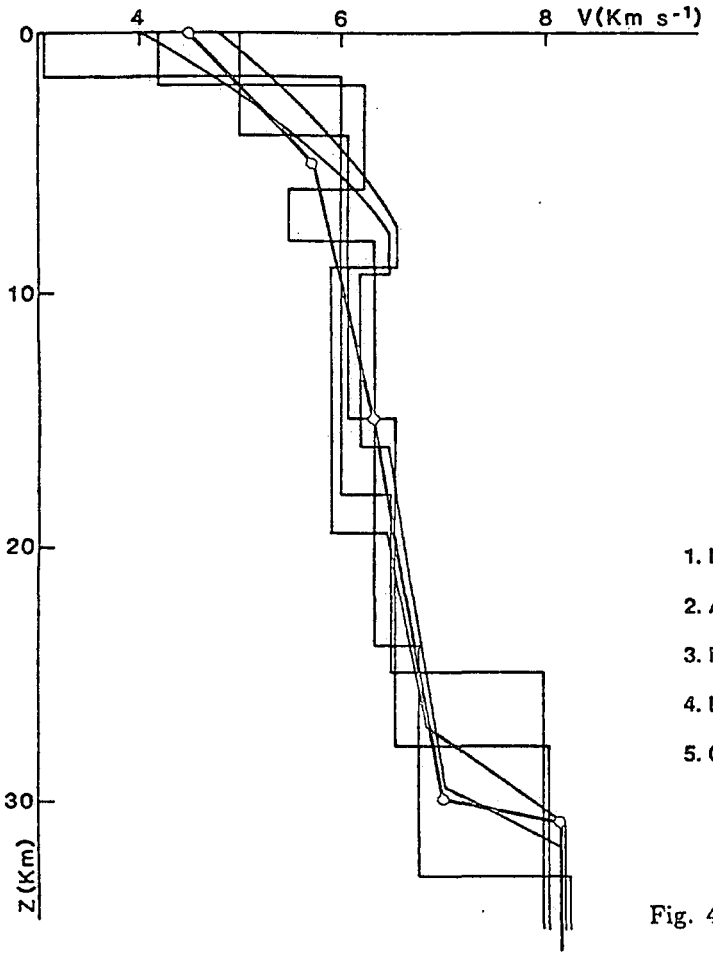

adopted velocity model :	
Z(Km)	V(Km s^{-1})
0.0	4.5
5.0	5.7
15.0	6.3
30.0	7.0
31.0	8.2
constant gradients in between	

1. Lower Tagus Basin (Mendes-Victor et al, 1980)
2. Aljustrel-Évora (Caetano, 1984)
3. Nazaré-Cabo Raso (Moreira et al, 1980)
4. Lusitanian Basin (Mendes-Victor et al, 1980)
5. Cabo Raso-Figueira da Foz (Moreira et al, 1980)

Fig. 4.11 - Comparison between the several velocity models proposed for the area of the RESTE Network and surroundings, and the velocity profile used in the location of the RESTE local events (thicker line). Velocity models after Mendes-Victor et al. (1980), Moreira et al. (1980) and Caetano (1984).

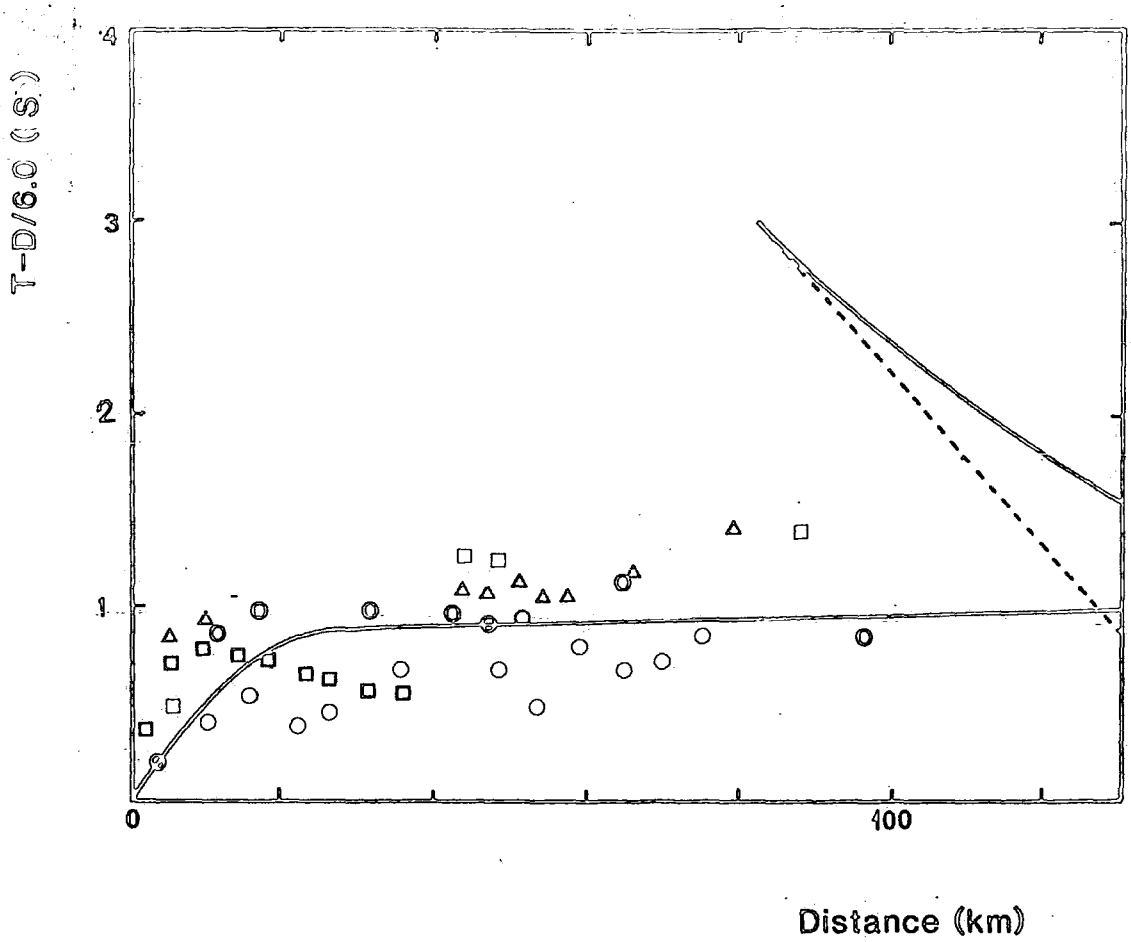

Fig. 4.12 - Comparison between the traveltime curve predicted for the adopted velocity model and for a source at the surface with a sample of first-arrival picks from some of the published refraction profiles. Refraction data after Mendes-Victor et al. (1980) and Moreira et al. (1980).

```
 18 NOV 87  9:43  EVENT NO.  1          RUN ..  5/19/88  AT 01:11:12

                                                          ADJUSTMENTS (KM)
 I ORIGIN    LAT N     LON W      Z   NWR  RMS    DT      DLAT     DLON      DZ      RR NF
 1  36.71  0 06.62  38 53.26   5.00  10 0.00 -4.789 0.000000000000000  0.000 0.000000  2
 2  31.92 38 38.56   9  7.29   5.00 107 0.06 -0.460 294.101 418.844    0.000 0.000000  3
RMS INCREASE - MOVE HYPO 0.60 BACK
 3  31.06 38 17.26  13 55.24   5.00 109 1.05  0.276 0.000000000000000  0.000 0.000000  3
 4  31.70 36 42.00  11  6.10   5.00 105 9.11 -0.295 291.914   3.623    0.000 0.000000  3
 5  31.00 39 19.96  11  8.63   5.00 103 9.88 -0.045 -99.495 0.000000   0.000 0.000000  3
 6  31.00 38 25.87   9 54.64   5.00 101 0.00  0.015 41.316 -21.682    0.000 0.660000  3
 7  31.01 38 08.17   9 39.63   5.00  10 2.20 -0.017 -5.110  -8.718    0.000 10.106 3
 8  31.00 38 06.41   9 33.60   5.00  10 0.30 -0.250 -0.368   0.409    0.000  0.550 3
FOCAL DEPTH FREED
 9  31.15 38 05.21   9 33.88   5.00  10 0.23 -0.103 -0.990  -1.103   -3.915  4.188 4
RMS INCREASE - MOVE HYPO 0.60 BACK
10  31.04 38 44.67   9 33.12   1.08   9 0.26  0.042  0.599   0.662    2.349  2.513 4
AIRQUAKE PREVENTED
11  31.10 38 45.00   9 33.57   3.43   9 0.22 -0.041 -0.171  -0.918   -1.717  1.954 4
AIRQUAKE PREVENTED
12  31.06 38 44.90   9 32.94   1.72   9 0.22 -0.025 -0.092  -1.391   -0.858  1.638 4
RMS INCREASE - MOVE HYPO 0.60 BACK
13  31.04 38 44.86   9 31.98   0.86  10 0.31  0.015  0.055   0.835    0.515  0.983 4
RMS INCREASE - MOVE HYPO 0.60 BACK
14  31.05 38 44.88   9 32.55   1.37   9 0.26  0.006  0.022   0.334    0.206  0.393 4
AIRQUAKE PREVENTED
15  31.06 38 44.90   9 32.79   1.58   9 0.23 -0.005 -0.059  -0.884   -0.790  1.187 4
RMS INCREASE - MOVE HYPO 0.60 BACK
16  31.05 38 44.86   9 32.17   0.79   9 0.26  0.003  0.036   0.530    0.474  0.712 4
RMS INCREASE - MOVE HYPO 0.60 BACK
17  31.06 38 44.88   9 32.54   1.26   9 0.24  0.001  0.014   0.212    0.190  0.285 4
AIRQUAKE PREVENTED
18  31.06 38 44.89   9 32.69   1.45   9 0.23 -0.001 -0.077  -0.892   -0.727  1.153 4
RMS INCREASE - MOVE HYPO 0.60 BACK
19  31.06 38 44.85   9 32.07   0.73   9 0.27  0.001  0.046   0.535    0.436  0.692 4
RMS INCREASE - MOVE HYPO 0.60 BACK
20  31.06 38 44.88   9 32.44   1.16   9 0.25  0.000  0.019   0.214    0.174  0.277 4
RMS INCREASE - MOVE HYPO 0.60 BACK
21  31.06 38 44.89   9 32.59   1.34   9 0.24  0.000  0.007   0.086    0.070  0.111 4
AIRQUAKE PREVENTED
22  31.06 38 44.89   9 32.65   1.41   9 0.24  0.000 -0.078  -1.129   -0.703  1.333 4

          EIGENVALUES
    (  3.464   0.246   0.203   0.020)
     EIGENVECTORS OF ADJUSTMENT          COVARIANCE                          ERRORS  #ERROR ELLIPSE
                                                                                  #   SERR AZ DIP
OT  ( -0.967   0.255  -0.022   0.003)(  0.079   0.060   0.050   0.544)   0.282  #  12.68 274 54
LAT (  0.045   0.254   0.965   0.048)(  0.060   1.952   4.526   6.205)   1.397  #   1.27 170 10
LON ( -0.206  -0.771   0.184   0.574)(  0.050   4.526  53.683  74.939)   7.327  #   1.02  73 33
Z   (  0.145   0.525  -0.186   0.817)(  0.544   6.205  74.939 107.812)  10.383  #

-------------------------------------------------------------------------------
YR MO DA    ORIGIN     LAT N     LON W    DEPTH  RMS   ERH    ERZ  GAP XMAG FMAG STAND
87-11-18   943 31.06 38 44.89   9 32.65   1.41  0.24  7.30  10.37  324                0.096

RMSWT DMIN ITR NFM NWR NWS REMK
 0.30 41.1  22   0   9   4

 STA DIST AZM  AN P/S W    SEC+CCOR (TOBS -TCAL -DLY  =RES) WT  XMG FMG R INFO
 AVL 41.1  66  57 P      38.71 0.00  7.65  7.87 0.00 -0.22 1.15          0.340
                  S      45.14 0.00 14.08 14.01 0.00  0.07 1.15          0.595

 ACA 64.8  82  55 P      43.30 0.00 12.24 11.98 0.00  0.26 1.15          0.313
                  S      51.76 0.00 20.70 21.32 0.00 -0.62 0.78          0.266
 ABV 65.6  66  55 P      43.47 0.00 12.41 12.10 0.00  0.31 1.15          0.283
                  S      52.71 0.00 21.65 21.54 0.00  0.11 1.15          0.680
 AMG 81.5  71  53 P      45.63 0.00 14.57 14.76 0.00 -0.19 1.15          0.380
                  S      56.46 0.00 25.40 26.27 0.00 -0.87 0.01          0.000
 AMT 83.8 102  63 P      46.13 0.00 15.07 15.15 0.00 -0.08 1.15          0.368
                  S      58.20 0.00 27.14 26.97 0.00  0.17 1.15          0.771
```

Fig. 4.13 - Hypoinverse report for the location of an explosion.

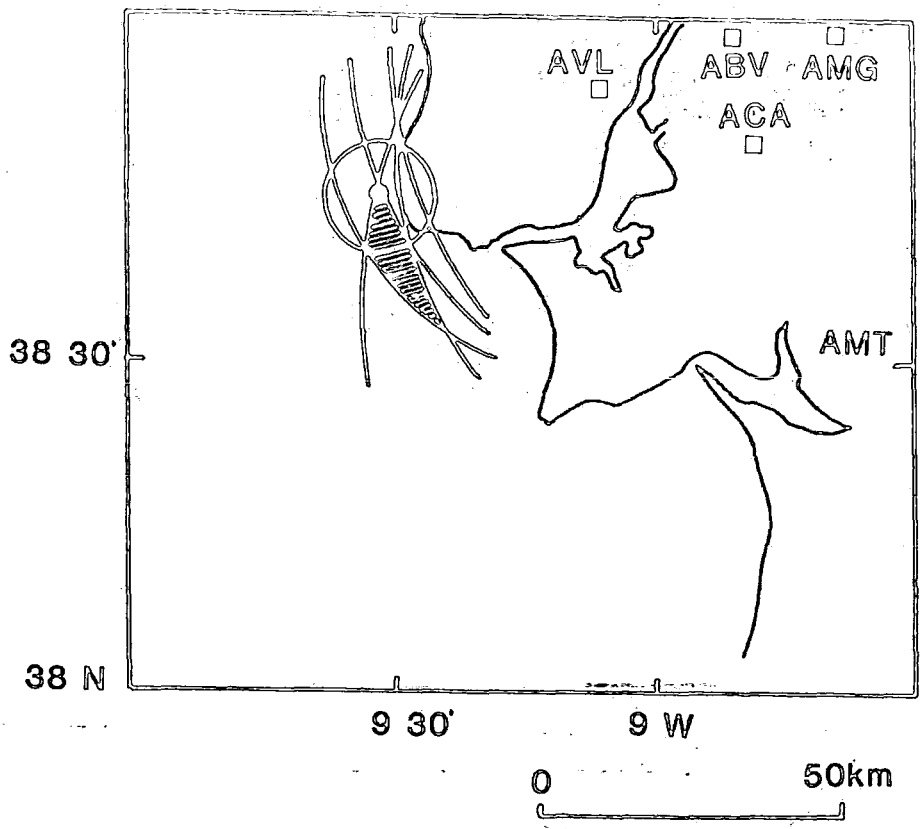

Fig. 4.14 - Location of an artificial explosion. The arcs were drawn using s-p traveltime differences. The circle is centred at the HYPOINVERSE epicentre, and its radius corresponds to the horizontal error. The dot corresponds to the true location of the explosion. The positions of the recording stations are shown by squares.

When a station is operated over a long period of time and used for the location of a large number of earthquakes, the statistical analysis of its traveltime residuals can provide a correction term, characteristic of the station. This quantity may then be added to the observed traveltimes to compensate for the effect of the shallow low-velocity layers underneath the station. Retrospective analysis of the HYPOINVERSE traveltime residuals for the different stations of the RESTE Network shows in fact that some stations have traveltime residuals that do not average to zero. The most significant cases are the stations ACA, with a mean traveltime residual of 0.26±0.11 s, and ASN, with -0.10 ±0.12 s. Since the residuals are the observed minus the predicted traveltimes, it can be inferred that ACA is situated on top of layers with lower velocities than modelled, and vice-versa for ASN. This is in very good agreement with the geology, since ACA is implaced on poorly consolidated river-terrace deposits of the southern margin of the Tagus River, whereas ASN is on top of a granitic outcrop (Sintra Granite). However, the number of events located with the stations was not adequate for an accurate statistical analysis, and the standard deviations of the residuals are large when compared with the mean value. For this reason, station corrections were not introduced, allowing therefore the error estimates for the location parameters to reflect more realistically the inaccuracy of the modeling.

Figures 4.13 and 4.14 correspond to the location of a shallow explosion to the W of the network, on November 18, 1987. This explosion was independent of the RESTE experiment, and was part of major offshore sewage works. No accurate origin time was available, but the location of the explosion was known with an error margin of about 500 m. Clear p-wave arrivals were recorded at five RESTE stations, and s-wave arrival times of variable reliability were also measured and used in the location. In Figure 4.14, the shaded circle is centred on the HYPOINVERSE epicentre, and its radius corresponds to the horizontal location error of 7.3 km. The depth was estimated as 1.4±10.4 km, and the real value was near zero. Within the margin of uncertainty associated with the true location of the source, the centre of the epicentral circle coincides with the location of the explosion. The condition number for this location was 173.2. The geometric method based on equation (4.9) was also used to locate this event, with h = 0 and a constant p-wave velocity of 5.5 km s^{-1}. The epicentral region

thus obtained is depicted in Figure 4.14, and one of its corners coincides roughly with the true position of the source.

Figures 4.15 and 4.16 correspond to another test of the location program, using a shallow quarry blast to the N of the network, at a point known within a margin of about 500 m. The HYPOINVERSE solution, based on five p-wave arrivals and four s-wave arrivals, had a depth of 1.2±2.8 km and a condition number of 46.1. The estimated horizontal error was 2.0 km, but the distance between the computed epicentre and the quarry was about 4 km. Using equation (4.9) with h = 0 and a velocity of 5.5 km s^{-1}, a small region was delimited which fell some 5 km away from the quarry.

The microearthquake EL06 (October 25/26, 1987), already mentioned in section 2.1, was used to test the performance of the location program for an event outside the network and towards the SE of it (in this case the real position is not known). The four useful traces in Figure 4.5 display very clear waveforms, and using larger playouts it was possible to obtain relative p- and s-wave arrival times for all of them. The location of the hypocentre was attempted in two stages: first, with the method based on the differences between s- and p-wave arrival times; then, with HYPOINVERSE.

Table 4.3 gives the p-wave arrival times (arbitrary clock), the measured differences between p- and s-wave arrivals, and the epicentral distances computed with (4.36) for a source depth of 15 km (this is close to the average of the best located hypocentres, as described later in this section) and a standard p-wave velocity of 6 km s^{-1}.

The origin time was estimated by dividing the distances by the standard velocity and subtracting from the p-wave arrival times. This is shown under $t_p - d/6$. Since the result for ASZ deviates significantly from the others it was considered anomalous, and the average of the other three values was taken as a trial origin time. This value was in turn subtracted from p-wave arrival times to give p-wave traveltimes, shown under $t_p - t_0$, and finally the distances were computed again using the standard p-wave velocity to test the internal consistency of the results. The last column on the right shows the differences between the

```
12 NOV 87  0: 0  EVENT NO.   1          RUN ..  5/17/88  AT 22:12:48

                                                                ADJUSTMENTS (KM)
 I ORIGIN    LAT N     LON W      Z   NWR  RMS    DT     DLAT    DLON     DZ     RR NF
 1    7.02 39 10.23    9  1.65 13.50   9 0.43 0.732 -2.407 -1.561  0.000 2.869 3
FOCAL DEPTH FREED
 2    7.75 39  8.93    9  0.56 13.50   9 0.35 0.113 -0.865 -0.072  1.625 1.843 4
 3    7.87 39  8.46    9  0.51 15.13   9 0.33 0.054 -0.706 -0.305  1.197 1.423 4
 4    7.92 39  8.08    9  0.30 16.32   9 0.26 0.192 -2.383 -1.174  3.678 4.537 4
 5    8.11 39  6.80    8 59.48 20.00   8 0.21-0.001 -0.314 -0.158 -0.188 0.399 4
 6    8.11 39  6.63    8 59.37 19.81   8 0.18 0.007 -0.032 -0.031 -0.064 0.078 4
 7    8.12 39  6.61    8 59.35 19.75   8 0.19-0.005 -0.024  0.043  0.055 0.073 4
 8    8.11 39  6.60    8 59.38 19.80   8 0.19 0.002 -0.064 -0.023  0.042 0.081 4
 9    8.11 39  6.56    8 59.37 19.85   8 0.19-0.001  0.156 -0.015 -0.166 0.228 4

        EIGENVALUES
   (  2.876   0.290   0.164   0.092)                                          #ERROR ELLIPSE
     EIGENVECTORS OF ADJUSTMENT          COVARIANCE                  ERRORS #  SERR AZ DIP
OT ( -0.983   0.029 -0.175   0.036)(  0.064 -0.322 -0.116 -0.049)   0.253 #  2.31 169 48
LAT( -0.138   0.287   0.682 -0.659)( -0.322  3.129  0.597 -1.830)   1.769 #  1.27 340 41
LON( -0.079  -0.953   0.263 -0.126)( -0.116  0.597  0.685 -0.254)   0.828 #  0.73  73  5
Z  ( -0.088   0.091   0.659  0.741)( -0.049 -1.830 -0.254  3.653)   1.911 #

YR MO DA   ORIGIN     LAT N     LON W    DEPTH  RMS   ERH   ERZ GAP XMAG FMAG STAND
87-11-12   0 0  8.11 39  6.56    8 59.37 19.85 0.19  1.54  1.71 272             0.531

RMSWT DMIN ITR NFM NWR NWS REMK
 0.19 18.6   9   0   8   4

 STA DIST AZM  AN P/S W   SEC+CCOR (TOBS -TCAL -DLY  =RES) WT  XMG FMG R INFO
 ABV 18.6 139 131 S      16.52 0.00  8.41  8.29 0.00  0.11 1.00          0.700
 AVL 26.1 204 119 P      13.76 0.00  5.65  5.58 0.00  0.07 1.00          0.460
                  S      17.85 0.00  9.74  9.93 0.00 -0.20 1.00          0.627
 AMG 32.4 116 112 P      14.74 0.00  6.63  6.46 0.00  0.17 1.00          0.378
                  S      19.37 0.00 11.26 11.50 0.00 -0.24 1.00          0.423
 ACA 35.7 153 109 P      15.28 0.00  7.17  6.93 0.00  0.24 1.00          0.223
                  S      20.60 0.00 12.49 12.34 0.00  0.15 1.00          0.796
 AST 50.4 127  81 P      16.99 0.00  8.88  9.12 0.00 -0.24 1.00          0.390
                  S      25.59 0.00 17.48 16.23 0.00  1.24 0.00          0.000
 AMT 67.4 150  89 P   4  17.21 0.00  9.10 11.72 0.00 -2.62 0.00          0.000
                  S   4  25.61 0.00 17.50 20.86 0.00 -3.37 0.00          0.000
 ASZ 72.8 187  89 P   4  17.54 0.00  9.43 12.56 0.00 -3.13 0.00          0.000
                  S   4  23.24 0.00 15.13 22.36 0.00 -7.23 0.00          0.000
```

Fig. 4.15 - HYPOINVERSE report for the location of a quarry blast.

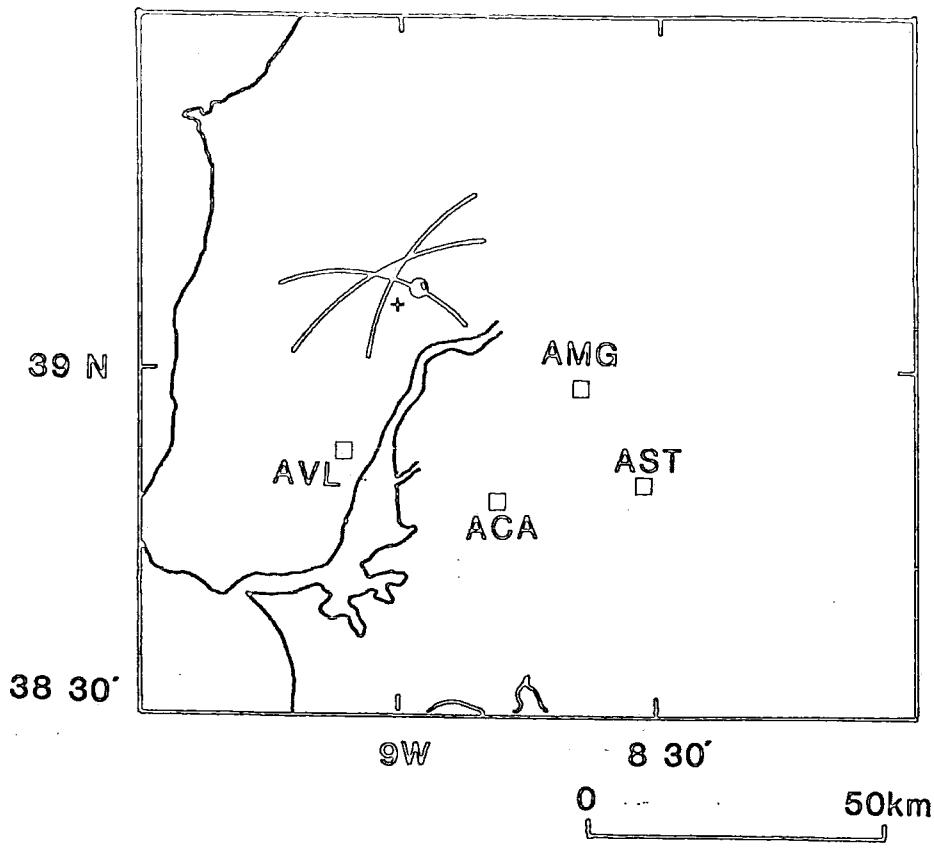

Fig. 4.16 - Location of a quarry blast. The cross shows the true location of the blast. See caption of Figure 4.14 for more details.

two estimates of epicentral distances, which are acceptable in view of the coarse nature of the method.

Station	t_p (s)	$t_s - t_p$ (s)	d (km)	$t_p - d/6$ (s)	$t_p - t_o$ (s)	d' (km)	$d - d'$ (km)
AST	06.87	06.08	43	-0.30	07.15	40.2	+2.8
ACA	10.37	08.88	65	-0.46	10.65	62.1	+2.9
AVL	15.41	12.56	93	-0.09	15.69	92.9	+0.1
ASZ	13.38	10.49	77	+0.55	13.66	80.6	-3.6

Table 4.3

Figure 4.17 shows the locations of the stations that recorded the event, and the arcs on the right were drawn according to the method described above. The source was located to the SE of the group of stations, near the point with coordinates (38° 33' N; 8° 11' W). The distance to the baricentre of the group of stations is comparable to its linear dimensions. The large uncertainty of the order of 10 km in the NNE-SSW direction results from the alignment of three of the four stations, which subtend a narrow angle with respect to the epicentre. Along the WNW-ESE direction the constraint is stronger, and the uncertainty is of the order of 3 km.

Different attempts were made to locate event EL06 with HYPOINVERSE, to check the sensitivity of the solution with respect to the different parameters. The different results are given in Table 4.4.

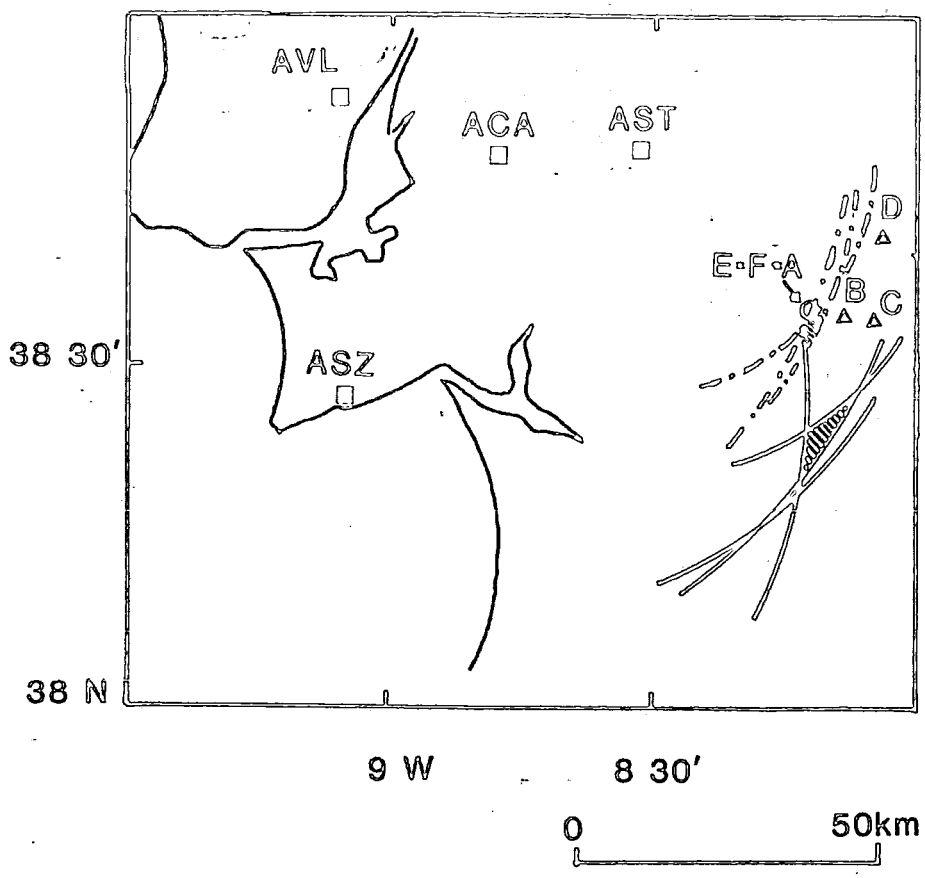

Fig. 4.17 - Test of the location program for an event outside the network (EL06). Squares indicate the positions of the recording stations. The letters correspond to those on the first column of Table 4.4. The arcs were drawn using s-p traveltime differences (equation 4.9).

Table 4.4

-	k	z (km)	ΔH (km)	Δz (km)	Δ (km)
A	130.0	4.5	9.5	21.0	$\sim$0
B	199.9	3.6	13.1	20.4	$\sim$5
C	540.5	3.5	19.2	31.8	$\sim$12
D	255.8	3.8	14.2	12.3	$\sim$20
E	1143.0	4.5	28.4	67.6	$\sim$0
F	110.8	6.1	5.4	15.4	-

A - Trial hypocentre underneath AST, at 5 km of depth; p and s weights 1.0. B - Trial depth 5 km; p weight 1.0; s weight 0.5. C - Trial depth 5 km; p weight 1.0; s weight 0.0. D - ASZ ignored; other weights as in A. E - AVL ignored; other weights as in A. F - As in B, with a trial depth of 15 km.

k is the condition number, z is the depth estimate, ΔH and Δz are the horizontal and vertical errors and Δ is the epicentral distance to the location F.

The location F had the lowest condition number and the smallest horizontal error, and is taken as the best possible location with the available data. The location of the epicentre of event EL06 could still be achieved with reasonable accuracy (error margin of the order of 5 km) despite the fact that the earthquake was outside the network. The use of s-wave arrival times was crucial for this purpose, although the reduction of the corresponding weights from 1.0 to 0.5 seems to have improved the solution. The source depth, as should be expected, could not be retrieved from the observations with any degree of accuracy. A

very steady convergence to a particular result does not necessarily mean a more accurate solution (the final solution had in fact a troublesome iteration progress, and yet reached the lowest variance).

The HYPOINVERSE location of event EL06 lies about 20 km away from the centre of the region defined by the method based on equation (4.9) (Figure 4.17); it is however very close to the arc corresponding to station ASZ. This suggests that the assumption of a constant velocity of 6 km s^{-1} is valid between the source and station ASZ, but not towards the other stations. With this possibility in mind, the three last columns of Table 4.3 were re-computed, this time with the origin time estimated with station ASZ. The results are given in Table 4.5, showing that the assumed velocity of 6 km s^{-1} leads to totally consistent results for station ASZ. For the remaining stations, an agreement with the adopted HYPOINVERSE solution can still be achieved if the constant velocity is made equal to 5.5 km. This is shown by the dashed arcs in Figure 4.17, and suggests that strong horizontal heterogeneities of the seismic velocities are likely to occur in the region, with a bearing on the quality of the locations. This possibility will be supported by the investigation of the broad velocity structure of the crust beneath the network, discussed in chapter 6.

Station	$d\ (km)$	$t_p - t_0\ (s)$	$d'\ (km)$
AST	43	05.53	37.9
ACA	65	08.33	58.9
AVL	93	12.01	89.2
ASZ	77	09.94	77.0

Table 4.5

4.3.3 Application to the RESTE data.

A total of twelve RESTE local earthquakes were located with HYPOINVERSE. Of these, seven occurred within the network and the remaining had minimum epicentral distances in the range 18 km to 61 km.

Whereas for the events outside the network it was generally possible to pick s-wave arrival times, for those inside the network only a few, if any, s phases were identifiable. Figure 4.18 shows a plot of s-p traveltime differences as a function of p-wave arrival time for those events with available s-wave data. It was shown above that the points for each event should plot along a straight line with slope 0.75 to 0.80. This is generally the case for the RESTE earthquakes. The curve for event ER02 shows clearly that beyond some distance a different phase was picked as being the s-wave, and those arrival times were ignored. Those readings that deviate significantly from the fitted lines were also abandoned.

The following iteration parameters (section 4.1.2) were used in the locations: step damping, 0.9; damping for iterations with RMS residual increase, 0.60; minimum iteration length, 0.04 km; minimum RMS traveltime residual improvement, 0.001 s; maximum number of iterations, 20. The several locations will now be discussed separately. The location of event EL06 was already discussed above. The results are summarized in Table 4.6, and plotted in Figure 4.36.

Figure 4.19 shows the iteration procedure for the location of the first local event (EL01) detected with the RESTE Network on July 23, 1987. The condition number is 30.1, and the horizontal and vertical errors are 0.6 km and 1.6 km respectively.

The HYPOINVERSE report for event ER02 (initially classified as regional, hence the code) is given in Figure 4.20. This event is outside the network, and its epicentre is 61.5 km distant from the closest station. Despite the adverse configuration the condition number was 21.4, and the RMS residual was 0.09 s. The large residual for the p-wave arrival time at station ASZ suggests that the onset of the signal was missed in the noise. Station AMJ was clearly mixed up with some other station, probably due to the swap of a pair of plugs in the multichannel recorder input. The result for the source depth is meaningless.

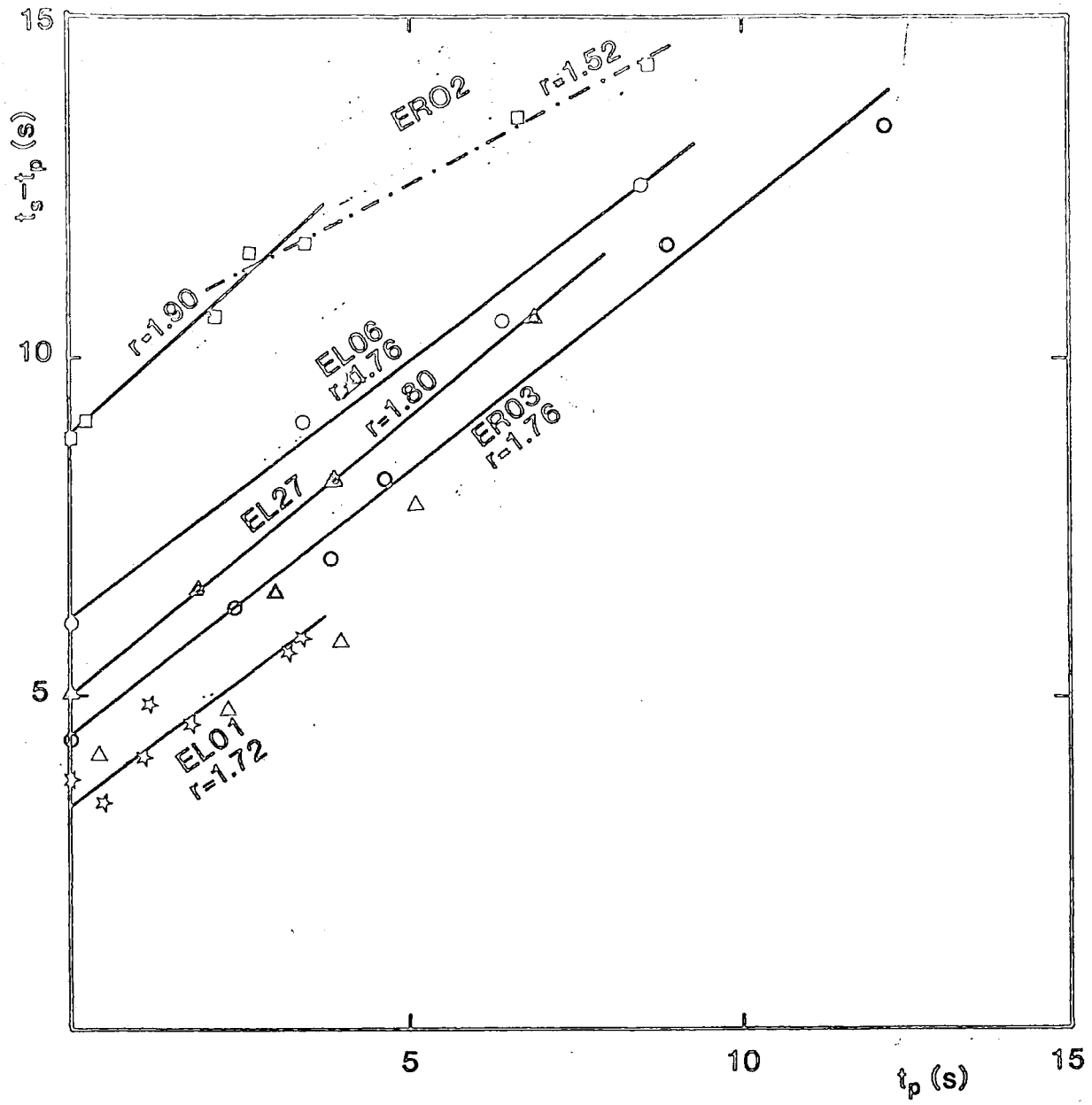

Fig. 4.18 - Plot of s-p traveltime differences as a function of p arrival time. For correctly picked s first arrivals, the points should plot along a straight line of slope 0.75 to 0.80 (r = 1.75 to 1.80).

Table 4.6 - Simplified HYPOINVERSE output for the RESTE events.

CODE	DATE	TIME	LAT	LON	Z(km)	ΔH (km)	ΔZ (km)	M_L	M_D^*	Obs.
EL01	23JUL87	12 58 12.74	38 43.84	9 02.54	20.0	0.6	1.6	2.3	-	-
ER02	28JUL87	20 24 18.65	39 30.24	9 05.06	-	0.6	-	-	3.1	-
ER03	29JUL87	13 07 35.87	38 47.90	8 12.11	-	1.2	-	2.4	-	outside
EL05	14OCT87	21 56 28.05	38 39.74	9 09.55	15.1	0.5	1.1	1.6	-	-
EL06	26OCT87	-	38 32.20	8 12.22	-	5.0	14.7	-	2.2	poor locat.
EL22	21JAN88	04 04 10.06	38 57.58	8 44.64	8.1	0.5	1.6	-	1.4	-
EL23	22JAN88	21 00 40.85	39 04.22	9 02.23	19.7	5.3	8.6	1.1	-	poor locat.
EL24	26JAN88	15 33 09.66	38 56.06	8 43.98	9.3	1.3	3.7	1.5	-	-
EL25	30APR88	07 47 12.78	38 51.26	9 08.43	12.8	0.6	0.9	1.3	-	-
EL26	06MAY88	02 45 00.33	38 43.45	9 36.06	-	1.4	-	-	2.9	outside
EL27	18MAY88	17 03 42.75	38 54.99	9 30.93	-	1.2	-	>3	-	outside
EL28	22MAY88	15 00 00.30	38 58.11	9 11.76	16.4	0.9	1.4	-	3.8	felt

* - Estimated by INMG, Lisbon.

Figure 4.21 concerns event ER03, also located outside the network and 28.2 km distant from the nearest station. The condition number was 33.7. Although the convergence towards an epicentral position was fast, the iterations became unstable when trying to select a value for the depth. The RMS residual was 0.17 s, and the error estimates were 1.2 km (horizontal) and 1.6 km (vertical). The vertical error is too small to be realistic, since this network-event configuration does not allow a reliable estimate of the depth.

The event EL05 (Figure 4.22) was located within the network, and the condition number was 45.9. It was located at a depth of 15.1±1.1 km, with a RMS residual of 0.02 s. The large p-wave traveltime residual (-0.42 s) for station AMJ (the closest station to the epicentre at only 11.1 km) suggests that the source might be slightly shallower than the estimated interval, close to 12.5 km (12.5 = 15.1 - 0.42x6.0).

Figure 4.23 corresponds to event EL22, located within the network, with condition number 35.6. Only five p-wave arrival times were used, and the RMS residual was 0.04 s. The depth was estimated at 8.1± 1.6 km, and the horizontal error was 0.5 km.

The location of event EL23 (Figure 4.24) was based on four p-wave arrival times, the minimum number of observations that still allows a location. The condition number was 201.6, on the limit of numerical instability, and the RMS residual was 0.02 s (it would have been zero if the problem were linear). The depth was estimated as 19.7± 8.6 km, and the horizontal error was 5.3 km. Naturally, this location has very poor quality.

Figure 4.25 corresponds to event EL24, located within the network at a depth of 9.3± 3.7 km. This case is interesting in that it had a large RMS residual (0.37 s), despite the fact that the network-event configuration was strong and the readings of the arrival times were clear and accurate. The condition number was 26.4, therefore the discrepancies between observations and predictions cannot be attributed to numerical instability. Because all other conditions were favourable, the limited success of this location seems to indicate that the linear approximations of Geiger's method were not valid. In the next section, a major basement fracture will be proposed that passes very close to the location of this event. The

associated horizontal heterogeneity is a possible explanation for the breakdown of the validity of the linear approximations.

The location of event EL25 is reported in Figure 4.26. It had a condition number of 20.2 and an RMS residual of 0.09 s. It is in a central position with respect to the stations, and the estimated depth is 12.8± 0.9 km. The horizontal error is 0.6 km. Station AMT was defective at the time, and the time read from the seismogram corresponded to an outburst of noise, hence the large residual.

Events EL26 and EL27 were both located outside the network, with minimum distances of 48.7 km and 18.1 km respectively. The corresponding iteration reports are given in Figures 4.27 and 4.28. The horizontal errors are probably underestimated, especially for event EL26, which shows very large p-wave residuals (-0.96 s and -0.76 s) for the two closest stations, although the remaining 11 phases had an RMS residual of only 0.07 s. The depths of the sources would not be recoverable from the data, and the given values are devoid of meaning.

Finally, Figure 4.29 gives the HYPOINVERSE output for event EL28, which was considerably larger than all the other earthquakes (section 4.3.6). This event was recorded by the stations MTH and MOE of the Portuguese National Network, and by nine RESTE stations (the number of operating stations had decayed by then, with the approach of the closing date for the experiment). Stations MTH and MOE had clear p and s arrivals, whereas the RESTE stations saturated and gave p arrivals only. However, the use of the permanent stations in the location resulted in very large residuals for the corresponding arrival times, with a mean value of 3.15 s. This value corresponds probably to the offset between the MSF time code used for the RESTE stations and the clock used for the permanent stations. At a second attempt (Figure 4.29) that average was subtracted from the arrival times for MTH and MOE and the residuals became more acceptable, although still large. These values were not used in the location, which was based on seven p-wave arrival times. The condition number was 29.2 and the RMS residual was 0.09 s. The depth was estimated at 16.4± 1.4 km, and the horizontal error was 0.9 km.

The average RMS traveltime residual for all the events located with the RESTE Network (except EL06) was 0.15 s, with individual values ranging from

```
23 JUL '87  12:58  EVENT NO:   1          RUN :: 11/28/89  AT 00:11:10

                                                                ADJUSTMENTS (KM)
 I ORIGIN   LAT N     LON W      Z   NWR  RMS    DT     DLAT    DLON     DZ     RR NF
 1  12.75 38 43.83     9  2.52 19.85 10 0.17 0.003   C.029   C.017  0.000 0.034 3
FOCAL DEPTH FREED
 2  12.75 38 43.65     9  2.53 19.85 10 0.18-0.009  -0.018   0.006  0.086 0.088 4
 3  12.74 38 43.84     9  2.54 19.94 10 C.17 0.000  -0.003   0.023  0.016 0.028 4

          EIGENVALUES
    (  3.494  0.487  0.308  0.116)                                          #ERROR ELLIPSE
     EIGENVECTORS OF ADJUSTMENT          COVARIANCE                  ERRORS #  SERR AZ DIP
DT ( -0.995  0.058 -0.012  0.061)(  0.023 -0.016 -0.063 -0.230)  0.152 #  1.72 292 72
LAT(  0.050  0.980 -0.286 -0.112)( -0.016  0.225  0.152  0.280)  0.474 #  0.65 107 17
LON( -0.029 -0.305 -0.913 -0.271)( -0.063  0.152  0.585  0.657)  0.765 #  0.41 196  1
Z  ( -0.082 -0.020  0.292 -0.953)( -0.230  0.280  0.657  2.736)  1.654 #

YR MO DA    ORIGIN     LAT N     LON W    DEPTH  RMS   ERH    ERZ  GAP XMAG FMAG STAND
87- 7-23 1258 12.74 38 43.84     9  2.54 19.94 0.17  0.62   1.64  113                0.865

RMSWT DMIN ITR NFM NWR NWS REMK
 0.17 19.1   3   9  10   3

 STA DIST AZM  AN P/S W    SEC  CCOR (TOBS -TCAL -DLY  =RES) WT  XMG FMG R INFO
 AVL 19.1 343 130 P      17.71 0.00  4.97  4.71 0.00  0.26 1.10                0.194
                  S      21.05 0.00  8.31  8.38 0.00 -0.08 1.10                0.679
 ACA 23.3  63 123 P      18.17 0.00  5.43  5.23 0.00  0.20 1.10                0.229
                  S   2  21.57 0.00  8.83  9.31 0.00 -0.48 0.00                0.000
 ASZ 30.5 188 114 P      18.90 0.00  6.16  6.20 0.00 -0.04 1.10                0.301
                  S      23.78 0.00 11.04 11.04 0.00  0.00 1.10                0.738
 ASN 30.6 283 114 P      18.80 0.00  6.06  6.21 0.00 -0.15 1.10                0.702
                  S   4  22.89 0.00 10.15 11.05 0.00 -0.91 0.00                0.000
 ADV 32.6  30 112 P      19.48 0.00  6.74  6.49 0.00  0.25 1.10                0.178
                  S      24.07 0.00 11.33 11.55 0.00 -0.23 1.10                0.365
 AMG 43.8  50  77 P      20.93 0.00  8.19  8.13 0.00  0.06 1.10                0.276
                  S   4  26.55 0.00 13.81 14.47 0.00 -0.67 0.00                0.000
 AST 46.5  75  79 P      21.05 0.00  8.31  8.53 0.00 -0.22 1.10                0.331
                  S   4  26.93 0.00 14.19 15.18 0.00 -1.00 0.00                0.000
```

Fig. 4.19 – HYPOINVERSE report for event EL01

```
28 JUL 87  20:24   EVENT NO.    1          RUN  11/25/89  AT 12:58:05

                                                                ADJUSTMENTS (KM)
 I ORIGIN    LAT N     LON W      Z   NWR  RMS    DT      DLAT     DLON      DZ      RR NF
 1  18.50 39 30.50     9  4.72 20.82 11 0.13 0.063 -0.291   0.250   0.000 0.376 3
FOCAL DEPTH FREED
 2  18.56 39 30.35     9  4.89 20.82 11 0.11 0.005 -0.146   0.170   0.978 1.005 4
 3  18.63 39 30.27     9  5.02 21.80 10 0.10 0.022 -0.060   0.057   0.020 0.081 4
 4  18.65 39 30.24     9  5.06 21.83 10 0.09 0.006 -0.035  -0.019  -0.004 0.040 4

        EIGENVALUES                                                          #ERROR ELLIPSE
   (  3.618   0.230   0.174   0.169)
     EIGENVECTORS OF ADJUSTMENT COVARIANCE                          ERRORS #  SERR AZ DIP
OT (-0.984   0.055 -0.126 -0.117)(  0.021 -0.101 -0.030   0.027)   0.146 #  0.80 337 46
LAT(-0.172  -0.429   0.444   0.768)( -0.101   0.573   0.109   0.024)   0.757 #  0.78 150 42
LON(-0.026   0.900   0.271   0.341)( -0.030   0.109   0.409  -0.007)   0.640 #  0.59 243  3
Z  (  0.048   0.055 -0.845   0.530)(  0.027   0.024 -0.007   0.629)   0.793 #

YR MO DA   ORIGIN     LAT N    LON W    DEPTH  RMS   ERH   ERZ GAP XMAG FMAG STAND
87  7 28 2024 18.65 39 30.24     9  5.06 21.83 0.09  0.59  0.59 307           0.586

RMSWT DMIN ITR NFM NWR NRS REMK
 0.10 61.5   4   0  10   4

STA  DIST AZM  AN P/S W    SEC  CCOR  TOBS  TCAL  DLY   =RES  WT  XMG FMG R INFO
ABV  61.5 160  85 P      29.42 0.00 10.77 10.83 0.00 -0.06 1.22          0.349
AVL  67.8 182  88 P      30.38 0.00 11.73 11.79 0.00 -0.06 1.22          0.324
                S  2 38.46 0.00 20.81 20.99 0.00 -0.18 0.61          0.173
AMG  69.0 147  89 P      30.17 0.00 11.52 11.96 0.00 -0.44 0.01          0.000
                S  2 41.04 0.00 21.39 21.29 0.00  0.10 0.61          0.242
ACA  79.6 162  89 P      32.40 0.00 13.75 13.56 0.00  0.19 1.22          0.174
                S      42.73 0.00 24.08 24.14 0.00 -0.06 1.22          0.615
ASN  83.8 199  89 P      32.80 0.00 14.15 14.20 0.00 -0.05 1.22          0.382
                S      44.01 0.00 25.36 25.28 0.00  0.08 1.22          0.722
AST  88.6 146  89 P      33.62 0.00 14.97 14.93 0.00  0.04 1.22          0.307
                S  4 45.41 0.00 26.76 26.58 0.00  0.19 0.00          0.000
AMJ  89.4 177  89 P  4 30.79 0.00 20.14 15.05 0.00  5.09 0.00          0.000
                S  4 53.13 0.00 34.48 26.79 0.00  7.69 0.00          0.000
AMT 110.5 157  89 P      36.82 0.00 18.17 18.25 0.00 -0.08 1.22          0.706
                S  4 50.58 0.00 31.93 32.49 0.00 -0.55 0.00          0.000
ASZ 116.2 181  89 P  4 38.79 0.00 20.14 19.11 0.00  1.03 0.00          0.000
                S  4 53.13 0.00 34.48 34.02 0.00  0.46 0.00          0.000
```

Fig. 4.20 – HYPOINVERSE report for event ER02

```
29 JUL 87  13: 7  EVENT NO.    1          RUN ..  11/25/89  AT 13:01:33

                                                                ADJUSTMENTS (KM)
 I ORIGIN  LAT N     LON W      Z  NWR  RMS    OT     DLAT    DLON     DZ      RR NF
 1  35.89 38 47.77    8 12.07 16.06 12 0.15-0.016 -0.057 -0.029  0.000 0.064 3
FOCAL DEPTH FREED
 2  35.87 38 47.74    8 12.05 16.06 12 0.15-0.007  0.277  0.021  0.982 1.021 4
RMS INCREASE - MOVE HYPO 0.60 BACK
 3  35.87 38 47.88    8 12.06 17.03 12 0.17 0.004 -0.166 -0.013 -0.589 0.613 4
 4  35.87 38 47.80    8 12.06 16.44 12 0.16 0.004  0.261  0.066  1.071 1.104 4
RMS INCREASE - MOVE HYPO 0.60 BACK
 5  35.87 38 47.94    8 12.10 17.51 12 0.17 0.002 -0.156 -0.039 -0.643 0.663 4
 6  35.87 38 47.86    8 12.07 16.87 12 0.17 0.003  0.218  0.145  1.108 1.139 4
RMS INCREASE - MOVE HYPO 0.60 BACK
 7  35.87 38 47.97    8 12.17 17.98 12 0.17-0.002 -0.131 -0.087 -0.665 0.683 4
RMS INCREASE - MOVE HYPO 0.60 BACK
 8  35.87 38 47.90    8 12.11 17.31 12 0.17-0.001 -0.052 -0.035 -0.266 0.273 4
 9  35.87 38 47.87    8 12.09 17.05 12 0.17 0.005  0.322  0.175  1.107 1.166 4
RMS INCREASE - MOVE HYPO 0.60 BACK
10  35.88 38 48.05    8 12.21 18.16 12 0.17-0.003 -0.193 -0.105 -0.664 0.699 4
RMS INCREASE - MOVE HYPO 0.60 BACK
11  35.87 38 47.94    8 12.14 17.49 12 0.17-0.001 -0.077 -0.042 -0.266 0.280 4
12  35.87 38 47.90    8 12.11 17.23 12 0.17 0.007  0.253  0.189  1.121 1.165 4
RMS INCREASE - MOVE HYPO 0.60 BACK
13  35.88 38 48.04    8 12.24 18.35 12 0.17-0.004 -0.152 -0.113 -0.673 0.699 4
RMS INCREASE - MOVE HYPO 0.60 BACK
14  35.87 38 47.96    8 12.16 17.67 12 0.17-0.002 -0.061 -0.045 -0.269 0.280 4
RMS INCREASE - MOVE HYPO 0.60 BACK
15  35.87 38 47.92    8 12.13 17.41 12 0.17-0.001 -0.024 -0.018 -0.108 0.112 4
RMS INCREASE - MOVE HYPO 0.60 BACK
16  35.87 38 47.91    8 12.12 17.30 12 0.17 0.000 -0.010 -0.007 -0.043 0.045 4
17  35.87 38 47.90    8 12.11 17.25 12 0.17 0.002  0.126  0.092  0.564 0.585 4

        EIGENVALUES                                                      #ERROR ELLIPSE
    ( 3.710  0.219  0.166  0.110)
      EIGENVECTORS OF ADJUSTMENT          COVARIANCE                ERRORS #  SERR AZ DIP
OT  ( -0.986  0.037 -0.163 -0.010)(  0.042 -0.002  0.234 -0.017) / 0.206 #  1.81  8 62
LAT(  0.019  0.890  0.064  0.451)( -0.002  1.323 -0.111  0.985)  1.150 #  1.18 266  6
LON(  0.166  0.098 -0.979 -0.063)(  0.234 -0.111  1.400 -0.074)  1.183 #  0.90 173 26
Z   ( -0.008 -0.443 -0.103  0.890)( -0.017  0.985 -0.074  2.780)  1.667 #

YR MO DA   ORIGIN     LAT N     LON W    DEPTH  RMS   ERH   ERZ  GAP  XMAG FMAG STAND
87- 7-29 13 7 35.87 38 47.90    8 12.11 17.25 0.17  1.18  1.61 306                0.514

RMSHT DMIN ITR NFM NWR NWS REMK
 0.18 28.2  17   0  12   6

 STA DIST AZM  AN P/S W    SEC  CCOR (TOBS -TCAL -DLY  =RES) WT  XMG FMG R INFO
 AST 28.2 279 112 P      41.51 0.00  5.64  5.71 0.00 -0.07 1.36          0.498
                  S    2 45.82 0.00  9.95 10.16 0.00 -0.22 0.68          0.438
 AMG 44.0 298  81 P      44.05 0.00  8.18  8.08 0.00  0.10 1.36          0.353
                  S    2 50.40 0.00 14.53 14.38 0.00  0.15 0.68          0.249
 ACA 52.0 274  85 P      45.45 0.00  9.58  9.33 0.00  0.25 1.36          0.155
                  S    2 52.46 0.00 16.59 16.61 0.00 -0.02 0.68          0.236
 ABV 59.6 291  88 P      46.25 0.00 10.38 10.51 0.00 -0.13 1.36          0.297
                  S    2 54.54 0.00 16.67 18.71 0.00 -0.04 0.68          0.266
 AVL 79.2 278  83 S    4 60.95 0.00 25.08 24.14 0.00  0.94 0.00          0.000
 ASZ 86.0 244  83 P      50.44 0.00 14.57 14.61 0.00 -0.04 1.36          0.520
                  S    2 62.05 0.00 26.18 26.01 0.00  0.17 0.68          0.388


 ASN102.7 270  83 P      62.77 0.00 16.90 17.21 0.00 -0.31 1.19          0.304
                  S    2 66.19 0.00 30.32 30.63 0.00 -0.32 0.58          0.289
```

Fig. 4.21 – HYPOINVERSE report for event ER03

```
14 OCT 87  21:56  EVENT NO:    1          RUN ..  11/27/89  AT 20:57:48

                                                          ADJUSTMENTS (KM)
 I ORIGIN    LAT N     LON W      Z   N#R  RMS    DT      DLAT    DLON     DZ      RR NF
 1  28.07 38 39.75    9  9.46 15.00    8 0.03-0.008 -0.030  0.052  0.000 0.060  3
FOCAL DEPTH FREED
 2  28.06 38 39.73    9  9.50 15.00    8 0.03-0.015  0.008  0.087  0.261 0.294  4
 3  28.05 38 39.74    9  9.56 15.28    7 0.02 0.002 -0.016 -0.010 -0.086 0.088  4
 4  28.05 38 39.73    9  9.55 15.20    7 0.02 0.004  0.014  0.002 -0.063 0.065  4
 5  28.05 38 39.74    9  9.55 15.13    8 0.02-0.003 -0.015  0.019  0.053 0.058  4

          EIGENVALUES
    (  3.476  0.467  0.250  0.081)
      EIGENVECTORS OF ADJUSTMENT          COVARIANCE                    ERRORS  #  SERR AZ DIP
DT  ( -0.992  0.076 -0.070 -0.072)(  0.010 -0.003 -0.058 -0.099)  0.101  #  1.26 279 64
LAT(  0.077  0.991 -0.085  0.066)( -0.003  0.056  0.034  0.097)  0.236  #  0.41  85 24
LON( -0.090  0.056  0.903  0.417)( -0.058  0.034  0.415  0.537)  0.644  #  0.22 178  5
Z   ( -0.043 -0.093 -0.416  0.903)( -0.099  0.097  0.537  1.331)  1.154  #

YR MO DA   ORIGIN     LAT N     LON W    DEPTH  RMS   ERH   ERZ  GAP  XMAG FMAG STAND
87-10-14 2156 28.05 38 39.74    9  9.55 15.13 0.02  0.53  1.14  204                0.882

RMSWT DMIN ITR NFM N#R NMS REMK
 0.08 11.1   5   0   8   3

 STA DIST AZM  AN P/S W    SEC+CCOR (TOBS -TCAL  -DLY   =RES) WT  XMG FMG R INFO
 AMJ 11.1  67 139 P       30.94 0.00  2.69  3.30  0.00 -0.41 0.11          0.011
 ASZ 23.4 165 114 P       32.94 0.00  4.89  4.88  0.00  0.01 1.47          0.863
                  S    4 38.05 0.00 10.00  8.69  0.00  1.31 0.00          0.000
 AVL 26.1   9 110 P       33.32 0.00  5.27  5.28  0.00 -0.01 1.47          0.496
                  S       37.47 0.00  9.42  9.40  0.00  0.02 1.47          0.764
 ACA 35.8  59 101 P    2  35.21 0.00  7.16  6.75  0.00  0.41 0.07          0.000
                  S    2  40.04 0.00 11.99 12.01  0.00 -0.03 0.73          0.579
 AMT 49.2 100  87 P       36.91 0.00  8.86  8.86  0.00  0.00 1.47          0.454
                  S    4  42.76 0.00 14.71 15.77  0.00 -1.06 0.00          0.000
 AMG 56.5  51  87 P       38.06 0.00 10.01 10.01  0.00  0.00 1.47          0.579
                  S    2  45.92 0.00 17.67 17.82  0.00  0.05 0.73          0.249
```

Fig. 4.22 – HYPOINVERSE report for event EL05

```
26 OCT 89  11: 0  EVENT NO.   1          RUN .. 11/24/89  AT 18:07:06

                                                                ADJUSTMENTS (KM)
 # ORIGIN    LAT N     LON W      Z   NWR  RMS    DT     DLAT     DLON     DZ      RR NF
 1  00 12 38 32.56   8 13.13 15.00   7 0.75-0.153  2.903 -5.345  0.000 0.002 3
 2  00 27 38 34.13   0  9.44 15.00   7 0.46 0.059  0.887 -0.019  0.000 0.007 3
FOCAL DEPTH FREED
AIRQUAKE PREVENTED
DEPTH VARIATION DAMPED
 3  00 28 38 34.60   8  9.43 15.00   7 0.45-0.104 -3.780  2.132 -3.021 3.665 4
RMS INCREASE = MOVE HYPO 0.60 BACK
 4  00 32 38 32.56   8 10.90 11.38   7 0.47 0.062  2.271 -1.279  2.172 3.393 4
AIRQUAKE PREVENTED
 5  00 28 38 33.79   8 10.02 13.55   7 0.44-0.078 -2.895  2.663 -0.776 7.895 4
AIRQUAKE PREVENTED
 6  04 33 38 32.23   8 11.85  6.78   7 0.43-0.106 -0.231  3.081 -3.388 4.585 4
RMS INCREASE = MOVE HYPO 0.60 BACK
 7  04 44 38 32.10   8 13.93  3.39   8 0.65 0.064  0.139 -1.848  2.033 2.781 4
RMS INCREASE = MOVE HYPO 0.60 BACK
 8  04 38 38 32.18   8 12.70  5.42   7 0.50 0.025  0.055 -0.739  0.083 1.180 4
AIRQUAKE PREVENTED
 9  04 38 38 32.21   8 12.19  6.23   7 0.45-0.100 -0.115  3.140 -3.117 4.428 4
RMS INCREASE = MOVE HYPO 0.60 BACK
10  04 45 38 32.14   8 14.36  3.12   8 0.71 0.060  0.069 -1.886  1.870 2.687 4
RMS INCREASE = MOVE HYPO 0.60 BACK
11  04 39 38 32.18   8 13.06  4.99   7 0.54 0.024  0.028 -0.754  0.748 1.063 4
RMS INCREASE = MOVE HYPO 0.60 BACK
12  04 37 38 32.20   8 12.56  5.74   7 0.48 0.010  0.011 -0.302  0.299 0.425 4
RMS INCREASE = MOVE HYPO 0.60 BACK
13  04 36 38 32.20   8 12.33  6.03   7 0.46 0.004  0.004 -0.121  0.120 0.170 4
RMS INCREASE = MOVE HYPO 0.60 BACK
14  04 35 38 32.20   6 12.25  6.15   7 0.46 0.002  0.002 -0.048  0.048 0.068 4
AIRQUAKE PREVENTED
15  04 35 38 32.21   8 12.21  6.24   7 0.45-0.050 -0.063  1.603 -3.101 3.491 4
RMS INCREASE = MOVE HYPO 0.60 BACK
16  04 40 38 32.17   6 13.32  3.10   7 0.49 0.030  0.038 -0.962  1.961 2.095 4
RMS INCREASE = MOVE HYPO 0.60 BACK
17  04 37 38 32.19   6 12.66  4.96   7 0.47 0.012  0.015 -0.385  0.744 0.838 4
RMS INCREASE = MOVE HYPO 0.60 BACK
18  04 36 38 32.20   8 12.39  5.71   7 0.46 0.005  0.006 -0.154  0.298 0.335 4
RMS INCREASE = MOVE HYPO 0.60 BACK
19  04 35 38 32.20   8 12.22  6.00   7 0.46 0.002  0.002 -0.062  0.119 0.134 4
RMS INCREASE = MOVE HYPO 0.60 BACK
20  04 35 38 32.20   6 12.24  6.12   7 0.45 0.001  0.001 -0.025  0.048 0.054 4
RMS INCREASE = MOVE HYPO 0.60 BACK
21  04 35 38 32.20   8 12.23  6.17   7 0.46 0.000  0.000 -0.010  0.019 0.021 4
RMS INCREASE = MOVE HYPO 0.60 BACK
22  04 35 38 32.20   8 12.22  6.19   7 0.45 0.000  0.000 -0.004  0.008 0.009 4
AIRQUAKE PREVENTED
23  04 35 38 32.20   8 12.22  6.20   7 0.45-0.050 -0.056  1.619 -3.098 3.496 4

        EIGENVALUES
    ( 3.210  0.229  0.140  0.030)
     EIGENVECTORS OF ADJUSTMENT          COVARIANCE                          ERRORS  #ERROR ELLIPSE
                                                                             #  ERR AZ DIP
OT ( -0.984  0.021  0.178 -0.007)( 0.384  0.699  1.213  2.071)  0.620 # 15.51  74 76
LAT(  0.077  0.942  0.313 -0.095)( 0.849  6.979 -5.088 21.693)  2.623 #  3.26 289 15
LON(  0.156 -0.278  0.895  0.312)( 1.213 -5.088 32.473-68.034)  8.699 #  2.03 197 10
Z  (  0.050 -0.166  0.262 -0.945)( 2.071 21.693-58.034215.894) 14.693 #

================================================================================


YR MO DA   ORIGIN     LAT N    LON W   DEPTH  RMS   ERH   ERZ GAP XMAG FMAG STAND
89-10-26  059 55.65 38 32.20   8 12.22   6.20 0.45  5.05 14.60 303              0.078

RMSWT DMIN ITR NFM NWR NWS REMK
 0.46 43.4  23   0   7   3

 STA DIST AZM  AN P/S W    SEC+CCOR (TOBS -TCAL -DLY  =RES) WT  XMG FMG R INFO
 AST 43.4 321  82 P       3.22 0.00  7.57  7.98 0.00 -0.41 1.45           0.612
                  S   2   9.29 0.00 13.64 14.20 0.00 -0.56 0.72           0.437
 ACA 61.0 302  76 P       6.73 0.00 11.08 10.96 0.00  0.12 1.45           0.267
                  S   2  15.82 0.00 20.17 19.51 0.00  0.66 0.72           0.448
 ASZ 77.7 269  71 P       9.73 0.00 14.08 13.74 0.00  0.34 1.45           0.689
                  S   2  20.29 0.00 24.64 24.46 0.00  0.18 0.72           0.551
 AVL 88.0 297  71 P      11.77 0.00 16.12 15.43 0.00  0.69 1.45           0.990
                  S   2  24.35 0.00 28.70 27.47 0.00  1.24 0.03           0.002
```

Fig. 4.23 – HYPOINVERSE report for event EL06

```
21 JAN 88  4: 4  EVENT NO.    1          RUN .. 11/24/89  AT 17:56:40

                                                          ADJUSTMENTS (KM)
 I ORIGIN    LAT N     LON W      Z   NWR  RMS    DT      DLAT    DLON     DZ      RR NF
 1  10.05 38 57.55    8 44.63  15.00   5 0.70 0.660  -0.488  -1.800   0.000  1.865 3
FOCAL DEPTH FREED
DEPTH VARIATION DAMPED
 2   9.39 38 57.29    8 43.38  15.00   5 0.17 0.802   0.577   2.119  -3.513  4.143 4
RMS INCREASE = MOVE HYPO 0.60 BACK
 3  10.19 38 57.60    8 44.85  11.49   5 0.45-0.481  -0.346  -1.272   2.108  2.486 4
RMS INCREASE = MOVE HYPO 0.60 BACK
 4   9.71 38 57.41    8 43.97  13.59   5 0.26-0.192  -0.138  -0.509   0.843  0.994 4
 5   9.52 38 57.34    8 43.62  14.44   5 0.19 0.648   0.448   1.667  -6.347  6.577 4
 6  10.17 38 57.58    8 44.77   8.09   5 0.11-0.098  -0.023  -0.144  -0.011  0.147 4
 7  10.07 38 57.57    8 44.67   8.08   5 0.04-0.011   0.022  -0.044  -0.023  0.055 4
 8  10.06 38 57.58    8 44.64   6.06   5 0.04-0.001  -0.036  -0.007  -0.003  0.036 4

        EIGENVALUES
   (  2.245   0.234   0.208   0.063)
     EIGENVECTORS OF ADJUSTMENT          COVARIANCE                          ERRORS #  #ERROR ELLIPSE
                                                                                      #  SERR AZ DIP
DT (  -0.996   0.002  -0.041  -0.082)(  0.022   0.008   0.055  -0.227)   0.148 #  1.69 106 77
LAT(  -0.020  -0.819   0.571  -0.059)(  0.008   0.237   0.006  -0.158)   0.487 #  0.51 235  7
LON(   0.048  -0.551  -0.809  -0.197)(  0.055   0.006   0.351  -0.509)   0.592 #  0.46 326  9
Z  (  -0.075  -0.162  -0.134   0.970)( -0.227  -0.158  -0.509   2.731)   1.653 #

YR MO DA    ORIGIN      LAT N     LON W    DEPTH  RMS   ERH    ERZ  GAP  XMAG FMAG STAND
88- 1-21   4 4 10.06  38 57.58    8 44.64   8.06 0.04  0.51   1.65  127                0.500

RMSWT DMIN ITR NFM NWR NWS REMK
 0.04   8.3   8   0   5   0

STA  DIST AZM  AN P/S W    SEC+CCOR (TOBS -TCAL -DLY  =RES) WT  XMG FMG R INFO
AMG   8.3  72 128 P      12.21 0.00  2.15  2.16 0.00 -0.01 1.00            0.993
BSE   8.5 200 127 P      12.30 0.00  2.24  2.19 0.00  0.05 1.00            0.542
ABV   9.4 286 124 P      12.33 0.00  2.27  2.31 0.00 -0.04 1.00            0.796
ACA  16.0 199 107 P      13.33 0.00  3.27  3.32 0.00 -0.05 1.00            0.775
BOT  25.6 307  95 P      15.00 0.00  4.94  4.91 0.00  0.03 1.00            0.892
                  S    4 18.00 0.00  7.94  8.74 0.00 -0.80 0.00            0.000
```

Fig. 4.23 – HYPOINVERSE report for event EL22

```
 22 JAN 86  21: C  EVENT NO.   1          RUN  11/24/89  AT 17:58:49

                                                                ADJUSTMENTS (KM)
 I ORIGIN    LAT N     LON W      Z   N#R  RMS    DT      DLAT     DLON     DZ      RR NF
 1  42 25 39  0.91    9  1.28 15.00   4 0.77-0.677   3.072    0.723    0.000  3.156 3
FOCAL DEPTH FREED
 2  41 57 39  2.57    9  1.78 15.00   4 0.12-0.679   2.793    0.604    4.876  5.652 4
 3  40 89 39  4.07    9  2.20 19.88   4 0.07-0.048   0.272    0.046   -0.173  0.326 3
 4  40 85 39  4.22    9  2.23 19.70   4 0.02-0.008  -0.019    0.006    0.009  0.021 3

          EIGENVALUES
    (  2.016   0.160   0.079   0.019)
     EIGENVECTORS OF ADJUSTMENT              COVARIANCE                          ERRORS #  #ERROR ELLIPSE
                                                                                        #   SERR AZ DIP
OT  ( -0.992   0.013  -0.036   0.118)(  1.436 -6.174 -1.347 -10.293)   1.198 #  10.10 348 58
LAT(  0.038  -0.404   0.758  -0.511)( -6.174  28.040  5.177  44.094)   5.295 #   1.29 214 23
LON(  0.043  -0.844  -0.524  -0.108)( -1.347   5.177  1.945   9.628)   1.395 #   0.64 116 20
Z   (  0.110   0.354  -0.387  -0.845)(-10.293  44.094  9.628  74.038)   8.605 #

YR MO DA   ORIGIN     LAT N    LON W   DEPTH  RMS   ERH    ERZ  GAP XMAG FMAG STAND
86  1 22 21 0 40.85 39  4.22    9  2.23 19.70 0.02  5.31   8.59 168                0.188

RMSWT DMIN ITR NFM NWR NWS REMK
 0.02  5.8   4   0   4   0

 STA DIST AZM  AN P/S W    SEC  CCOR (TOBS -TCAL -DLY  =RES) WT   XMG FMG R INFO
 BOT 15.8  68 161 P     44.35 0.00  3.50  3.52  0.00 -0.02 1.00              1.000
 BSM  9.7 250 150 P     44.60 0.00  3.75  3.76  0.00 -0.01 1.00              1.000
 ABV 19.0 121 130 P     45.54 0.00  4.69  4.68  0.00  0.01 1.00              1.000
 BSE 30.3 132 114 P     46.98 0.00  6.13  6.16  0.00 -0.03 1.00              1.000
```

Fig . 4.24 – HYPOINVERSE report for event EL23

```
26 JAN 88  15:33  EVENT NO:    1          RUN :: 11/23/89  AT 09:28:13

                                                                ADJUSTMENTS (KM)
I ORIGIN    LAT N     LON W      Z  NWR  RMS    DT     DLAT    DLON     DZ      RR NF
1   9.66 38 56.06   8 43.96   9.36   7 0.37 0.003 -0.010   0.017  0.000  0.020  3
OCAL DEPTH FREED
2   9.66 38 56.05   8 43.97   9.36   7 0.37 0.003  0.005   0.003 -0.053  0.053  4
3   9.67 38 56.06   8 43.97   9.31   7 0.37 0.004 -0.011  -0.009 -0.058  0.060  4
4   9.67 38 56.05   8 43.97   9.25   7 0.37-0.007  0.025   0.025  0.092  0.098  4
5   9.66 38 56.06   8 43.98   9.34   7 0.37 0.009 -0.017  -0.055 -0.132  0.144  4

        EIGENVALUES                                                      #ERROR ELLIPSE
   (  2.665   0.349   0.289   0.101)                                      ERRORS #  SERR AZ DIP
     EIGENVECTORS OF ADJUSTMENT          COVARIANCE
T (  -0.993   0.022  -0.083  -0.085)(  0.135 -0.233 -0.189 -1.190)  0.371 #  3.78 298 81
AT(  -0.089   0.017   0.993   0.073)( -0.233  1.829  0.126  0.889)  1.352 #  1.33 180  4
ON(  -0.036  -0.998   0.005   0.133)( -0.189  0.126  1.444  1.723)  1.202 #  1.10  90  7
  (  -0.075   0.134  -0.081   0.985)( -1.190  0.889  1.723 14.002)  3.742 #

R MO DA   ORIGIN     LAT N     LON W   DEPTH  RMS   ERH   ERZ GAP XMAG FMAG STAND
8  1 26 1533   9.66 38 56.06   8 43.98   9.34 0.37  1.32  3.74 115                0.404

MSHT DMIN ITR NFM NWR NRS REMK
0.37  8.8   5   0   7   2

STA  DIST AZM  AN P/S W    SEC+CCOR (TOBS -TCAL -DLY  =RES) WT  XMG FMG R INFO
AMG   8.8  53 132 P      12.25 0.00  2.59  2.36 0.00   0.23 1.00              0.610
ABV  11.3 298 123 P      11.92 0.00  2.26  2.70 0.00  -0.44 1.00              0.650
ACA  13.8 206 117 P      13.08 0.00  3.42  3.05 0.00   0.37 1.00              0.255
                 S       15.08 0.00  5.42  5.43 0.00  -0.01 1.00              0.844
AST  21.1 120 104 P      14.42 0.00  4.76  4.22 0.00   0.54 1.00              0.282
                 S       16.67 0.00  7.01  7.51 0.00  -0.50 1.00              0.651
AMT  40.7 163  88 P      16.92 0.00  7.26  7.46 0.00  -0.20 1.00              0.705
                 S    4  21.46 0.00 11.80 13.28 0.00  -1.48 0.00              0.000
```

Fig. 4.25 – HYPOINVERSE report for event EL24

```
30 APR 88  7:47  EVENT NO  1          RUN  11/27/89  AT 16:41:39

                                                    ADJUSTMENTS (KM)
I ORIGIN   LAT N     LON W      Z   NWR  RMS    DT      DLAT    DLON     DZ      RR NF
8  13.16 38 51.02    9  6.67 15.00   6 0.79 0.574   2.070   3.276   0.000   3.875 3
OCAL DEPTH FREED
2  12.99 38 52.14    9  8.94 15.00   5 0.15 0.189  -1.629  -0.769  -1.909   2.625 4
3  12.78 38 51.26    9  8.41 13.09   5 0.06 0.005   0.004   0.092  -0.901   0.903 4
4  12.78 38 51.26    9  8.43 12.79   6 0.08 0.032   0.060  -0.075  -0.931   0.940 4
MS INCREASE - MOVE HYPO 0.60 BACK
5  12.81 38 51.29    9  8.38 12.26   6 0.10-0.019  -0.036   0.045   0.319   0.324 4
MS INCREASE - MOVE HYPO 0.60 BACK
6  12.79 38 51.27    9  8.41 12.68   6 0.11-0.008  -0.014   0.018   0.128   0.130 4
MS INCREASE - MOVE HYPO 0.60 BACK
7  12.79 38 51.27    9  8.42 12.70   6 0.10-0.003  -0.006   0.007   0.051   0.052 4
MS INCREASE - MOVE HYPO 0.60 BACK
8  12.78 38 51.26    9  8.43 12.76   6 0.09 0.001  -0.002   0.003   0.020   0.021 4
9  12.78 38 51.25    9  8.43 12.78   6 0.08 0.030   0.059  -0.073  -0.519   0.528 4
MS INCREASE - MOVE HYPO 0.60 BACK
0  12.81 38 51.29    9  8.38 12.26   6 0.10-0.018  -0.035   0.044   0.312   0.317 4
MS INCREASE - MOVE HYPO 0.60 BACK
1  12.79 38 51.27    9  8.41 12.57   6 0.11-0.007  -0.014   0.018   0.125   0.127 4
MS INCREASE - MOVE HYPO 0.60 BACK
2  12.79 38 51.27    9  8.42 12.69   6 0.10-0.003  -0.006   0.007   0.050   0.051 4
MS INCREASE - MOVE HYPO 0.60 BACK
3  12.78 38 51.26    9  8.42 12.74   6 0.09 0.001  -0.002   0.003   0.020   0.020 4
4  12.78 38 51.26    9  8.43 12.76   6 0.09 0.021   0.058  -0.041  -0.333   0.340 4

        EIGENVALUES                                                          ERROR ELLIPSE
   (  2.511   0.391   0.165   0.124)
     EIGENVECTORS OF ADJUSTMENT          COVARIANCE                    ERRORS #  SERR AZ DIP
T (  -0.996   0.013   0.037   0.077)(  0.010 -0.025 -0.026 -0.083)   0.102 #  1.07 324 55
AT(  -0.001   0.376   0.805  -0.459)( -0.025  0.598  0.236  0.215)   0.773 #  0.72 164 33
ON(  -0.029  -0.912   0.236  -0.333)( -0.026  0.236  0.255  0.232)   0.505 #  0.34  68  9
   (  -0.081   0.161  -0.543  -0.820)( -0.083  0.215  0.232  0.935)   0.967 #

R MO DA   ORIGIN     LAT N     LON W    DEPTH  RMS   ERH   ERZ  GAP XMAG FMAG STAND
8  4 30   747 12.78 38 51.26    9  8.43 12.76 0.09  0.61  0.88  141              1.000

MSNT DMIN ITR NFM NWR NWS RLMK
0.11  5.3  14   0   6   2

STA DIST AZM  AN P/S W    SEC+CCOR (TOBS -TCAL -DLY  =RES) WT  XMG FMG R INFO
AVL  5.3  32 155 P      15.23 0.00  2.45  2.47 0.00 -0.02 1.09          0.491
                S      16.85 0.00  4.07  4.40 0.00 -0.33 0.53          0.533
AMJ 19.1 153 115 P      16.89 0.00  4.11  4.09 0.00  0.02 1.09          0.991
ASN 22.6 251 110 S      20.98 0.00  8.20  8.21 0.00 -0.01 1.09          0.983
ABV 29.0  60 103 P      18.47 0.00  5.69  5.60 0.00  0.09 1.09          0.447
AMG 44.5  71  87 P      20.81 0.00  8.03  8.11 0.00 -0.08 1.09          0.551
AMT 55.6 122  85 P    4 21.70 0.00  8.92  9.90 0.00 -0.98 0.00          0.000
```

Fig. 4.26 – HYPOINVERSE report for event EL25

```
 6 MAY 88  2:45  EVENT NO.  1          RUN .. 11/27/89  AT 20:56:12

                                                          ADJUSTMENTS (KM)
 I ORIGIN    LAT N     LON W      Z  NWR  RMS    DT     DLAT    DLON     DZ     RR NF
 1   0.32 38 43.43   9 36.06 15.00  11 0.17-0.100 -0.262  1.336  0.000 1.961 3
FOCAL DEPTH FREED
 2   0.22 38 43.29   9 37.00 15.00  11 0.09 0.112  0.206 -1.136 -0.167 0.315 4
 3   0.33 38 43.43   9 36.22 10.84  11 0.08-0.004  0.084 -0.222 -0.259 0.351 4
 4   0.33 38 43.45   9 36.06 10.58  11 0.07 0.001  0.023 -0.027  0.000 0.035 4

     EIGENVALUES                                                        ERROR ELLIPSE
 (   3.368   0.226   0.177   0.038)
     EIGENVECTORS OF ADJUSTMENT          COVARIANCE                     ERRORS #   SERR AZ DIP
OT ( -0.985 -0.042   0.165   0.036)(   0.029   0.057 -0.235 -0.313)   0.171 #   3.28 259 63
LAT(  0.035  0.904   0.416   0.089)(   0.057   0.412 -0.461 -0.802)   0.642 #   0.69  62 25
LON(-0.165  0.415  0.786 -0.431)(  -0.235 -0.461   2.349   3.983)   1.533 #   0.64 154  6
Z (  0.043 -0.109   0.426 -0.897)(  -0.313 -0.802   3.983   8.744)   2.957 #

YR MO DA   ORIGIN      LAT N     LON W    DEPTH  RMS   ERH   ERZ  GAP XMAG FMAG STAND
88- 5- 6   245   0.33 38 43.45   9 36.06 10.58 0.07  1.44  2.94  280                0.643

RMSWT DMIN ITR NFM NWR NWS REMK
 0.07 48.7   4   0  11   2

STA DIST AZM  AN P/S W    SEC CCOR (TOBS -TCAL -DLY  =RES) WT  XMG FMG R INFO
ASN 19.9  69 109 P   4  3.45 0.00  3.12  4.08 0.00 -0.96 0.00              0.000
AVL 46.7  66  87 P   4  8.04 0.00  7.71  8.47 0.00 -0.76 0.00              0.000
AMJ 48.7  93  86 P      8.98 0.00  8.65  8.79 0.00 -0.14 1.00              0.588
ASZ 53.3 123  84 P      9.96 0.00  9.63  9.55 0.00  0.08 1.00              0.519
BCR 60.2  61  81 P     11.04 0.00 10.71 10.69 0.00  0.02 1.00              0.209
BPA 64.5  72  79 P     11.83 0.00 11.50 11.39 0.00  0.11 1.00              0.148
BOT 67.8  52  78 P     12.25 0.00 11.92 11.94 0.00 -0.02 1.00              0.209
BMJ 69.1  63  77 P     12.42 0.00 12.09 12.13 0.00 -0.04 1.00              0.351
ABV 71.2  66  77 P     12.85 0.00 12.52 12.48 0.00  0.04 1.00              0.117
AMG 87.0  70  74 P     15.23 0.00 14.90 15.01 0.00 -0.11 1.00              0.223
                  S    27.08 0.00 26.75 26.72 0.00  0.03 1.00              0.608
AMT 88.2 100  74 P     15.51 0.00 15.18 15.19 0.00 -0.01 1.00              0.415
                  S    27.33 0.00 27.00 27.04 0.00 -0.04 1.00              0.607
BMU 88.6  63  74 P   4 11.04 0.00 10.71 15.25 0.00 -4.54 0.00              0.000
```

Fig. 4.27 – HYPOINVERSE report for event EL26

```
16 MAY 88  17: 3  EVENT NO.    1          RUN ..  11/27/89  AT 20:54:08

                                                                ADJUSTMENTS (KM)
I ORIGIN     LAT N      LON W       Z    NWR  RMS     DT      DLAT     DLON     DZ      RR NF
1  42.88 36 53.50    9 29.28  15.00  14  0.44-0.007   1.781    1.779   0.000  2.468  3
FOCAL DEPTH FREED
2  42.87 38 54.42    9 30.51  15.00  13  0.24 0.084   0.797    0.635   1.497  1.811  4
3  42.79 38 54.85    9 30.95  16.50  11  0.21-0.023   0.187    0.039   0.193  0.271  4
4  42.77 38 54.95    9 30.98  16.69  11  0.20 0.002   0.009   -0.136   0.303  0.332  4
5  42.77 38 54.96    9 30.89  16.99  11  0.20 0.012   0.035    0.045   0.013  0.060  4
6  42.76 38 54.96    9 30.92  17.01  11  0.19-0.009   0.013    0.017   0.181  0.183  4
7  42.75 38 54.99    9 30.93  17.19  11  0.20 0.001  -0.019    0.004   0.026  0.032  4

          EIGENVALUES
   (  3.680   0.252   0.162   0.098)
     EIGENVECTORS OF ADJUSTMENT                COVARIANCE                          ERRORS #  SERR AZ DIP
DT (-0.989   0.035  -0.140  -0.025)(  0.043  -0.073  -0.273   0.021)   0.208 #  2.23 128 65
AT(-0.010   0.932   0.256   0.255)(  -0.073   1.099   0.583  -0.878)   1.048 #  1.34 287 22
ON(-0.144  -0.339   0.876   0.320)(  -0.273   0.583   1.993  -0.877)   1.412 #  0.87  20  8
Z  (-0.026   0.144   0.383  -0.912)(   0.021  -0.878  -0.877   4.424)   2.103 #

YR MO DA   ORIGIN      LAT N     LON W    DEPTH   RMS    ERH    ERZ  GAP XMAG FMAG STAND
86- 5-18 17 3 42.75 38 54.99    9 30.93 17.19  0.20   1.24   2.04  270                0.512

RMSWT DMIN ITR NFM NWR NWS REMK
 0.22 18.1   7   0  11   1

STA  DIST  AZM  AN P/S W    SEC  CCOR (TOBS -TCAL -DLY  =RES)  WT   XMG FMG R INFO
ASN 18.1  141  127 P      47.04  0.00   4.29   4.33  0.00 -0.04  1.13              0.863
AVL 35.3   94  105 P      49.62  0.00   6.87   6.75  0.00  0.12  1.13              0.120
                   S      54.62  0.00  11.87  12.01  0.00 -0.14  1.13              0.892
BCR 45.9   80   82 P      51.16  0.00   5.41   8.37  0.00  0.04  1.13              0.126
                   S  4   61.50  0.00  18.75  14.90  0.00  3.85  0.00              0.000
AMJ 67.5  120   83 P      51.50  0.00   8.75   8.63  0.00  0.12  1.13              0.240
BMJ 49.4   54   84 P      51.54  0.00   8.79   8.91  0.00 -0.12  1.13              0.431
                   S  2   59.33  0.00  16.58  15.86  0.00  0.72  0.00              0.000
BOT 60.4   66   84 P      51.83  0.00   9.08   9.07  0.00  0.01  1.13              0.235
BPA 54.3   92   86 P      52.74  0.00   9.99   9.67  0.00  0.32  1.13              0.143
                   S  2   59.29  0.00  16.54  17.21  0.00 -0.67  0.00              0.000
ABV 58.2   82   89 P      53.50  0.00  10.75  10.28  0.00  0.47  0.71              0.063
ASZ 62.9  144   86 P      53.58  0.00  10.83  11.02  0.00 -0.19  1.13              0.622
                   S  4   63.00  0.00  20.25  19.62  0.00  0.64  0.00              0.000
BMU 74.1   76   84 P      55.20  0.00  12.45  12.77  0.00 -0.32  1.13              0.260
AMT 67.5  115   83 P  2   56.67  0.00  13.92  14.84  0.00 -0.92  0.00              0.000
                   S  4   67.33  0.00  24.58  26.42  0.00 -1.83  0.00              0.000
```

Fig. 4.28 – HYPOINVERSE report for event EL27

```
22 MAY 88  15: 0   EVENT NO.  1          RUN .. 11/27/89  AT 20:49:09

                                                    ADJUSTMENTS (KM)
I  ORIGIN    LAT N     LON W      Z   NWR  RMS    DT      DLAT    DLON     DZ      RR NF
1   0.38 38 58.79    9 11.82  15.00   6 0.87 0.894 -1.566 -1.295  0.000  2.032  3
DCAL DEPTH FREED
2   0.31 38 57.95    9 10.92  15.00   8 0.20 0.020 -0.032 -0.056  1.019  1.022  4
3   0.33 38 57.93    9 10.88  16.02   8 0.14 0.022  0.202  0.001  0.282  0.965  4
4   0.31 38 58.04    9 11.51  16.30   7 0.09-0.016  0.135  0.360  0.065  0.394  4
5   0.30 38 58.11    9 11.75  16.39   7 0.09-0.002 -0.009  0.013  0.002  0.016  4

      EIGENVALUES
   (  2.655   0.305   0.145   0.091)
     EIGENVECTORS OF ADJUSTMENT          COVARIANCE                          ERRORS  #  ERROR ELLIPSE
T (  -0.996   0.000  -0.046  -0.071)(   0.015 -0.041 -0.059 -0.134)   0.123  #   1.46 304 73
AT(  -0.031   0.892   0.420   0.166)(  -0.041  0.358  0.313  0.229)   0.599  #   0.92 116 16
ON(  -0.056  -0.451   0.858   0.240)(  -0.059  0.313  0.782  0.284)   0.884  #   0.48 207  2
   (  -0.054  -0.042  -0.293   0.954)(  -0.134  0.229  0.284  2.025)   1.423  #

R MO DA   ORIGIN     LAT N     LON W    DEPTH   RMS   ERH   ERZ  GAP XMAG FMAG STAND
8- 6-22 15  0.30 38 58.11    9 11.76  16.39 0.09  0.08  1.40  160                0.000

MSWI DMIN ITR NFM NWR NWS REMK
0.09 11.2   5   0   7   0

STA  DIST AZM  AN P/S W    SEC  CCOR (TOBS -TCAL -DLY  =RES) WT  XMG FMG R INFO
MTH   8.0 177 151 P    4  4.05 0.00  3.75  3.18 0.00  0.57 0.00            0.000
                  S    4  5.05 0.00  5.55  5.66 0.00 -0.11 0.00            0.000
AVL  11.2 137 141 P       3.07 0.00  3.07  3.47 0.00 -0.10 1.00            0.827
BOT  23.5  52 117 P       5.40 0.00  5.10  4.98 0.00  0.12 1.00            0.336
BMJ  26.0  29 113 P       5.60 0.00  5.00  5.33 0.00 -0.03 1.00            0.553
ASN  26.0 220 113 P       5.62 0.00  5.32  5.33 0.00 -0.01 1.00            0.818
ABV  30.1  87 109 P       5.70 0.00  5.40  5.93 0.00 -0.53 0.00            0.000
AMJ  32.7 155 106 P       6.75 0.00  6.45  6.32 0.00  0.13 1.00            0.378
BMU  45.9  74  83 P       8.57 0.00  8.27  8.36 0.00 -0.09 1.00            0.518
ASZ  57.4 170  89 P      10.40 0.00 10.10 10.16 0.00 -0.06 1.00            0.566
AMT  67.0 129  86 P    4 10.77 0.00 10.47 11.66 0.00 -1.19 0.00            0.000
MOE  85.5 124  83 P    4 15.85 0.00 15.25 15.03 0.00  0.22 0.00            0.000
                     S    4 26.35 0.00 26.05 26.75 0.00 -0.70 0.00            0.000
```

Fig. 4.29 – HYPOINVERSE report for event EL28.

0.02 s to 0.37 s. In the next section, this value will be compared with the likely traveltime errors arising from the limitations of the velocity model.

4.3.4 Analysis of the location errors.

When the traveltime curve for a source at the surface was modelled in section 4.3.2 and compared to the picks of the published refraction profiles (Figure 4.12), the scatter of the data around the predicted values was within ± 0.33 s. This corresponds to the situation when each ray travels through the shallow layers twice. For an earthquake source at depth, the shallow structures affect the rays only once and the estimate of the scatter may be halved. Hence, a value of ± 0.17 will be assigned to the typical error in traveltime due to shallow velocity heterogeneities not accounted for by the model.

Discrepancies between the real and modelled velocities at depth can also make significant contributions to the traveltime errors. In chapter 6 the tomographic inversion of teleseismic traveltime residuals will reveal that the vertically averaged p-wave velocity of the crust underneath the RESTE Network may vary laterally by as much as ± 5% and locally by more. If a ray travels a length l through a region where the velocity of the model has an error δv with respect to the true velocity v, the corresponding error in traveltime will be $\delta t = (l/v^2)\ \delta v$. For values l = 20 km, v = 6 km s^{-1} and $\delta v = 0.05v$, δt is 0.17 s. (The same traveltime error would arise from an error of 1 km in the estimate of the total length of the ray.) If the velocity anomaly were crossed by all the rays used in the location, it would lead to an inaccurate focal depth, but would have little bearing on the traveltime residuals (unless s-wave traveltimes with large weight were also used), for reasons discussed below. If one isolated ray were affected by such an anomaly, its traveltime residual could reach the value estimated above, apart from other contributions. That value is the same that was previously estimated for errors due to shallow heterogeneities, and the two could combine for a particular ray. A realistic upper limit of the error in traveltime due to the limitations of the velocity model is therefore $\delta t = \pm 0.24$ s. This value compares well with the RMS traveltime residual of 0.15±0.13 s obtained in the previous section, suggesting that the velocity model was in fact a major contributor to the location errors.

In the previous section, the standard timing error for first arrivals was estimated as ± 0.02 s. Now it is found that the error associated with the use of a horizontally homogeneous velocity model to predict the traveltimes can be as high as ± 0.24 s. In view of the uncertainties introduced by the velocity modeling the input data can be considered virtually error-free, with the exception of seismic traces contaminated by extreme noise (e.g., radio-interference, or very weak seismic signals). The error estimates for the locations of the RESTE events were obtained by equating the error in the input data with the geometrical average of the timing error and the RMS traveltime residual, although the contribution of the former was always insignificant.

The location tests using artificial sources were made with unfavourable conditions, both because the epicentre was outside the network and because the source was close to the surface. Even in those conditions, the location program gave reasonable results, albeit with large error margins, when s-wave arrival times were included in the data. It can be expected from the tests that with a stronger configuration, i.e., for an earthquake underneath the network, the program will provide accurate estimates of the position of the source. On the other hand, such locations would be more vulnerable to errors in the deeper parts of the velocity model, in particular regarding the depth estimates, and this possibility is not so easy to test directly. The velocity model used in connection with HYPOINVERSE has an average p-wave velocity of 5.9 km s^{-1} for the first 20 km of the crust, yet for some of the stations an average velocity of 5.5 km s^{-1} gave better results with the geometric method. It is therefore advisable to place an upper bond on the possible error in focal depth arising from unaccounted low velocity anomalies. To do this, a selection of local events were located three times each, first with the adopted velocity model and then after uniform variations of the velocities by -10% and (for completeness) +10%.

The epicentre of event EL01 was located well within the network, and the estimated depth was 20.0 km. This event was located with seven p-wave arrival times and three s-wave arrival times. When the velocities in the model were reduced by 10%, the position of the epicentre was displaced 1.3 km, and the source was located at a depth of 17.3 km, i.e., 2.7 km shallower. The horizontal and vertical errors were 1.0 km and 2.7 km respectively, and the RMS traveltime

residual, originally 0.17 s, became 0.34 s. These error margins do not encompass the previous solution, nor is this solution within the earlier error margins. With a velocity increase of 10%, the depth became 20.2±1.5 km, the horizontal error was 0.6 km and the RMS residual was 0.08 s.

The estimated depth of event EL05, also within the network and for which only two out of a total of seven arrival times were for s-waves, was virtually unaffected by the reduction of 10% in the velocity model. The value for the unperturbed model was 15.1± 1.1 km, and it was increased by 0.4 km. The epicentre migrated 2.9 km, and the RMS residual changed from 0.02 s to 0.09 s. When the velocities of the model were increased the depth became 15.5±1.8 km and the horizontal error became 0.9 km. The RMS residual was 0.09 s again.

For events EL22 and EL23 no s-wave arrivals could be picked, due to the vicinity of the recording stations. Depth estimates were 8.1 ±1.6 km and 19.7±8.6 km respectively. After reducing the velocities in the model by 10%, those values became 10.9± 1.5 km and 20.8±8.1 km. Variations in the RMS traveltime residuals were not significant, and had opposite senses. A faster velocity model led to depth estimates of 5.5±2.0 km and 14.7±8.1 km respectively, 2.6 km and 5.0 km shallower than with the adopted model.

The effects of the uniform variations of velocity upon the estimates of focal depths agree with the theoretical discussion at the end of section 4.3.1. Since a uniform variation of ±10% exceeds by far any error likely to affect the adopted velocity model, errors occurring in the depth estimates for the RESTE events, as a result of errors in the velocity model, will be considerably smaller than the artificial results obtained above and are therefore acceptable.

4.4 Magnitude estimates.

4.4.1 Richter's scale of local magnitudes (M_L).

The quantity that best describes the "size" of an earthquake is the seismic moment, defined by equation A17 (Appendix A). That equation cannot, however, be used for the computation of seismic moment for the RESTE events,

due to the lack of knowledge about the dimensions of the ruptured surface. Alternatively, seismic moment can be estimated from the displacement spectrum (e.g., Bullen and Bolt, 1985, p. 426). This requires the calibration of the seismic stations, a condition usually not met by microearthquake networks (Lee and Stewart, 1981). In fact, quantitative parameters such as seismic moment (or stress drop and source dimensions) are not particularly relevant to the applications of microearthquake surveys. It usually suffices to classify the earthquakes according to size using a coarser criterion. This option was also made regarding the RESTE Survey.

The routine procedure to measure the size of the earthquakes is to use some empirical scale based on quantities read directly from a seismogram, such as maximum trace amplitude or event duration. A large number of such empirical scales exist, and the one that will be adopted here is a variation of Richter's (1935) scale of local magnitudes (M_L).

The M_L scale is a means of comparing the amounts of energy released by different earthquakes, based on the inspection of the maximum amplitudes recorded by a standard instrument at a standard distance. Strictly speaking, it would only fulfil that role accurately for events with the same focus and the same source mechanism. Under these conditions, and assuming that the recording instrumentation has a linear response, the ratio between the maximum amplitudes of two seismograms at a particular station should be equal to the square-root of the ratio between the energies released by the two earthquakes. In practice, the use of Richter's M_L scale is extended to allow the comparison of earthquakes with different sources. The implicit assumption is that the ratio between the maximum recorded amplitudes of two earthquakes observed at equal (and varying) epicentral distances is a constant. In other words, the logarithmic plot of maximum amplitudes for a pair of earthquakes as a function of epicentral distance should be a pair of parallel curves. This is a very crude assumption, since in general the two events will have different source depths and different mechanisms, the wavefronts will be distorted by the heterogeneities of the medium and the instrument sites will have different geological conditions and will therefore respond differently to the seismic excitation. Despite its crude nature, the M_L scale is very useful because the amount of energy released by earthquakes covers

an immense range, and "even so rough a division separates it into a convenient number of levels" (Richter, 1935).

The Richter scale of local magnitude (M_L) is defined as the base 10 logarithm of the maximum trace amplitude, expressed in μm, with which the standard Wood-Anderson short-period torsion seismometer (natural period 0.8 s, statical magnification 2800 and damping constant 0.8) would register the earthquake at an epicentral distance of 100 km. Since it is assumed implicitly that the maximum amplitude ratio for two events does not vary with epicentral distance, any earthquake will register at a distance x with maximum amplitude A(x) verifying

$$\frac{A(x)}{A^*(x)} = \frac{A(100km)}{A^*(100km)}, \tag{4.14}$$

where (*) denotes some standard earthquake used as comparison. Richter (1935) selected as standard earthquake one that would have maximum amplitude 1 micron at 100 km if recorded with the standard seismometer, and tabulated the function A*(x). This was done by studying a small number of earthquakes (those of January, 1932) in Southern California, whose maximum amplitudes were plotted as a function of epicentral distance. Since the resulting curves were nearly parallel, a new curve was drawn passing through the point with coordinates (100 km; 1 micron) and adopted as A*(x). From (4.14), the local magnitude M_L of an earthquake recorded (with the standard seismometer) at a distance x with amplitude A (μm) becomes

$$M_L = log_{10}A(100km) = M^* + log_{10}A - log_{10}A(x). \tag{4.15}$$

The zero of the M_L scale was fixed by assigning a zero magnitude to the standard earthquake (M* = 0).

Besides those inherent to the definition of the M_L scale, other approximations have to be accepted if it is to be applied in a region other than Southern

California. Since the scale was devised empirically from observations in that region, results for other areas are not necessarily comparable (hence the adjective "local"). Equation (4.15) would give different results for events of the same size (in terms of released energy) in regions with different attenuation laws or different average source-depths, for example. At any rate, it can be argued that the formula may still be used with the standard A*(x), in which case the results for a particular region should only be compared between themselves. Finally, it must be stressed that even in Southern California independent estimates of the M_L magnitude of the same earthquake tend to agree within one logarithmic unit only, i.e., the minimum error associated with a local magnitude estimate is of about 0.5 units (Richter, 1935).

4.4.2 Application to the RESTE data.

In this section, the Richter local magnitudes of the local RESTE events will be estimated. All independent magnitude estimates (INMG) used the duration magnitude M_D, a scale calibrated to conform with M_L (Lee and Stewart, 1981), so the comparison of the overlapping estimates allowed the calibration of the RESTE estimates. The scale of duration magnitudes was not used directly because the RESTE events had in some cases low signal-to-noise ratio, and the estimate of the duration of those signals would not be accurate. The use of Richter's scale of local magnitudes will be made with the limited accuracy intrinsic to the method, discussed in section 4.1.3, further reduced by other sources of error specific to this application.

The amplitude to which the definition of local magnitude refers is the average of the maximum amplitudes of the two horizontal component seismograms, recorded with the standard instrument. In the RESTE experiment, the seismometers were different from the standard, which is a common situation. With calibrated instruments, the combined use of the two transfer functions allows the conversion of the recorded signal to that corresponding to the standard instrument. With uncalibrated instruments, the conversion has to be made by multiplying the maximum recorded amplitude by a constant scale factor. Because the RESTE instruments recorded the vertical component only, such scale factor

should convert maximum vertical component amplitude into the horizontal component amplitude that would have been recorded with the standard instrument. It is very unlikely that the ratio between the two quantities be constant irrespective of event or station, particularly since at the range of distances of this study the maximum amplitude corresponds to an s-wave phase, and shear waveforms are not accurately depicted by the vertical component alone. However, such proportionality will have to be assumed, adding coarseness to the estimates. It is only with the arguments already invoked in section 4.1.3 that the use of such an inaccurate procedure can be justified.

Figure 4.30 shows a logarithmic plot of the maximum amplitude (in arbitrary units) as a function of epicentral distance, for a sample of five RESTE earthquakes. Also shown is the standard curve A*(x) (section 4.1.3) of Richter (1935). It can be estimated from the figure that the scatter around the "theoretical" curves parallel to A*(x) is within one logarithmic unit, which was the intrinsic innaccuracy of the M_L scale given in section 4.1.3. This observation justifies the computation of local magnitudes for the RESTE events, despite all the sources of error already discussed.

In the absence of calibrated and corrected (Wood-Anderson) amplitudes, the formula for the computation of M_L magnitudes was re-written as

$$M_L = log_{10}A - log_{10}A^*(x) + k. \tag{4.16}$$

The constant k, which may be regarded as the logarithm of a scale factor to A(x), was determined by entering A(x) in arbitrary (yet fixed) units and equating (4.16) with magnitudes computed independently. Unfortunately, the RESTE events were too small to be reported by the seismological bulletins, and only four of them were recorded and analysed by the INMG. For those cases, duration magnitudes computed with the FORTRAN program HYPO71 (Lee and Lahr, 1975) were available. In the absence of alternatives, they were used to compute the constant k for several of the RESTE stations. Some of the RESTE events were digitized, and since the entire electronic chain from the seismometer to

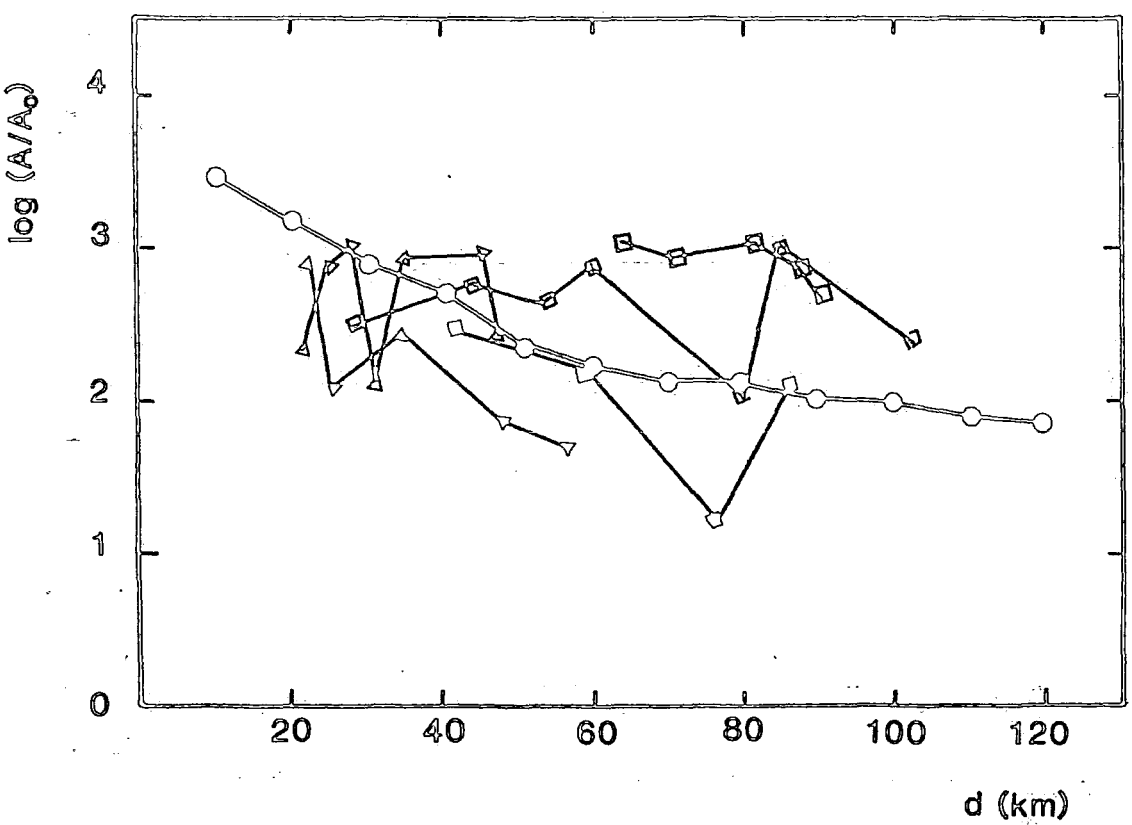

Fig. 4.30 - Logarithmic plot of maximum amplitude as a function of epicentral distance for five RESTE local earthquakes (thinner lines), and comparison with the function A*(x) of Richter (1935). Amplitude units are arbitrary.

Table 4.7

Ref. station	k	EL01	ER03	EL05	EL06
ABV	-5.2	2.6	3.0	-	-
AMG	-5.3	2.8	2.5	1.6	-
AVL	-5.3	2.0	-	1.5	2.3
ACA	-5.4	2.1	2.5	2.0	2.1
ASN	-5.4	1.6	2.6	-	-
AST	-5.2	2.5	2.1	-	2.2
.	.	2.3±0.7	2.4±0.6	1.7	2.2

the A/D converter had the same nominal specifications the units of the digital signals were used for the RESTE standard amplitude. For those events that were not digitized, a jet-pen seismogram with fixed gain was used to read standard amplitudes in mm. The constants k were calculated separately for each set of events.

The internal consistency of the local magnitude estimates for the RESTE events was tested by computing repeatedly the magnitude of the same event using different stations. The event ER02, with duration magnitude 3.1 (INMG), was used to compute the "scale factor" k for six stations, and the M_L magnitudes for two other events were then calculated repeatedly. The results are given in Table 4.7. The standard errors, taken as the maximum deviation from the mean, have values of 0.6 and 0.7, in good agreement with the inherent inaccuracy of local magnitude estimates.

Station AMG was adopted as the reference station for magnitude estimates, and the values obtained by the process described above were included in Table 4.6. They suggest that the detection threshold of the RESTE Network corresponds to a local magnitude of about $M_L = 1.0$. The threshold of felt events (onshore only) was between $M_L = 3.1$ and $M_L = 3.8$, which is a sensible result.

4.5 Source mechanisms.

4.5.1 The double-couple model of the earthquake source.

When the displacements at the free surface are observed at several points around the epicentre, and provided that the coverage in azimuth and range is good, the kinematics of the earthquake source can be inferred from the distribution of polarities (compression/dilatation) of the p-wave first motions. This practice is based on the important result that slip on a buried fault is dynamically equivalent, from the viewpoint of the radiated waves, to a distribution of double couples of forces on the surface of the fault. This is the "double couple" model of the earthquake source, and its theoretical justification is given in Appendix A. The displacement field predicted by this model (equation A22) is compatible with the common observation that seismic radiation patterns have

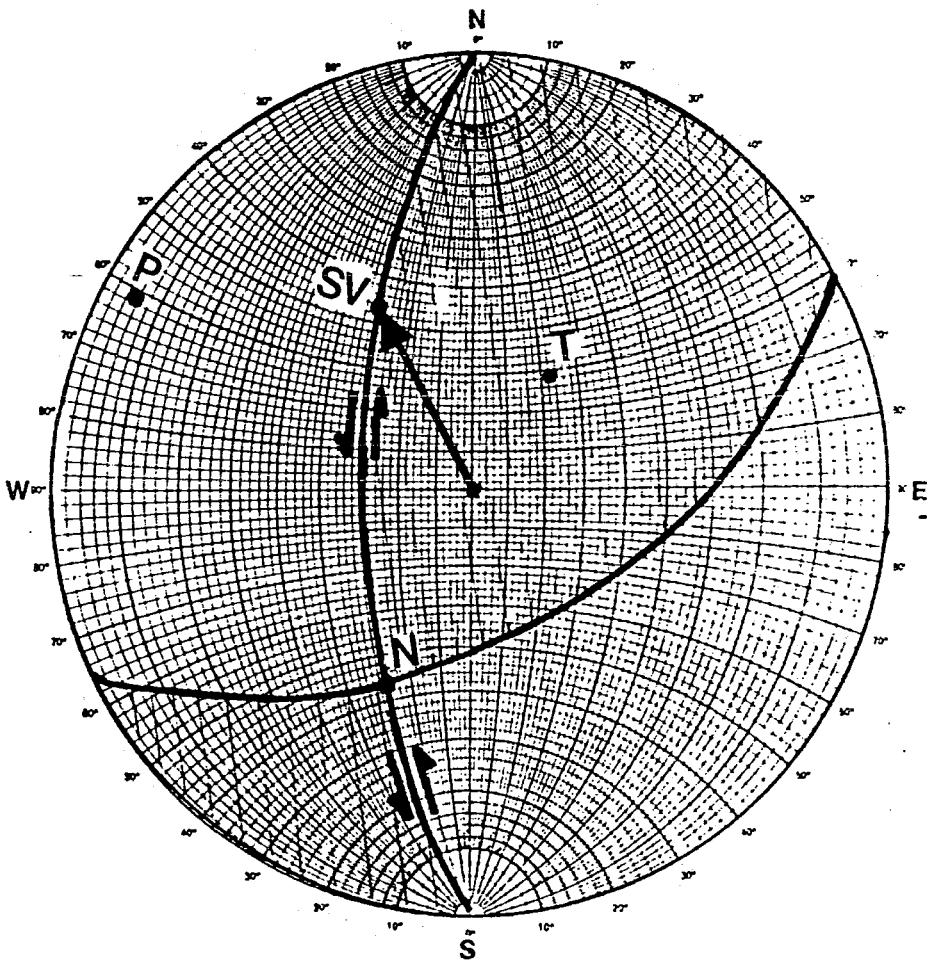

Fig. 4.31 - Radiation pattern of a double-couple earthquake, plotted on a Wulff stereonet (upper hemisphere projection). The fault plane strikes N-S and dips 30° towards the W. The arrow indicates the slip vector (SV), with azimuth 330° and making an angle of 40° above the horizontal. P, T and N indicate the P-axis, the T-axis and the null axis respectively. The type of movement is sinistral strike-slip with a component of reverse faulting (oblique slip).

a quadrantal distribution of the polarities of p-wave first motions, the compressional (away from the source) and dilatational (towards the source) quadrants being separated by two nodal planes. Figure 4.31 exemplifies the geometrical relationship between dilatational and compressional quadrants, fault plane, auxiliary plane and direction of slip. One of the nodal planes coincides with the fault plane, and the other is prependicular to the direction of slip and is called the "auxiliary plane". The intersection of the two nodal planes is the "null axis". The direction that bissects the compressional quadrants and is orthogonal to the null axis is the T axis, and the P axis is defined similarly for the dilatational quadrants. *If* the medium obeyed Coulomb's criterion of failure, the P and T axes would correspond to the directions of maximum and minimum compressive stresses respectively.

Since seismic waves are usually observed at the free surface, the first motion polarities must be traced back along the corresponding ray-paths and projected onto a small sphere surrounding the source, before the radiation pattern can be analysed. This stage should correct the distortions caused not only by the mapping onto the bi-dimensional free-surface but also by the bending of the rays due to velocity heterogeneities. The focal sphere can in turn be plotted using one of several projections, the most commonly used being the Wulff stereographic projection and the Schmidt equal-area projection (Lee and Stewart, 1981).

4.5.2 Application to the RESTE data.

In this section, the methodology described in section 4.1.1 will be used to investigate the kinematics of the faulting associated with the local RESTE events. Because the levels of released energy were low, often a microearthquake was clearly recorded at a small number of stations only, and an individual fault plane solution could not be obtained. To circumvent this difficulty, events occurring closely in space, and sometimes also in time, were used jointly whenever this would lead to a coherent pattern of polarities. The ambiguity between auxiliary plane and fault plane was alleviated by the use of the independent knowledge about the structural trends of the region. The azimuth and take-off angles at the focal sphere were read from the printed output of the location program HYPOINVERSE.

Figure 4.32 shows the joint solution for the microearthquakes EL01 (23JUL87) and EL05 (14OCT87), with $M_L = 2.3$ and 1.6 respectively (next section). These events, with source depths of 20.0±1.6 km and 15.1±1.1 km and epicentres ca. 12 km apart, can be interpreted as normal faulting on a high-angle fault dipping 70^o towards the NW and with strike 030^o. This interpretation is supported by the fact that the strike coincides with that defined by the two epicentres. Alternatively, normal faulting on a low-angle fault with 30^o of dip and the same strike as above is also compatible with the first motion data, if the roles of auxiliary plane and fault plane are interchanged. The former interpretation is in better agreement with the positions of the sources, and is also consistent with the dominant geological trend of the region.

Figure 4.33 gives two alternative joint solutions for the events EL22 (21JAN88; $M_L = 1.4$) and EL24 (26JAN88; $M_L = 1.5$). One solution involves reverse faulting and the other strike-slip faulting. Besides being close in time, these microearthquakes had very close epicentres. The prefered interpretation is reverse faulting on a fault dipping 70^o towards the SE and with strike 030^o, since this strike coincides with that of the previous solution and also with the trend defined by the four events discussed so far. These joint solutions are still coherent if the polarities observed for the event EL26 (30APR88) are included. For different choices of auxiliary plane and fault plane, the alternative interpretations are thrusting on a fault dipping 20^o towards the NW (first solution with steep auxiliary plane) , sinistral strike-slip on a N-S vertical fault or dextral strike-slip on an E-W fault with a gentle dip towards the N (second solution).

The event in Figure 4.34 was a macroearthquake of duration magnitude 3.8, felt with maximum intensity IV modified Mercalli (INMG, unpublished data). The first motion data indicates clearly a strike-slip mechanism, which depending on the choice of fault plane may be either sinistral on a vertical fault with strike 015^o or dextral with strike 285^o. The first hypothesis is favoured, because it corresponds to the dominant orientation of the Hercynian basement faults (the depth of the source was 16.4±1.4 km).

Finally, Figure 4.35 shows the first motion data for events EL26 and EL27, with M_L magnitudes 2.9 and >3 respectively, located slightly to the W of the

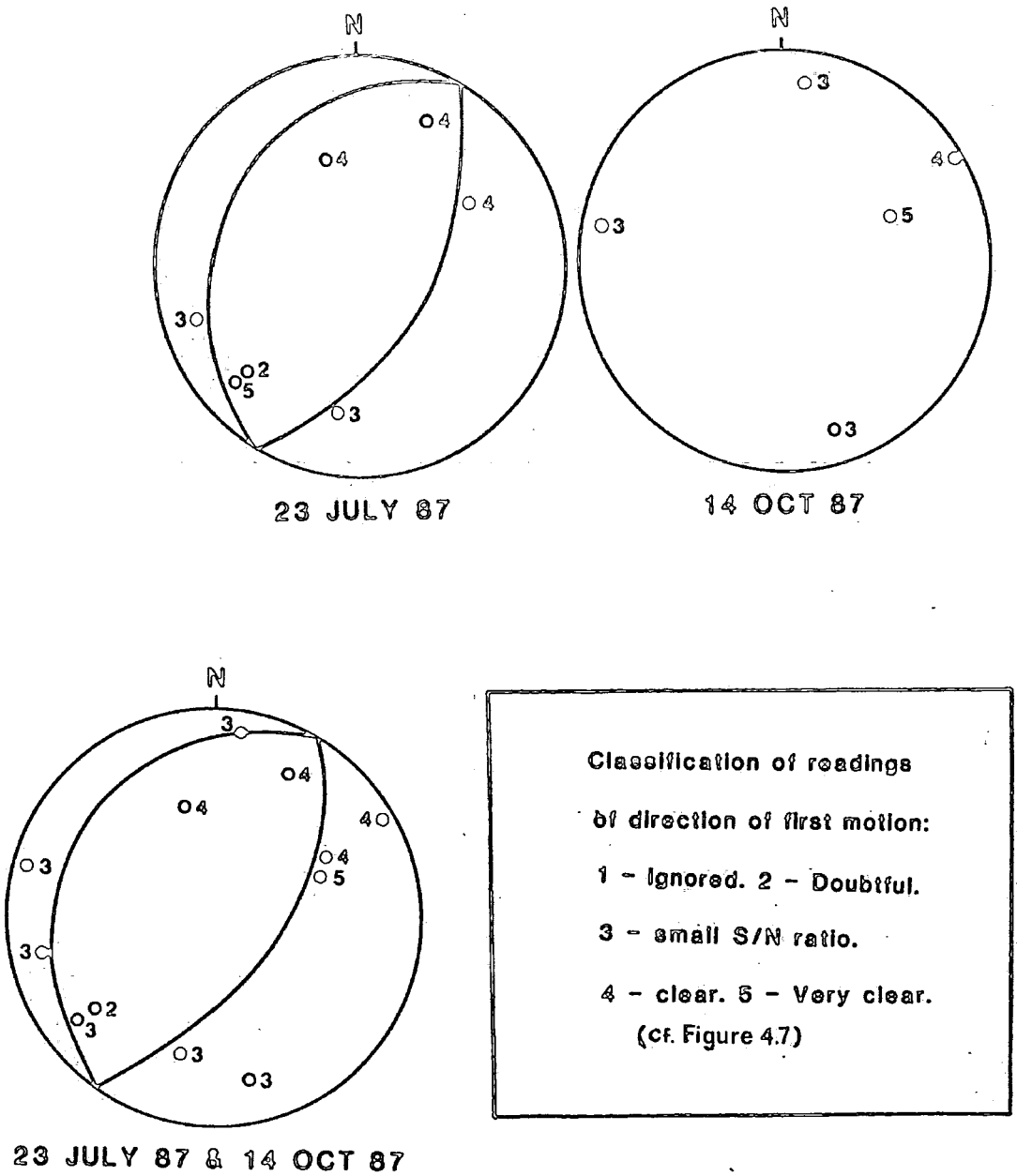

Fig. 4.32 - First motion data for events EL01 and EL05, and joint interpretation. Event EL05 is very poorly constrained, and may correspond to a different direction of faulting. This joint solution was favoured because the strike of the fault plane coincides with that defined by the epicentres.

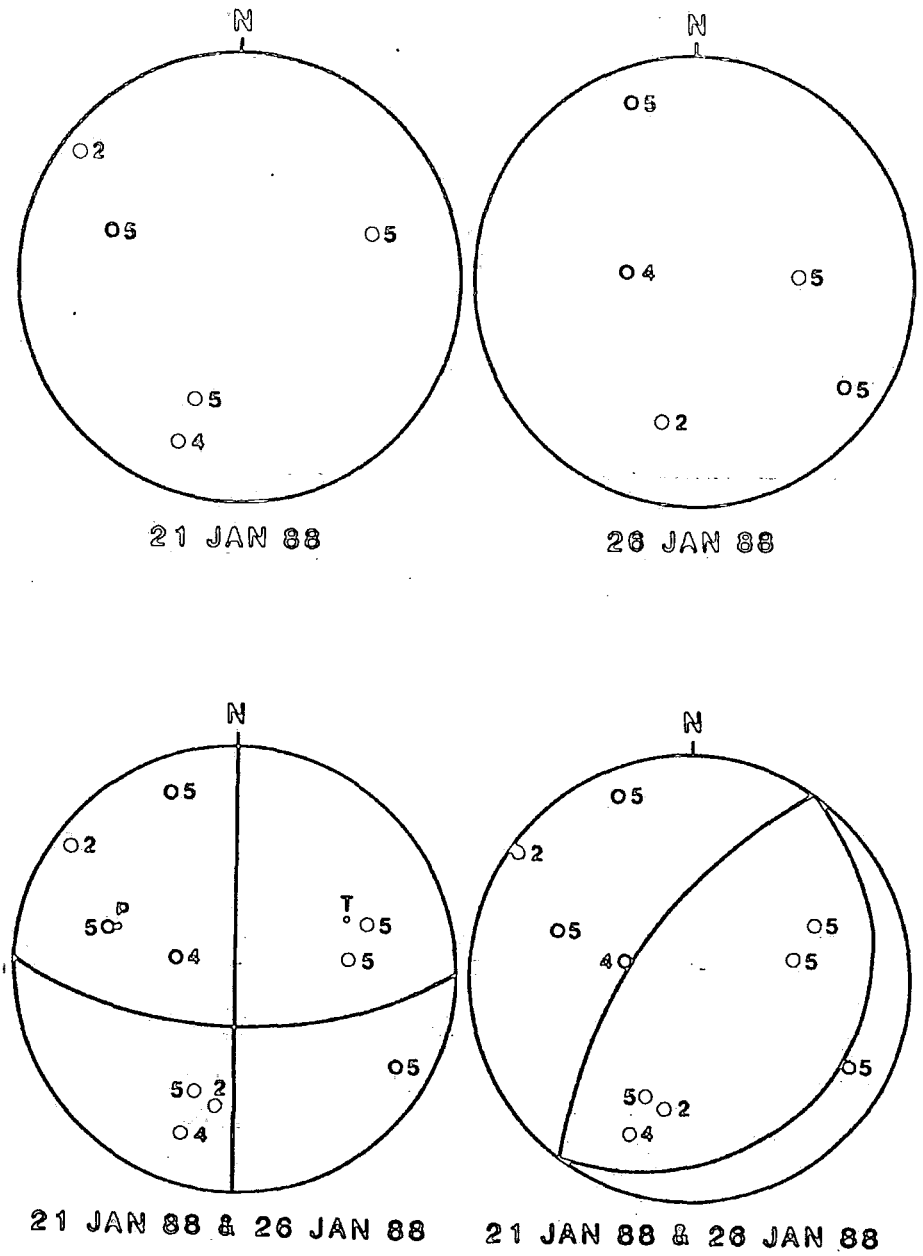

Fig. 4.33 - First motion data for events EL22 and EL24, and two alternative joint interpretations. The solution involving reverse faulting is prefered, because the strike of the fault plane coincides with that defined by the four epicentres along the Lower Tagus Valley (Figure 4.36).

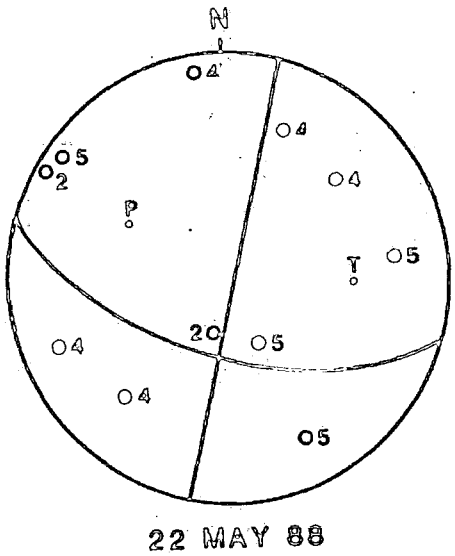

Fig. 4.34 - First motion data for event EL28, and interpretation.

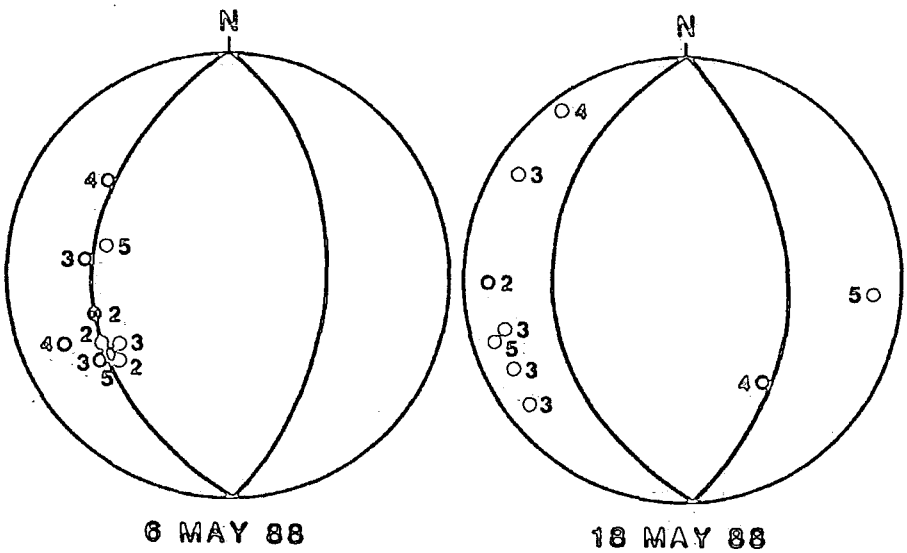

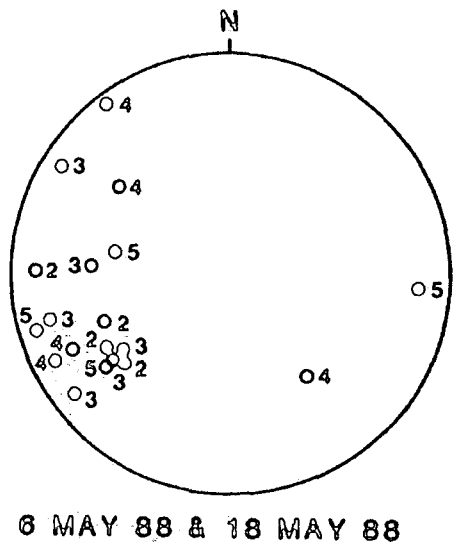

Fig. 4.35 - First motion data for events EL26 and EL27, and tentative interpretation.

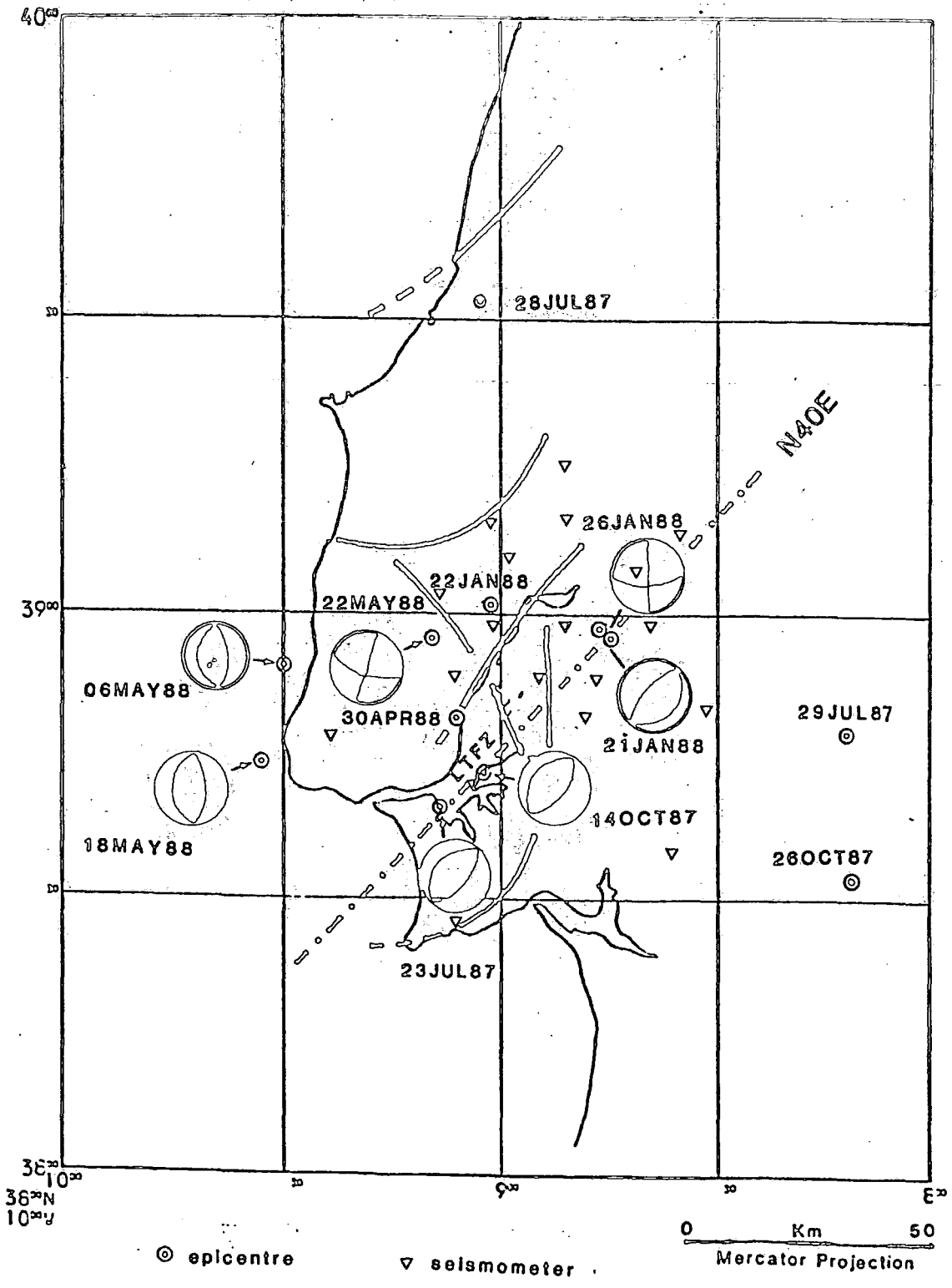

Fig. 4.36 - Epicentres and focal mechanisms of the local earthquakes recorded with the RESTE Network.

network. Although the focal mechanisms for these events are very poorly constrained, as is always the case when the epicentre is not surrounded by stations, the clustered data for the first event seem to delineate a nodal plane, and jointly with that of the second event the data are compatible with dip-slip movement on a fault striking N-S, either dipping 30^o towards the W or 60^o towards the E. If this was the case, the movements could have taken place on the same fault but with a different sense of dip-slip for each event, normal for the first and reverse for the second.

Although it was in general possible to fit the data with double-couple solutions with a minimum number of polarity violations, the predicted near-zero amplitudes close to the nodal planes were not always observed. Velocity heterogeneities, responsible for the distortion of the ray-paths, are the likely causes of these discrepancies.

Figure 4.36 shows the spatial distribution of the several source mechanisms obtained above.

4.6 Tectonic implications of the seismicity of the Estremadura.

4.6.1 Crustal structure.

The understanding of intraplate neotectonics requires the close interplay of structural geology and seismological observation. Most interplate seismogenic faults are not associated with surface rupture (Blenkinsop et al., 1986; Zoback et al., 1986; Long, 1988; Talwani, 1989), and this is particularly relevant in areas covered by sediments. In the Lusitanian and Lower Tagus Basins the existence of a thick evaporitic layer near the bottom of the sedimentary column provides an effective detachment level, where the deformation at depth can be decoupled from that of the shallow cover. This fact has to be taken into account when studying the neotectonics of the region.

The historical seismicity of the Estremadura is clear evidence that some form of tectonic process is presently active in the area. Since the region is covered by sedimentary basins, studies of the surface geology do not provide all the elements needed to locate the active structures and to characterize the style of the active

tectonics. The microearthquake data presented in the previous section are the first set of accurate seismological information for the region of the Lusitanian and Lower Tagus Basins. In this section, its tectonic implications will be discussed, taking note that it is a limited data set, acquired over a limited period of 11 months, and that more elaborate conclusions would and should be drawn from more extensive surveys of this nature.

The surface geology of the Lower Tagus Basin shows no direct sign of the active geologic structure or structures responsible for the large magnitude historical Benavente earthquakes (section 4.2). Yet this strong seismicity proves that the Lower Tagus Valley is associated with one or more important active faults. Small-scale reverse faulting affecting Plio-Quaternary formations, reported by Cabral et al. (1984) on the coastal cliffs S of the Tagus mouth, are the only satisfactory evidence of neotectonic deformation at the surface of the basin. A commercial seismic reflection profile parallel to the coast across the Lower Tagus Basin, already mentioned in section 2.3.6 (section Ca1-81, GPEP unpublished data; Figure 2.11), shows onlap of Mid Miocene and younger sediments on Lower Miocene strata towards the northern boundary of the basin and, less clearly, along its axis. It can be concluded that those regions were uplifted after the Mid Miocene, but since the section is not clear at very shallow levels it cannot be established whether or not the instability continued into the Quaternary. It is nevertheless worth noting that the uplifted region near the axis of the basin coincides with the region where the neotectonic reverse faulting was observed at the surface.

The clearest result of the RESTE microearthquake survey is the existence of a NE-SW seismic lineament to the S of the Tagus River (Figure 4.36). As discussed in the previous section, the first motion data for the four aligned events is compatible with faulting along the direction defined by the epicentres. This also coincides with the orientation of one of the dominant Hercynian trends. Furthermore, comparison between Figure 4.36 and Figure 1.4b) shows that the lineament is along the strike of a major Hercynian strike-slip fault, exposed to the NE of the Lower Tagus Basin, where according to Dias and Cabral (in press) it controlled the localized deposition of Quaternary sediments. It is however impossible to trace such faulting continuously towards the boundary of the basin

(Cabral, pers. comm.). The extrapolation of the seismic lineament cuts the shoreline near the area where the deformation of the sedimentary layers was observed, both on a seismic section and at the surface. Towards the SW the lineament is continued by the Cascais Submarine Valley (Figure 1.4 b), a fault-related structure of the continental shelf (Vanney and Mougenot, 1981). In view of this continuity, the seismic lineament is interpreted as the buried connection between the two structures.

The hidden basement fracture proposed above was already suggested by Arthaud and Matte (1975) in a study of the Late Hercynian tectonics, and the onshore continuation of the Cascais Submarine Valley as a "zone of weakness" along the Tagus Valley had already been proposed by Freire-Andrade (1938). Both classic (Choffat, 1907) and more recent studies already referred in section 2.3.7 have proposed the existence of a deep basement active fault associated with the Lower Tagus Valley. This "Lower Tagus Fault" would form the northwestern limit of the Lower Tagus Basin (Carvalho et al., 1983; Cabral et al., 1984), and its trend differs by about 10^o (counterclockwise) from that of the seismic lineament discussed above.

The seismic data presented here are the first evidence of the existence, and the proof of the activity, of a fracture of crustal scale along the Lower Tagus Valley. According to the interpretations proposed for the focal mechanisms, the along-dip component of movement changes polarity along strike, a feature characteristic of small earthquakes on strike-slip faults (Nicholson et al., 1986; Talwani, 1988). It is therefore proposed that under the present stress field the Lower Tagus Valley is the locus of strike-slip deformation on a reactivated concealed Hercynian fault, with orientation 040^o as indicated by the microearthquake epicentres. The designation of "Benavente Fault" is proposed for this active structure (Figure 4.36).

The relationship between the Benavente Fault and the shallow geological structures observed in the Lower Tagus Basin could hardly be a direct one, in view of the effective mechanical decoupling provided by the thick evaporitic layer that underlies the bulk of the sedimentary cover (section 2.2.2). Moreover, strike-slip faults tend to splay upwards at shallow levels into "flower structures",

generating a complex pattern of braided faults separating compressive and dilatational compartments (Wilcox et al., 1973; Crowell, 1974; Rodgers, 1980). Block rotations are also common in areas of strike-slip deformation, and the resulting space problems lead to a variety of shallow structures ranging from normal faulting to thrusting, all within the same area (Nicholson et al., 1986; Molnar, 1988). In section 2.4, it was argued that the shallow structure of the Lower Tagus Valley is compatible with Miocene strike-slip tectonics, and the system of faults that cut across the sediments were then regarded as a releasing bend on a sinistral shear zone (Figure 2.9). This configuration can now be related to the activity of the Benavente Fault.

Buried strike-slip faults that do not develop throughgoing fracture at the surface are usually associated with oblique secondary (Riedel) shears that in three dimensions have an helicoidal shape (Sylvester, 1988). The Vila-Franca Fault and the Arrábida Thrust, together with the Alcochete Fault Zone, could form such a configuration if they joined at depth a single basement fault, as depicted in Figure 4.37. The results shown in Figure 4.38, where the selected focal planes of the Lower Tagus Valley microearthquakes are extrapolated to intersect the surface, suggest that this may be the case. However, the detailed mapping of the fault surface at depth requires the monitoring of the seismic activity over a much longer period of time.

Alternatively, the faults that cut through the sedimentary basins could correspond in a more direct manner to several basement fractures. In view of the comments already made on the likelihood of existence of an effective detachment between basement and cover, it is preferable to use the seismicity rather than the internal structure of the basins to infer the underlying structure. This choice may lead to an underestimate of the degree of fracturing of the basement, but will prevent an inflated assessment of potential neotectonic structures.

Because the RESTE earthquakes had very low magnitude, it is not appropriate to infer from their focal mechanisms the current kinematics of the associated faults (with the possible exception of the $M_L = 3.8$ event of 22MAY88). Such small events are usually local readjustments to previous episodes of deformation, and the corresponding motions may eventually oppose the dominant direction

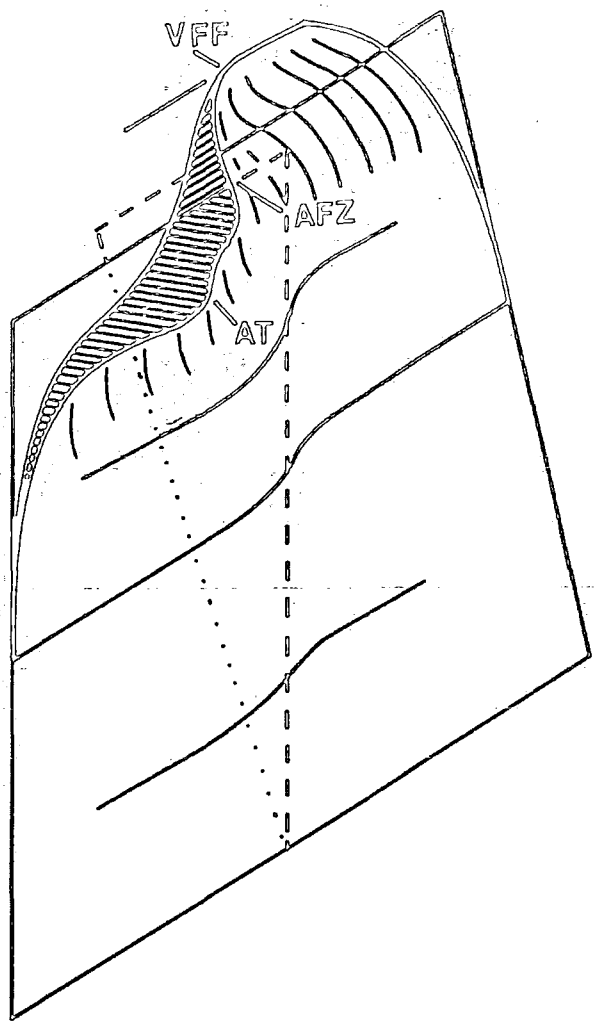

Fig. 4.37 - Possible configuration of the Benavente Fault at depth, and speculative relation to the Arrábida, Alcochete and Vila Franca Faults.

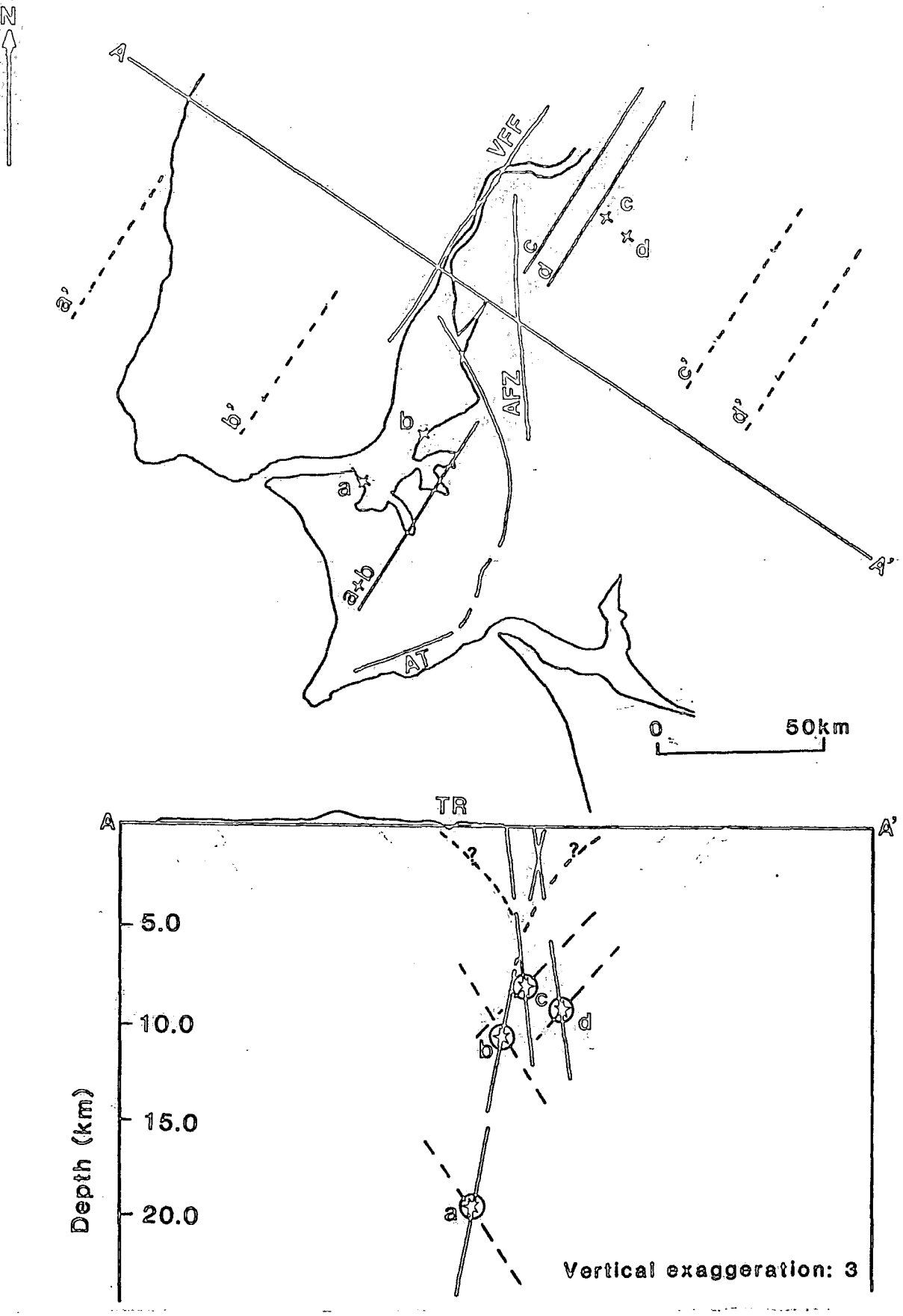

Fig. 4.38 - Comparison between the shallow faulting and the extrapolated fault planes of the microearthquakes along the Lower Tagus Valley. Assuming that the dips of the faults increase with depth and have different orientations on the two sides of A-A', it is possible to relate the seismogenic fault planes to the surface structures.

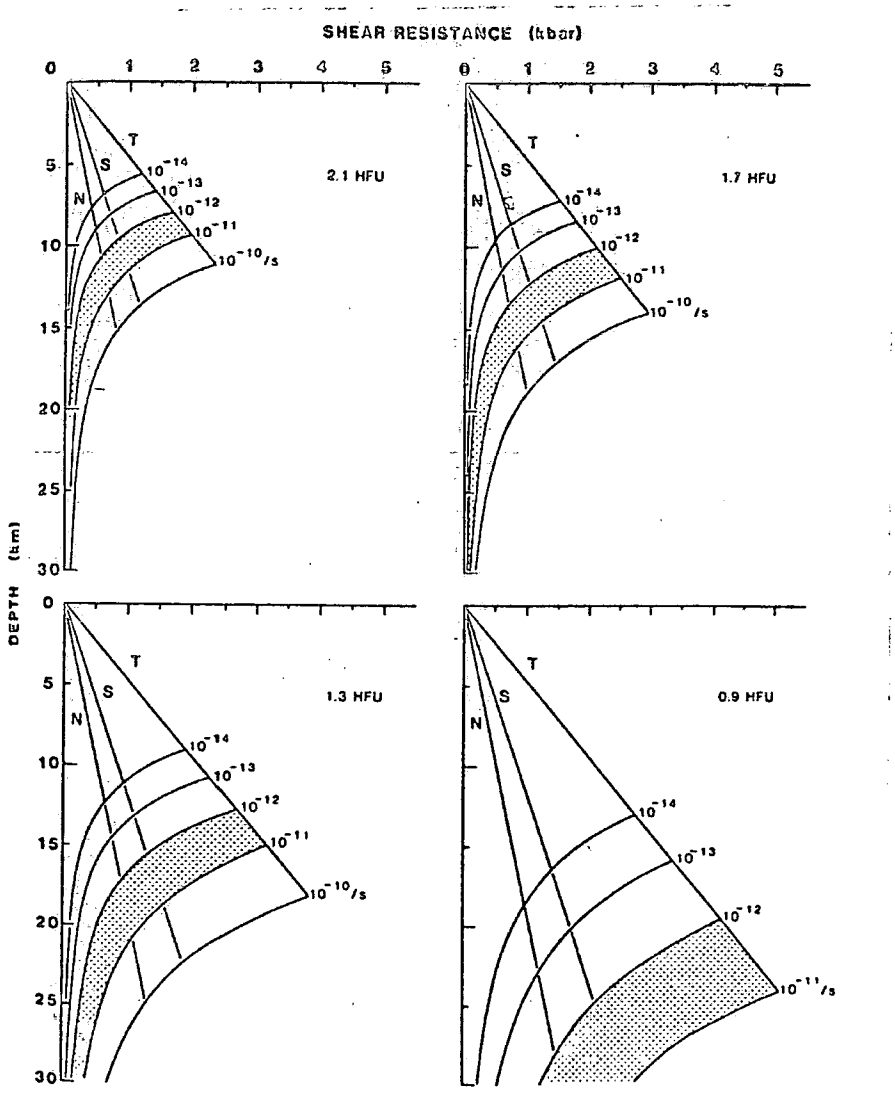

Fig. 4.39 - Sibson's (1983) theoretical profiles of shear resistance versus depth, for different values of heat-flow and strain rate, and for different types of faulting. 1 HFU = 41.8 mWm^{-2}.

of slip. It is only indirectly that such features as the along-strike reversal of the vertical component of slip or the coexistence at the same region of different types of movement can be interpreted as being diagnostic of strike-slip deformation. Regarding the polarity of strike-slip motion, it can only be advanced that in view of a history of sinistral strike-slip during the Miocene, and since no radical changes of the plate tectonic setting have occurred since then, this same type of motion is the most likely to be associated with the current deformation. This is supported by the fact that the only macroearthquake registered during the RESTE Survey is compatible with the assumption of sinistral strike-slip along the NNE-SSW Late Hercynian trend.

The deep (16.4±1.4 km) earthquake of 22MAY88 (M_D=3.8) is interpreted as sinistral strike-slip on a separate NNE-SSW buried fault, for which no direct evidence can be found at the surface. It is reasonable to assume that the density of basement faulting underneath the sedimentary basins is similar to that observed in the exposed basement, and several faults can be expected to have been reactivated, in view of the historical seismicity. For example, the Setúbal Earthquake of 1858 originated in an area where the continental shelf is cut by a submarine valley, suggesting the existence of another concealed basement fracture sub-parallel to the Benavente Fault.

The range of depths at which the microearthquake activity is taking place shows clearly that the neotectonics of the Estremadura involve at least the full thickness of the upper crust, and in some cases extend to the lower crust. The rheological implications of this observation will be considered in the next section. As far as the RESTE data are concerned, there is no evidence to support the existence of a mid-crustal detachment limiting the vertical extent of the faults.

Based on the study of a number of faults in different environments, Leminsky and Brown (1988) conclude that a mid crustal detachment usually limits the vertical extent of intraplate strike-slip faults, whereas strike-slip faults that cut across the entire crust are characteristic of intracontinental plate boundaries.

The RESTE hypocentral data (and also the tomographic study of chapter 6) suggest that the faults of the Estremadura may extend through the entire

thickness of the crust. Although the current level of deformation is not compatible with the existence of a plate boundary in the region, the criterion of Leminsky and Brown (1988) may still be valid if the Miocene tectonics of the Estremadura (section 1.5.2) are taken into account. Together with the Central Cordillera of Spain, the mountain ranges of the Estremadura and those of eastern Portugal could have been part of an intracontinental transform during that period, separating Iberia into two microplates.

A structure of crustal blocks separated by deep basement faults could lead to a complex pattern of earthquake migrations, as the movement of one particular block would disturb the state of those adjacent to it and induce new earthquakes at their boundaries. More importantly, such configuration could lead to specific patterns of foreshocks for the larger events. Although the set of the RESTE events is too short to be representative, it seems very probable that the earthquakes of 30APR88, 06MAY88 and 18MAY88 had some precursory relationship to the larger ($M_D = 3.8$) event of 22MAY88. If this assumption is correct, the pattern of migration of the epicentres, jumping distances of several tens of kilometres, should be related to the dynamic interaction between adjacent crustal blocks. Only a continuation of the RESTE experiment over a longer period of time would allow the adequate study of this hypothesis, which may have a potential for application to earthquake prediction studies.

4.6.2 Crustal rheology.

One of the interesting aspects of the hypocentral data given in the previous section is the range of depths at which the microearthquakes occur. Seismicity in intraplate areas is usually restricted to the upper crust, typically between 5 km and 15 km of depth. The maximum depth reached by the earthquakes is dependent on the geothermal gradient (hence on the age and tectonic history of the lithosphere) and on the rate and style of deformation (Sibson, 1982, 1983; Chen and Molnar, 1983; Kusznir and Park, 1984; Meissner and Wever, 1986; Dewey et al., 1986). The uppermost mantle of many intraplate regions is also seismically active, but the lower crust is generally aseismic (Sibson, 1982; Chen and Molnar, 1983). This widely recognized feature of the lithosphere has been explained with rheological models that emphasize the control of the deformation

by the temperature-dependent rheology of the quartz in the crust and that of the olivine in the uppermost mantle (Meissner and Strehlau, 1982; Sibson, 1983; Kusznir and Park, 1984; Figure 4.39).

Comparison of seismological and heat-flow data indicate limiting temperatures between 250°C and 450°C and between 600°C and 800°C for brittle failure in the crustal and mantle rocks respectively (Chen and Molnar, 1983). Above these temperatures, ductile deformation takes over as the response to applied stresses. With the exception of regions of abnormally low geothermal gradient, these values explain the existence of a ductile lower crust. Because the shear strength at shallow levels is pressure-controlled, it increases with depth until a maximum value is reached, originating the brittle seismogenic layer that has been identified in most areas of intraplate seismicity. Below that level ductile deformation becomes dominant as a consequence of the increase in temperature. Since large earthquakes imply the storage of large amounts of strain energy, they are likely to nucleate where the shear strength of the crust reaches a maximum. This is verified in practice, since there is a good correlation between the mid-crustal peak of shear strength and the depth of the largest intraplate earthquakes (e.g., Sibson, 1982).

Once the lithosphere starts undergoing deformation, its rheological stratification may lead to important amplifications of the applied stresses at certain levels (Kusznir and Bott, 1977). This effect was modelled numerically by Kusznir and Park (1984) for different tectonic regimes and different geothermal gradients. In the case of a high heat-flow (Basin and Range type) lithosphere subjected to an average compressive stress of 20 MPa (the normal range of intraplate compressive stresses being estimated by the authors as 0 - 25 MPa), the model predicted amplifications of the applied stress by a factor of x8 to x11. The maximum amplifications occurred in the upper crust (0 - 15 km of depth) and were induced by the complete stress decay in the ductile lower crust. Despite this effect, the modeling indicated that geologically observable deformation was unlikely to occur in an intraplate compressive setting, with the exception of regions with either large heat-flow (above 80 mW m^{-2}) or a particularly weak crust due to previous fracturing.

The hypocentral data given in the previous section, although too short to be statistically representative, shows that in the Lower Tagus Valley the seismicity can extend to depths of the order of 20 km. Moreira et al. (1980) use a mid-crustal boundary at depths of 16 km and 19 km to interpret a pair of refraction profiles along the western flank of the onshore Lusitanian Basin, and Mendes-Victor et al. (1980) modelled the same refractor as an undulated interface with depths ranging between 15 km and 25 km (Figure 2.5). If this interface is taken as the upper limit of the lower crust, two of the events observed during the RESTE Survey (EL01 and EL23) took place probably within this crustal unit, albeit in its upper part. This fact will now be discussed in connection with the limited available data on the thermal state of the lithosphere.

Accurate heat-flow data for the Lusitanian and Lower Tagus Basins is non-existent. However, bottom-hole temperatures measured on commercial exploration wells have been used to estimate the heat-flow, leading to values of the order of 80 mW m^{-2} and higher (Camelo, 1988). For comparison, the Basin-and-Range province of the United States, characterized by a strong geothermal gradient, has heat-flow values in the range 71.4 mW m^{-2} to 88.2 mW m^{-2} (Sibson, 1983). The occurrence of thermal springs within the Lusitanian Basin is another indication of heat-flow levels above the average for continental crust (Ribeiro and Almeida, 1981). Although the available data for the Lusitanian Basin has to be used with caution, it seems reasonable to dismiss the hypothesis of a low lithospheric temperature as the reason for the deep seismicity. Furthermore, the fact that the Lower Tagus Valley is tectonically active in a compressive tectonic setting is another argument in favour of a high heat-flow regime, according to the earlier remarks concerning the modeling of lithospheric deformation. But if the vertical profiles of shear strength depicted in Figure 4.39a) or b) applied in this region, the ductility of the crust below 15 km would probably prevent the occurrence of the events observed at a depth of about 20 km.

In the area of the RESTE Survey, there are no reliable estimates of depth for the large earthquakes of the past. The Benavente Earthquake of 1909, in the Lower Tagus Valley, is sometimes described as very shallow, on account of the rapid decay of seismic intensities away from the epicentre, but this observation is more likely to be due to site effects related to the distribution of alluvial deposits

in that region. Two of the RESTE microearthquakes (EL22 and EL24), with local magnitudes 1.4 and 1.5, were located close to the epicentral region of the historic event, and had depths of 8.1±1.6 km and 9.4±3.7 km. More likely the large (estimated $M_L = 6.7$) historical earthquake was located close to the brittle-ductile transition, below the level of the microseismic activity now observed.

The event EL01 (23JUL87; $M_L = 2.3$) had a depth of 20.0± 1.6 km. If projected laterally onto the refraction profile of Mendes-Victor et al. (1980), it plots in an area where the interpreted Moho reaches a minimum depth of about 25 km and the mid-crustal refractor is about 15 km deep (the hypocentre is 50 km distant from the section, but the projection is parallel to the dominant structural trend). The event seems therefore to be located within the lower crust, in which case the "rule" of lower-crustal aseismicity was violated.

The event EL28 (22MAY88; MD=3.8) occurred at a depth of 16.4±1.4 km, in an area where the Moho depth is, according to the refraction models discussed in section 2.1, of the order of 30 km, and the mid-crustal boundary is close to 18 km. Although the source was probably above the mid-crustal refractor, its depth would be excessive if a heat-flow value of 80 mW m^{-2} were to apply (cf. Figure 4.39a). Together with event EL01, this earthquake suggests that the widely observed depth distribution of seismicity in intraplate continental crust and its relation to the level of heat-flow may not apply in this particular region.

If the above discussion can be taken one step further, it is tempting to speculate on the link between an hypothetical abnormal rigidity of the lower crust underneath the Lusitanian Basin and the process of magmatic underplating suggested in section 3.4 for the evolution of the passive margin at the Jurassic/Cretaceous boundary. Although several studies have been published recently on the velocity structure, thermal properties and petrological characteristics of underplated crust (e.g., Furlong and Fountain, 1986; McKenzie and Bickle, 1988), its influence on the vertical distribution of seismicity in continental crust seems to be as yet unassessed. If a contrast in mechanical properties is likely to occur at a depth corresponding to the transition between "normal" and underplated lower crust, then the mechanism of stress amplification (Kusznir and Park, 1984)

might propitiate the conditions for the occurrence of earthquakes at depths that would be aseismic in the absence of the underplated layer.

During the operation of the RESTE Network, several teleseisms were recorded for which preliminary hypocentral parameters were released in useful time. The investigation of the delays suffered by these waves as they approached the different stations can be used to gain information on the broad velocity anomalies of the lithosphere underneath the network. This study, using the technique of tomographic inversion, will be undertaken in chapter 6, as a further contribution to the constraint of the structural characteristics of the Estremadura. Before that, the next chapter is a reappraisal of the current plate tectonic setting of Iberia, within which the seismotectonics of the Estremadura has to be integrated. Since it was claimed already that no drastic changes have occurred in the plate tectonic framework of the Peninsula since the collision with Africa in the Miocene (section 1.5.2), it is adequate to start the next chapter with a critical overview of the Cainozoic evolution.

Então, a Península Ibérica moveu-se um pouco mais, um metro, dois metros, a experimentar forças. ... Houve depois uma pausa, sentiu-se passar nos ares um grande sopro, como a primeira respiração profunda de quem acorda, e a massa de pedra e terra, coberta de cidades, aldeias, rios, bosques, fábricas, matos bravios, campos cultivados, com a sua gente e os seus animais, começou a mover-se, barca que se afasta do porto e aponta ao mar outra vez desconhecido.

J. Saramago, in *A Jangada de Pedra.*

Chapter V

The Tectonics of Western Portugal within the context of the Geodynamics of Iberia

5.1 A new model for the Cainozoic Plate Kinematics of Iberia.

5.1.1 Tertiary Tectonics of Iberia.

In section 1.5.1 the evidence in support of an Early Cainozoic plate boundary through the Bay of Biscay and the Pyrenees was discussed. Klitgord and Schouten (1986) take the argument one step further to conclude that Iberia was an integral part of the African Plate until Mid Oligocene, when it was sutured to Eurasia by the Pyrenean continental collision. But since the movement of Africa relative to Eurasia during the Early Cainozoic was directed towards the NNE (Dewey et al., in press), the SE-NW direction of movement between Iberia and Europe given by Grimaud et al. (1982) indicates a considerable degree of independence between Iberia and Africa, with a nearly westward motion of the former with respect to the latter (Figure 1.7). The movement of Iberia towards the W, to avoid excessive lithospheric thickening due to the convergence between Africa and Eurasia, would be compatible with the principles of extrusion tectonics (Molnar and Tapponier, 1975; Tapponier et al., 1982; Sengör et al., 1985; Dewey et al., 1986). The application of this model to the Cainozoic evolution of Iberia will be developed in this chapter.

The structural inversion of the High Atlas Trough, uplifted to heights above 4000 metres during the Cainozoic (Stetz and Wurster, 1982), was a major tectonic event that mirrored in several ways the evolution of the Pyrenees. The parallels between the two belts throughout geological time are remarkable: both originated as first order Late Hercynian shears, evolved into seaways during the Triassic Tethyan transgression, and when the Early Cainozoic reorganization of plate tectonics caused the compression of Iberia they became mountain belts. If in the Pyrenees evidence is available for dextral shear during this stage, it is not clear from the literature whether or not any along-strike movement ocurred in the Atlas during its inversion, although Stetz and Wurster (1982) remark that there is no field evidence for strong crustal shortening. This may be an example of the common difficulty of identifying strike-slip induced deformation. It is here postulated that the structural inversion of the High Atlas was caused by transpressive sinistral movement, allowing for the westward extrusion of an Ibero-Moroccan coherent block which lay to the N. The northern boundary of the extruded block is defined by the Pyrenees (transpressive dextral movement; Schott and Peres, 1989). The southern boundary is the South Atlas Fault, a major geological frontier whose importance has been stressed by Weijermaars (1988).

According to the extrusional model here put forward, the movement of Iberia (and Morocco) had a continental origin (onset of Alpine convergence to the E) and therefore this motion is to some extent independent of the precise location of the boundary between Africa and Eurasia, and does not need to be extrapolated all the way to the Mid Atlantic Ridge.

Whilst the detailed configuration of the western margin of Iberia during the Early Cainozoic cannot be located precisely with the data available, its compressive nature is well illustrated. The effects of the Pyrenean Orogeny in Portugal decrease rapidly towards the SW (Ribeiro et al., 1980) and seem to consist of a regional upwarp rather than a localized deformation, but they change towards more intense tectonism on the continental margin at the approach of the slope. The Palaeogene is very poorly represented in the Portuguese basins, indicating that the post-Turonian regional uplift was still taking place. This is clearly shown at the continental shelf as a vast erosional surface (Vanney and Mougenot,

1981), also found off the western coast of Morocco (Hinz et al., 1982). Contrasting with this homogeneous uplift, several crustal blocks were cut and uplifted on the continental slope offshore Portugal during the Eocene, giving rise to several structural highs that still persist, like the Descobridores and Vigo Seamounts and the Galicia Bank to the N and the Principes de Avis Seamounts to the S (Vanney and Mougenot, 1981). This scenario is compatible with a microplate-confining boundary not very far from the coast, as is now proposed.

With the re-orientation of the convergent motion between Africa and Eurasia at the end of the Eocene (section 1.5.2), the boundary conditions presented two novelties: to the S and SE a reorganization of the tectonic style of the active structures had to take place, to account for the new direction of maximum compressive stress; and to the W the dextral strike-slip movement along the Azores Transform introduced what will be called "differential confinement": the northwestern coast of Portugal and the western coast of Galicia were facing a (relatively) eastward moving Eurasian Plate; the southwestern coast of Portugal and the northwestern coast of Morocco were facing a (relatively) westward moving African Plate. Even more than during the Palaeogene, in the Neogene the Ibero-Moroccan block was being "pushed" towards the ocean by the convergence of the larger plates. The re-orientation of stresses rotated the direction of extrusion of Iberia in a counterclockwise sense, probably to the southwestern quadrant, towards the direction of lesser confinement.

To the S of the Ibero-Moroccan block, the postulated Palaeogene South Atlas Transform was replaced by a set of more distributed sinistral strike-slip faults, striking NNE-SSW to NE-SW: the Palomares, Almeria and Alhama de Murcia Faults in southeastern Spain; the Nekor and Jedha Faults in Morocco. Only recently has the importance of the sinistral movement on these faults been described (Weijermaars, 1987; Osete et al., in press). The NE-SW orientation of the Middle Atlas Trough (also inverted to become a mountain range during the Tertiary) and its alignment with the system of faults described above suggest that it took over the role of guiding the deformation towards the ocean during the later stages of extrusion.

The differential confinement on the western coast led to differential oceanward movement of sub-microplate size crustal blocks, accommodated by slip along numerous faults trending E-W to ENE-WSW. Such faults have been recently described (de Smet, 1984; Weijermaars, 1987; Osete et al, in press), and major members are the Crevillente and the Alpujarras Faults. Their importance led deSmet (1984) to re-interpret the External Zone of the Betics Orogen as a dextral shear zone. The palaeomagnetic data of Osete et al. (in press) strongly support the model, indicating important clockwise block rotations during the Miocene. The incompatibility between the structural style of the Betic Cordillera and its classical interpretation as the continuation of the Alpine thrust belt had already been pointed out by Julivert et al. (1974).

The relative orientation of the two systems of faults described above, forming an acute diverging wedge, is not in good agreement with what is usually observed in conjugate systems of strike-slip faults (e.g., Pratsch, 1982; Christie-Blick and Biddle, 1985; Sylvester, 1988). This supports the assumption that each fault system responds to separate aspects of the tectonic setting: a) NW-SE compression (NNE-SSW sinistral shears) and b) E-W differential confinement (ENE-SSW dextral shears).

5.1.2 Seismotectonics of Iberia.

In the previous section it was contended that the Cainozoic evolution of Iberia was better interpreted in terms of continental extrusion, whereby the Ibero-Moroccan Block was being forced sideways into the Atlantic. It will now be argued that this scheme also fits observations of neotectonic activity.

Figure 5.1 is a synthesis of results reported by several authors concerning focal mechanisms, active faulting and volcanism in and around Iberia. Main inputs are from Bellon and Letouzey (1977), Philip (1982), Grimison and Chen (1986) and Buforn et al. (1988). For some of the earthquakes different authors proposed different mechanisms and the alternative results are shown, illustrating the difficulties in constraining fault plane solutions at a continental margin. Four trends of neotectonic activity can be inferred from the figure. They will be described separately.

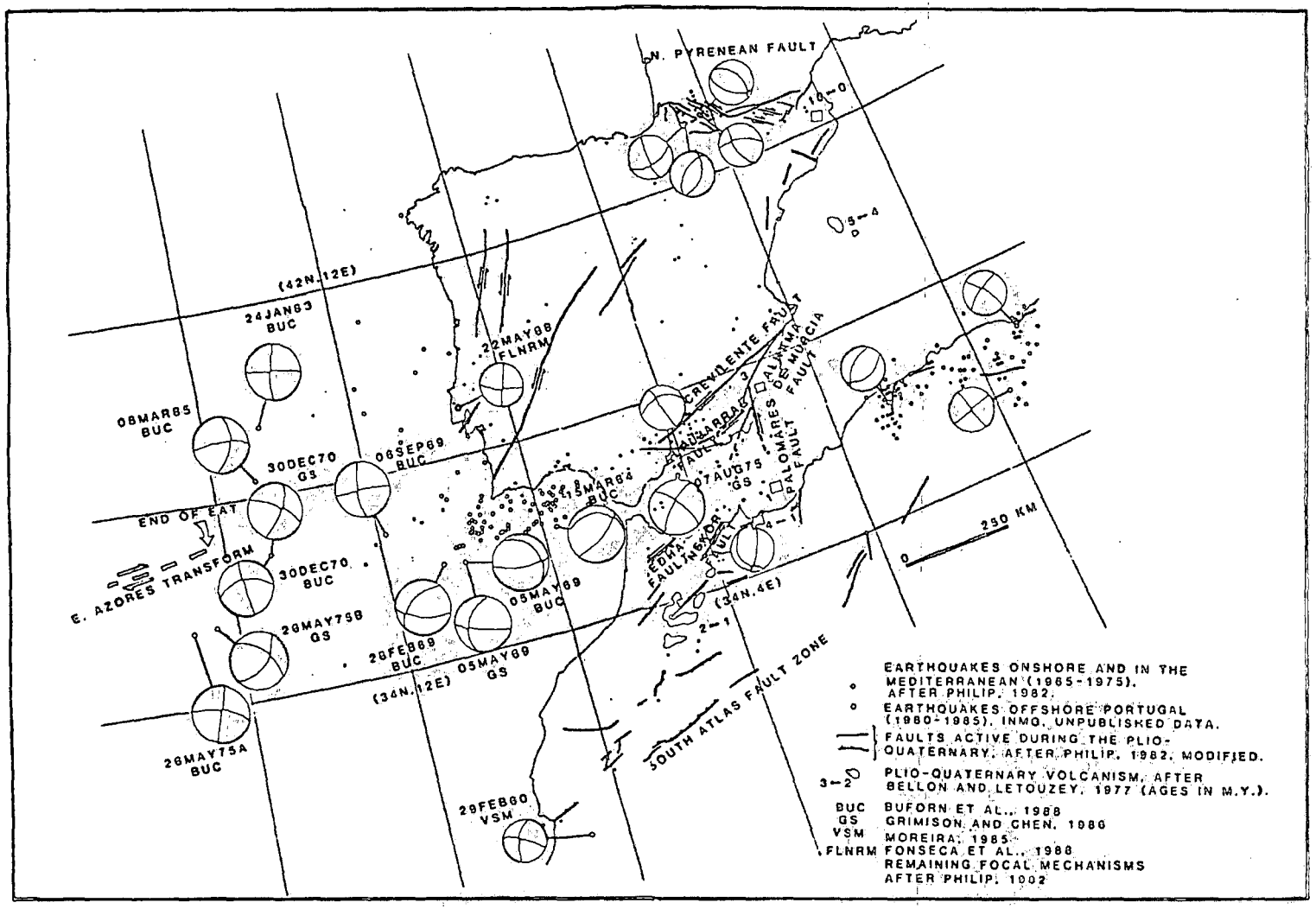

Fig. 5.1 - Neotectonic synthesis of Iberia. Main sources are listen in the figure.

i) The Southern Spain-Middle Atlas trend.

This trend is defined by a number of NE-SW faults associated with numerous deep-focus earthquakes, in the depth range 40-180 km (Lopez-Casado and Sanz-de-Galdeano, 1988). The information from fault plane solutions is poor, but the surface geology indicates sinistral strike-slip on the NE-SW faults (Philip, 1982; Weijermaars, 1987). The trend is marked at several points by Late Pliocene and Quaternary volcanics: the former are calc-alcaline in composition, and the latter are basaltic (Bellon and Letouzey, 1977).

ii) The North Pyrenean Fault Zone.

Although very large earthquakes in this area are not documented, its seismic activity was recently illustrated by two moderate ($M_L > 5$) events in 1967 and 1980. The focal mechanisms of these shocks are poorly constrained, but Philip (1982) proposed dextral shear sub-parallel to the E-W direction. Gagnepain-Beneix et al. (1982) recorded 50 aftershocks following the second event, with a preponderance of E-W dextral strike-slip and NW-SE normal faulting.

iii) The continental margin.

The bathymetric expression of the East Azores Transform vanishes close to the meridian 16° W (e.g., Laughton et al, 1975). The pure dextral strike-slip earthquakes associated with the transform give place to a more complex and diffuse pattern towards the E, from which no clear inference can be made. The P-axes have a consistent NW-SE orientation, but the focal mechanisms are poorly constrained and in some cases the published solutions are in conflict (e.g., the event of 30DEC70).

iv) The Cadiz Gulf-Betics trend.

This trend is offset some 400 km southwards with respect to the extrapolation of the East Azores Transform. Its western extreme corresponds to the Gorringe Bank, locus of large earthquakes like the 28FEB69 ($M_b = 7.4$, Lopez-Arroyo and Udias, 1972) and possibly the Lisbon Earthquake of 1755. Here, the available source data indicate an important component of reverse faulting, usually interpreted as underthrusting of the African Plate (e.g., Purdy, 1975).

In southern Spain this trend corresponds to the External Betics dextral Shear Zone (de Smet, 1984), comprising major ENE-WSW strike-slip fractures such as the Alpujarras and Crevillente Faults. Some published focal plane solutions (Buforn et al., 1988b) are in good agreement with this interpretation. However, the region shows the complexity that is characteristic of most intra-continental strike-slip zones, with events that seem to be in conflict with the expected orientation of the regional stress field, especially for magnitudes below $M_L = 5$. Across the Mediterranean, this trend may perhaps be extended to include the active tectonics of the Tunisian Atlas dextral Shear Zone (Caire, 1979).

Figure 5.2 is an interpretative diagram where the trends discussed above are integrated in a consistent geodynamic model. Comparison with what was described in section 1.5.2 regarding the Miocene tectonic evolution shows that the proposed neotectonic scheme is a subdued continuation of the deformation caused by the continental collision between Africa and Southern Iberia during the last 10 million years. Extrusion of the Ibero-Moroccan Block in a southwesterly direction (to avoid excessive lithospheric thickening in the zone of convergence) is indicated by earthquakes with a component of dextral strike-slip in the Pyrenees and by sinistral strike-slip movement along the NE-SW trend of southeastern Spain and northwestern Africa. The variable resistance offered by the oceanic parts of the African and Eurasian plates as a consequence of the movement on the East Azores Transform leads to the dextral shearing of the Ibero-Moroccan Block across the Cadiz Gulf and the External Betics, and by this mechanism the important ESE-WNW shear component in southern Iberia can be accounted for, which would not be the case for a straightforward prediction of slip directions based on the position of the pole of rotation.

In Figure 5.2 the shaded area to the W of Portugal corresponds to the region where the extrusional model predicts E-W compression and crustal shortening. Off the western coast of Portugal the seismicity is poorly constrained, but the Quaternary geology is compatible with E-W compression (Vanney and Mougenot, 1981; Cabral, 1989). Cabral (1989) uses such indications to introduce the hypothesis of an incipient easterly subduction offshore western Portugal, albeit within a different tectonic framework to the one now presented.

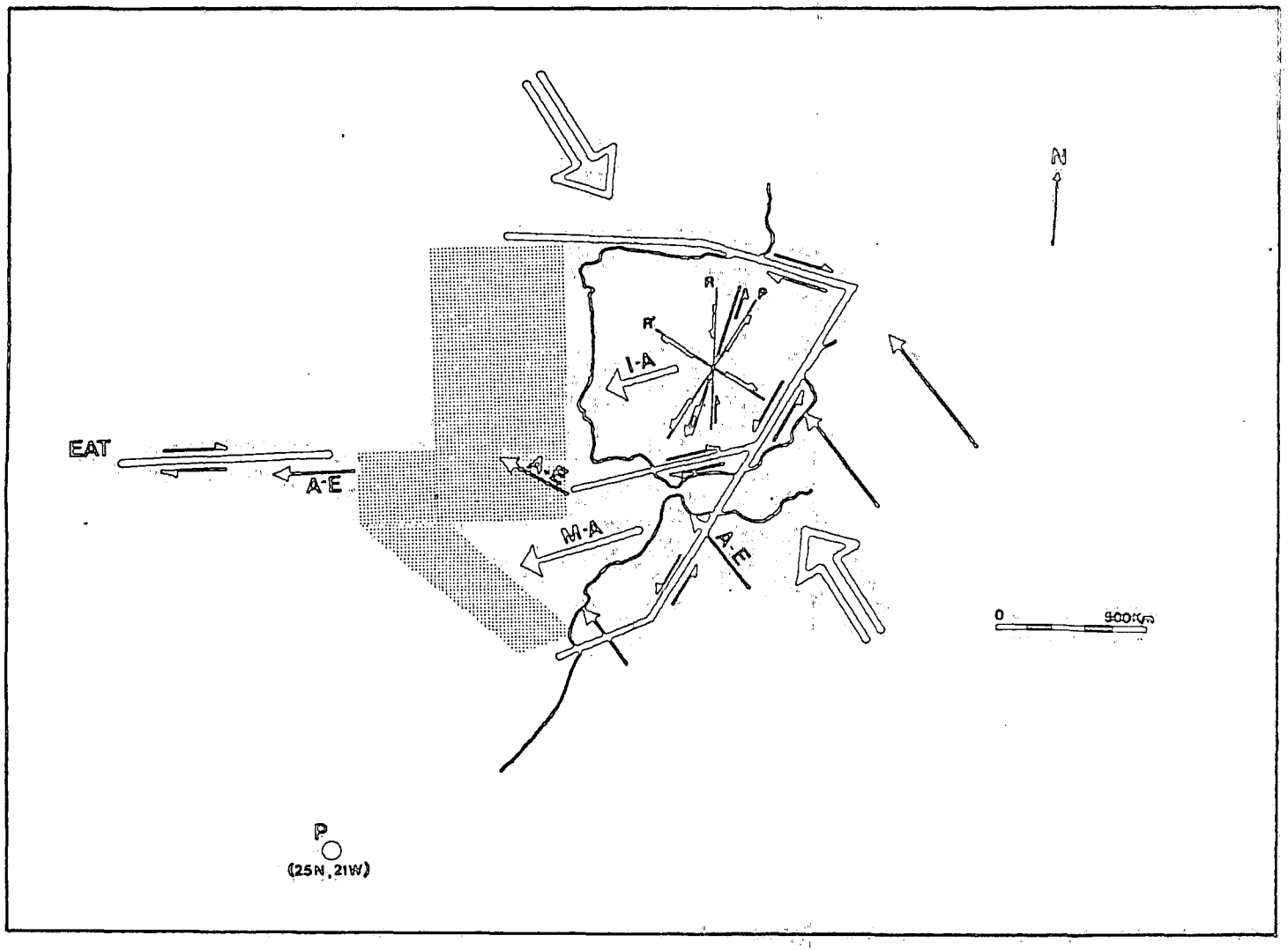

Fig. 5.2 - Proposed neotectonic model of extrusion with differential confinement. P is the African pole of rotation of Minster and Jordan (1978). Thin arrows indicate the direction of convergence predicted by the pole of rotation, length being proportional to velocity. Thick arrows are extrusion velocities with respect to stable Africa. Large open arrows show the regional direction of the maximum compressive stress. EAT = East Azores Transform. Shaded area is the proposed zone of continent-ocean convergence.

East of the East Azores Transform, the shaded area in the diagram includes the Gorringe Bank and the Tagus Abyssal Plain, which rank among the most conspicuous structural features of the region. Since the dextral motion of the Transform is offset towards the S by about 400 km before it can be recognized in the Cadiz Gulf, important WSW-ENE extensional deviatoric stresses can be expected to occur. This extension would weaken the lithosphere, and could explain why the regional NW-SE compression caused such extreme deformation as the upthrust of the Gorringe slab (Purdy, 1975; Ryan and Hsu, 1973). This process of lithospheric attenuation would lead to high heat flow, contrary to the assumption of a cold lithosphere by Purdy (1975) and Karner et al. (1985). Although this uncertainty was not lifted by the ODP Site 120 Report, oxygen isotope observations given by the report indicate high temperatures during the Cainozoic, and high heat flow through a thinned lithosphere may be an alternative to the suggested intrusive or shearing heat source (Ryan and Hsu, 1973). It is widely accepted that the basement rocks drilled immediately below the sediments of the Gorringe Bank are lower crustal units, a hypothesis supported by the very large (~350 mgal) free-air gravity anomaly associated with the ridge. It can be argued that the proposed "pull-apart" ENE-WSW extension could have caused such tectonic denudation prior to the upthrusting in a NNW-SSE direction.

Another tectonic problem which is directly affected by the assumptions regarding the kinematics of the convergence zone to the S of Iberia is the evolution of the Alboran Sea, in the westernmost Mediterranean. This is a narrow sea, surrounded in the N by the Betic Chain and in the S by the Rif Chain; the bending of the Betic-Rif Orogen around the depressed area gave rise to the Gibraltar Arc (Olivet et al., 1973). It is widely accepted that the continental crust in the Alboran Sea was more than 50 km thick during the Palaeogene as a consequence of the convergence between Africa and Eurasia, and that parts of it have subsided by at least 5 km since Mid Miocene times, always within a tectonic setting of overall convergence (Platt, 1988; Dewey, 1988). This has led to the suggestion that the collapse of the central region of the Betic-Rif Orogen was due to the convective removal of the lithospheric mantle root (Platt, 1988). Outward radial thrusting in the Betic and Rif Chains would be the compensatory effect of the gravitational collapse. However, as Dewey (1988) pointed out, it is difficult to

see how such a gravity-driven mechanism would cause thrusting in regions that are now above the subsided area.

The tectonic scheme proposed in Figure 5.2 supports the alternative view that large amounts of localized extension in the Alboran Sea may be related to strike-slip wedges (Crowell, 1974) formed by the interference of the southeastern Spain-Middle Atlas NE-SW sinistral trend with the Gulf of Cadiz-Betics WSW-ENE dextral trend (Fonseca and Long, in press). According to this interpretation, the Alboran Sea would be a mature version of the Karliova Basin of Anatolia, formed by compatibility problems at the junction of the North Anatolian and East Anatolian Faults, which is also surrounded by mountain chains but is still at an elevation of 1750 metres above sea-level (Dewey et al., 1986). One of the difficulties with such model is that it does not predict the outward-fanning thrusts that have been described around the Alboran Sea. This may be a false shortcoming, since deSmet (1984) proposes a symmetrical (flower) structure for the External Betics, with the axis along the Crevillente dextral fault, rather than the nappe model with vergence towards the N usually described in the literature.

5.2 Plate tectonics and continental deformation: the Iberian case.

Sykes (1978) observed that the distribution of intraplate seismicity is linked to the location of pre-existing zones of weakness, often inherited from the youngest orogeny. This principle has been confirmed by a large number of intraplate deformation studies (e.g.,Blenkinsop et al, 1986; Meissner and Wever, 1986; Zoback et al., 1986; Long, 1988; Talwani, 1989). A different idea also proposed by Sykes (1978), that seismically active trends within the continents tend to be located near the end of oceanic transform faults, was not met with such wholehearted agreement. Zoback et al. (1986) refuted a clear link between oceanic fracture zones and areas of continental deformation, although recognizing that the location of pre-split orogenic belts probably influenced the distribution of major oceanic transform faults.

The study of the seismotectonics of Iberia is relevant to both aspects of the above discussion. All four seismogenic trends described in the previous section coincide with zones of rifting and basin development during the Mesozoic and, in most if not all cases, the rifting was controlled by basement faults inherited from

the Late Hercynian Megashear Zone. The regional stress orientation in Iberia is not dissimilar to that of the late stages of the Hercynian Orogeny (Arthaud and Matte, 1977, their Figure 4), and the reactivation of so many Late Hercynian structures during the Cainozoic (section 1.5) is a prime example of the type of "tectonic memory" proposed by Sykes (1978).

The possible connection between the East Azores Transform and the internal deformation of Iberia is not so straightforward. It has already been pointed out that the continental margin W of Portugal and Morocco shows signs of being under compression (previous section). In other areas where a similar observation has been made, like the eastern United States margin, it has been attributed to the effect of distributed ridge push at the mid-ocean ridge (Richardson et al., 1979; Zoback et al., 1986). In Iberia, however, the geodynamic boundary conditions are bound to be more complex, in view of its position with respect to the Afro-Eurasian pole of rotation. Along the western coast of Portugal, compressive stresses are likely to increase towards the N as a consequence of the differential movement of the two sides of the East Azores Transform. Along the southern margin of Iberia, the N-S component of the convergence velocity must increase towards the E, since Africa is rotating about a point near the Canary Islands. It has been submitted above (previous section) that the seismic activity of southern and southeastern Spain (Cadiz Gulf-Betics) resulted from the need to accommodate dextral shear along the East Azores Transform. This is in line with the causal link proposed by Sykes (1978). On the other hand, in the extrusional model the driving force behind the deformation in the Cadiz Gulf-Betics trend is the compression associated with the convergence between Africa and Eurasia, and the oceanic plates are restricted to a more passive (resistent) role, which was described as "differential confinement".

Besides southern and southeastern Spain, many other regions of Iberia have undergone deformation during the Cainozoic, and some are still active now. Western Portugal is well situated for the analysis of the relationship between plate tectonics and continental deformation. The paucity of well constrained focal plane solutions limits however the extent of the conclusions. The geological investigation described in section 2.2.7 and the microearthquake data discussed in section 4.6 point towards the activity, during the Neogene and at present, of

sinistral strike-slip basement faults trending between NE-SW and NNE-SSW. In Figure 5.2 it is shown how the reactivation of these basement fractures can be explained by the compression caused by continental collision in terms of simple-shear. It is not easy to reconcile these observations with suggestions that the basement fractures of southwestern Iberia form a fan-shaped system of splay faults diverging from the eastern end of the East Azores Transform and picking up its dextral strike-slip movement (Weijermaars, 1988). It must be pointed out, however, that the Nazaré Fault, a first-order active tectonic boundary that cuts the coast of central Portugal in a NE-SW direction, may have that type of relation with the transform, as Moreira (1985) gives a dextral strike-slip solution for a magnitude (M_L?) 5 earthquake (26DEC62) on the extrapolated strike of the fault. If this is the case, then the Nazaré Fault can be considered another accommodating structure for the differential confinement of the continental margin.

Chapter VI

Tomographic Inversion of Teleseismic Traveltime Residuals

6.1 Introduction.

As a by-product of the operation of the RESTE seismographic network, several records of teleseismic events were obtained. These were used to gain some knowledge about the broad lithospheric structure underneath the area of the survey. The true p-wave velocity distribution can be regarded as a perturbation around a suitable initial model, and the traveltime residuals (observed minus predicted) can be related to such perturbation through a linear functional or, in the case of a discretized model, through a system of linear equations. In the latter case the system is often underdetermined, and special optimization techniques must be used to provide particular solutions of interest.

The estimate of the velocity structure of the lithosphere from observations of seismic wave traveltime residuals is an example of what is usually called an "inverse problem"; the antonymous designation of "direct problem" applies to the situation where the knowledge (or assumption) of the characteristics of a physical system is used to predict the results of an experiment (i.e., modelling).

6.2 Underdetermined geophysical inverse problems.

6.2.1 General formulation.

In the special case of a spherically stratified Earth, the traveltime of a seismic ray is related to the velocity model v(r) by

$$T = p\Delta + 2\int_{r_p}^{r_E} r^{-1}(\eta^2 - p^2)^{1/2} dr \tag{6.1}$$

where the meaning of the variables is given by Figure 6.1 and by

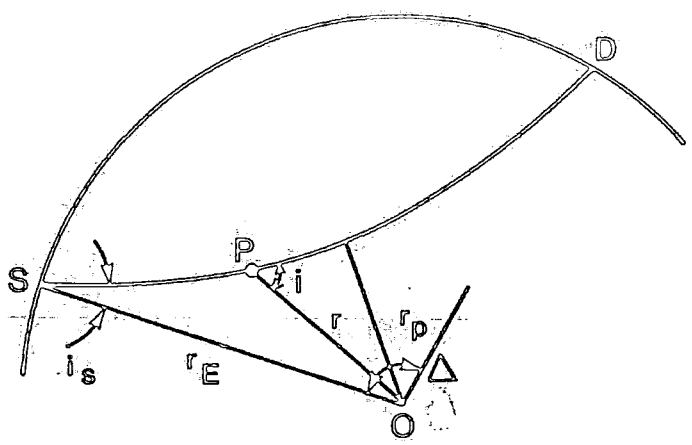

Fig. 6.1 - Seismic ray geometry for a spherically symmetric Earth velocity model.

(6.2) $$p = \frac{r\ sin\ i}{v}; \qquad \eta = \frac{r}{v}$$

(e.g., Bullen and Bolt, 1985, p.158). If the direct problem is solved for a trial velocity model $v_0(r)$, the residual δT can be related to $\delta v(r)$, the error in $v_0(r)$, by the first order approximation (assuming $v_0(r) \sim v(r)$)

(6.3) $$\delta T = -2 \int_{r_p}^{r_E} \eta_o v_o^{-2} (\eta_o^2 - p^2)^{-1/2} \delta v(r)\ dr$$

(ibid.), taking into account that traveltime is stationary with respect to ray-path perturbations (Fermat's Principle).

For a set of n observations d_i of δT, and changing the independent variable to $\nu = r/r_E$, equation (6.3) can be rewritten as

(6.4) $$d_i = \int_0^1 G_i(\nu) m(\nu) d\nu, \qquad i = 1, 2, ..., n,$$

with $m(\nu) = \delta v(r)$ and $G_i(\nu) = -2w(\nu) r_E \eta_0 \nu_0^{-2} (\eta_0^2 - p^2)^{-1/2}$; $w(\nu)$ is zero if $\nu < r_p/r_E$, unity otherwise. Equation (6.4) is a general formulation valid for many geophysical inverse problems, and received special attention during the last two decades, following the pioneer work of Backus and Gilbert (1967, 1968, 1969, 1970).

6.2.2 The method of Backus and Gilbert.

The goal of the inverse problem is to gain information about $m(\nu)$ from the observations d_i. Two different approaches can be taken: the most common consists of discretizing the model $m(\nu)$ to reduce the degree of underconstrainment in (6.4), where the unknown is a continuous function; the second approach, developed by P. Backus and F. Gilbert, consists of designing "averaging kernels" $A(\nu_0, \nu)$ which verify

(6.5) $$\int_0^1 A(\nu_0, \nu)\, d\nu = 1,$$

and use them to compute estimates $< m >_0$ of the value of $m(\nu_0)$ by

(6.6) $$< m >_o = \int_0^1 A(\nu_0, \nu) m(\nu) d\nu$$

(Backus and Gilbert, 1967). The averages must be related to the data by linear relations of the type

(6.7) $$< m >_o = \sum_{i=1}^{n} a_i(\nu_o)\, d_i.$$

Combining (6.4), (6.5) and (6.7) yields

(6.8) $$A(\nu_0, \nu) = \sum_{i=1}^{n} a_i(\nu_o) G_i(\nu).$$

Selecting an averaging kernel that approaches a Dirac-δ would make $< m >_0$ approach the real value of $m(\nu_0)$, as shown by equation (6.6). This can be achieved by a variety of numerical "δ-ness criteria" (Backus and Gilbert, 1968). But the choice in design of $A(\nu_0, \nu)$is limited by the fact that the sum in equation (6.8) has a finite number of parcels, equal to the number of observations. With $n = \infty$ (i.e., with infinite data) the real value of $m(\nu_0)$ would be accessible by making $A(\nu_0, \nu) = \delta(\nu - \nu_0)$ in equation (6.6), assuming error-free data and linearly independent $G_i(\nu)$.

Backus and Gilbert's method was applied to one dimensional (Backus and Gilbert, 1969) as well as three-dimensional velocity modelling from seismic traveltime residuals (Chou and Booker, 1979). Although it will not be used in this

study, it was presented here because it highlights the main aspects of inversion theory: non-uniqueness, resolution and error propagation.

The solution to equation (6.4) will be non-unique if it is possible to obtain a non-trivial solution to the homogeneous integral equation

$$\int_0^1 G_i(\nu)m(\nu)d\nu = 0. \tag{6.9}$$

If $m^*(\nu)$ is such a non-trivial solution and $m_p(\nu)$ is a solution of equation (6.4), then by linearity it follows that any function of the type

$$m(\nu) = m_p(\nu) + \lambda\, m^*(\nu) \qquad (\lambda\ constant), \tag{6.10}$$

will also verify equation (6.4). This type of severe non-uniqueness (infinite number of solutions compatible with the data) is intrinsic to most inverse problems with geophysical interest, since the spacial functions describing the distribution of physical properties of the real Earth are too general to be determined from a finite set of numbers.

Rather than attempting to obtain one among the infinity of possible solutions, the method of Backus and Gilbert focuses on the search for those properties which are common to all the data-compatible solutions: if for a particular ν_0 and for a given "width" of the averaging kernel all such solutions average to the same value (within some accuracy threshold), it can be concluded that such "smoothed" property pertains to the true model as a particular case. The minimum width for which this occurs (for each ν_0) is called the "resolving length" of the data set (Backus and Gilbert, 1970).

If the observations d_i are contaminated by experimental errors Δd_i (i.e., if the d_i are real data), these errors will propagate through equation (6.7) to cause an error in the average $< m >_0$. If the variance of the observations can be quantified by a matrix E_{ij}, the variance in $< m >_0$ will be

(6.11) $$\sigma^2 = \sum_i \sum_j a_i a_j E_{ij}.$$

If some control is to be exerted on the admissible level of variance in the resulting model, further constraints must be imposed on the selection of the coefficients a_i, besides the chosen δ-ness criterion. Backus and Gilbert (1970) developed the algebra associated with this problem and established the existence of a trade-off between loss of resolution (measured by the spread of the averaging kernel around ν_0) and model variance. This leads to a subjective element on the choice of the coeficients a_i, which may be explored according to the objectives of any particular inverse problem.

6.2.3 Discrete inverse problems.

Dividing the area to be modelled into boxes where the parametres are kept constant is a convenient procedure for three dimensional problems. This was first applied by Ellsworth (1977) and by Aki et al. (1977) to obtain the lithospheric velocity structure underneath a local seismic network from teleseismic traveltime residuals, and by Aki and Lee (1976) to use microearthquakes from within the volume to be modelled. In the latter case the hypocentre parametres and time of origin must be included among the unknowns.

For teleseismic data, some standard Earth model is assumed outside the volume being studied, and the focal parametres of the earthquakes are obtained from a catalogue. An initial model for the velocities of the boxes is stipulated, and traveltimes are predicted for each event and each station, usually using published tables for the standard Earth and ray-tracing through the boxes. The traveltime residual for each ray is thus computed. It is related to the fractional perturbation of slowness (inverse of phase velocity) in the blocks hit by the ray through

(6.12) $$\Delta t_{ij} = \sum_k \frac{l_k}{v_k} m_k.$$

Here, i indicates a particular event and j indicates a particular station, and the summation takes place over all the blocks hit by the ray; l_k is the length of the raypath within block k, v_k is the velocity of the block in the initial model, and m_k is the fractional perturbation of slowness, related to the perturbation of the velocity of the block by

$$\frac{1}{v_k + \Delta v_k} = \frac{1}{v_k}(1 + m_k) \tag{6.13}$$

(Aki et al., 1977; Aki and Richards, 1980, p. 712). The contribution of raypath distortion to the Δt_{ij} can be ignored in equation (6.12) in view of Fermat's Principle.

The system of linear equations (6.12) is suitably treated with matricial notation. Summation can easily be extended to all the blocks by introducing a discriminating operator h_{ijk} which is zero if the ray corresponding to event i and station j does not cross block k, and unity if it does. If all the traveltime residuals are organized into a nx1 array d, (6.12) then reads

$$d_r = \sum_{s=1}^{m} g_{rs} m_s \qquad r = 1, ..., n; \qquad or \qquad \mathbf{d} = G\mathbf{m}, \tag{6.14}$$

where n is the number of data, m is the number of blocks (equal to the number of unknowns) and the g_{rs} can be computed from the initial model.

Jackson (1972) formulated the problem of solving (6.14) as the search for a matrix F which operates on both sides of the system to give a particular solution

$$\widehat{\mathbf{m}} = FG\mathbf{m} = F\mathbf{d} \tag{6.15}$$

and additionally has the following properties:

i) $GF \sim I_n$ (i.e., $G\widehat{\mathrm{m}} \sim \mathrm{d}$, and the particular solution fits the data well);

ii $FG \sim I_m$ (i.e., $\widehat{\mathrm{m}}$ is well resolved);

iii) the variance of $\widehat{\mathrm{m}}$ is small.

The matrix $R = FG$ is called the "resolution matrix", and since $\widehat{\mathrm{m}} = R\mathrm{m}$ the rows of R can be seen as discrete averaging kernels. The matrix $H = GF$ is called the "information density matrix" (Jackson, 1972), and measures the degree of independence of the data, of particular importance in overconstrained problems (n>m). The variance of $\widehat{\mathrm{m}}$ is given by the covariance matrix

$$C = F\ \Delta\mathrm{d}\ \Delta\mathrm{d}^T F^T \tag{6.16}$$

(throughout this chapter "A^T" means the transposed of A), where the elements of Δd are the standard errors in observations. If the covariance matrix of the data has the form $\sigma_d^2 I_n$ (i.e., all observations have the same standard error σ_d and are uncorrelated) the covariance matrix for the model becomes

$$C = \sigma_d^2 F F^T. \tag{6.17}$$

The standard error in the ith parameter of the model is $\sigma_i = (c_{ii})^{1/2}$ (no sum).

The solution of linear systems of the type (6.14) with m$\neq$ n was discussed in detail by Lanczos (1961, chapter 3). The nature of the problem depends on the relative size of p, the number of linearly independent rows in the matrix G, the number m of unknowns in the model, and n, the number of observations. If p=m=n the system has an exact solution (G is square and non-singular) ; if p<m the solution (if existent) is non-unique, i.e., the problem is underdetermined; if p=m<n the problem is strictly overconstrained and no solution exists which verifies exactly the observations. In the latter case the standard least-squares technique can be used to produce the optimum least-squares solution

(6.18) $$\mathbb{m}_{LS} = (G^T G)^{-1} G^T \mathbb{d}.$$

When p < m, $G^T G$ is singular and (6.18) cannot be applied. If p<m<n the system is both overconstrained and underdetermined.

Lanczos's method considers simultaneously the system (6.18) and its adjoint system

(6.19) $$b_j = \sum_{k=1}^{n} g_{kj} a_k \qquad j = 1, ..., m; \qquad or \qquad \mathbf{b} = G^T \mathbf{a}.$$

Problems (6.14) and (6.19) can be merged into a single linear system given by

(6.20) $$\left[\frac{\mathbf{d}}{\mathbf{b}}\right] = S \left[\frac{\mathbf{a}}{\mathbf{m}}\right]; \qquad S = \left[\frac{O \mid G}{G^T \mid O}\right].$$

The matrix S is now (m+n)x(m+n) and symmetric, and can be treated with the algebraic methods pertinent to such matrices. Of particular importance is the fact that the eigenvalue problem

(6.21) $$S\mathbf{w} = \lambda \mathbf{w}$$

can be solved for S (eigenvalues are not defined for rectangular matrices like G), and since S is symmetric it always has (n+m) real eigenvalues. The eigenvectors w can be decomposed as

(6.22) $$\mathbf{w} = \left[\frac{\mathbf{u}}{\mathbf{v}}\right],$$

and equation (6.21) breaks into

$$G\mathrm{v} = \lambda \mathrm{u}, \tag{6.23a}$$

$$G^T \mathrm{u} = \lambda \mathrm{v}, \tag{6.23b}$$

taking into account the shape of the matrix S. Premultiplying G by G^T and G^T by G gives

$$G^T G\ \mathrm{v} = \lambda^2 \mathrm{v}, \tag{6.24a}$$

$$GG^T\ \mathrm{u} = \lambda^2 \mathrm{u}, \tag{6.24b}$$

which are eigenvalue problems, since $G^T G$ is (mxm) and GG^T is (nxn). Equations (6.24) lead to (n+m) solutions λ_i^2, corresponding to 2p non-zero eigenvalues of the matrix S plus a zero eigenvalue of multiplicity (n+m-2p).

Equations (6.23) provide some insight into the nature of the inverse problem. The eigenvectors v_i verifying (6.24a) can be regarded as elements of the space formed by all models, and the u_j as elements of the space of all data-sets. Furthermore, in view of the symmetry of GG^T and $G^T G$ the eigenvectors associated with non-zero eigenvalues are orthogonal or can be orthogonalized (e.g., Lanczos, 1961), and the linear combinations of the v_i ($\lambda_i \neq 0$) span a sub-set of the space of all models. Also the linear combinations of the u_j ($\lambda_j \neq 0$) span a sub-set of the space of all data-sets. If a particular data-set belongs to such a sub-set, it can be decomposed on the base (v_i) and will be "mapped" onto the model space

via the relations $G\mathbf{v}_i = \lambda_i \mathbf{u}_i$. The non-zero eigenvalues therefore act as "links" between data space and model space.

If a particular data-set has a component which is a linear combination of eigenvectors $\mathbf{u}_j$ associated with the zero eigenvalue, then this component cannot be obtained by forward modelling, since (6.23b) becomes

$$G\mathbf{v}_j = 0. \tag{6.25}$$

If the true model has a component which is a linear combination of eigenvectors $\mathbf{v}_i$ associated with the zero eigenvalue, this component cannot be obtained by inversion, since (6.23a) results

$$G^T\mathbf{u}_i = 0. \tag{6.26}$$

The two last statements synthesize the limitations of solving either the inverse or the direct problem when p<m (some $\mathbf{v}_i$ have $\lambda_i = 0$) and p<n (some $\mathbf{u}_j$ have $\lambda_j = 0$). If some particular model verifies the data it can be modified by adding a linear combination of the $\mathbf{v}_i$ with $\lambda_i = 0$ and it will still verify the data, and this is the source of non-uniqueness. On the other hand, discrepancy between real data and synthetic data will arise unless the real data is orthogonal to all the $\mathbf{u}_j$ with $\lambda_j = 0$ (Aki and Richards, 1980).

In view of the previous comments, it is "natural" to seek a particular solution for problem (6.14) which only involves the non-zero eigenvalues of S and the associated eigenvectors. In the particular case when p=m=n, the matrix G can be decomposed as

$$G = U\ \Lambda\ U^T, \tag{6.27}$$

where Λ is a diagonal matrix containing the eigenvalues λ_i and the rows of U contain the associated eigenvectors. Lanczos (1961) shows that for the general case it is still possible to write

$$G = U\,\Lambda\,V^T, \tag{6.28}$$

where U is (nxp), Λ is (pxp) and V is (mxp). The matrices U and V contain the eigenvectors that verify (6.24) for non-zero eigenvalues. That author then proposed as the "natural" inverse of G the matrix defined by

$$F = V\,\Lambda^{-1}U^T, \tag{6.29}$$

where the elements of the diagonal of Λ^{-1} are λ_i^{-1}. The resolution matrix and the information density matrix are given by

$$R = FG = VV^T; \qquad H = GF = UU^T. \tag{6.30}$$

The right-hand sides (unlike U^TU and V^TV) are only I_p if p=n and p=m respectively.

The "natural" inverse of Lanczos is usually refered to as "generalized inverse" (e.g., Aki and Richards, 1980), and leads to the following solution to (6.14):

$$\mathbf{m}_g = F_g\,\mathbf{d} \qquad with \qquad F_g = V\,\Lambda^{-1}U^T. \tag{6.31}$$

The generalized inverse has the minimum euclidean norm among all the models verifying the data: any such model is of the form

(6.32) $$\mathbf{m} = \mathbf{m}_g + \sum_i c_i \mathbf{v}_i \qquad (c_i \text{ arbitrary}),$$

where the $\mathbf{v}_i$ are eigenvectors associated with the zero eigenvalue, and it follows that

(6.33) $$|\mathbf{m}| = [|\mathbf{m}_g|^2 + \sum_i c_i^2]^{1/2} \geq |\mathbf{m}_g|.$$

This property makes the generalized inverse particularly suitable for iterative numerical techniques. It can also be shown that the residuals given by

(6.34) $$\epsilon = \mathbf{d} - F_g \mathbf{m}$$

have no contribution from the $\mathbf{u}_j$ associated with the zero eigenvalue, and for this reason the residual vector has a minimum euclidean norm as well. The generalized inverse solution is therefore a "natural" extension of the standard least-squares technique to the case p<m (underdetermined problem).

If the errors in the data are non-correlated, the variance of the model parameters can be written, making use of equation (6.31), as

(6.35) $$var(m_k) = \sum_i \sum_j [v_{kj} \lambda_j^{-1} u_{ij}]^2 \; var(d_i),$$

where v_{kj} and u_{ij} are the elements of V and U respectively. The last expression shows that the small eigenvalues contribute strongly to the variance of the model. It may be preferable to exclude from (6.31) those eigenvalues too close

to zero, thereby reducing artificially the number p to reduce the variance, at the cost of degrading the resolution.

When m=p<n (strictly overconstrained problem), the minimization of the norm of the residuals leads to a unique solution, and the generalized inverse reduces to the standard least-squares solution. It may still be prefered, however, because it allows the inspection of the eigenvalues and therefore the control of the stability of the model parameters. Hypocentral location is usually a highly overconstrained inverse problem, where the unknowns are the spacial coordinates of the focus (assumed to be a point) and the origin time (m=4). The number of seismic stations reporting the arrival time, if only one phase is used, gives the number of observations. The matrix G^TG is non-singular and (4x4), and has therefore 4 non-zero eigenvalues, i.e., p=m=4. In this case, the resolution matrix is equal to the identity matrix, and the computation of the different parametres is independent. Klein (1978) explores this to propose an iterative scheme of hypocentral location where in each iteration the eigenvalues are inspected after the inversion has been carried out. Those components of the adjustment which are associated with eigenvalues below some user-defined tolerance level are simply ignored. The program HYPOINVERSE (Klein, 1978), used in chapter 4 to locate the RESTE local earthquakes, is an implementation of this method.

An algorithm was developed under the name of "damped least-squares" which addresses the problem of instability associated with small eigenvalues in a different way. It can be derived by minimizing a combination of the norm of the model and the residuals of the form

$$|\mathbf{d} - G\mathbf{m}|^2 + \theta^2|\mathbf{m}|^2, \tag{6.36}$$

and is given by the "inverse operator"

$$F_D = (G^TG + \theta^2 I_n)^{-1}G^T. \tag{6.37}$$

The "damping factor" θ , which is arbitrary, makes the expression within brackets always non-singular, and can be used to control the size of the minimum eigenvalue, in order to limit the variance in the solution. The same operator can be derived alternatively by considering data and model as stochastic processes (i.e., families of aleatory variables) with zero mean and known covariance matrices of the form $\sigma_n^2 I_n$ and $\sigma_m^2 I_m$, θ being now equal to the ratio σ_n/σ_m (Aki and Richards, 1980). For this reason this particular operator is also known as "stochastic inverse". The resolution matrix for the damped least-squares inverse is

$$R = (G^T G + \theta^2 I_n)^{-1} G^T G, \tag{6.38}$$

and the covariance matrix, assuming uncorrelated observations with common standard errors σ_d, is

$$C = \sigma_d^2 (G^T G + \theta^2 I_n)^{-1} R. \tag{6.39}$$

The FORTRAN77 program THRD (Evans, 1986), written by W. Ellsworth and G. Zandt and improved by D. Stauber, D. Oppenheimer and J. Evans, uses the damped least-squares inversion algorithm described above in an implementation fully described by Aki et al.(1977). Some details of the program will be considered next, before it is used to invert a data set obtained with the RESTE Network.

Equation (6.12) can be rewritten for the observations of a particular event as

$$t_j = \tau_j + \tau' + \sum_k g_{jk} m_k + \epsilon_j, \qquad j = 1, ..., N, \tag{6.40}$$

where j is the station index, τ_j is the arrival time at the bottom of the volume being modelled and τ' (common to all stations) is the traveltime through

the model with the initial horizontally homogeneous velocity distribution. The quantities g_{jk} and m_k are as defined by (6.14) and (6.13) and the quantities ϵ_j account for the observation errors and neglected higher order terms. The τ_j may be obtained from the seismological tables of Herrin (1968), and τ' is computed by ray-tracing from the surface to the bottom of the model. Errors that are common to all stations, like those due to the estimate of origin time or to the standard Earth model, can be absorbed by the parameter τ' by rewriting (6.40) as

$$t_j = \tau_j + \tau' + \sum_k [(g_{jk} - \frac{1}{N}\sum_{l=1}^{N} g_{lk})m_k + \frac{1}{N}\sum_{l=1}^{N} g_{lk}m_k] + \epsilon_j, \tag{6.41}$$

and making $\tau'' = \tau' + \frac{1}{N}\sum_l \sum_k g_{lk}m_k$ and $g'_{jk} = g_{jk} - \frac{1}{N}\sum_{l=1}^{N} g_{lk}$. With these changes, (6.40) becomes

$$t_j = \tau_j + \tau'' + \sum_k g'_{jk}m_k + \epsilon_j, \qquad j = 1, ..., N. \tag{6.42}$$

The quantity τ" corresponds to the "nuisance parameter" of Aki et al. (1977), which is characteristic to each event. Assuming that the contributions of the last two terms of (6.42) average to zero when summed over all stations, τ" can be equated to the average of the traveltimes through the model,

$$\tau'' = \frac{1}{N}\sum_{j=1}^{N}(t_j - \tau_j). \tag{6.43}$$

The quantities d_j defined by

$$d_j = t_j - \tau_j - \tau'' \tag{6.44}$$

are traveltime residuals from which the average per event has been subtracted. In terms of these zero-mean residuals, equation (6.42) becomes

$$d_j = \sum_k g'_{jk} m_k + \epsilon_j, \qquad j = 1, ..., N. \tag{6.45}$$

If M events are recorded, an equivalent number of sets of equations like (6.45) can be established, and in this way a linear system is built where the number of equations is NxM and the number of unknowns is equal to the number of blocks in the model.

The process of subtracting the average per event from the traveltime residuals reduces all the stations to the same status (no reference station is needed), whilst adding a component of non-uniqueness to the solution, since the new quantities d_j are insensitive to a uniform change in the velocity in all the blocks of any particular layer (Aki et al., 1977) In this way, absolute velocities are determined only if at least one station is in an area of known lithospheric velocity structure.

To estimate the improvement in the fitting of the observations by a particular solution $\mathbf{m}^*$, program THRD uses the statistics $VI = 100.0(1 - r)$, where

$$r = \frac{\sum_j (d_j - \sum_k g'_{jk} m^*_k)^2}{\sum_j d_j^2} \tag{6.46}$$

is the ratio between the variance of the solution residuals and the variance of the observation residuals.

6.3 Application to the RESTE Network teleseismic data.

After minor modifications to run on the MTS System (Rowntree, 1987; this thesis, Appendix C), the program THRD was used to perform the tomographic inversion of teleseismic data recorded with the RESTE Network. Figure 4.6e) shows the printout of the digital version of one of these records. Readings of

arrival times where made on enlarged copies (1 s = 4.9 cm) using the technique of waveform matching: although the shape of the signals for a particular event may vary between stations, some features of the first few (typically two) cycles, such as zero-crossings and peak positions, showed good consistency and were used to determine the relative time shifts between records, by overlapping the traces on a drawing table. The reading error was of the order of ±0.04 s (±2 mm lateral shift).

A total of 20 teleseisms were used in this study. The epicentres are plotted in Figure 6.1, and the focal data is given in Table 6.1. The traveltimes of these events were in agreement with the predictions of the Herrin (1968) tables to within 6 seconds. This generous allowance was made because the focal parameters were preliminary (data released by the American Geophysical Union), and also because the algorithm is not sensitive to errors in traveltime that are shared by all the records of the same event. The total number of traveltime observations was 140, distributed over 10 stations (Figure 6.2). This data set is reproduced in Table 6.2.

Prior to the inversion a straightforward analysis of the traveltime residuals was carried out, grouping the values according to recording station, to get a first and very smoothed picture of the distribution of velocity anomalies. For this purpose, the residuals were calculated according to

$$r_j = t_j - t_o - (\tau_j - \tau_o), \tag{6.47}$$

where the variables have the same meaning as in equation (6.40) and the index 0 corresponds to a reference station (AMG). These residuals integrate contributions from the entire thickness of the model, and also average laterally since different rays arrive obliquely from different azimuths. For this reason they show large standard deviations, as indicated in Table 6.3 and in Figure 6.3. In Figure 6.3 the results were projected onto a N-S line coinciding with the 9°W meridian, showing a tendency towards more negative residuals as the latitude increases. The stations which deviate from this tendency are those farther away

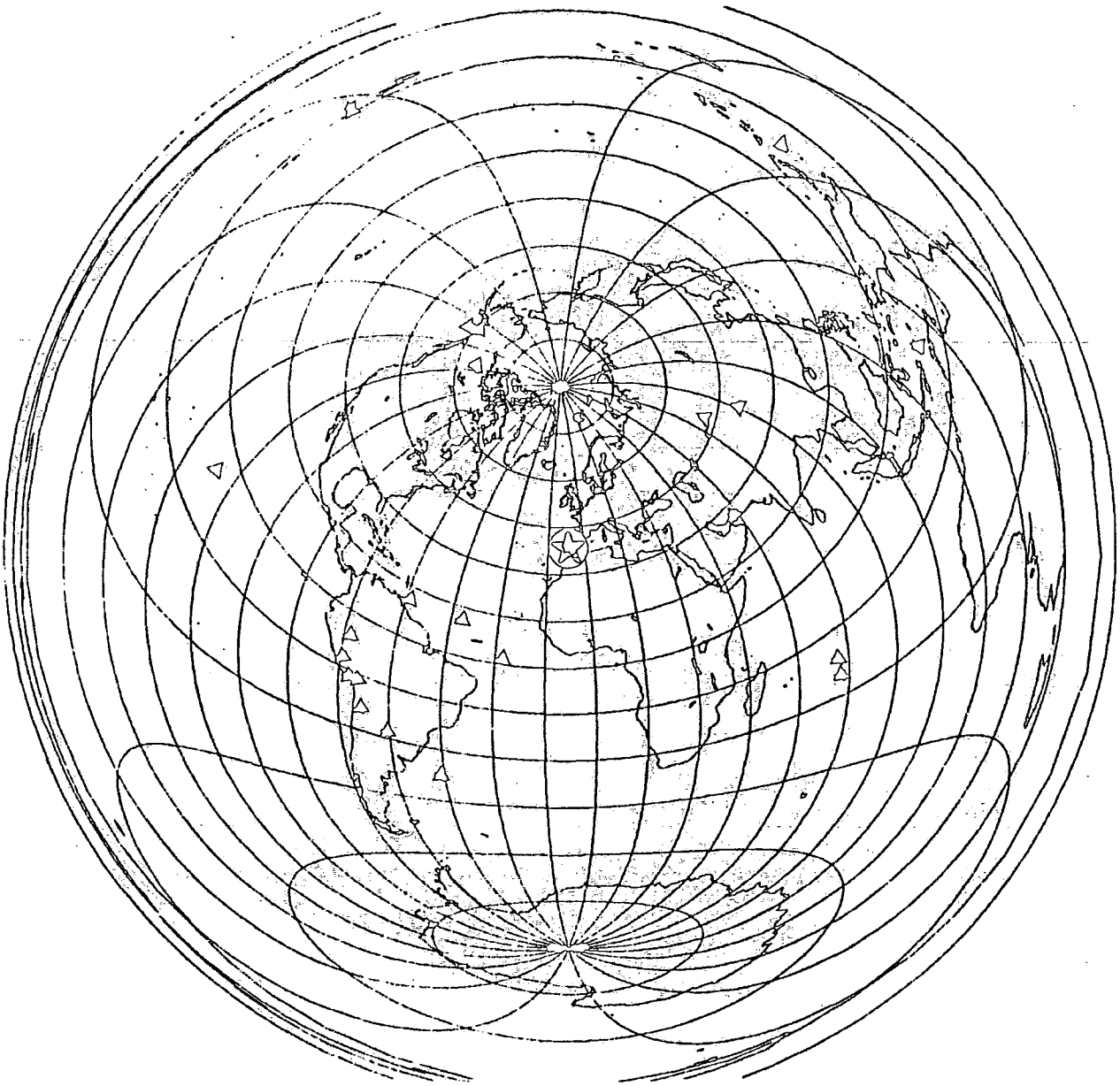

Fig. 6.1 - Epicentres of the teleseisms used for tomographic inversion, shown on equidistant projection.

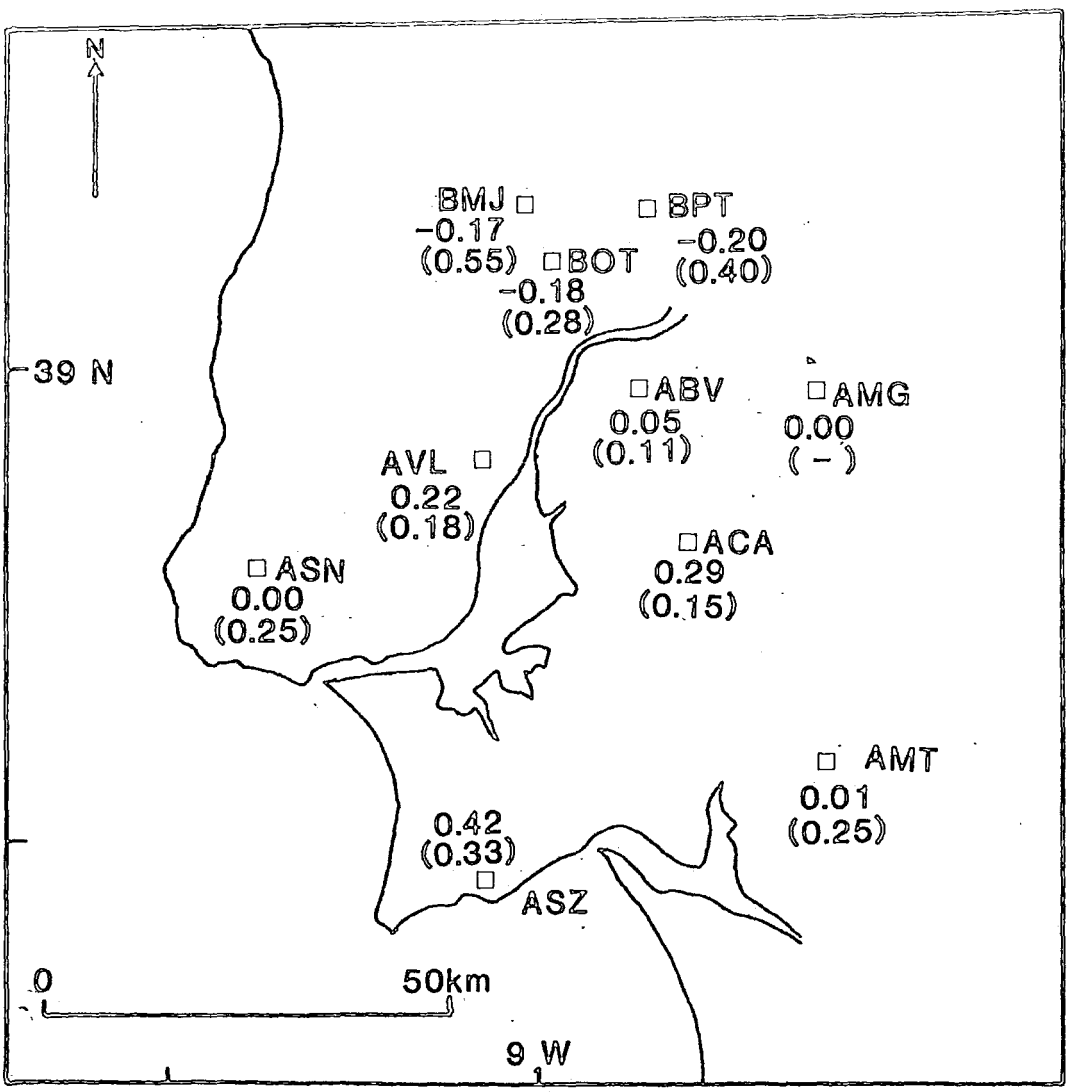

Fig. 6.2 - Stations used for tomographic inversion, and preliminary analysis of travel-time delays. The numbers are the average residuals with respect to station AMG (in seconds), and the standard deviations (in parenthesis).

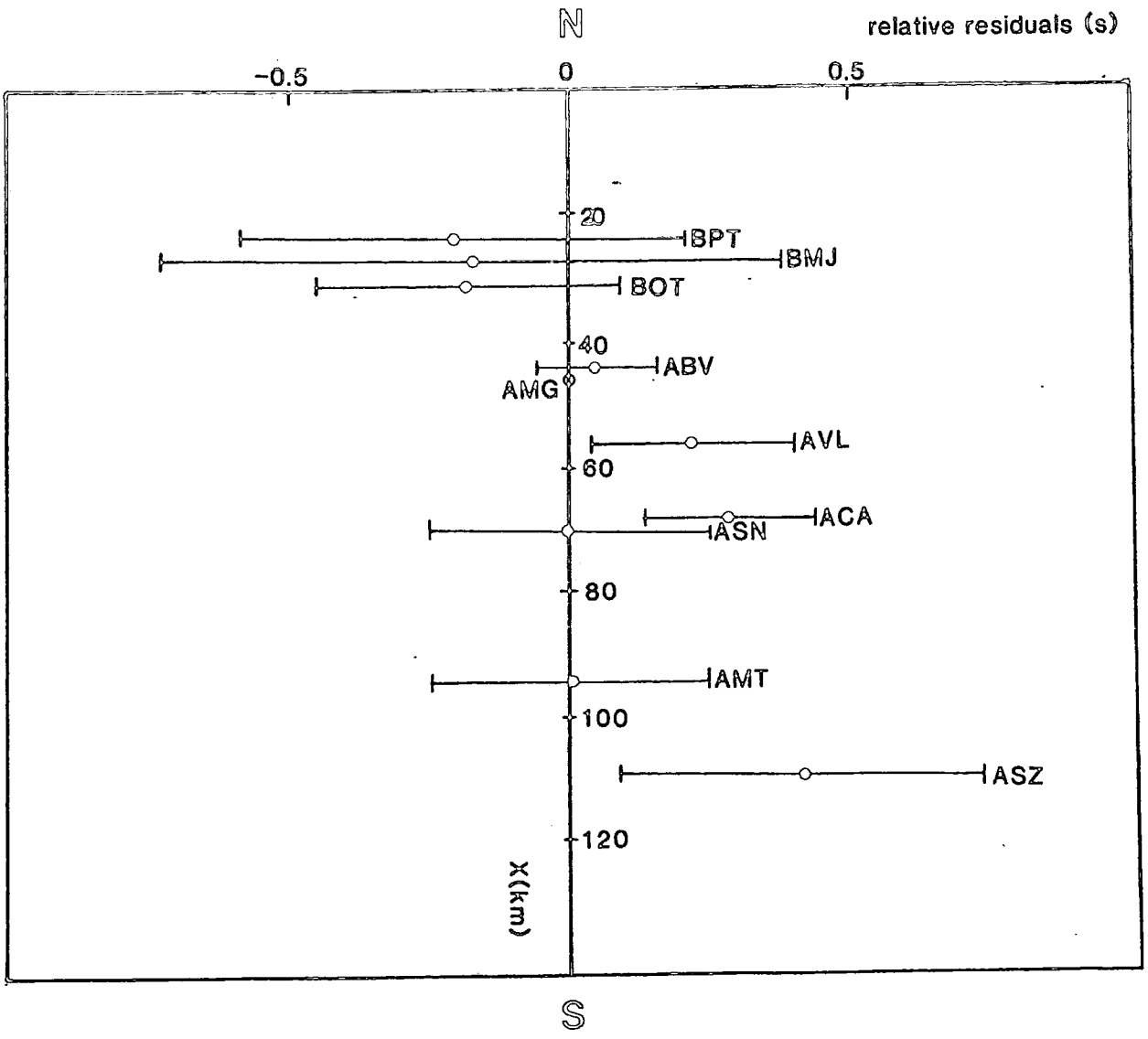

Fig. 6.3 - Same data as in Figure 6.2, projected on a N-S profile. The residuals tend to become more negative towards the N.

TELESEISMS USED FOR TOMOGRAPHIC INVERSION

EPICENTRAL DATA

Code	Date	H	M	S	Depth	Lat	Long
ET03FB	12-10-88	13.	57.	4.7	5.	(-7.-17.40 N,	-154.-22.20 W)
ET04FB	27-10-88	21.	58.	17.0	605.	(-28.-40.80 N,	62. 55.80 W)
ET11FB	13-12-88	3.	21.	4.8	10.	(49. 59.40 N,	-78.-50.40 W)
ER13FB	17-11-88	8.	46.	53.3	10.	(58. 35.40 N,	143. 16.20 W)
ET13FB	22-12-88	0.	16.	39.0	21.	(41. 21.60 N,	-89.-38.40 W)
ET15FB	19-01-88	7.	30.	31.8	33.	(-24.-42.60 N,	70. 34.20 W)
ER18FB	30-11-87	19.	23.	19.5	10.	(58. 40.80 N,	142. 47.40 W)
ET19FB	05-02-88	14.	1.	2.2	33.	(-24.-46.20 N,	70. 22.20 W)
ET23FB	26-02-88	6.	17.	31.4	10.	(-37.-18.00 N,	-47.-58.20 W)
ET24FB	06-03-88	22.	35.	35.8	10.	(57. 16.20 N,	142. 47.40 W)
ET28FB	09-03-88	21.	33.	53.6	33.	(-17.-21.00 N,	74. 12.60 W)
ET29FB	14-03-88	12.	29.	46.8	116.	(-7.-18.60 N,	74. 45.60 W)
ET17FB	24-01-89	16.	0.	4.5	566.	(-17.-45.60 N,	178. 44.40 W)
ET30FB	23-03-89	15.	50.	17.9	10.	(10. 54.00 N,	43. 33.60 W)
ET31FB	25-03-89	19.	36.	46.4	10.	(62. 9.60 N,	124. 12.00 W)
ET32FB	31-03-89	23.	50.	56.2	37.	(-24.-54.60 N,	70. 24.60 W)
ET33FB	03-04-89	1.	33.	5.7	10.	(49. 52.80 N,	-78.-57.60 W)
ET35FB	20-04-89	4.	25.	36.5	10.	(0. 56.40 N,	30. 14.40 W)
ET36FB	06-05-89	16.	34.	5.5	51.	(-13.-22.80 N,	76. 12.60 W)
ET34FB	13-04-89	23.	19.	57.3	54.	(-17.-19.20 N,	72. 24.00 W)

Table 6.1

Table 6.2

TOMOGRAPHIC INVERSION

ARRIVAL TIME DATA

mat:

Event Date
e Station Dist.(deg.) a.t.
e Station Dist.(deg.) a.t
.... etc .....

****

ET03 12-10-88
BV 145.009 14 16 41.8
MG 144.932 14 16 41.5
VL 145.186 14 16 42.5
MJ 145.327 14 16 43.4
SZ 145.556 14 16 43.8

ET04 27-10-88
BV 84.109 22 9 45.7
VL 83.902 22 9 45.7
CA 84.024 22 9 46.5
ST 84.189 22 9 47.3
SZ 83.608 22 9 44.5
MT 83.969 22 9 45.9

ET11 13-12-88
BV 60.078 3 31 15.3
MG 59.965 3 31 14.6
SN 60.520 3 31 18.6
VL 60.288 3 31 17.0
CA 60.157 3 31 16.2
MT 60.201 3 31 16.6

ER13 17-11-88
BV 75.640 8 58 36.2
MG 75.700 8 58 36.3
VL 75.643 8 58 36.3
CA 75.801 8 58 37.3
SZ 76.049 8 58 38.9
MT 76.082 8 58 38.6

ET13 22-12-88
MG 70.865 0 27 56.8
SN 71.435 0 27 60.2
VL 71.199 0 27 59.1
CA 71.054 0 27 58.2
MT 71.079 0 27 58.3

ET15 19-01-88
BV 85.676 7 43 12.5
MG 85.799 7 43 13.1
VL 85.461 7 43 11.5
CA 85.611 7 43 12.4
ST 85.794 7 43 13.0
MT 85.594 7 43 12.0

* ER18 30-11-87
B ABV 75.421 19 35 0.3
B AMG 75.482 19 35 0.6
B AVL 75.424 19 35 0.6
B ACA 75.582 19 35 1.5
B AMT 75.863 19 35 3.0

* ET19 05-02-88
B ABV 85.594 14 13 40.5
B AMG 85.717 14 13 41.0
B ASN 85.142 14 13 38.2
B AVL 85.379 14 13 39.4
B ACA 85.529 14 13 40.3
B ASZ 85.130 14 13 38.6
B AMT 85.511 14 13 40.0

* ET23 26-02-88
B ABV 92.171 6 30 44.5
B AMG 92.068 6 30 44.2
B ASN 92.308 6 30 44.8
B AVL 92.241 6 30 44.9
B ACA 92.028 6 30 44.0
B ASZ 91.909 6 30 43.4
B AMT 91.745 6 30 42.4
B BMJ 92.500 6 30 45.6
B BPT 92.306 6 30 45.0
B BOT 92.325 6 30 45.0
B BSE 92.063 6 30 44.2

* ET24 06-03-88
B ABV 76.575 22 47 28.8
B AMG 76.637 22 47 29.0
B ASN 76.583 22 47 28.9
B AVL 76.574 22 47 29.0
B ACA 76.735 22 47 29.9
B ASZ 76.977 22 47 31.6
B AMT 77.017 22 47 31.2
B BMJ 76.235 22 47 27.5
B BPT 76.408 22 47 27.7
B BOT 76.428 22 47 27.8
B BSM 76.430 22 47 27.8
B BSE 76.684 22 47 29.6

* ET28 09-03-88
B ABV 82.839 21 46 17.6
B AMG 82.973 21 46 18.2
B ASN 82.378 21 46 15.1
B AVL 82.620 21 46 16.5
B ACA 82.795 21 46 17.5
B ASZ 82.420 21 46 15.7
B BMJ 82.852 21 46 17.4
B BPT 82.929 21 46 18.0
B BOT 82.806 21 46 17.4

* ET29 14-03-88
B AMG 76.470 12 41 26.4
B AVL 76.106 12 41 24.5
B ASZ 75.961 12 41 23.9
B BMJ 76.294 12 41 25.1

```
OT    76.273      12 41 25.2

ET17  24-01-89
MG   157.159      16 18 57.7
CA   157.252      16 18 58.2
ST   157.333      16 18 58.1
MT   157.536      16 18 58.5
MM   156.843      16 18 57.5
MJ   156.752      16 18 57.5
PT   156.928      16 18 57.5
OT   156.945      16 18 57.5

ET30  23-03-89
MG    41.798      15 58 12.5
VL    41.451      15 58  9.8
CA    41.615      15 58 11.4
SZ    41.228      15 58  8.2
MJ    41.705      15 58 11.3
OT    41.646      15 58 11.3

ET31  25-03-89
MG    66.711      19 47 38.2
MT    67.082      19 47 40.1
MJ    66.299      19 47 35.9
PT    66.478      19 47 35.9
OT    66.490      19 47 36.0
CR    66.584      19 47 37.0

ET32  31-03-89
BV    85.721       0  3 34.5
MG    85.843       0  3 35.1
CA    85.655       0  3 34.3
SZ    85.256       0  3 32.6
MT    85.637       0  3 34.0
MJ    85.779       0  3 34.3
OT    85.708       0  3 34.2
CR    85.633       0  3 34.0

ET33  03-04-89
BV    60.196       1 43 16.8
CA    60.275       1 43 17.8
SZ    60.687       1 43 20.7
MT    60.319       1 43 18.1
MM    60.011       1 43 15.6
MJ    60.109       1 43 16.7
OT    60.196       1 43 16.7
CR    60.278       1 43 17.3

ET35  20-04-89
BV    42.622       4 33 36.0
MG    42.705       4 33 36.6
SZ    42.080       4 33 31.6
MT    42.393       4 33 33.9
MJ    42.796       4 33 36.4
OT    42.665       4 33 36.0
MU    42.772       4 33 37.2

ET36  06-05-89
BV    81.494      16 46 21.0
MG    81.633      16 46 21.7

B ASN    81.031      16 46 18.4
B AVL    81.273      16 46 19.9
B ASZ    81.103      16 46 19.1
B AMT    81.503      16 46 20.8

*  ET34FB
B ABV    81.591      23 32 12.0
B ACA    81.543      23 32 11.8
B AST    81.738      23 32 12.6
B AMT    81.559      23 32 11.6
B BMM    81.732      23 32 12.6
B BMJ    81.611      23 32 11.6
B BOT    81.561      23 32 12.6
B BMU    81.750      23 32 12.7

**********
```

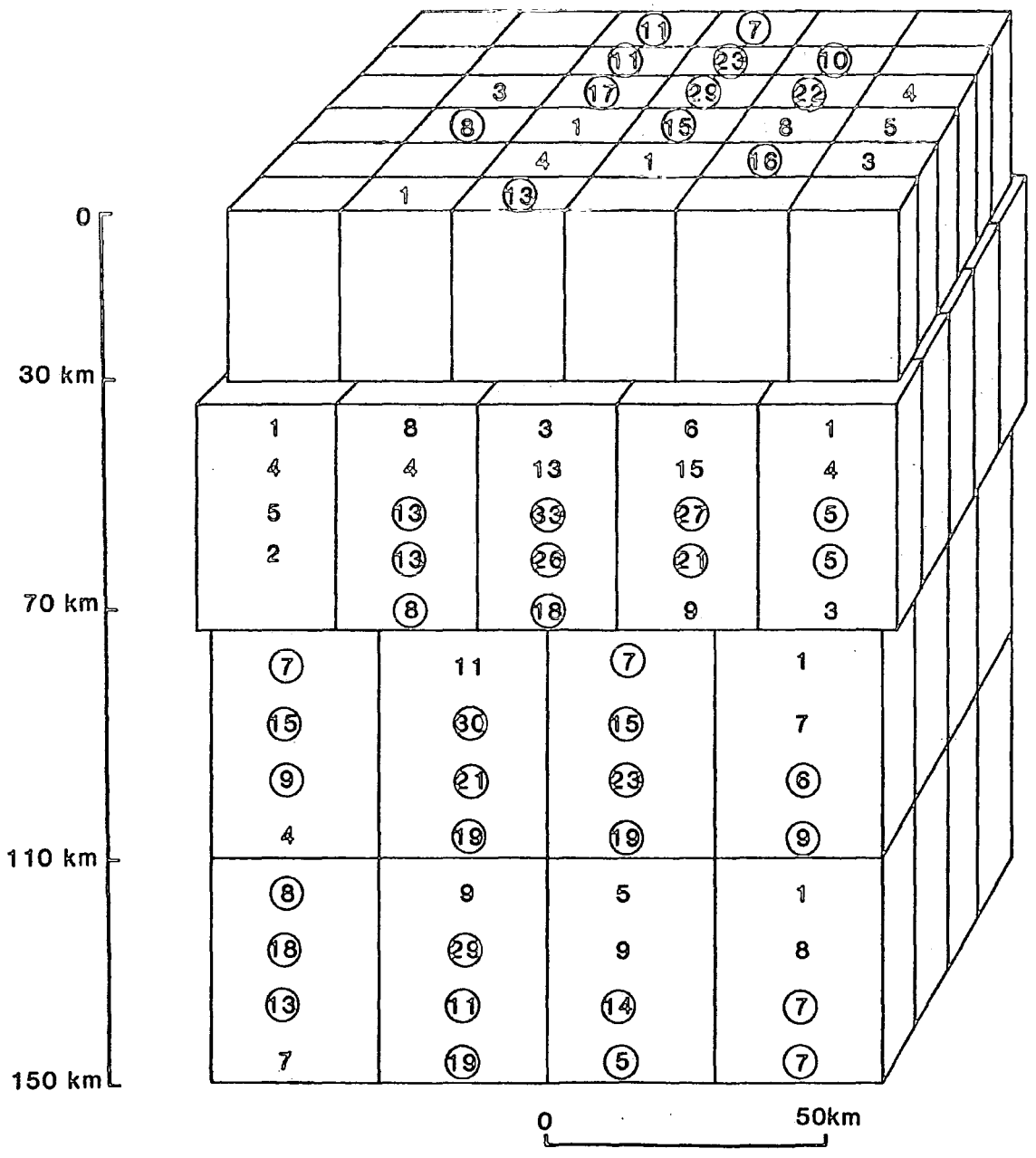

Fig. 6.4 - Adopted configuration for the velocity model. Number of hits per block is shown (top is front, bottom is back), circles indicate the blocks that were modelled.

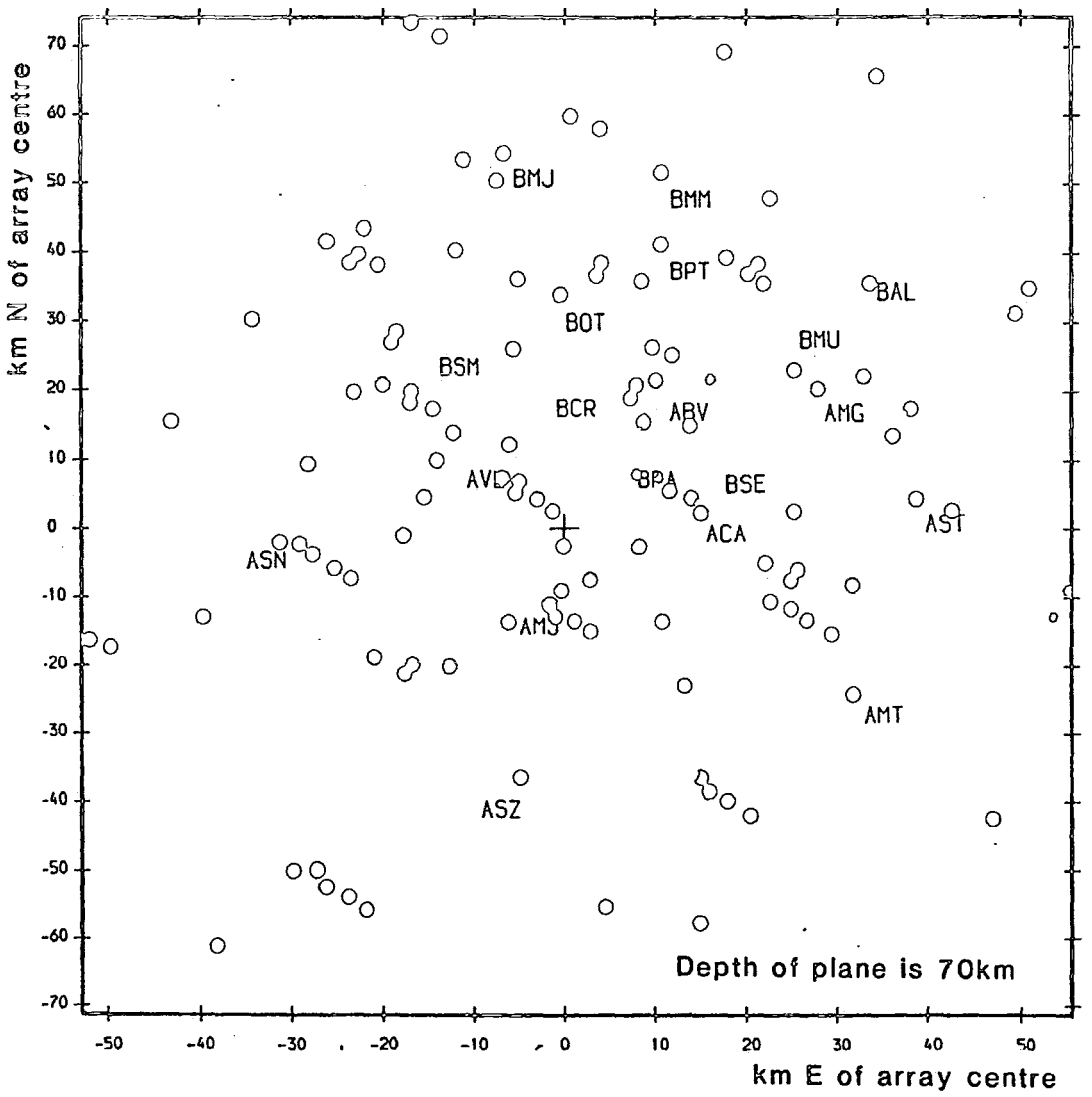

Fig. 6.5 - Distribution of the seismic rays as they cross the base of the 2nd layer (70 km).

from the line (ASN and AMT). Since negative residuals correspond to positive velocity anomalies, an increase in velocity from S to N should be expected in the volume studied.

The first step in the inversion for velocity anomalies is to choose a preliminary velocity model and the size of the model blocks. The preliminary velocity model was a combination of the crustal model of Moreira et al. (1980) for the Nazaré-Cabo Raso profile with the "normal Earth" model of Herrin (1968) for sub-Moho depths. The size of the blocks was selected by trial and error, until all but a few blocks were hit by at least five rays (this was the adopted minimum for a block to be included in the inversion).

Once the criterion concerning the number of hits was satisfied, further adjustments were made by carrying out the inversion with different configurations and investigating the changes in resolution caused by changes in block sizes, layer thicknesses and number of layers. To guide the search for a suitable configuration a value of 0.70 was established for the minimum acceptable diagonal element of the resolution matrix (with a damping constant of 0.10). Since the rows of the resolution matrix are averaging kernels (section 6.2.3), a diagonal element of 0.70 in the resolution matrix means that the estimate of the velocity anomaly for the corresponding block had a contribution of 70% from that block and a global contribution of 30% from the surrounding blocks. This criterion was verified with the configuration shown in Figure 6.4, which was then adopted. The number of hits per block is also shown in the figure. Apart from two exceptions in the upper layer, only some peripheral blocks are hit by less than five rays, and the number of hits increases substantially towards the central zone of the model. Figure 6.5 shows the distribution of the seismic rays as they cross the bottom of the second layer, at a depth of 70 km. The average velocities for the different layers with the preliminary velocity model mentioned above were, from top to bottom, 6.13 km s^{-1}, 8.06 km s^{-1}, 8.11 km s^{-1} and 8.16 km s^{-1}.

When choosing a suitable value for the damping factor θ, the trade-off between resolution loss and model error, discussed in the previous section, was taken into account. Figure 6.6 shows the average standard error for the top layer of the model and the resolution loss, as a function of the damping factor. The

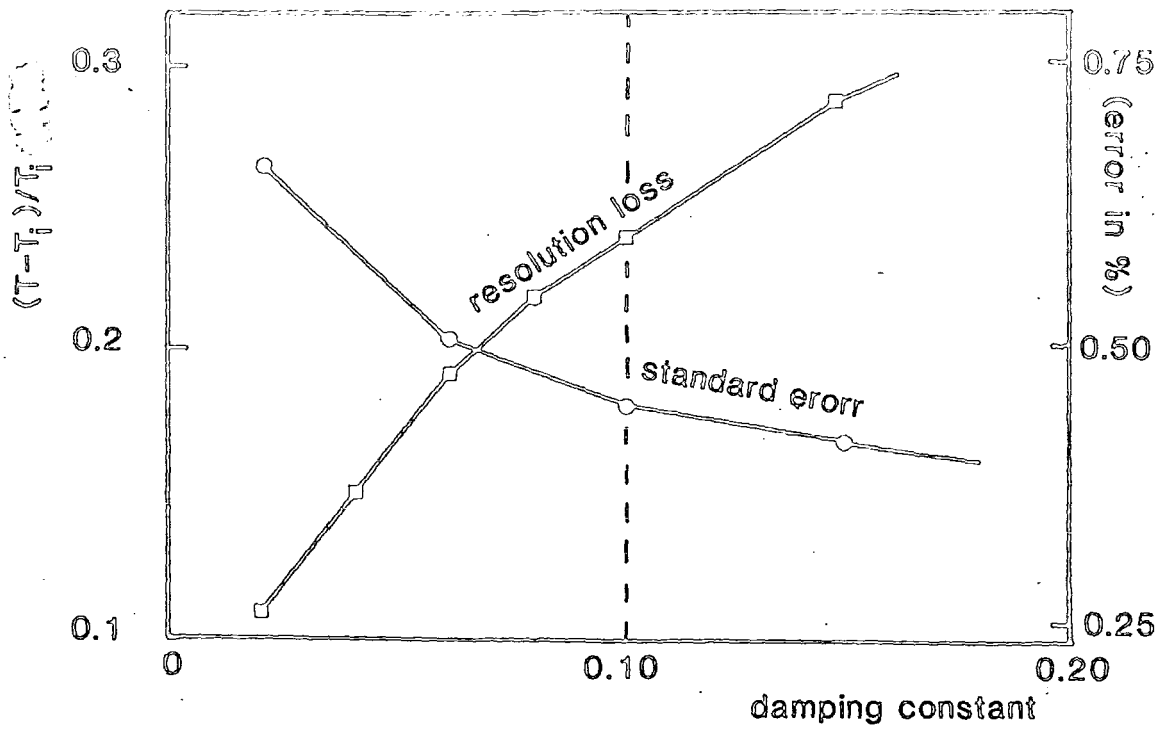

Fig. 6.6 - Trade-off between resolution loss and average standard error as a consequence of the variation of the amount of damping.

resolution loss was quantified by the percent reduction of the trace (sum of the diagonal elements) of the resolution matrix with respect to the identity matrix. A value of $\theta = 0.10$ was adopted: a higher damping causes limited reduction of the standard errors, at the cost of a significant decrease in resolution; at smaller values of θ the errors increase considerably. An average loss of about 25% in resolution results with $\theta = 0.10$, i.e., the average contribution of a particular block (in the top layer) to the estimate of its own velocity anomaly is of about 75%.

An element which is arbitrarily imposed on the final solution is the orientation of the boundaries between the blocks. In an attempt to smooth out the effect of this factor upon the solution, the inversion was carried out separately for three different orientations of the boundaries: first with N-S and E-W strikes and then with rotations of 30 and 60 degrees. The solutions for each layer were subsequently merged.

Figure 6.7 shows the final result of the inversion for the different layers, and Figure 6.8 reproduces the same result on a convenient display. Figure 6.7e) shows the vertical average of a slightly different solution, having the same configuration for all layers (that of layers 3 and 4 in figures a) to d)). The contoured quantities lack physical meaning, since they are averages of deviations with respect to different mean values, but the figure illustrates the relative importance of the anomalies observed in the different layers. It agrees with the earlier prediction of an increase of seismic velocity across the network towards the N, based on the preliminary analysis of the traveltime residuals.

The inspection of the resolution and covariance matrices is an effective way of assessing the quality of the final solution[1]. The elements of the covariance matrix are proportional to the square of the standard error of the input data (equation 6.16), and a value of 0.05 s was used for the reading error of the arrival times. The program THRD combines (sums) this value with the RMS traveltime residual for the solution, which was 0.12 s, so an effective standard error of 0.17 s in the

[1] Ellsworth (1977) demonstrates that for the damped least-squares solution the two matrices are related by $C = \frac{\sigma_d^2}{\theta^2} R(I - R)$, were I is the identity matrix. Although interdependent, the two matrices emphasize different aspects of the solution.

input data was assumed when computing the covariance matrix. The resulting standard deviation for the velocity perturbations were typically of about ± 5% (absolute errors of percentage variations).

The adopted solution was in general well resolved, most individual blocks having resolution (i.e., diagonal elements of the resolution matrix) higher than 0.75. Considering, for example, the top layer with N-S and E-W boundaries, 58% of the elements of the diagonal of the resolution matrix are above 0.85, and 83% are above 0.80. The deeper layers have slightly inferior resolution, but still, with few exceptions, above 0.75. The variance improvement defined in the previous section was 65.4%.

The off-diagonal elements of the resolution and covariance matrices elucidate the reciprocal influences between different blocks. A velocity anomaly contained totally in block i may "leak" to block j if the element r_{ij} of the resolution matrix is significantly different from zero. An error in the estimate of the velocity perturbation of block i causes an error in block j if c_{ij} is significantly different from zero. When $c_{ij} < 0$, spurious patterns of positive and negative anomalies may arise. The rows of both matrices for a selection of blocks with large anomalies are given in Appendix D, to check for the possibility of this type of "coupling" (large negative covariance) between adjacent blocks. The values show that limited coupling occurred between a number of blocks vertically adjacent (3-38; 4-39-79; 22-54; 43-66-78; 48-70; 58-75-90). This is due to the fact that those blocks shared a large number of rays, and it is therefore difficult to determine in which way they affected the traveltimes between themselves. Table 6.3 shows the largest off-diagonal elements detected. The coupling was not strong in terms of resolution (i.e., the blocks were reasonably well resolved from each other), but had significant effect on the errors. However, for the velocity perturbations of geological interest the standard errors were small anyway, so coupling does not seem to have affected the solution significantly. The detailed information pertinent to the solution is given in Appendix E.

The contoured quantity in Figures 6.7 and 6.8 is the percentage fluctuation of the velocity in each block with respect to the average velocity of the layer to which it belongs (this results from the fact that the method cannot differentiate

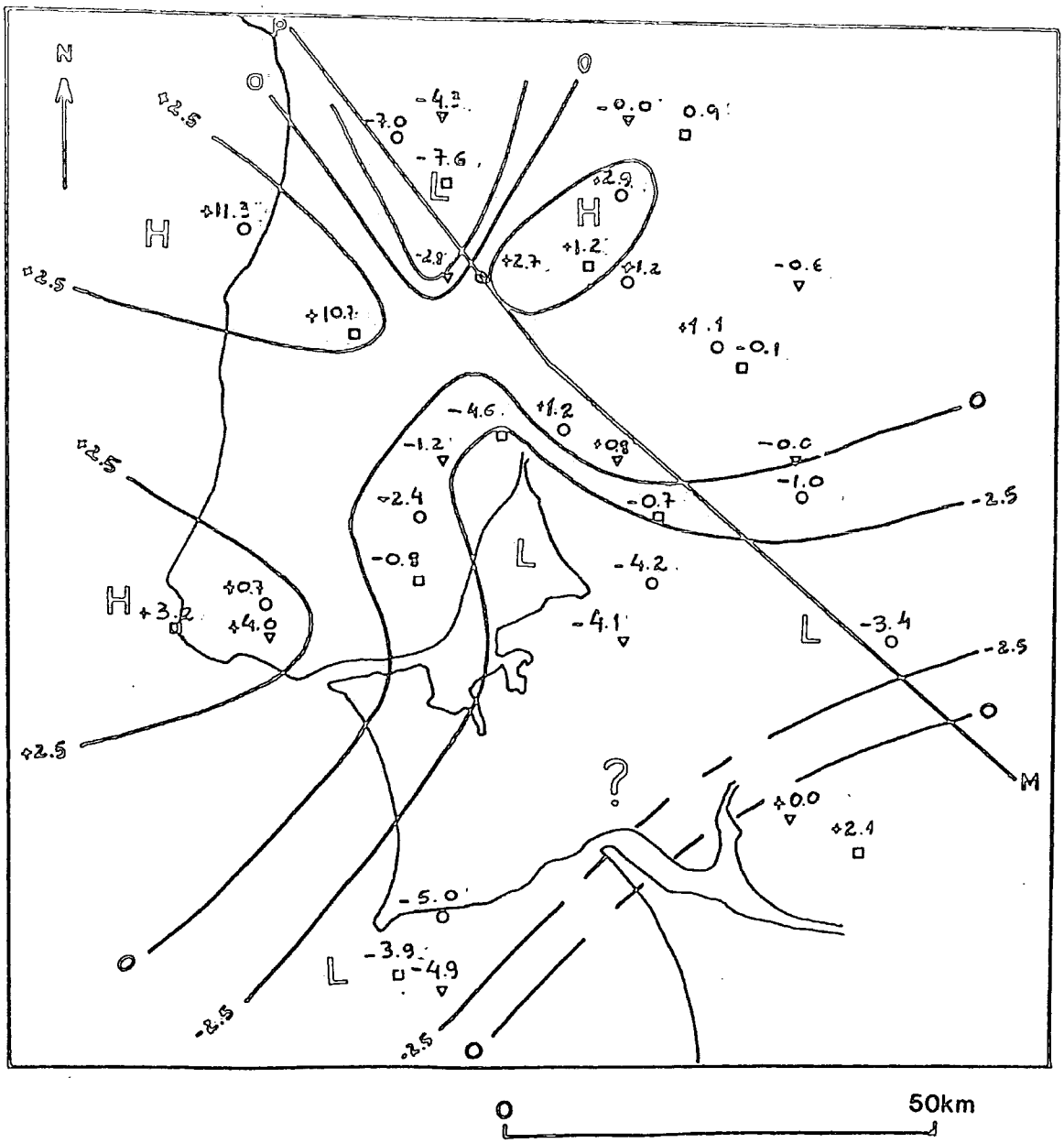

Fig. 6.7a - Tomographic inversion: solution for the top layer.

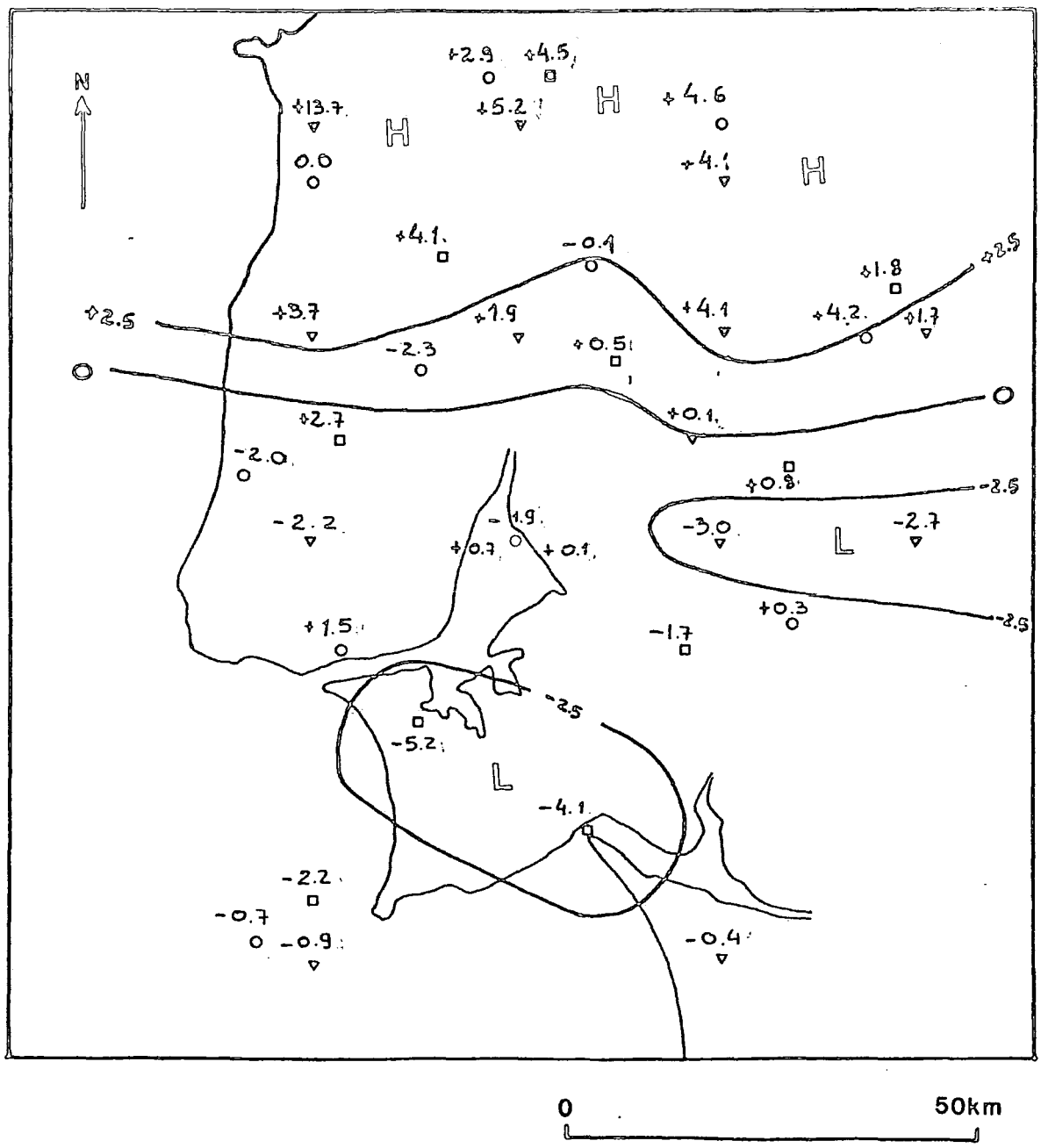

Fig. 6.7b - Tomographic inversion: solution for the second layer.

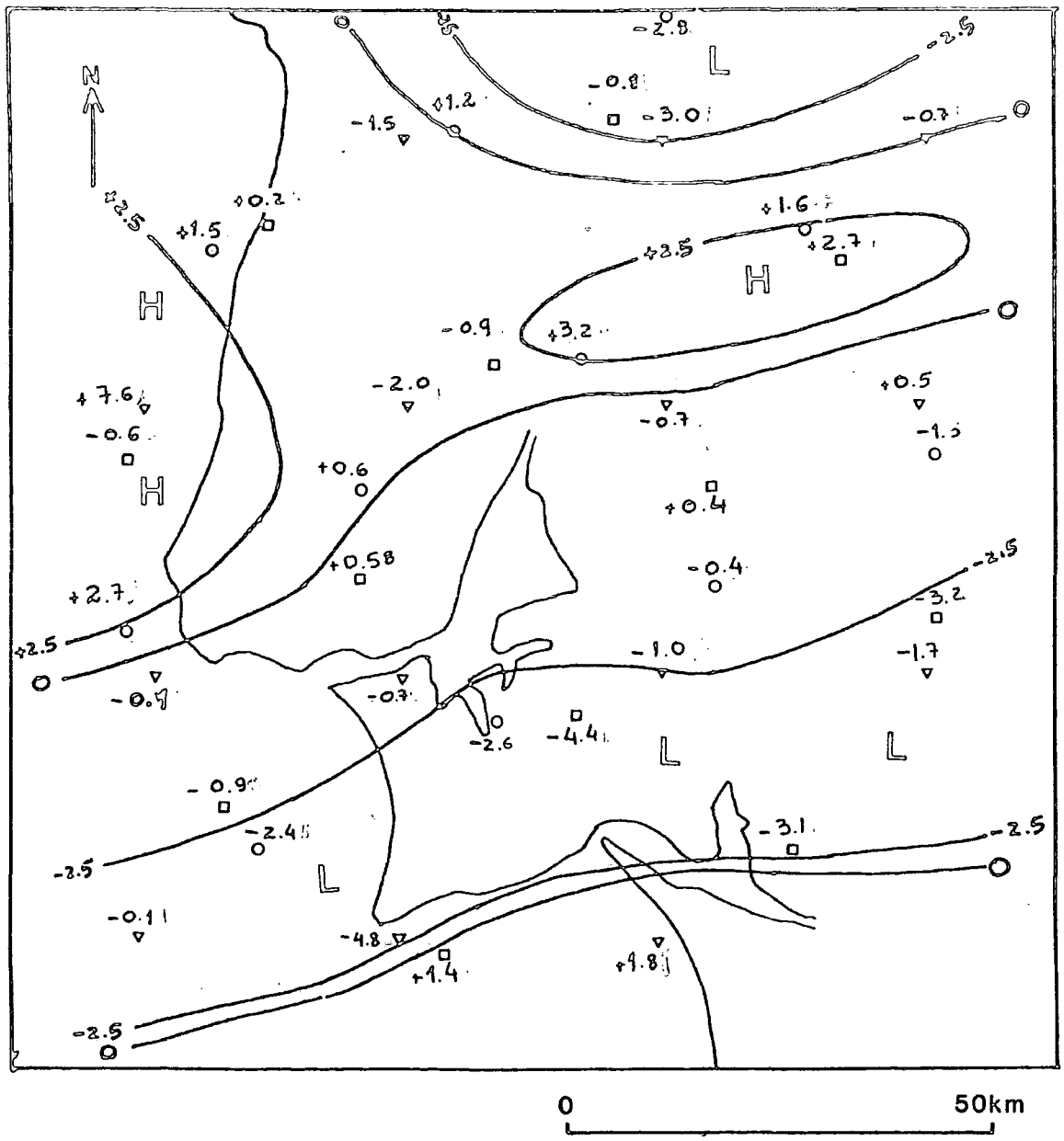

Fig. 6.7c - Tomographic inversion: solution for the third layer.

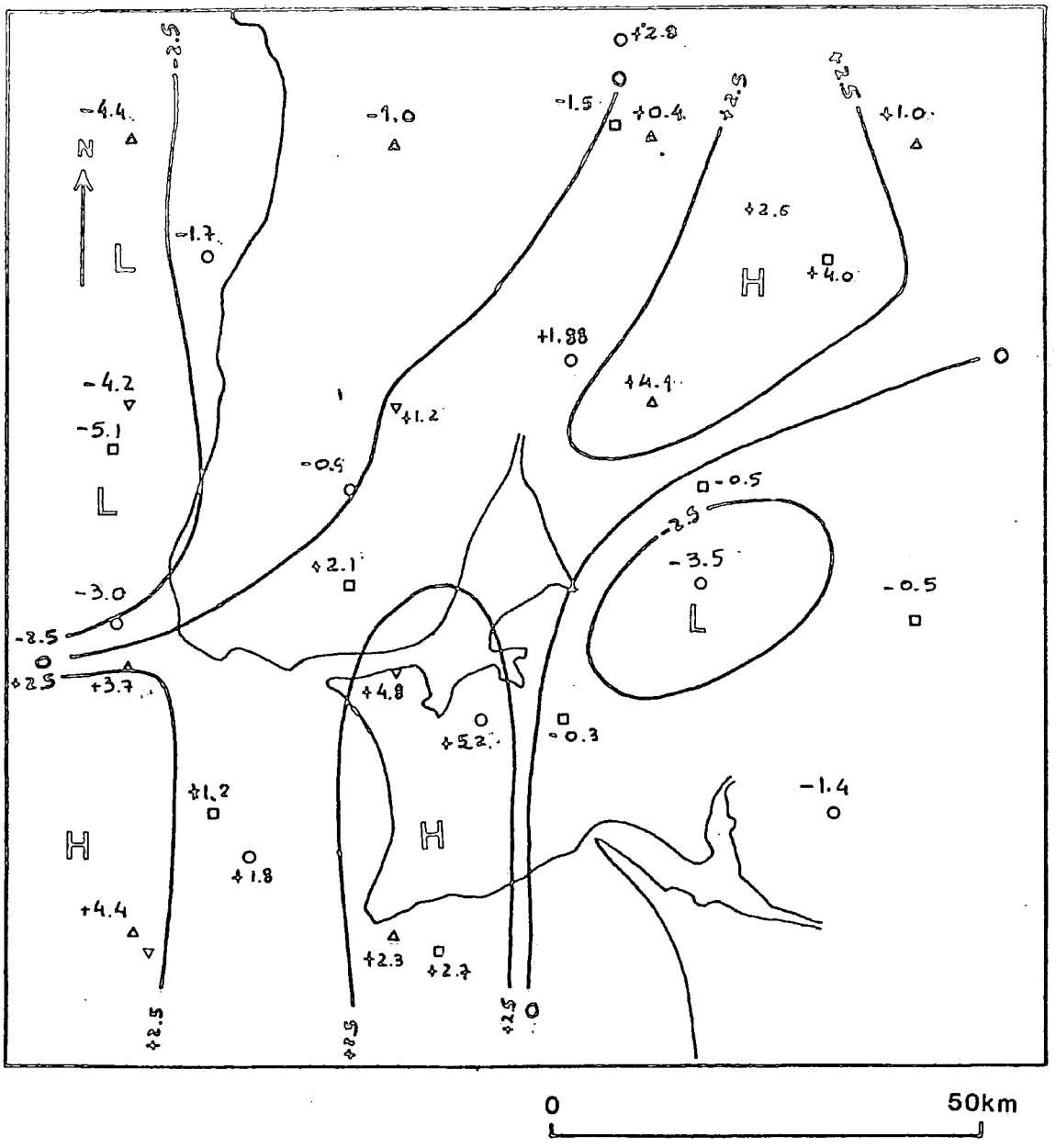

Fig. 6.7d - Tomographic inversion: solution for the bottom layer.

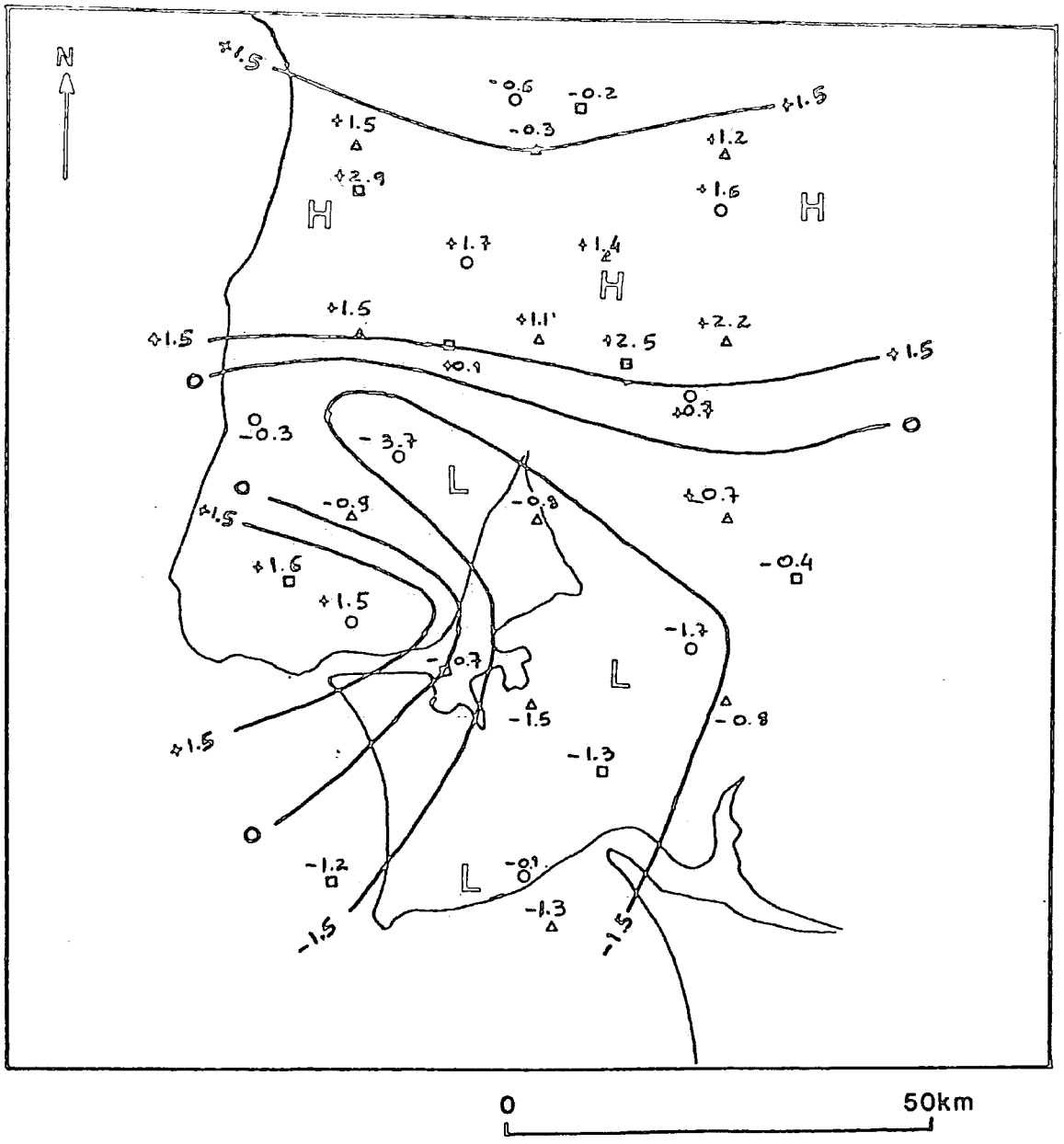

Fig. 6.7e - Tomographic inversion: vertically averaged solution.

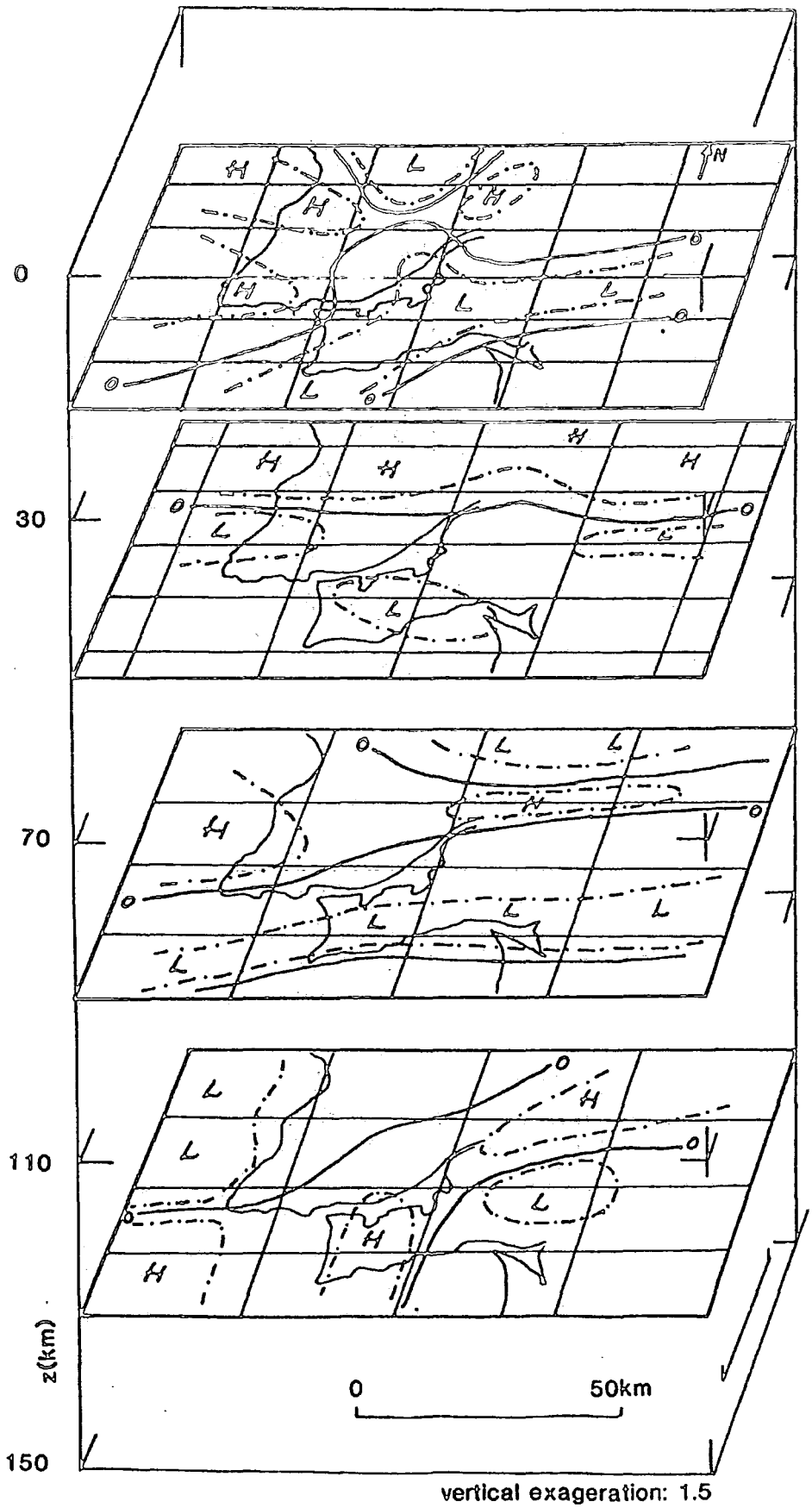

Fig. 6.8 - 3-D view of the adopted tomographic solution.

Fig. 6.9 - Magnetic anomalies (total field minus normal field) associated with the Sintra Granite. Anomalies in γ, contour interval 100 γ. Redrawn after data made available by GPEP, Lisbon.

Table 6.3 - Maximum off-diagonal elements.

i	j	r_{ij}	r_{ii}	c_{ij}	c_{ii}
3	38	0.09	0.90	-0.01	0.18
4	39	0.12	0.82	-0.12	0.28
20	47	0.16	0.84	-0.09	0.23
22	54	0.12	0.85	-0.08	0.21
39	79	0.09	0.79	-0.11	0.25
43	66	0.10	0.82	-0.10	0.25
43	78	0.07	0.82	-0.08	0.25
58	90	0.15	0.61	-0.12	0.34
75	90	0.09	0.67	-0.04	0.34

between a uniform change of velocity in any particular layer and a variation in origin time, and can be regarded as a form of horizontal coupling). A contour spacing of 2.5% is used in order to stay well above the standard deviations for the different blocks, which are always less than ±0.75%. Hence, those areas with values above +2.5% or below -2.5% can be considered significantly anomalous.

6.4 Discussion of the velocity anomalies underneath the RESTE Network.

The thickness of the top layer of the model, 30 Km (Figure 6.4), coincides roughly with the thickness of the crust. Several values were tried, but this one was selected because it provided the best resolution. The top layer exhibits the strongest anomalies, with a conspicuous zone above +10% towards the N of the model (Figure 6.7a). A second zone of weaker anomalies, with deviations of +2.9%, is located towards the W. Through the centre of the layer runs a band of low velocity, with values in the range -4.0% to -5.0% in the SW and E. This band seems to branch out near the centre of the model, nearly connecting with another zone of low velocities in the N of the top layer of the model. There, the values are in the range -4.4% to -7.7%. The central low-velocity band is consistent with the remarks made in section 4.3.2 regarding the location of event EL06: the ray that seemed then to be associated with a higher velocity (~6.0 km s^{-1}) was travelling along the southern flank of the anomaly, whereas the rays with lower average velocities (~5.5 km s^{-1}) where mostly within the anomalous zone. The inflection of one of the branches of the low-velocity zone from NE-SW to NW-SE was one of the features enhanced by the vertical average given in Figure 6.7e).

The southeastern corner of the top layer was not involved in the Mesozoic rifting process and was free from Meso-Cainozoic magmatism, and for those reasons can be considered to represent normal Iberian crust of Hercynian age. This agrees with the fact that in Figure 6.7e) that zone is free of velocity perturbations. The zone of mild positive anomalies in the W, also preserved by the vertically averaged solution, correlates well with the magnetic anomalies associated with the Sintra Granite (Figure 6.9) and may correspond to magmatic intrusions forming a high density residual root through the crust under the exposed granite.

The strong positive anomaly in the N of the top layer cannot be associated with any known magmatic body, nor does it correlate with magnetic anomalies.

The allocation of the velocity anomaly to either the top or the second layer was very unstable with respect to model parameters such as horizontal block dimensions and boundary orientations. Without changing the depth of the interface (30 Km), the anomaly was shifted to the second layer when the block size was increased from 20x20 Km^2 to 25x25 Km^2. One of the three boundary orientations used to produce the adopted solution had the same effect. This suggests that the anomalous zone straddles the interface and is artificially pulled up or down by the different configurations of the model. Together with a second zone of high velocity to its E, it is rooted on a zone of positive velocity anomalies of the uppermost mantle, discussed below.

The velocity anomalies of the crustal layer may be related to two main factors: variations of the thickness of the sediment cover, and variations of the thickness of the crust. The inclusion of 2 km of Tertiary sediments with a velocity of 3.0 km s^{-1} and 3 km of Mesozoic sediments with a velocity of 5.0 km s^{-1} (values from the refraction model of Mendes-Victor et al., 1980) in an originally homogeneous crust with a velocity of 6.13 km s^{-1} (the average crustal velocity of the initial model) causes a reduction of 5% in the average crustal velocity. However, if the sediment cover were the dominant factor, a clear correlation should emerge between the velocity anomalies and the distribution of sediments, which is not the case. For example, the negative anomalies reach maximum absolute values in the Arrábida Range, without Tertiary cover and where the Mesozoic cover was inverted, and are still large towards the E of the model, where the basement becomes shallow. Although in some areas the sediment cover may have contributed to the observed anomalies, such as in the Bombarral Sub-basin (thick Mesozoic cover) or in the Lower Tagus Valley (thick Tertiary cover), it does not always seem to be the main factor. In the Ribatejo Sub-basin (NE Lower Tagus Basin), one of the areas with thicker Tertiary cover, the observed anomalies are near zero. An explanation may be found in the structure of the Moho.

Figure 6.7a) shows the location of the Peniche-Montemor o Novo profile of Mendes-Victor et al. (1980). A clear correlation exists between the results of the profile concerning the depth of the Moho (Figure 2.4b) and the pattern of the anomalies. Zones of low velocity correspond to zones of deeper Moho (~32 km),

whereas the zone of mildly positive anomalies coincides roughly with the rise of the Moho to depths of ~25 km.

The Nazaré-Cabo Raso profile of Moreira et al. (1980), with shot point slightly to the N of the model in a region where negative velocities can be extrapolated, led to a velocity model with a sharp gradient at the bottom of the lower crust, starting at ~29 km. In the model corresponding to the Cabo Raso-Figueira da Foz profile (ibid.), the same gradient starts at ~27 km, the shot point being now in a region of positive velocity anomalies. Again, the depth to the Moho seems to have controlled the estimated average velocity of the crustal layer.

Accepting as a working hypothesis that the top layer velocity anomalies can be used to infer variations of the depth to the Moho, it becomes apparent that a contrast in crustal thickness occurs immediately to the SW of the Peniche-Montemor o Novo profile (Figure 6.7a). This contrast defines a NW-SE trend that corresponds closely to the "probable Bombarral-Vendas Novas Fault" of Cabral (1986), a surface lineament identified in satellite imagery but without any clear geological expression.

Variations in crustal thickness under the Lusitanian and Lower Tagus Basins may be related to the Miocene tectonics, which were the last deformational episode and were recent enough for the lithosphere not to have recovered its normal profile. The NNE-SSW Hercynian trend, which had an active role in the Miocene deformation (section 2.3.6), can be identified at places in Figure 6.7a). Together with the NW-SE trend mentioned above (itself Hercynian), it separates the crust into compartments with different velocity anomalies.

In Figure 6.10, the topography of the surface of the basins, a good indicator of the degree of structural inversion, is compared with the pattern of crustal velocity anomalies. It is noticeable that the two areas of low velocity are "linked" by the central inverted region of the Lusitanian Basin. Areas of positive anomaly do not overlap with the inverted regions, and the zones of highest topography (Arrábida and Montejunto Ranges) are close to the borders of the regions of negative anomaly. This may indicate that the structural inversion was part of a crustal scale deformational process. The mountain ranges of Arrábida and

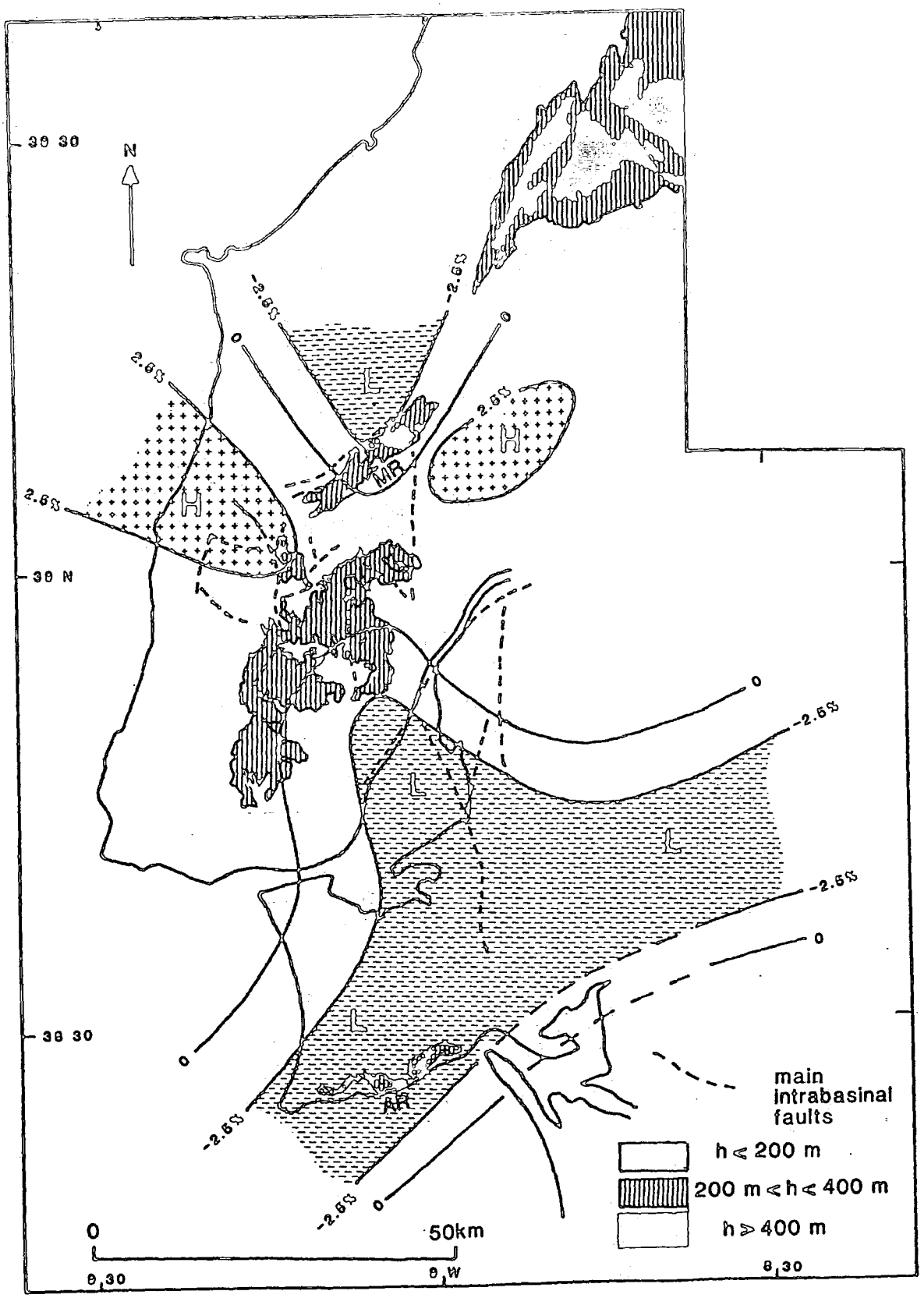

Fig. 6.10 - Comparison between the top layer velocity anomalies and the pattern of structural inversion of the Lusitanian Basin.

Montejunto were related in section 3.4 to the activity of basement strike-slip faults which were active during the Miocene (Hutton and Gawthorpe, 1988), and the correlation between structural inversion and (possibly) Moho depth would indicate that those fractures affect the entire thickness of the crust.

Although the correlation between the velocity anomalies and the areas of structural inversion is remarkable, a clear link between Moho depth and the observed velocity anomalies is probably an over-simplification. The Lower Tagus Valley was modelled in section 3.2, and interpreted in section 3.3, in a way that implied crustal thinning during the Miocene, yet it is an area of large negative anomalies, possibly as a result of sedimentation. The extension of the tomographic study to the region in the northeastern corner of Figure 6.10 would probably provide further insight into the relationship between basin inversion, velocity structure and the deformation of the crust.

Besides undulations of the Moho, another possible cause for velocity anomalies in the lower crust is magmatic underplating, a process discussed in section 3.3 in connection with the evolution of the passive margin. Magma underplated at lower crustal levels may have velocities that are between those characteristic of the lower crust and those characteristic of the upper mantle (Furlong and Fountain, 1986). It would show on a seismic sounding as a zone of anomalously high velocity, and this may be the explanation for the anomalies observed towards the northwestern corner ($> +10\%$).

With increasing depth, the interpretation of the velocity anomalies can not be supported either by the surface geology or by seismic profiles, and therefore becomes more speculative. The second layer (30 - 70 Km) corresponds to the uppermost mantle and shows a marked contrast when compared to the top layer. Two broad zones can be identified which are separated by a narrow E-W band, the one to the S with negative anomalies and the one to the N with positive anomalies. In both cases the anomalies are moderate, only exceeding $\pm 5.0\%$ in a small number of blocks. This E-W strike, which was enhanced by the vertical average shown in Figure 6.7e), bears no relation to any observable features of the surface geology (at the most, the southern edge of the positive velocity anomaly correlates well with the positive anomalies observed in the crustal layer). On the

other hand, when extrapolated westwards the trend coincides with the strike of an elongated bathymetric and gravimetric anomaly which extends offshore from the coast (Bowin et al, 1981). The free-air gravity anomaly is of the order of +200 mgal, and this large value has led to the suggestion that it may correspond to a fold in the Moho, bringing mantle rocks close to the surface (G. Karner, pers. comm.). No evidence for such a feature of the Moho can be found in the top layer of the model, indicating that the structure responsible for the offshore gravity anomaly is truncated. The trend in the uppermost mantle may nevertheless be related to the offshore structure, if the upper-plate configuration discussed in section 3.3 is adopted: the "tectonic denudation" would occur to the W of the easterly dipping detachment only, but underneath the detached crust the uppermost mantle might exhibit some structural continuity with the offshore region.

The low velocities of the uppermost mantle in the southern part of the model may be related to the upwelling of hot asthenosphere to anomalously shallow depths (<70 Km), an explanation proposed by Zandt (1981) for similar observations in California. This is suggested by the data of Camelo (1988), which shows an increase of heat flow from N to S across the trend now identified in the uppermost mantle (77, 79 and 83 mW m^{-2} to the N and 90 and 91 mW m^{-2} to the S). If this interpretation is correct, the same type of asthenospheric upwarp could be at the origin of the offshore structure responsible for the very large gravity anomaly.

Any interpretation of the velocity anomalies in layers 3 and 4 has to be highly speculative, due to the absence of any independent evidence. Furthermore, the bottom of the model is likely to incorporate velocity heterogeneities located at deeper levels (Zandt, 1981). Despite the uncertainties, layer 3 retains the broad pattern of layer 2, although the dominant trend seems to have rotated to a ENE-WSW direction, and a new (and poorly constrained) zone of low velocity anomalies emerged towards the N of the model. The band of low velocity anomalies in the southern half of the model is compatible with the previously suggested asthenospheric upwarp. The zone of positive anomalies near the northeastern corner of the model is also observed in layers 2 and 4 and, less clearly, in layer 1.

Layer 4 shows a quadrantal distribution of velocity anomalies. The two quadrants on the eastern half reproduce the pattern of layer 3, except for the northern edge. The two quadrants on the western half show the reverse of layer 3. In the northwestern quadrant this reversal does not seem to be due to vertical coupling (block 82 is well resolved and has a small covariance with block 66). The possibility of coupling cannot be ignored in the southwestern quadrant (block 90 is relatively coupled to blocks 75 and 58). Since the bottom of layer 4 is at a depth of 150 km, these anomalies may be related to the topography of the base of the lithosphere.

Suggestions for further work

Throughout this thesis, different types of information were brought together which are relevant to the tectonic characterization of the Portuguese Estremadura, with a view to improve the understanding of the intraplate seismotectonic activity of the region. Several hypotheses were put forward regarding a variety of geological aspects, which could be investigated with specific studies.

Of critical importance would be the detailed survey of heat flow in the Meso-Cainozoic sedimentary basins, which would provide further constrainment on the evolution of the basins, discussed in chapter 3.

The study of the deep crustal structure off the western coast of Portugal with high-resolution normal-incidence reflection and wide-angle reflection seismic profiles would allow a better understanding of the rifting mechanism at the Portuguese margin. In addition, it would probably help understanding the Cainozoic geodynamics and the current seismotectonics. (This study is the object of a research proposal currently pending approval.)

The complexities of the structural inversion of the Lusitanian Basin, which motivated a preliminary field survey under the RESTE Programme, deserve further research in order to characterize better the basin as a geodynamic entity. (In fact, this research topic outlasted the Programme, and is becoming increasingly active.)

Finally, the monitoring of the microearthquake activity in the Estremadura should become a routine, ideally in the context of a broader programme of seismic hazard assessment and earthquake prediction. The knowledge of the neotectonics would be augmented by palaeoseismicity studies on trenches dug in the fluvial

terraces of the southern margin of the Tagus River. Direct stress measurements would also provide important information on the state of the crust.

To provide information on co-seismic deformation in the event of a large ($M_L \sim 7$) earthquake in the Lower Tagus Valley, the improvement of the standards of the regional seismographic network would be beneficcialy complemented by the installation of a GPS geodetic network in the region (Fonseca and Foulger, 1989).

Cited References

1. Adams, R. D., 1977.*Survey on practice for determining magnitudes of near earthquakes*, Report SE-8, World Data Center A, Boulder, Colorado.
2. Aires-Barros, L., 1979. Actividade ígnea pos-Paleozóica no continente Português (elementos para uma síntese crítica), *Ciências da Terra*, **5**, 145-198.
3. Aki, K., Christoffersson, A. and Husebye, E., 1977. Determination of the three-dimensional seismic structure of the lithosphere, *J. Geophys. Res.*, **82** (2), 277-296.
4. Aki, K. and Lee, W. H. K., 1976. Determination of the three-dimensional velocities under a seismic array using first P-arrival times from local earthquakes; 1 - a homogeneous model, *J. Geophys. Res.*, **81** (23), 4381-4399.
5. Aki, K. and Richards, P. R., 1980. *Quantitative Seismology, Vol. 2*, W. H. Freeman and Company, New York.
6. Arthaud, F. and Matte, Ph., 1975. Les décrochements tardi-Hercyniens du sud-ouest de l'Europe. Geometrie et essai de reconstrution des conditions de deformation, *Tectonophysics*, **25**, 139-171.
7. Arthaud F. and Matte Ph., 1977. Late Palaeozoic strike-slip faulting in southern Europe and northwest Africa: result of a right-lateral shear zone between the Appalachians and the Urals, *Geol. Soc. Am. Bull.*, **88**, 1305-1320.
8. Backus, G. E. and Gilbert, J. F., 1967. Numerical applications of a formalism for geophysical inverse problems, *J. Geophys. Res.*, **13**, 247-276.
9. Backus, G. E. and Gilbert, J. F., 1968. The resolving power of gross Earth data, *Geophys. J.R. astr. Soc.*, **16** , 169-205.
10. Backus, G.E. and Gilbert, J. F., 1969. Constructing P-velocity models to fit restricted sets of traveltime data, *Bull. Seism. Soc. Am.*, **59** (3), 1407-1414.
11. Backus, G. E. and Gilbert, J. F., 1970. Uniqueness in the inversion of inaccurate gross Earth data, *Phil. Trans. R. Soc. Lond.*, **A266**, 123-192.
12. Bally, A. W., 1981. Atlantic type margins , in *Geology of passive continental margins*, Education Course Note Series 19, American Association of Petroleum Geologists.
13. Bellon, H. and Letouzey, J., 1977. Volcanism related to plate-tectonics in the western and eastern Mediterranean, in B. Biju-Duval and L. Montadert (eds.), *Proccedings of the International Symposium on the structural history of the Mediterranean Basins, Split, October, 1976*, Technip, Paris.
14. Berthou, P. Y. and Lauverjat, J., 1979. Essai de synthese paleogeographique et paleobiostratigraphique du Bassin Occidental Portugais au cours du Cretace Superieur, *Ciências da Terra*, **5**, 121-144.

15. Blenkinsop, T.G., Long, R.E., Kusznir, N.J. and Smith, M.J., 1986. Structural control of intraplate earthquakes, *J. Geol. Soc. Lond.*, 143, 327 - 334.

16. Boillot, G., Mallod, J. A., Dupeuble, P. A. and CYBERE Group, 1987. Mesozoic evolution of Ortegal Spur, North Galicia Margin: comparison with adjacent margins, Initial Reports of the Deep Sea Drilling Project (Part A), Volume CIII, U. S. Government Printing Office, Washington D.C.

17. Bott, M. H. P., 1971. Evolution of young continental margins and formation of shelf basins, *Tectonophysics*, 11, 319-327.

18. Bott, M. H. P., 1980. Problems of passive continental margins from the viewpoint of the geodynamics project: a review, *Phil. Trans. R. Soc. Lond.*, A294, 5-16.

19. Bott, M. H. P., 1982. *The interior of the Earth*, Arnold, London.

20. Bott, M. H. P. and Dean, D. S., 1972. Stress systems at young continental margins, *Nature*, 235 (54), 23-25.

21. Bowin, C., Warsi, W. and Milligan, J., 1981. *Free air gravity anomaly map of the world*, Woods Hole Oceanographic Institution, Woods Hole, Massachusets.

22. Buforn, E., Udias, A. and Colomas M., 1988. Seismicity, source mechanisms and tectonics of the Azores-Gibraltar plate boundary, *Tectonophysics*, 152, 89-118.

23. Buforn, E., Udias, A. and Mezcua, J., 1988. Seismicity and focal mechanisms in South Spain, *Bull. Seism. Soc. Am.*, 78 (6), 2008-2024.

24. Buland, R., 1976. The mechanisms of locating earthquakes. *Bull. Seismol. Soc. Am.*, 66, 173-187.

25. Burg, J. P., Iglesias, M., Laurent, P., Matte, P. and Ribeiro, A., 1981. Variscan intracontinental deformation: the Coimbra-Cordoba Shear Zone (SW Iberian Peninsula), *Tectonophysics*, 78, 161-177.

26. Burke, K., 1976. Development of graben associated with the initial ruptures of the Atlantic Ocean, *Tectonophysics*, 36.

27. Bullard, E. C., Everett, J. E. and Smith, A. G. , 1965. The fit of the continents around the Atlantic, *Phil. Trans. R. Soc. Lond.*, A258, 41-51.

28. Bullen, K. E. and Bolt, B. A., 1985. *An introduction to the theory of Seismology*, 4th edition, Cambridge University Press, Cambridge.

29. C.N.F.G., 1980. Geologie des pays europeens: Espagne, 26e Congres Geologique International, Paris.

30. Cabral, J., 1986. A Neotectónica em Portugal Continental - estado actual dos conhecimentos, *Maleo*, 2, 3-5.

31. Cabral, J. 1989. An example of intraplate neotectonic activity, Vilariça Basin, Northeast Portugal, *Tectonics*, 8 (2), - .

32. Cabral, J., Dias, R. and Brum, A., 1984. Estudo de falhas afectando formações Plio-Quaternárias na zona da Fonte da Telha (Península de Setubal), *Comunicações dos Serviços Geológicos de Portugal*, 70 (1), 83-91.

33. Caetano, H., 1984. Structure crustale de la zone sud-portugaise et de la zone Ossa-Morena d'apres les etudes de sismologie experimentale, unpublished Ph.D. Thesis, Université Pierre et Marie Curie, Paris.

34. Caire, A., 1979. Geotéctonique giratoire, *Geologie en Mijnbouw*, 58 (2), 241-252.

35. Camelo, S. M. L., 1987. Analysis of bottom-hole temperature and preliminary estimation of heat flow in the portuguese sedimentary basins, *Revista Brasileira de Geofísica*, 5, 139-142.

36. Carvalho, A. M. G., 1968. *Contribuição para o conhecimento geológico da Bacia Terciaria do Tejo*, Memória 15 (Nova Série), Serviços Geológicos de Portugal, Lisbon.

37. Chen, W. P. and Molnar, P., 1983. Focal depth of intracontinental and intraplate earthquakes and their implications for the thermal and mechanical properties of the lithosphere. *J. Geophys. Res.*, 88 (B5), 4183-4214.

38. Choffat, P., 1907. *Notícia sobre a Carta Hypsométrica de Portugal*, Comissão do Serviço Geológico de Portugal, Lisbon.

39. Choffat, P. and Bensaúde, A., 1912. *Estudos sobre o sismo do Ribatejo de 23 de Abril de 1909*, Comissão do Servico Geológico de Portugal, Lisbon.

40. Chow, C. W. and Booker, J. R., 1979. A Backus-Gilbert approach to inversion of travel-time data for three-dimensional velocity structure, *Geophys. J. R. astr.Soc.*, 59, 325-344.

41. Coelho, A. G., 1986. *Aproveitamento de Almourol; estudo por detecção remota do Vale do Tejo e do Sítio do Almourol com base em imagens MSS do LANDSAT*, Report 33-86-NP, LNEC, Lisbon (unpublished).

42. Cox, K. G., 1980. A model for flood basalt volcanism, *J. Petrology*, 21 (4), 625-650.

43. Crowell, J.C., 1974. Origin of Late Cenozoic basins in Southern California, in Dickinson, W.R. (ed.), *Tectonics and sedimentation*, Special Publication no. 22, Society of Economic Palaeontology and Mineralogy, Tulsa.

44. Davis, D.M. and Engelder, T., 1987. Thin skinned deformation over salt, in Lerche, I. and O'Brien, J.J. (eds.), *Dynamical geology of salt and related structures*, Academic Press, 1987.

45. Dewey, J. F., 1988. Extensional collapse of orogens, *Tectonics*, 7 (6), 1123-1139.

46. Dewey, J. F., Pitman III, W., Ryan, W. and Bonnin, J., 1973. Plate Tectonics and the evolution of the Alpine System, *Geol. Soc. Am. Bull.*, 84, 3137-3180.

47. Dewey, J.F., Helman, M.L., Turco, E., Hutton, D.H.W. and Knott, S.D., in press. Kinematics of the western Mediterranean.

48. Dewey, J.F., Hempton, M.R., Kidd, W.S.F., Saroglu, F., Sengör, A.M.S., 1986. Shortening of continental lithosphere : the neotectonics of Eastern Anatolia - a young collision zone, in Coward, M.P. and Ries, A.C. (eds), *Collision tectonics*, Special Publication no. 19, Geological Society, London, 1986.

49. Dias, R. P. and Cabral, J., in press. Neogene and Quaternary reactivation of the Ponsul River Fault, in *Proceedings of the Symposium on the Seismicity, Seismotectonics and Seismic Risk of the Ibero-Moghrebi Region, Madrid, April 1989*, Instituto Geografico Nacional, Madrid.

50. Ellsworth, W. L., 1977. Three-dimensional structure of the crust and mantle beneath the island of Hawaii, unpublished Ph.D. Thesis, Massachusetts Institute of Technology.

51. Evans, J. R., 1986. Teleseismic traveltime residual analysis system: a user's manual (draft), U. S. Geological Survey, Menlo Park.

52. Fonseca, J. F. B. D., Long, R. E., Costa-Nunes, J. A., Reis, P. A. and Moreira, V. J. S., 1988. Seismicity and regional Tectonics of the Portuguese Estremadura, in *Proceedings of the International Seminar on the Prediction of Earthquakes, Lisbon, November 14-18, 1988*, LNEC, Lisbon.

53. Fonseca, J. F. B. D. and Foulger, G. R., 1989. Geodesia Espacial GPS e o estudo de sismos destructivos: razões para uma rede GPS em Portugal, paper presented at the *Encontro sobre Sismologia e Engenharia Sísmica*, LNEC, Lisbon, November 6-7, 1989.

54. Fonseca, J. F. B. D. and Long R. E., in press. Seismotectonics of SW Iberia: a distributed plate margin?, in *Proceedings of the Symposium on the Seismicity, Seismotectonics and Seismic Risk of the Ibero-Moghrebian Region, Madrid, April 12-14, 1989*, Instituto Geografico Nacional, Madrid.

55. Fonseca, J. F. B. D. and Long, R. E., in press. Seismotectonics of Western Portugal, in *Proceedings of the 4th International Symposium on the Analysis of Seismicity and Seismic Risk, Bechyne Castle, Czechoslovakia, September 1989*, Czechoslovak Academy of Science, Prague.

56. Freire-Andrade, C., 1938. *Os vales submarinos portugueses e o diastrofismo das Berlengas e da Estremadura (english summary)*, Serviços Geológicos de Portugal, Lisbon.

57. Furlong, K. P. and Fountain, D. M., 1986. Continental crustal underplating: thermal considerations and seismic-petrological consequences, *J. Geophys. Res.*, **91** (B8), 8285-8294.

58. Gagnepain-Beneix, J., Haessler, H. and Modiano, T., 1982. The Pyrenean Earthquake of February 29, 1980: an example of complex faulting, *Tectonophysics*, **85** , 273-290.

59. Galdeano, A., Moreau, M. G., Pozzi, J. P., Berthou, P. Y. and Malod, J. A., 1989. New palaeomagnetic results from Cretaceous sediments near Lisboa (Portugal) and implications for the rotation of Iberia, *Earth Planet. Sci. Lett.*, **92**, 95-106.

60. Gealey, W. K., 1988. Plate tectonic evolution of the Mediterranean-Middle East region, *Tectonophysics*, **155**, 285-306.

61. Gibbs, A. D., 1984. Structural evolution of extensional basin margins, *J. geol. Soc. London*, **141**, 609-620.

62. Gibbs, A. D., 1985. Structural Geology Course Notes: basin development, Midland Valley Exploration Ltd, Glasgow (unpublished).

63. Grimaud, S., Boillot, G., Collette, B. J., Mauffret, A., Miles, P. R. and Roberts, D. B., 1982. Western extension of the Iberian-European plate boundary during the Early Cenozoic (Pyrenean) convergence: a new model, *Marine Geology*, **45**, 63-77.

64. Grimison N. and Chen W. (1986). The Azores-Gibraltar plate boundary: focal mechanisms, depth of earthquakes and their tectonic implications, *J. Geoph. Res.*, **91** (B2), 2029-2047.

65. Groupe Galice, 1976. The continental margin off Galicia and Portugal: acoustical stratigraphy, dredge stratigraphy, and structural evolution, Initial Reports of the Deep Sea Drilling Project, Volume XLVIII (2), U. S. Government Printing Office, Washington D.C.

66. Grow, J. A., 1981. Structure of the Atlantic margin of the United States, in *Geology of passive continental margins*, Education Course Note Series 19, American Association of Petroleum Geology.

67. Guery, F., 1984. Evolution sedimentaire et dynamique du bassin marginal ouest-portugais au Jurassique, Province d'Estremadura (secteur de Caldas da Rainha-Montejunto), unpublished Ph.D. Thesis, Université de Lion I.

68. Guery, F., Montenat, G. and Vachard, D., 1986. Evolution tectono-sedimentaire du Bassin Portugais au Mesozoique suivant la transversale de Peniche (Estremadura) , *Bull. Centre Rech. Explor.-Prod. Elf-Aquitaine*, **10** (1), 83-94.

69. Gutemberg, B. and Richter, C. F., 1942. Earthquake magnitude, intensity, energy and acceleration, *Bull. Seism. Soc. Am.*, **32**, 163-191.

70. Harding, T. P., 1985. Seismic characteristics and identification of negative flower structures, positive flower structures and positive structural inversion, *Am. Assoc. Petr. Geol. Bull.*, **69** (4), 582-600.

71. Harding, T. P. and Tuminas, A. C., 1988. Interpretation of footwall (lowside) fault traps sealed by reverse faults and convergent wrench faults, *Am. Assoc. Petr. Geol. Bull.*, 72 (6), 738-757.

73. Houseman, G. and England, P., 1986. Finite strain calculations and continental deformation I - Method and general results for convergent zones, *J. Geophys. Res.*, **91** (B3), 3651-3663.

74. Hubbard, R. J., 1988. Age and significance of sequence boundaries on Jurassic and Early Cretaceous rifted continental margins, *Am. Assoc. Petr. Geol. Bull.*, 72 (1), 49-72.

75. Hutton, D. and Gawthorpe R., 1988. Strike-slip inversion of the Lusitanian Basin, Portugal (abstract), Meeting of the Tectonic Studies Group of the Royal Geological Society, London, December 1988.

76. Jackson, D. D., 1972. Interpretation of inaccurate, insufficient and inconsistent data, *Geophys. J. R. astr. Soc.*, **28**, 97-109.

77. Jackson, J. and McKenzie, D., 1988. The relationship between plate motions and seismic moment tensors, and the rates of active deformation in the Mediterranean and Middle East,*Geophys. J. R. astr. Soc.*, **93**, 45-73.

78. Jaritz, W., 1987. The origin and development of salt structures in Northwest Germany, in I. Lerche and J. J. O'Brien (eds.),*Dynamical Geology of salt and related structures*, Academic Press, New York.

79. Julivert, M., Fontbote, J. M., Ribeiro, A. and Conde, L., 1974. Mapa Tectonico de la Peninsula Iberica y Baleares, Instituto Geologico y Minero de Espana, Madrid.

80. Karner, J. D., Grimison, N. L. and Weissel, J. K., 1985. SEASAT derived gravity and geoid anomalies of the Azores-Gibraltar plate boundary: a difuse zone of ocean-ocean convergence near Gibraltar (abstract), *EOS Transactions*, **66** (18), 631.

81. Keen, C. E., 1982. The continental margins of Eastern Canada: a review, in R. A. Scrutton (ed.), *Dynamics of passive margins*, American Geophysical Union and Geological Society of America, Washington D.C.

82. Keen, C. E. and deVoogd, B., 1988. The continent-ocean boundary at the rifted margin off Eastern Canada: new results from deep seismic reflection studies, *Tectonics*, 7 (1), 107-124.

83. Kidd, R. B., Searle, R. C., Ramsay, A. T. S., Prichard, H. and Mitchell, J., 1982. The geology and formation of King's Trough, Northeast Atlantic Ocean, *Marine Geology*, **48**, 1-30.

84. Klein, F.W., 1978. *Hypocentre location program HYPOINVERSE*, U.S. Geological Survey Open File Report 78-694.

85. Klitgord, K. D. and Schouten, H., 1986. Plate kinematics of the Central Atlantic,in *The geology of North America, Vol. M, the Western North Atlantic Region*, Geological Society of America, Boulder, Colorado.

86. Kristofferssen, Y., 1978. Sea-floor spreading and the early openning of the North Atlantic, *Earth Planet. Sci. Lett.*, **38**, 273-290.

87. Kusznir, N. J. and Bott, M. H. P., 1977. Stress concentrations in the upper lithosphere caused by the underlying visco-elastic creep, *Tectonophysics*, 43, 247-256.

88. Kusznir, N. J. and Park, R. K., 1984. Intraplate lithosphere deformation and the strength of the lithosphere, *Geophys. J. R. astr. Soc.*, 79, 513-538.

89. Kusznir, N. J. and Egan, S. S., in press. Simple-shear and pure-shear models of extensional sedimentary basin formation: application to the Jeanne D'Arc Basin, Grand Banks of Newfoundland.

90. Lanczos, C., 1961. *Linear differential operators*, D. Van Nostrand Company Limited, London.

91. Laughton, A. S., Roberts, D. G. and Graves, R. , 1975. Bathymetry of the Northeast Atlantic: Mid Atlantic Ridge to Southwest Europe, *Deep-Sea Res.*, 22, 791-810.

92. Lee, W. H. K. and Stewart, S. W., 1981. *Principles and applications of microearthquake networks*, Academic Press, New York.

93. Leminsky, P. J. and Brown, L. D., 1988. Variable crustal structure of strike-slip fault zones as observed on deep seismic refraction profiles, *Geol. Soc. Am. Bull.*, 100, 665-676.

94. LePichon, X. and Sibuet, J. C., 1971. Comments on the evolution of the Northeast Atlantic, *Nature*, 233, 257-258.

95. LePichon, X., Sibuet, J. C. and Francheteau, J., 1977. The fit of the continents around the North Atlantic Ocean, *Tectonophysics*, 38, 169-209.

96. Lister, G. S., Etheridge, M. A. and Symonds, P. A., 1986. Detachment faulting and the evolution of passive continental margins, *Geology*, 14, 246-250.

97. Long, R.E., 1988. A seismotectonic model for NW Europe and its significance in hazard assessment, in *Proceedings of the International Seminar on Earthquake Prediction, Lisbon, November 1988*, LNEC, Lisbon.

98. Lopez-Arroyo, A. and Udias, A., 1972. Aftershock sequence and focal parameters of the February 28, 1969 Earthquake of the Azores-Gibraltar Fracture Zone, *Bull. Seism. Soc. Am.*, 62 (3), 699-720.

99. Lopez-Casado, C. and Sanz-de-Galdeano, C., 1988. Earthquakes with a focal depth measuring between 40 and 180 km and tectonics in Southern Spain and Northwest Africa, in *Proceedings of the International Seminar on the Prediction of Earthquakes, Lisbon, November 1988*, LNEC, Lisbon.

100. Manspeizer, W., 1981. Early Mesozoic basins of the Central Atlantic passive margins : History, structure and sedimentologic record, with special emphasis on the Atlantic Margin, in *Geology of passive continental margins*, Education Course Note Series 19, American Association of Petroleum Geology.

101. Manspeizer, W., Puffer, F. H. and Cousminer, H. L., 1978. Separation of Morocco and eastern North America: a Triassic-Liassic stratigraphic record, *Geol. Soc. Am. Bull.*, 89, 901-920.

102. Masson, D. G. and Miles, P. R., 1984. Mesozoic sea-floor spreading between Iberia, Europe and North America, *Marine Geology*, 56, 279-287.

103. Masson, D. G. and Miles, P. R., 1986. Development and hydrocarbon potential of Mesozoic sedimentary basins around margins of the North Atlantic, *Am. Assoc. Petr. Geol. Bull.*, 70 (6), 721-729.

104. Mauffret, A., Mougenot, D., Miles, P. R. and Malod, J. A., in press. Cenozoic deformation and Mesozoic abandoned spreading centre in the Tagus Abyssal Plain (West of Portugal): results of a multichannel seismic survey, *Can. J. Earth Sci.*

105. McKenzie, D., 1978. Some remarks on the development of sedimentary basins, *Earth Planet. Sci. Lett.*, 40, 25-32.

106. McKenzie, D. and Bickle, M. J., 1988. The volume and composition of melt generated by extension of the lithosphere, *J. Petrology*, 29 (3), 625-679.

107. Meissner, R. and Strehlau, J., 1982. Limits of stress in continental crusts and their relation to the depth-frequency distribution of shallow earthquakes, *Tectonics*, 1, 73-89.

108. Meissner, R. and Wever, T., 1986. Intracontinental seismicity, strenght of crustal units, and the seismic signature of faults, *Phil. Trans. R. Soc. Lond.*, A317, 45-61.

109. Mendes-Victor, L.A., Hirn, A. and Veinante, J., 1980. A seismic line across the Tagus Valley: possible evolution of the crust. Annales de Geophysique, 36 (4), 469-476.

110. Minster, J. B. and Jordan, T. H., 1978. Present day plate motions, *J. Geophys. Res.*, 83 (B11), 5331-5354.

111. Molnar, P., 1988. Continental tectonics in the aftermath of plate tectonics, *Nature*, 335, 131-137.

112. Molnar, P. and Tapponier, P., 1975. Cenozoic tectonics of Asia: effects of a continental collision, *Science*, 189, 419-426.

113. Montadert, L., Roberts, D. G., Auffret, G. A. and Gennoc, P., 1979. Rifting and the subsidence of Northern continental margin of the Bay of Biscay, in *Initial Reports of the Deep Sea Drilling Project*, U. S. Government Printing Office, Washington D.C.

114. Montenat, C., Guery, F., Jamet, M. and Berthou, P., 1988. Mesozoic evolution of the Lusitanian Basin: comparison with the adjacent margin, in *Proceedings of the Ocean Drilling Program (Scientific Results), Volume CIII*, U. S. Government Printing Office, Washington D.C.

115. Moreira, V.J.S., 1984. Sismicidade histórica de Portugal Continental, *Revista do Instituto Nacional de Meteorologia e Geofísica*, special publication.

116. Moreira, V.J.S., 1985. Seismotectonics of Portugal and its adjacent area in the Atlantic, *Tectonophysics*, 117, 85-96.

117. Moreira, V. J. S., Prodehl, C., Mueller, St. and Mendes, A. S., 1980. Crustal Structure of Western Portugal, in *Proceedings of the 17th Assembly of the ESC, Budapest, 1980*, Hungarian Academy of Science, Budapest.

118. Mougenot, D., 1976. Géologie du plateau continental portugais (entre le Cap Carvoeiro et le Cap de Sines), unpublished thesis, Université de Rennes.

119. Mougenot, D., Monteiro, J. H., Dupeuble, P. A. and Malod, J. A., 1979. La marge continentale sud-portugaise: évolution structurale et sedientaire, *Ciências da Terra*, 5, 223-246.

120. Mouterde, R., Rocha, R. B., Ruget, C. and Tintant, H., 1979. Facies, biostratigraphie et paleogeographie du Jurassique Portugais, *Ciências da Terra*, 5, 29-51.

121. Moutinho-Almeida, F., 1986. *Carta Geológica do Concelho de Lisboa, escala 1:10000*, Serviços Geológicos de Portugal, Lisbon.

122. Nicholson, C., Seeber, L., Williams, P. and Sykes, L. R., 1986. Seismicity and fault kinematics through the Eastern Transverse Range, California: block rotation, strike-slip faulting and low-angle thrusts, *J. Geophys. Res.*, 91 (B5), 4891-4908.

123. Oliveira, C.S., 1986. *A sismicidade histórica e a revisão do catálogo sísmico.* Internal Report, LNEC, Lisbon.

124. Olivet, T. L., Pautot, G. and Auzende, J. M., 1973. Structural framework of selected regions of the Western Mediterranean: Alboran Sea, in *Initial Reports of the Deep Sea Drilling Project, Volume XIII (2)*, U. S. Government Printing Office, Washington D.C.

125. Ortega, J. M., 1972. *Numerical Analysis: a second course*, Academic Press, New York.

126. Osete, M. L., Freeman, R. and Vegas. R., in press. Paleomagnetic evidence for block rotations and distributed deformation of the Ibero-African plate boundary, *Phys. Earth. Planet. Interiors.*

127. Palain, C., 1979. Conaissances stratigraphiques sur la base du Mesozoique Portugais, *Ciências da Terra*, 5, 11-28.

128. Philip, H., 1982. *Carte de la tectonique actuelle et recente du domaine mediterraneen et de la Chaine Alpine*, Laboratoire de Geologie Structurale, USTL, Montpellier.

129. Pitman III, W.C. and Andrews, J.A., 1985. Subsidence and thermal history of small pull-apart basins, in Biddle, K.T. and Christie-Blick, N., (eds.), *Strike- slip deformation, basin formation and sedimentation*, Special Publication no. 37, Society of Economic Paleontologists and Mineralogists, Tulsa, Oklahoma.

130. Platt, J., 1988. The Alboran Basin and Gibraltar Arc: a collapsed collisional ridge (abstract), 19th Annual Metting of the Tectonic Studies Group of the Royal Geological Society, Cambridge, December 1988.

131. Pratsch, J., 1982. Wedge Tectonics along continental margins, in J. Watkins and C. Drake (eds.) *Studies in continental margins*, AAPG Memoir 34.

132. Purdy, G. M., 1975. The Eastern end of the Azores-Gibraltar plate boundary, *Geophys. J. R. astr. Soc.*, 43, 973-1000.

133. Rabinowitz, N. and Kulhanec, O., 1988. Application of a non-linear algorithm to teleseismic locations using p-wave readings from the Swedish seismographic network, *Phys. Earth Planet. Interiors*, 50, 111-115.

134. Ralston, A. and Rabinowitz, P., 1978. *A first course in numerical analysis*, McGraw-Hill, New York.

136. Ribeiro, A., Antunes, M.T., Ferreira, M.P., Rocha, R.B., Soares, A.F., Zbyszewski, G., Almeida, F.M., Carvalho, D. and Monteiro, J.H., 1979, *Introduction a la géologie generale du Portugal.* Serviços Geológicos de Portugal, Lisbon.

137. Ribeiro, A. and Almeida, F. M., 1981. Geotermia de baixa entalpia em Portugal Continental, *Geonovas*, 1 (2), 61-71.

138. Richardson, R.M., Solomon, S.C. and Sleep, N.H., 1979. Tectonic stresses in the plates,*Rev. Geophys. Space Phys.*, 17 (5), 981-1019.

139. Richter, C. F., 1935. An intrumental earthquake magnitude scale, *Bull. Seism. Soc. Am.*, 25 (1), 1-32.

140. Rona, P. A. and Richardson, E. S., 1978. Early Cainozoic global plate reorganization, *Earth Planet. Sci. Lett.*, 40, 1-11.

141. Rodgers, D.A., 1980. Analysis of pull-apart basin development produced by en echelon strike-slip faults, in Ballance, P.F. and Reading, H.G., (eds.), *Sedimentation in oblique-slip mobile zones*, Special Publication no. 4, International Association of Sedimentologists.

142. Rowntree, R. A., 1987. Investigation of the possibility of using the ACH inversion technique to model the velocity structure beneath Southern Africa, unpublished M.Sc. Thesis, University of Durham.

143. Royden, L. and Keen, C., 1980. Rifting processes and thermal evolution of the continental margin of eastern Canada determined from subsidence curves, *Earth Plan. Sci. Letters*, **51**, 343-361.

144. Royden, L., Sclater, J. G. and von Herzen, R. P., 1980. Continental margin subsidence and heat flow: important parameters in formation of petroleum hydrocarbons , *Am. Assoc. Petr. Geol. Bull.*, **64** (2), 173-187.

145. Ryan, W. B. F. and Hsu, K. J. et al., 1973. *Initial Reports of the Deep Sea Drilling Project, Volume XIII (1)*, U. S. Government Printing Office, Washington D.C.

146. Schlumberger Ltd, 1972. *Log Interpretation, Vol. 1 - Principles*, Schlumberger Ltd, New York.

147. Schmoker, J. W. and Halley, R. B., 1982. Carbonate porosity versus depth: a predictale relation for South Florida, *Am. Assoc. Petr. Geol. Bull.*, **66** (12), 2561-2570.

148. Schott, J. J. and Peres, A., 1988. Paleomagnetism of Permo-Triassic red beds in the Western Pyrenees: evidence for strong clockwise rotations of the Paleozoic units, *Tectonophysics*, **156**, 75-88.

149. Sclater, J.G. and Christie, P.A.F., 1980. Continental stretching: an explanation of the post-Mid-Cretaceous subsidence of the Central North Sea Basin, *J. Geophys. Res.*, **85** (B7), 3711-3739.

150. Sclater, J. G., Royden, L., Howath, F., Burchfield, B. C., Semken, S. and Stegena, L., 1980. The formation of the intra-carpatian basins as determined from susidence data, *Earth Planet. Sci. Lett.*, **51**, 139-162.

151. Searle, R., 1980. Tectonic pattern of the Azores spreading centre and triple junction, *Earth Planet. Sci. Lett.*, **51**, 415-434.

152. Sengör, A. M. C., Gorur, N. and Saroglu, F., 1985. Strike-slip faulting and related basin formation in zones of tectonic escape: Turkey as a case study, in K. T. Biddle and N. Christie-Blick (eds.), *Strike-slip deformation, basin formation and sedimentation*, Society of Economic Paleontologists and Mineralogists, Tulsa, Oklahoma.

153. Sibson, R. H., 1982. Fault zone models, heat flow, and the depth distribution of earthquakes in the continental crust of the United States, *Bull. Seism. Soc. Am.*, **72** (1), 151-163.

154. Sibson, R. H., 1983. Continental fault structure and the shallow earthquake source, *J. geol. Soc. London*, **140**, 741-767.

155. Sibson, R. H., 1986. Earthquakes and rock deformation in crustal fault zones, *Ann. Rev. Earth Planet. Sci.*, **14**, 149-175.

156. Sibson, R. H., 1989. Earthquake faulting as a structural process, *J. Struct. Geol.*, **11** (1/2), 1-14.

157. Sleep, N. H., 1971. Thermal effects of the formation of Atlantic continental margins by continental break-up, *Geophys. J. R. astr. Soc.*, **24**, 325-337.

158. de Smet, M. E. M., 1984. Wrenching in the external zone of the Betic Cordilleras, Southern Spain, *Tectonophysics*, 107, 57-79.

159. Smith, M.J., Foulger, G.R., 1987. *DUEDROPS-HLPS: hypocentre locator system, user manual*, Internal report 87-02, Dept. Geological Sciences, University of Durham.

160. Srivastara, S.P., Tapscott, C.R., 1986. Plate Kinematics of the North Atlantic, in Vogt, P.R. and Tucholke, B.E., (eds.), *The Geology of North America, Vol. M, The western North Atlantic region*, The Geological Society of America, 1986.

161. Steckler, M. S. and Watts, A., 1978. Subsidence of the Atlantic-type continental margins off New York, *Earth Planet. Sci. Lett.*, 41, 1-13.

162. Stetz, J. and Wurster, P., 1982. Atlas and Atlantic: structural relationships, in U. Von Rad, K. Hinz, M. Sarnthein and E. Seibold (eds.), *Geology of the Northwest African continental margin*, Springer-Verlag, Berlin.

163. Stevenson, D., 1986. *Seismic Processing Lab - User's Manual* (unpublished), University of Durham.

164. Sykes, L.R., 1978. Intraplate seismicity, reactivation of pre-existing zones of weakness, alkaline magmatism, and other tectonism postdating continental fragmentation, *Rev. Geophys. Space Phys.*, 16 (4), 621-688.

165. Sylvester, A., 1988. Strike-slip faults, *Geol. Soc. Am. Bull.*, 100, 1666-1703.

166. Talwani, P., 1988. Characteristic features of intraplate earthquakes and the models proposed to explain them, in Basham, P. and Gregersen, S., (eds.), *Proceedings of the NATO workshop on causes and effects of earthquakes at passive margins and in areas of postglacial rebound on both sides of the Atlantic, Vordingborg, 1988*, Kluwer Academic Publishers, Dordrecht.

167. Talwani, P., in press. The intersection model for intraplate earthquakes, *Seism. Res. Lett.*

168. Tankard, A. J. and Welsink, H. J., 1987. Extensional tectonics and stratigraphy of Hibernia oil field, Grand Banks, Newfoundland, *Am. Assoc. Petr. Geol. Bull.*, 71, 1210-1232.

169. Tapponier, P., Peltzer, G., LeDain, A., Armijo, R. and Cobbold, P., 1982. Propagating extrusion tectonics in Asia: new insights from simple experiments with plasticine, *Geology*, 10, - .

170. Teixeira, C. 1981. *A Geologia de Portugal (vol. I)*, Fundação Calouste Gulbenkian, Lisbon.

171. Telford, W. M., Geldart, L. P., Sheriff, R. E. and Keys, D. A., 1976. *Applied Geophysics*, Cambridge University Press, Cambridge.

172. Telles-Antunes, M., 1979. Ensaio de síntese crítica acerca do Cretácico Terminal e do Paleogénico de Portugal, *Ciências da Terra*, 5, 145-174.

173. Thurber, C., 1985. Non-linear earthquake location: theory and examples, *Bull. Seism. Soc. Am.*, 75 (3), 779-790.

174. Tucker, M. E., 1981. *Sedimentary Petrology, an introduction*, Blackwell Scientific Publications, Oxford.

175. Udias, A., Lopez-Arroyo A. and Mezcua, J., 1976. Seismotectonic of the Azores-Alboran region, *Tectonophysics*, 31, 259-289.

176. Van der Voo, R., 1969. Paleomagnetic evidence for the rotation of the Iberian Peninsula, *Tectonophysics*, 7, 5-56.

177. Van der Voo, R. and Zijderveld, J. D. A., 1971. Renewed paleomagnetic study of the Lisbon Volcanics and implications for the rotation of the Iberian Peninsula, *J. Geophys. Res.*, 76 (17), 3913-3921.

178. Vanney, J. and Mougenot, D., 1981. *La plateforme continentale du Portugal et les provinces adjacentes: analyse géomorphologique*, Memórias dos Serviços Geológicos de Portugal, 28, Lisbon.

179. Verhoef, J., Collette, B. J., Miles, P. R., Searle, R. C., Sibuet, J. C. and Williams, C. A., 1986. Magnetic anomalies in the northeastern Atlantic Ocean (35 to 50 degrees N), *Marine Geophys. Res.*, 8, 1-25 .

180. Watts, A. B., 1981. The U.S. Atlantic continental margin: subsidence history, crustal structure and thermal evolution, in *Geology of passive continental margins*, Education Course Note Series 19, American Association of Petroleum Geologists.

181. Weijermaars, R., 1987. The Palomares britlle-ductile Shear Zone of Souther Spain, *J. Struct. Geol.*, 4 (2), 105-115.

182. Weijermaars, R., 1988. Where does Africa meet Europe?, *Nature*, **332**, p. 118.

183. Wernicke, B. and Burchfield, B. C., 1982. Modes of extensional tectonics, *J. Struct. Geol.*, 4 (2), 105-115.

184. Wilcox, R.E., Harding, T.P. and Seely, D.R., 1973. Basic wrench tectonics,*Am. Assoc. Petrol. Geol. Bull.*, 57 (1), 74-96.

185. Wilson, R. C. L., 1975. Atlantic opening and Mesozoic continental margin basins of Iberia, *Earth Plan. Sci. Letters*, **25**, 33-43.

186. Wilson, R. C. L., 1988. Mesozoic development of the Lusitanian Basin, Portugal, *Rev. Soc. Geol. Espana*, 1 (3/4), - .

187. Wilson, R. C. L., Hiscott, R.N., Willis, M.G. and Gradstein, F.M., in press. The Lusitanian Basin of west central Portugal: mesozoic and tertiary tectonic, stratigraphic and subsidence history, *J. Can. Earth. Sci.*

188. Wurster, P. and Stetz, J., 1982. Sedimentation in the Atlas Gulf II: Mid Cretaceous events, in U. von Rad, K. Hinz, M. Sarnthein and E. Seibold (eds.), *Geology of the Northwest African Continental Margin*, Springer-Verlag, Berlin.

189. Wyllie, C. R., 1975, *Advanced Engineering Mathematics*, McGraw-Hill Kogakusha, Tokyo.

190. Zandt, G., 1981. Seismic images of the deep structure of the San Andreas Fault System, Central Coast Ranges, California, *J. Geophys. Res.*, **86** (B6), 5039-5052.

191. Zbyszewski, G., Veiga-Ferreira, O., Manupella, G. and Torre da Assunção, C., 1966. *Carta geológica de Portugal - Notícia explicativa da folha 30B, Bombarral*, Serviços Geológicos de Portugal, Lisbon.

192. Ziegler, P., 1982.*Geological Atlas of Western and Central Europe*, Shell, The Hague.

193. Zoback, M.L., Nishenko, S.P., Richardson, R.M., Hasegawa, H.S. and Zoback, M.D., 1986. Mid-plate stress, deformation, and seismicity, in Vogt, P.R. and Tucholke, B.E., (eds.), *The Geology of North America, volume M, The western North Atlantic region*, Geological Society of America, 1986.

APPENDIX A - The double-couple model of the seismic source

Although seismic waves can be generated by underground explosions, cavity collapse or movements of magma in volcanic regions, the commonest seismic source is the one that consists of rupture and slip along an internal rock surface. Once seismic waves have been generated, their propagation away from the source region can be studied with the theory of elasticity, because the displacements associated with the passage of the waves are small, and the wavelenghts are large enough for the small-scale heterogeneities of the rocks to be ignored. The physics of the source, however, is no longer within the scope of elasticity, since the kinematic variables will present discontinuities and static displacements will persist after the earthquake.

The theory of elasticity has developed tools to deal with displacement discontinuities (i.e., slip) in the interior of an otherwise elastic medium. These discontinuities were named "dislocations" by Love (1927), and the particular case of slip parallel to the surface of rupture is called "shear dislocation". The following discussion of the representation of a dislocation source follows closely the formal development of Aki and Richards (1980, chapter 3).

The deformation of a medium due to the occurrence of an earthquake in its interior is totally described by specifying the displacement field $\mathbf{u}(\mathbf{r}_0, t)$, defined by

$$\mathbf{u}(\mathbf{r}_o, t) = \mathbf{r}(\mathbf{r}_o, t) - \mathbf{r}_o \tag{A1}$$

where $\mathbf{r}_0$ is the position vector, in some reference frame, of a particular material point of the medium in an initial configuration and $\mathbf{r}(\mathbf{r}_0, t)$ is the general position of the same material point.

For a perfectly elastic and isotropic medium, the displacement field is the solution of the elastodynamic equation of motion

$$\rho\ddot{\mathbf{u}} = \mathbf{f} + (\lambda + 2\mu)\ grad\ div\mathbf{u} - \mu\ rot\mathbf{u}, \tag{A2}$$

where $\mathbb{f}$ =f(r,t) is the distributed body force, ρ is the mass per unit volume and λ and μ are the Lamé elastic parameters (e.g., Bullen and Bolt, 1985). Solutions of (A2) with particular initial and boundary conditions and with arbitrary forces $\mathbb{f}$ can be conveniently built up with the use of Green functions (e.g., Wylie, 1975). These are the solutions of (A2) under the specified initial and boundary conditions and with a unidirectional unit impulse applied at one point in space and at one instant in time. When applied at point ξ and time τ and along the j-th axis, this unit impulse body force has the components

$$(A3) \qquad g_i(\mathbb{r},t) = \delta_{ij}\delta(\mathbb{r}-\xi)\delta(t-\tau), \qquad i=1,2,3,$$

where $\delta(\cdot)$ is the Dirac-δ distribution.

When applying Green functions to obtain a representation of the dislocation source, a reciprocity result known as Betti's Theorem is fundamental. This theorem states that if u and s are solutions of (A2) inside a volume V limited by a surface S when the body forces are $\mathbb{f}$ and g respectively, than they verify the relation

$$(A4) \quad \int_V (\mathbf{f}-\rho\ddot{\mathbf{u}}).\mathbf{s}\ dV + \int_S \mathbf{T}_u(\hat{\gamma}).\mathbf{s}\ dS = \int_V (\mathbf{g}-\rho\ddot{\mathbf{s}}).\mathbf{u}\ dV + \int_S \mathbf{T}_s(\hat{\gamma}).\mathbf{u}\ dS.$$

Here, T_u and T_s are the tension vectors in the direction normal to S for each of the displacement fields, and $\hat{\gamma}$ is the unit vector normal to S.

Manipulation of (A4) by evaluating u,ü, T_u andf at time t, evaluating s, s̈, T_s and g at time τ -t (which is compatible with the conditions of validity) and integrating both sides between times t=0 and t=τ leads to the following result, for the case of a quiescent past (u = s = 0 before some particular instant):

$$(A5) \qquad \int_{-\infty}^{+\infty}\int_V [\mathbf{u}(\mathbf{r},t).\mathbf{g}(\mathbf{r},\tau-t) - \mathbf{s}(\mathbf{r},\tau-t).\mathbf{f}(\mathbf{r},t)\ dV\ dt =$$

$$= \int_{-\infty}^{+\infty}\int_S [\mathbf{s}(\mathbf{r},\tau-t).\mathbf{T}_u(\hat{\gamma},t) - \mathbf{u}(\mathbf{r},t).\mathbf{T}_s(\hat{\gamma},\tau-t)]\ dS\ dt.$$

If in the above equation the body force g(r,t) is replaced by the unit impulse force given by (A3) and s(r,t) is replaced accordingly by the Green function tensor $G(\mathbf{r},t;\xi,\tau)$, and if only rigid surfaces S are admited, it becomes

$$(A6) \qquad u_n(\mathbf{r},t) = \int_{-\infty}^{+\infty}\int_V f_i(\eta,\tau)G_{in}(\mathbf{r},t-\tau;\eta,0)\ dV\ dt\ -$$

$$-\int_{-\infty}^{+\infty}\int_S u_i(\eta,\tau)C_{ijkl}\gamma_j G_{nk,l}(\mathbb{r},t-\tau;\eta,0)\,dS\,dt.$$

Here, $G_{nk,l}$ stands for $\frac{\partial G_{nk}}{\partial x_l}$, the quantities γ_1,γ_2 and γ_3 are the components of the unit vector normal to the surface S and the generalized Hooke's Law (e.g., Aki and Richards, 1980) was used to introduce the 4-th order tensor of elastic parameters C. Einstein's convention applies here and in the remainder of the section, i.e., a repeated subscript indicates a sum.

If the volume V contains an internal surface Σ accross which displacement discontinuities occur, like in the case of a geological fault undergoing slippage, the surface S can be made to include the external surface of the volume plus two adjacent surfaces on both sides of Σ , which can be assumed to have no finite sepparation and may be represented by Σ^+ and Σ^-. The contribution of the external surface to the integral in (A6) can be made null by stipulating adequate boundary conditions, and in the absence of body forces equation (A6) becomes

$$(A7)\qquad u_n(\mathbf{r},t)=\int_{-\infty}^{+\infty}\int_\Sigma \Delta u_i(\mathbf{r}',\tau)C_{ijpq}\gamma_j G_{np,q}(\mathbf{r},t-\tau;\mathbf{r}',0)\,d\Sigma\,dt$$

where r' = (x',y',z') is the position vector for the general point of the surface Σ and $\Delta\mathbf{u}_i(\mathbf{r}',\tau)$ is the difference between $\mathbf{u}_i(\mathbf{r}',\tau)$ evaluated on Σ^+ and on Σ^-, i.e., the displacement discontinuity.

Using the equality

$$(A8)\qquad G_{np,q}(\mathbf{r},t-\tau;\mathbf{r}',0)=-\int_V \frac{\partial}{\partial\eta_q}[\delta(\eta-\mathbb{r}')]G_{np}(\mathbf{r},t-\tau;\eta,0)\,dV$$

(Aki and Richards, 1980), equation (A7) may be re-written as

$$(A9)\qquad u_n(\mathbf{r},t)=\int_{-\infty}^{+\infty}\int_V[-\int_\Sigma \Delta u_i(\mathbf{r}',\tau)C_{ijpq}\gamma_j\frac{\partial}{\partial\eta_q}(\eta-\mathbb{r}')\,d\Sigma].$$

$$.G_{np}(\mathbf{r}',t-\tau;\eta,0)\,dV\,dt,\qquad n=1,2,3.$$

Comparison with the first term of the right hand side of (A6) shows that a displacement discontinuity accross an internal surface Σ is dynamically equivalent, as far as the resulting displacement field is concerned, to a body force distribution given by

$$(A10) \qquad f_p^{\Delta u}(\eta,\tau) = -\int_\Sigma \Delta u_i(\mathbb{r}',\tau) C_{ijpq}\gamma_j \frac{\partial}{\partial \eta_q}(\eta - \mathbb{r}')\, d\Sigma \qquad p = 1,2,3.$$

This body force equivalent is subjacent to most discriptions of earthquake fault mechanisms. Particular models can now be discussed under the light of this last result.

If the surface of the ruptured fault is made to coincide with the plane z' = 0, and for the isotropic case when the tensor of elastic parameters reduces to

$$(A11) \qquad C_{ijpq} = \lambda\delta_{ij}\delta_{pq} + \mu(\delta_{ip}\delta_{jq} + \delta_{iq}\delta_{jp}),$$

equation (A10) becomes, after computation of the integrals,

$$(A12a) \qquad f_1^{\Delta u}(\mathbf{r}',\tau) = -\mu\Delta u_1(\mathbf{r}',\tau)\frac{\partial}{\partial z'}[\delta(z')]$$

$$(A12b) \qquad f_2^{\Delta u}(\mathbf{r}',\tau) = 0$$

$$(A12c) \qquad f_3^{\Delta u}(\mathbf{r}',\tau) = -\frac{\partial}{\partial x'}[\mu\Delta u_1(\mathbf{r}',\tau)]\delta(z')$$

The derivative of the Dirac-δ, $\frac{\partial\delta(z')}{\partial z'}$, is $+\infty$ at points of the semi-space z'>0 infinitely close to the plane z' = 0, and $-\infty$ at points of the semi-space z'<0 infinitely close to the same plane. For a particular r', i.e., for each point of the surface of the fault, equation (A12a) gives a pair of point forces with opposite senses along the x'-axis, or a single-couple, sepparated by an infinitesimal distance. Integration of (A12a) over V gives a null resultant, but the integrated moment about the y'-axis takes the non-zero value

$$(A13) \qquad M_{y'}(\tau) = \int_\Sigma \mu\Delta u_1(\mathbf{r}',\tau) d\Sigma$$

or, for constant μ, total fault surface A and average slip $\widetilde{\Delta u}(\tau)$,

$$M_{y'}(\tau) = \mu \widetilde{\Delta u}(\tau) A. \tag{A14}$$

Equation (A12c) does not correspond to a single-couple distribution in the same sense that (A12a) does, but to a single-force distribution. This result is rather arbitrary, because the body-force equivalent of a displacement discontinuity is not unique. At any rate, the conservation of angular moment requires that the net contribution of (A12c) in terms of moment cancel the quantity given by (A14), since the slip at Σ is an internal process of V.

If the displacement field is observed at large distances from the fault, the surface Σ may be approximated by a point source, and the displacement discontinuity may then be described by the distribution

$$\Delta u_1(x', y') = \widetilde{\Delta u}(\tau) A \delta(x') \delta(y'). \tag{A15}$$

Equations (A12) become now

$$f_1^{\Delta u}(\mathbf{r}', \tau) = -\mu \widetilde{\Delta u}(\tau) A \delta(x') \delta(y') \frac{\partial}{\partial z'} [\delta(z')] \tag{A16a}$$

$$f_2^{\Delta u}(\mathbf{r}', \tau) = 0 \tag{A16b}$$

$$f_3^{\Delta u}(\mathbf{r}', \tau) = -\mu \widetilde{\Delta u}(\tau) A \frac{\partial}{\partial x'} [\delta(x')] \delta(y') \delta(z'), \tag{A16c}$$

which correspond to a double-couple distribution. The quantity

$$M_o(\tau) = \mu \widetilde{\Delta u}(\tau) A \tag{A17}$$

is the "seismic moment". Naturally, there is no net moment arising from the double-couple distribution (A16).

Although the slip on the fault is by hypothesis parallel to the x'-axis, the equivalent body-force distribution has components along the x'- and z'-axes which

are undistiguishable. For this reason, it is not possible to gain information to differenciate between the fault plane z' = 0 and the "auxiliary plane" x' = 0 from the observation of the radiation pattern only. In the general case, the auxiliary plane is the plane normal to the direction of slip.

For a general orientation of the fault surface Σ with respect to the coordinate axes the seismic moment is represented by a second-order tensor, which for a shear dislocation in an isotropic medium has the elements

$$(A18) \qquad M_{pq} = \int_S \mu(\gamma_p \Delta u_q + \gamma_q \Delta u_p)\, dS,$$

where $\hat{\gamma} = (\gamma_1, \gamma_2, \gamma_3)$ is the unit vector normal to the fault. With this notation, and considering a point source at $\mathbf{r}_s$, equation (A7) becomes

$$(A19) \qquad u_n(\mathbf{r}, t) = \int_{-\infty}^{+\infty} M_{pq}(\tau) G_{np,q}(\mathbf{r}, t-\tau; \mathbf{r}_s, 0)\, dt,$$

i.e., the displacement field is the convolution of the seismic moment tensor with the 3rd order tensor obtained by spatial differentiation of the elastodinamic Green function tensor G_{np}.

To obtain the relationship between the radiation pattern and the orientation of, and the slip direction at, the fault, it remains to obtain an explicit expression for G_{np}. This can be done by solving equation (A2) for a body force of the type

$$(A20) \qquad \mathbf{f} = X_o(t)\delta(\mathbf{r}_s)\hat{\mathbf{e}}_1,$$

where without loss of generality the unit vector $\hat{e}_1$ was chosen to be along the x-axis. The solution contains several terms that attenuate differently with the distance from the source (Aki and Richards, 1980). Retaining only those terms that have the slowest decrease with distance, the following result is obtained, which is valid at large distances (far-field displacements):

$$(A21) \qquad u_n(\mathbf{r}, t) = \int_{-\infty}^{+\infty} X_o(t) G_{n1}(\mathbf{r}, t-\tau; \mathbf{r}_s, 0)\, d\Sigma =$$

$$= \frac{1}{4\pi\rho\alpha^2}\gamma_k\gamma_l\left(\frac{1}{r}\right)X_o(t - r/\alpha) + \frac{1}{4\pi\rho\beta^2}(\delta_{kl} - \gamma_k\gamma_l)\left(\frac{1}{r}\right)X_o(t - r/\beta).$$

Here, $\alpha = \sqrt{\frac{(\lambda+2\mu)}{\rho}}$ and $\beta = \sqrt{\frac{\mu}{\rho}}$ are the phase velocities for the p- and s-waves, which correspond to the first and second term of the right-hand-side respectively, r is $|\mathbb{r} - \mathbb{r}_s|$ and the ν_k are the direction cosines of $\mathbb{r}$.

Finally, the displacement field corresponding to the double-couple distribution (A16) can be obtained through (A19), using (4.18) and the Green function (4.21). For a fault plane of equation z = 0 with slip parallel to the x-axis, it is

$$(A22) \qquad \mathbb{u}(\mathbb{r},t) = \frac{1}{4\pi\rho\alpha^2} sin2\theta cos\phi (\frac{1}{r}) \frac{\partial}{\partial t}[M_o(t - r/\alpha)]\hat{\mathbb{e}}_r +$$

$$+ \frac{1}{4\pi\rho\beta^2}(\frac{1}{r})\frac{\partial}{\partial t}[M_o(t - r/\beta)][cos2\theta cos\phi\hat{\mathbb{e}}_\theta - cos\theta sin\phi\hat{\mathbb{e}}_\phi]$$

(Aki and Richards, 1980). M_0 is the scalar seismic moment given by (A17), r, θ and ϕ are spherical coordinates and $\hat{\mathbb{e}}_r$, $\hat{\mathbb{e}}_\theta$ and $\hat{\mathbb{e}}_\phi$ are the associated unit vectors. Since M_0 is proportional to the average slip on the fault, the factor $\frac{\partial M_0(t-r/\alpha)}{\partial t}$ is proportional to average slip speed.

In most studies of seismic waves, and particularly when vertical component instruments only are used, all the recoverable information on polarity of motion concerns the onset of the p-wave. According to (A22), the polarity distribution for the p-wave first motions is controlled by the factor $sin2\phi cos\theta$, and corresponds to the quadrantal pattern exemplified in Figure 4.1. Rays with take-off directions parallel to the fault plane have $2\theta = \pi$, hence null amplitudes; rays parallel to the plane x = 0 have $\theta = 0$, and the amplitudes are also null. The polarity distribution has therefore two nodal planes, one coinciding with the fault plane and the other coinciding with the auxiliary plane. One plane cannot be distinguished from the other using p-wave polarity observations only, a result that had already been anticipated on dynamic grounds.

Appendix B

```
      PROGRAM BACKSTRIP
      THIS PROGRAM CORRECTS A SEQUENCE OF STRATIGRAPHIC HORIZONS
      FOR THE EFFECTS OF COMPACTION, ASSSUMING THAT THE BASEMENT
      RESPONDS TO THE SEDIMENT LOAD ACCORDING TO THE AIRY ISOSTASY
      MODEL. POROSITY DEPTH RELATIONSHIPS ARE ASSUMED WITHIN THE
      WELL BEING BACKSTRIPPED.
      IN THIS VERSION, DIFFERENT POROSITY-DEPTH PROFILES ARE ASSU-
      MED FOR DIFFERENT FORMATIONS. THEREFORE, IT IS NOT POSTULATED
      THAT THE SAME PROFILE IS VALID THROUGHOUT GEOLOGICAL TIME.
      THE USER MAY CHOOSE BETWEEN PUBLISHED PROFILES DEFINED BY POW-
      ER LAWS (SHALE AND LIMESTONE) OR EXPONENTIAL LAW (SANDSTONE).
      THE LITHOLOGY OF EACH UNIT IS SPECIFIED IN THE INPUT FILE, ACCOR-
      TO THE FOLLOWING CODE:

      1 = NORMAL SHALE ; 2 = UNCONSOLIDATED SHALE ; 3 = SANDSTONE ;
      4 = LIMESTONE ; 5 = BASEMENT.

      THE LITHOLOGY SPECIFIED AT EACH HORIZON APPLIES TO THE FORMATION
      BELOW IT.
      THE PROGRAM CONSISTS OF TWO NESTED LOOPS, THE OUTER ONE ALONG
      INTERMEDIATE STATES OF DECOMPACTION (THE GEOLOGICAL UNITS OF THE
      COLUMN BEING REMOVED ONE BY ONE) , AND THE INNER ONE ALONG THE
      REMAINING UNITS OF THE COLUMN, WHICH ARE EXPLICITLY DECOMPACTED
      ONE BY ONE, BY BALANCING THE MASS OF SEDIMENTS BEFORE AND AFTER.
      OUTPUT IS THE DEPTH AND AGE OF THE INPUT HORIZONS, THE DENSITY
      OF THE SEDIMENTS THROUGH TIME, AND THE DEPTH TO BASEMENT WITH
      AND WITHOUT (BACKSTRIPPED) SEDIMENTS.

      AUTHOR:  ORIGINAL - M.S. STECKLER (COLUMBIA, 1978)
               REWRITTEN- G.D. KARNER   (DURHAM,   1984)
               MODIFIED - WEBSTER MOHRIAK (DURHAM, 1986)
               MODIFIED - J.F.B.D. FONSECA (DURHAM,1988)

      DIMENSION AGE(250),HRZN(250),ZT(250,250),LC(250),FI(250)
      DIMENSION PHI(5000,10),RPHI(250),ZPHI(250),RSL(250),BAT(250)
      DIMENSION BSMT(250,2),RHO(250),XW(100),YW(100),NAME(40)
      DIMENSION BSMTN(250), BSMTT(250),BSMTB(250)
      DATA      PM1,PS1,PW/3.4,2.65,1.03/

      INPUT THE NAME OF THE WELL (FILE 1) *10A1*
      INPUT THE NUMBER OF POINTS TO BE BACKSTRIPPED ( MAXIMUM 250 )


          INPUT HORIZON, LITHOLOGY, AGE, RELATIVE SEA-LEVEL,PALEOBATHYMETRY


      READ(1,5) NAME
      FORMAT(40A1)
      READ(1,*) NPTS


      WRITE(6,10)
      FORMAT(' ENTER:   STEPPING INTERPOLATION INTERVAL ',/,
     1       '          SEDIMENT GRAIN DENSITY          ',/,
     2       '          MANTLE DENSITY                  ')
      READ(5,*) ZSTEP,PS,PM
      IF(PS   .EQ.0.0) PS   =PS1
      IF(PM   .EQ.0.0) PM   =PM1
      FEET =1.0
```

```
DO 15 I = 1,NPTS
READ(1,*) ZPHI(I),RPHI(I),LC(I),AGE(I),RSL(I),BAT(I)
ZPHI(I) = ZPHI(I)*FEET
HRZN(I) = ( ZPHI(I) - BAT(1) )   /ZSTEP
CONTINUE


LOOP =2*INT(HRZN(NPTS))
BAT0 = BAT(1)
NPTSM1=NPTS-1

THE FOLLOWING LAWS ARE USED TO CALCULATE POROSITY-DEPT PROFILES:

    - BALDWIN-BUTLER POWER LAW:    Z=6020.0*(1-PHI)**6.35   (M)
                                   (SHALE AND LIMESTONE)
    - SCLATER-CHRISTIE EXP LAW:    Z=3700.0*LN(0.49/PHI)    (M)
                                   (SANDSTONE)
    - DICKINSON POWER LAW:         Z=15000.0*(1-PHI)**8.0   (M)
                                   (UNCONS. SHALE)
    - USER-SPECIFIED LAW           (NOT YET IMPLEMENTED)


DO 530 K=1,LOOP
Z=BAT0+FLOAT(K)*ZSTEP
REXP=1.0/6.35
RBAS=Z/6020.
PHI(K,1)=1.0-RBAS**REXP
REXP=1.0/8.0
RBAS=Z/15000.
PHI(K,2)=1.0-RBAS**REXP
REXP=-Z/3700.0
PHI(K,3)=0.49*EXP(REXP)
PHI(K,4)=PHI(K,1)
PHI(K,5)=0.0
DO 532 J=1,NPTSM1
L=LC(J)
DO 534 K=1,LOOP
IF(FLOAT(K).GE.HRZN(J).AND.FLOAT(K).LT.HRZN(J+1))FI(K)=PHI(K,L)
CONTINUE
CONTINUE


PLOT THE POROSITY X DEPTH CURVE ( UNIT = METERS )

LOOPS2=INT(FLOAT(LOOP)/2.0)
CALL GRAPH1(RPHI,ZPHI,NPTS,FI,LOOPS2,ZSTEP,NAME,BAT0)


AT THIS POINT, THE WATER LOAD ABOVE THE BASEMENT IS COMPUTED.
THE METHOD OF INTEGRATION, WHICH IS USED THROUGHOUT THE PROGRAM,
STARTS BY LOCATING THE INTEGRATION LIMITS WITH RESPECT TO NEAR
MULTIPLES OF THE STEPPING INTERVAL, AND THEN DEALING SEPARATELY
WITH THE CONTRIBUTIONS OF INTEGER STEPS AND TOP AND BOTTOM LEFT-
OVERS.

NPTSM1=NPTS-1
DO 535  J=1,NPTSM1
LCOD=LC(J)
TH1=AINT(HRZN(J))+1.0-HRZN(J)
TH2=HRZN(J+1)-AINT(HRZN(J+1))
```

```
IL1=INT(HRZN(J))+1
IL2=INT(HRZN(J+1))
IL3=IL2-1
IF(IL2-IL1) 550,545,540
DO 542 K=IL1,IL3
WT=WT+PHI(K+1,LCOD)
WT=WT+TH1*PHI(IL1,LCOD)+TH2*PHI(IL2+1,LCOD)
GO TO 555
WT=WT+(HRZN(J+1)-HRZN(J))*PHI(IL1,LCOD)
CONTINUE
CONTINUE


    CALCULATE AVERAGE DENSITY AND BACK-STRIP BASEMENT DEPTH
    FOR TIME = 0 M.Y.B.P.
RHO(1) =PS+(1.0-PS)*WT/(HRZN(NPTS))
BSMT(1,1)=HRZN(NPTS)
BSMT(1,2)=BSMT(1,1)*(PM-RHO(1))/(PM-PW)

    THE NEW VARIABLE ZT(I,J) IS INTRODUCED, WHICH ACCOUNTS FOR
    THE POSITIONS OF THE BOUNDARIES ALONG THE INTERMEDIATE STA-
    GES OF DECOMPACTION. ZT(1,L)=HRZN(L), L=1,..,NPTS; ZT(K,K)=
    0.0 ,L=1,NPTS.

IHRZN  =1
AHRZN  =0.0

DO 560 J=1,NPTS
ZT(1,J)=HRZN(J)

    THE INTEGRAL OF SOLIDITY (1.0-POROSITY) FOR THE JTH FORMATION
    PRIOR TO THE REMOVAL OF THE (I-1)TH FORMATION IS CALCULATED.
    ALONG THIS LOOP, (I-1) IS ALWAYS THE INDEX OF THE FORMATION AT
    THE SURFACE. THIS LOOP IS ALONG INTERMEDIATE STAGES OF DECOM-
    PACTION.

DO 100 I=2,NPTSM1
WT=0.0
ZT(I,I)=0.0
DO 610 J=I,NPTSM1
LCOD=LC(J)
SUM=0.0
TH1=AINT(ZT(I-1,J))+1.0-ZT(I-1,J)
TH2=ZT(I-1,J+1)-AINT(ZT(I-1,J+1))
IL1=INT(ZT(I-1,J))+1
IL2=INT(ZT(I-1,J+1))
IL3=IL2-1
IF(IL2-IL1) 50,45,40
DO 42 K=IL1,IL3
SUM=SUM+(1.0-PHI(K+1,LCOD))
SUM=SUM+TH1*(1.0-PHI(IL1,LCOD))+TH2*(1.0-PHI(IL2+1,LCOD))
GO TO 55
SUM=SUM+(ZT(I-1,J+1)-ZT(I-1,J))*(1.0-PHI(IL1,LCOD))
CONTINUE

AT THIS POINT,THE (I-1)TH FORMATION IS REMOVED, AND THE JTH FORMATION
IS ALLOWED TO DECOMPACT. THE INTEGRAL OF SOLIDITY IS CALCULATED WITH
THE ITH FORMATION AT THE SURFACE, THENCE DEFINING THE DEPTH OF THE BA-
SE OF THE JTH FORMATION. THE WATER LOAD FOR THE NEW CONFIGURATION  IS
ALSO INTEGRATED. THE LOOP IS ABANDONED WHEN THE BALANCING OF THE MAS-
```

```
SES OVERSHOOTS (SUM<0.0).

TH3=AINT(ZT(I,J))+1.0-ZT(I,J)
IL1=INT(ZT(I,J))+1
SUM=SUM-TH3*(1.0-PHI(IL1,LCOD))
WT=WT+TH3*PHI(IL1,LCOD)
DO 60 K=IL1,LOOP
SUM=SUM-(1.0-PHI(K+1,LCOD))
WT=WT+PHI(K+1,LCOD)
IF(SUM.LT.0.0) GO TO 70
CONTINUE
WRITE(6,65)
FORMAT(4X,'*** WARNING:  DECOMPACTED FORMATION TOO THICK! ***')
ZT(I,J+1)=FLOAT(K+1)+SUM/(1.0-PHI(K+1,LCOD))
WT=WT+PHI(K+1,LCOD)*SUM/(1.0-PHI(K+1,LCOD))

    END OF LOOP ALONG STRATIGRAPHIC COLUMN.

CONTINUE

THE DEPTH OF THE BASEMENT AFTER REMOVAL OF THE (I-1)TH STEP OF
DECOMPACTION IS NOW MADE EQUAL TO THE DEPTH OF THE BASE OF THE
DEEPEST LAYER OF SEDIMENTS.

BSMT(I,1)=ZT(I,NPTS)

THE AVERAGE DENSITY OF THE STRATIGRAPHIC COLUMN IS NOW COMPUTED.
NEXT, THE BASEMENT IS BACKSTRIPPED ASSUMING AIRY ISOSTASY.

RHO(I)=PS+(1.0-PS)*WT/BSMT(I,1)
BSMT(I,2)=BSMT(I,1)*(PM-RHO(I))/(PM-PW)

END OF LOOP ALONG INTERMEDIATE STAGES OF DECOMPACTION.

CONTINUE


BSMT(NPTS,1)=0.0
BSMT(NPTS,2)=0.0
RHO(NPTS)=0.0

    REMOVE NORMALISATION FROM DEPTH DATA AND OUTPUT
```

(Cont.)

Appendix C

```
4567890123456789012345678901234567890123456789012345678901234567890123456789012345678901234567890

  PROGRAM THRDJR

C-----------------------------------------------------------------------
C       WRITTEN BY W.L. ELLSWORTH AND G. ZANDT                         |
C       REVISED 17 MARCH 1977 (CALLED "THREED")                        |
C-----------------------------------------------------------------------

C-----------------------------------------------------------------------
C       REVISED BY D. STAUBER AUGUST 1982 (CALLED "THREEDDLS")         |
C-----------------------------------------------------------------------

C-----------------------------------------------------------------------
C       ADAPTED TO VAX, DOCUMENTATION, WEIGHTING, AND DIPPING INTERFACE |
C       ADDED BY D. OPPENHEIMER OCTOBER 1984 (CALLED "THRD")           |
C-----------------------------------------------------------------------

C-----------------------------------------------------------------------
C       REVISED BY J. R. EVANS, JUNE-AUGUST, 1986.                     |
C-----------------------------------------------------------------------

C-----------------------------------------------------------------------
C       ADAPTED TO  RUN ON MTS AND TO USE THE NAG SUBROUTINES          |
C       BY R. ROWNTREE, DURHAM, 1987                                   |
C-----------------------------------------------------------------------

C-----------------------------------------------------------------------
C       BUGS DETECTED  IN, AND REMOVED FROM, THE MTS INTERFACE         |
C       BY J. FONSECA, DURHAM, 1988                                    |
C-----------------------------------------------------------------------

                              (..........)

C     *****  THE FOLLOWING BLOCK IS SPECIFIC TO MTS  ****

  CALL SOLVE1(G,MBL,IFAIL)

  IF(IFAIL.NE.0) WRITE(OUNIT,*)
 1  '     ****** ERROR RETURN FROM F01BQF: IFAIL = ',IFAIL

C-----------------------------------------------------------------------
C   SOLVE FOR PERTURBATIONS BY GAUSSIAN ELIMINATION. RHS STORES SOLUTION ON
C   OUTPUT.
C-----------------------------------------------------------------------
  CALL SOLVE2(G,MBL,RHS)

                  END OF BLOCK SPECIFIC TO MTS

                              (..........)
```

```
      THIS ROUTINE IS AN INTERFACE BETWEEN PROGRAM THRDJR AND THE NAG
      LIBRARY SUBROUTINE F01BQF , AND ALLOWS THE PROGRAM TO RUN
      ON THE NUMAC MTS SYSTEM


      INCLUDE(THRDEF)

      REAL*4 G(((MXBLK+1)*MXBLK)/2)
      REAL*8 G1((MXBLK*(MXBLK+1))/2)
      REAL*8 P(MXBLK)
      REAL*8 EPS
      REAL*8 X02AAF
      INTEGER IFAIL
      INTEGER M1
      INTEGER MBL

      M1=(MXBLK*(MXBLK+1))/2
      EPS=X02AAF(0.0D0)
      IFAIL=0
      K1=0
      K2=0

      DO 100 I=1,MBL
      DO 100 L=1,I
      K1=K1+1
      IF(I.EQ.L) THEN
      P(I)=DBLE(G(K1))
      ELSE
      K2=K2+1
      G1(K2)=DBLE(G(K1))
      ENDIF
  100 CONTINUE

      CALL F01BQF(MBL,EPS,G1,M1,P,IFAIL)

      K1=0
      K2=0
      DO 110 I=1,MBL
      DO 110 L=1,I
      K1=K1+1
      IF(I.EQ.L) THEN
      G(K1)=SNGL(P(I))
      ELSE
      K2=K2+1
      G(K1)=SNGL(G1(K2))
      ENDIF
  110 CONTINUE
      RETURN
      END


      SUBROUTINE SOLVE2(G,MBL,RHS)

      THIS SUBROUTINE IS AN INTERFACE BETWEEN PROGRAM THRDJR AND THE
      NAG LIBRARY SUBROUTINE F04AQF, AND ALLOWS THE PROGRAM TO RUN
```

```
      ON THE NUMAC MTS SYSTEM


      INCLUDE (THRDEF)

      REAL*4 G(((MXBLK+1)*MXBLK)/2)
      REAL*4 RHS(MXBLK)
      REAL*8 G1(((MXBLK+1)*MXBLK)/2)
      REAL*8 AHS(MXBLK)
      REAL*8 S(MXBLK)
      REAL*8 P(MXBLK)
      REAL*8 EPS
      REAL*8 X02AAF
      INTEGER   M1
      INTEGER   MBL

      M1=(MBL*(MBL-1))/2
      EPS=X02AAF(0.0D0)
      K1=0
      K2=0

      DO 215 I=1,MBL
      AHS(I)=DBLE(RHS(I))
215   CONTINUE

      DO 210 I=1,MBL
      DO 210 L=1,I
      K1=K1+1
      IF(I.EQ.L) THEN
      P(I)=DBLE(G(K1))
      ELSE
      K2=K2+1
      G1(K2)=DBLE(G(K1))
      ENDIF
210   CONTINUE

      CALL F04AQF(MBL,M1,G1,P,AHS,S)

      K1=0
      K2=0
      DO 220 I=1,MBL
      DO 220 L=1,I
      K1=K1+1
      IF(I.EQ.L) THEN
      G(K1)=SNGL(P(I))
      ELSE
      K2=K2+1
      G(K1)=SNGL(G1(K2))
      ENDIF
220   CONTINUE

      DO 230 I=1,MBL
      RHS(I)=SNGL(S(I))
230   CONTINUE

      RETURN
      END
```

Appendix D

LEGEND:

BLOCK NUMBER
VELOCITY PERTURBATION
NUMBER OF HITS (RAYS)
COLUMN OF THE RESOLUTION MATRIX FOR BLOCK 4
COLUMN OF THE COVARIENCE MATRIX FOR BLOCK 4

LAYER IS TWO-DIMENSIONAL.

-UP=N OW-						
1	2	3	4	5	6	
		-4.59	-0.28			
0	0	11	7	1	0	
		-0.0296	0.8177			
		0.017	0.290			
7	8	9	10	11	12	
		-1.01	0.88	-1.32		
0	0	11	23	10	0	
		-0.0529	-0.0497	-0.0315		
		0.027	0.033	0.006		
13	14	15	16	17	18	
		-0.10	1.42	0.11		
0	3	17	29	22	4	
		-0.0260	-0.0067	-0.0127		
		0.006	-0.006	-0.003		
19	20	21	22	23	24	
	2.92		-4.31	4.26	-0.70	
3	8	1	15	8	5	
	-0.0047		-0.0016	-0.0102	-0.0032	
	0.001		-0.008	-0.007	-0.006	
25	26	27	28	29	30	
				0.05		
0	0	4	1	16	3	
				0.0023		
				-0.002		
31	32	33	34	35	36	
		-4.96				
0	1	13	0	0	0	
		-0.0031				
		0.004				

FOLLOWING LAYER IS NUMBER 2 OF 4; MODEL= VELMOD-05

LEGEND:

BLOCK NUMBER
VELOCITY PERTURBATION
NUMBER OF HITS (RAYS)
COLUMN OF THE RESOLUTION MATRIX FOR BLOCK 4
COLUMN OF THE COVARIENCE MATRIX FOR BLOCK 4

LAYER IS TWO-DIMENSIONAL.

-UP=N OW-							
37	38	39	40	41			
	14.90	5.98	4.65				
0	8	18	9	3			
	0.0183	0.1162	0.0384				
	0.006	-0.120	-0.009				
42	43	44	45	46			
	3.54	2.83	3.67	1.88			
2	13	26	21	5			
	0.0291	0.0394	0.0159	0.0215			
	-0.004	0.003	0.022	0.009			
47	48	49	50	51			
-0.24	-4.04	-2.28	-3.18	-3.11			
5	13	33	27	5			
-0.0049	0.0175	0.0060	0.0058	0.0000			
0.004	0.001	0.013	0.017	0.010			
52	53	54	55	56			
		-5.59	-0.30				
4	4	13	15	4			
		-0.0061	-0.0014				
		0.006	0.008				
57	58	59	60	61			
	-1.21		-0.91				
1	8	3	6	1			
	-0.0003		-0.0047				
	-0.001		0.001				

FOLLOWING LAYER IS NUMBER 3 OF 4; MODEL= VELMOD-05

LEGEND:

BLOCK NUMBER
VELOCITY PERTURBATION
NUMBER OF HITS (RAYS)
COLUMN OF THE RESOLUTION MATRIX FOR BLOCK 4
COLUMN OF THE COVARIENCE MATRIX FOR BLOCK 4

LAYER IS TWO-DIMENSIONAL.

-UP-N OW-			
62	63	64	65
	-1.04	-5.91	-0.04
4	19	19	9
	-0.0096	-0.0266	-0.0094
	-0.002	0.007	-0.004
66	67	68	69
7.36	-2.88	-0.96	-0.06
9	21	23	6
0.0000	0.0072	0.0149	0.0034
0.000	-0.016	-0.022	-0.015
70	71	72	73
-0.19	-1.01	-1.12	-1.06
15	30	15	7
0.0121	0.0005	0.0041	-0.0003
-0.008	0.002	-0.005	0.003
74	75	76	77
0.41	-4.71	1.09	
7	11	7	1
0.0023	0.0054	-0.0038	
0.001	-0.001	-0.001	

FOLLOWING LAYER IS NUMBER 4 OF 4; MODEL= VELMOD-05

LEGEND:

BLOCK NUMBER
VELOCITY PERTURBATION
NUMBER OF HITS (RAYS)
COLUMN OF THE RESOLUTION MATRIX FOR BLOCK 4
COLUMN OF THE COVARIENCE MATRIX FOR BLOCK 4

LAYER IS TWO-DIMENSIONAL.

-UP-N OW-			
78	79	80	81
-4.53	-1.26	4.16	0.12
7	19	5	7
0.0151	-0.0206	0.0384	0.0360
0.001	0.012	-0.043	-0.048
82	83	84	85
-5.12	1.16	4.07	1.62
13	11	14	7
0.0133	0.0109	-0.0212	0.0014
-0.022	-0.026	0.013	-0.006
86	87	88	89
4.76	5.09	-2.92	-0.23
18	29	9	8
-0.0008	-0.0017	0.0029	0.0048
-0.004	-0.003	-0.007	-0.012
90	91	92	93
0.27	1.69	0.59	
8	9	5	1
0.0023	0.0061	0.0027	
-0.004	-0.002	0.000	

FOLLOWING LAYER IS NUMBER 1 OF 4; MODEL= VELMOD-05

LEGEND:

BLOCK NUMBER
VELOCITY PERTURBATION
NUMBER OF HITS (RAYS)
COLUMN OF THE RESOLUTION MATRIX FOR BLOCK 9
COLUMN OF THE COVARIENCE MATRIX FOR BLOCK 9

LAYER IS TWO-DIMENSIONAL.

1	2	3	4	5	6
		-4.59	-0.28		
0	0	11	7	1	0
		-0.0415	-0.0529		
		0.047	0.027		
7	8	9	10	11	12
		-1.01	0.88	-1.32	
0	0	11	23	10	0
		0.8428	-0.0329	-0.0185	
		0.236	0.006	-0.014	
13	14	15	16	17	18
		-0.10	1.42	0.11	
0	3	17	29	22	4
		-0.0517	-0.0228	-0.0154	
		0.047	0.009	-0.006	
19	20	21	22	23	24
	2.92		-4.31	4.26	-0.70
3	8	1	15	8	5
	-0.0201		-0.0086	-0.0176	-0.0041
	0.025		-0.002	-0.005	-0.005
25	26	27	28	29	30
				0.05	
0	0	4	1	16	3
				0.0012	
				-0.005	
31	32	33	34	35	36
		-4.96			
0	1	13	0	0	0
		-0.0009			
		0.005			

FOLLOWING LAYER IS NUMBER 2 OF 4; MODEL= VELMOD-05

LEGEND:

BLOCK NUMBER
VELOCITY PERTURBATION
NUMBER OF HITS (RAYS)
COLUMN OF THE RESOLUTION MATRIX FOR BLOCK 9
COLUMN OF THE COVARIENCE MATRIX FOR BLOCK 9

LAYER IS TWO-DIMENSIONAL.

37	38	39	40	41			
	14.90	5.98	4.65				
0	8	18	9	3			
	0.0323	0.0664	0.0214				
	-0.028	-0.037	0.013				
42	43	44	45	46			
	3.54	2.83	3.67	1.88			
2	13	26	21	5			
	0.0418	0.0597	0.0223	0.0157			
	-0.052	-0.033	0.015	0.018			
47	48	49	50	51			
-0.24	-4.04	-2.28	-3.18	-3.11			
5	13	33	27	5			
-0.0180	0.0222	0.0157	0.0174	0.0022			
0.006	-0.018	0.004	0.010	0.009			
52	53	54	55	56			
		-5.59	-0.30				
4	4	13	15	4			
		-0.0072	0.0003				
		0.005	0.006				
57	58	59	60	61			
	-1.21		-0.91				
1	8	3	6	1			
	-0.0085		-0.0015				
	0.003		0.005				

FOLLOWING LAYER IS NUMBER 3 OF 4; MODEL= VELMOD-05

LEGEND:

BLOCK NUMBER
VELOCITY PERTURBATION
NUMBER OF HITS (RAYS)
COLUMN OF THE RESOLUTION MATRIX FOR BLOCK 9
COLUMN OF THE COVARIENCE MATRIX FOR BLOCK 9

LAYER IS TWO-DIMENSIONAL.

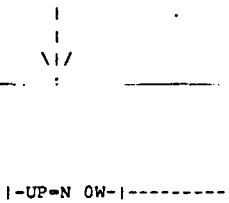

-UP=N OW-				
62	63	64	65	
	-1.04	-5.91	-0.04	
4	19	19	9	
	-0.0235	-0.0220	-0.0026	
	0.013	0.012	-0.013	
66	67	68	69	
7.36	-2.88	-0.96	-0.06	
9	21	23	6	
0.0304	0.0274	0.0060	-0.0035	
-0.039	-0.040	-0.006	-0.005	
70	71	72	73	
-0.19	-1.01	-1.12	-1.06	
15	30	15	7	
0.0487	0.0148	0.0065	0.0076	
-0.046	-0.012	-0.006	0.004	
74	75	76	77	
0.41	-4.71	1.09		
7	11	7	1	
0.0063	0.0090	0.0029		
0.001	0.002	0.000		

FOLLOWING LAYER IS NUMBER 4 OF 4; MODEL= VELMOD-05

LEGEND:

BLOCK NUMBER
VELOCITY PERTURBATION
NUMBER OF HITS (RAYS)
COLUMN OF THE RESOLUTION MATRIX FOR BLOCK 9
COLUMN OF THE COVARIENCE MATRIX FOR BLOCK 9

LAYER IS TWO-DIMENSIONAL.

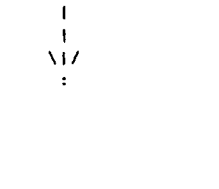

-UP=N OW-				
78	79	80	81	
-4.53	-1.26	4.16	0.12	
7	19	5	7	
0.0781	0.0024	0.0138	0.0147	
-0.070	-0.020	-0.009	-0.013	
82	83	84	85	
-5.12	1.16	4.07	1.62	
13	11	14	7	
0.0210	-0.0280	-0.0174	0.0026	
-0.039	0.031	0.004	-0.009	
86	87	88	89	
4.76	5.09	-2.92	-0.27	
18	29	9	8	
-0.0112	-0.0135	0.0006	-0.0071	
0.003	0.007	-0.010	-0.009	
90	91	92	93	
0.27	1.69	0.59		
8	9	5	1	
0.0076	-0.0031	-0.0012		
-0.014	-0.001	-0.003		

FOLLOWING LAYER IS NUMBER 1 OF 4; MODEL= VELMOD-05

LEGEND:

BLOCK NUMBER
VELOCITY PERTURBATION
NUMBER OF HITS (RAYS)
COLUMN OF THE RESOLUTION MATRIX FOR BLOCK 20
COLUMN OF THE COVARIENCE MATRIX FOR BLOCK 20

LAYER IS TWO-DIMENSIONAL.

-UP=N OW-						
1	2	3	4	5	6	
		-4.59	-0.28			
0	0	11	7	1	0	
		-0.0083	-0.0047			
		0.002	0.001			
7	8	9	10	11	12	
		-1.01	0.88	-1.32		
0	0	11	23	10	0	
		-0.0201	-0.0182	-0.0140		
		0.025	0.012	0.002		
13	14	15	16	17	18	
		-0.10	1.42	0.11		
0	3	17	29	22	4	
		-0.0225	-0.0131	-0.0075		
		0.024	0.014	0.006		
19	20	21	22	23	24	
	2.92		-4.31	4.26	-0.70	
3	8	1	15	8	5	
	0.8397		-0.0136	-0.0155	0.0022	
	0.236		0.022	0.000	0.005	
25	26	27	28	29	30	
				0.05		
0	0	4	1	16	3	
				-0.0057		
				0.012		
31	32	33	34	35	36	
		-4.96				
0	1	13	0	0	0	
		-0.0134				
		0.001				

FOLLOWING LAYER IS NUMBER 2 OF 4; MODEL= VELMOD-05

LEGEND:

BLOCK NUMBER
VELOCITY PERTURBATION
NUMBER OF HITS (RAYS)
COLUMN OF THE RESOLUTION MATRIX FOR BLOCK 20
COLUMN OF THE COVARIENCE MATRIX FOR BLOCK 20

LAYER IS TWO-DIMENSIONAL.

-UP=N OW-						
37	38	39	40	41		
	14.90	5.98	4.65			
0	8	18	9	3		
	0.0169	-0.0107	0.0028			
	0.011	0.008	-0.002			
42	43	44	45	46		
	3.54	2.83	3.67	1.88		
2	13	26	21	5		
	0.0048	0.0039	-0.0090	0.0044		
	0.009	-0.009	0.000	0.000		
47	48	49	50	51		
-0.24	-4.04	-2.28	-3.18	-3.11		
5	13	33	27	5		
0.1626	0.0126	-0.0246	-0.0146	-0.0083		
-0.089	-0.022	0.008	0.005	-0.003		
52	53	54	55	56		
		-5.59	-0.30			
4	4	13	15	4		
		-0.0253	-0.0177			
		-0.008	0.001			
57	58	59	60	61		
	-1.21		-0.91			
1	8	3	6	1		
	0.0062		0.0047			
	0.004		-0.009			

FOLLOWING LAYER IS NUMBER 3 OF 4; MODEL= VELMOD-05

LEGEND:

BLOCK NUMBER
VELOCITY PERTURBATION
NUMBER OF HITS (RAYS)
COLUMN OF THE RESOLUTION MATRIX FOR BLOCK 20
COLUMN OF THE COVARIENCE MATRIX FOR BLOCK 20

LAYER IS TWO-DIMENSIONAL.

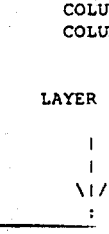

-UP=N OW-								
62	63	64	65					
	-1.04	-5.91	-0.04					
4	19	19	9					
	0.0062	0.0043	0.0165					
	-0.003	-0.007	-0.004					
66	67	68	69					
7.36	-2.88	-0.96	-0.06					
9	21	23	6					
0.0054	0.0373	-0.0097	0.0080					
-0.018	-0.025	0.017	-0.005					
70	71	72	73					
-0.19	-1.01	-1.12	-1.06					
15	30	15	7					
0.0318	0.0319	0.0105	0.0060					
-0.045	-0.021	0.006	-0.006					
74	75	76	77					
0.41	-4.71	1.09						
7	11	7	1					
0.0122	0.0286	0.0074						
-0.004	0.000	-0.003						

FOLLOWING LAYER IS NUMBER 4 OF 4; MODEL= VELMOD-05

LEGEND:

BLOCK NUMBER
VELOCITY PERTURBATION
NUMBER OF HITS (RAYS)
COLUMN OF THE RESOLUTION MATRIX FOR BLOCK 20
COLUMN OF THE COVARIENCE MATRIX FOR BLOCK 20

LAYER IS TWO-DIMENSIONAL.

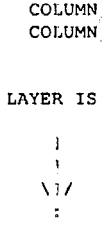

-UP=N OW-								
78	79	80	81					
-4.53	-1.26	4.16	0.12					
7	19	5	7					
0.0062	0.0172	0.0109	0.0083					
-0.034	-0.009	0.005	-0.003					
82	83	84	85					
-5.12	1.16	4.07	1.62					
13	11	14	7					
-0.0136	-0.0034	0.0366	0.0125					
-0.008	0.010	-0.041	0.000					
86	87	88	89					
4.76	5.09	-2.92	-0.23					
18	29	9	8					
-0.0156	0.0143	0.0208	0.0182					
0.026	-0.015	-0.016	-0.003					
90	91	92	93					
0.27	1.69	0.59						
8	9	5	1					
-0.0018	0.0010	0.0077						
-0.003	-0.005	0.002						

FOLLOWING LAYER IS NUMBER 1 OF 4; MODEL= VELMOD-05

LEGEND:

BLOCK NUMBER
VELOCITY PERTURBATION
NUMBER OF HITS (RAYS)
COLUMN OF THE RESOLUTION MATRIX FOR BLOCK 38
COLUMN OF THE COVARIENCE MATRIX FOR BLOCK 38

LAYER IS TWO-DIMENSIONAL.

-UP=N OW-						
1	2	3	4	5	6	
		-4.59	-0.28			
0	0	11	7	1	0	
		0.0892	0.0183			
		-0.114	0.006			
7	8	9	10	11	12	
		-1.01	0.88	-1.32		
0	0	11	23	10	0	
		0.0323	0.0198	0.0088		
		-0.028	0.001	0.004		
13	14	15	16	17	18	
		-0.10	1.42	0.11		
0	3	17	29	22	4	
		-0.0036	0.0038	0.0019		
		0.008	-0.006	0.003		
19	20	21	22	23	24	
	2.92		-4.31	4.26	-0.70	
3	8	1	15	8	5	
	0.0169		0.0058	0.0100	0.0014	
	0.011		-0.004	0.006	0.002	
25	26	27	28	29	30	
				0.05		
0	0	4	1	16	3	
				0.0008		
				-0.001		
31	32	33	34	35	36	
		-4.96				
0	1	13	0	0	0	
		-0.0024				
		0.001				

FOLLOWING LAYER IS NUMBER 2 OF 4; MODEL= VELMOD-05

LEGEND:

BLOCK NUMBER
VELOCITY PERTURBATION
NUMBER OF HITS (RAYS)
COLUMN OF THE RESOLUTION MATRIX FOR BLOCK 38
COLUMN OF THE COVARIENCE MATRIX FOR BLOCK 38

LAYER IS TWO-DIMENSIONAL.

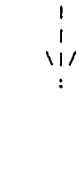

-UP=N OW-						
37	38	39	40	41		
	14.90	5.98	4.65			
0	8	18	9	3		
	0.7606	-0.0416	-0.0130			
	0.348	0.019	-0.008			
42	43	44	45	46		
	3.54	2.83	3.67	1.88		
2	13	26	21	5		
	-0.0660	-0.0305	-0.0052	-0.0045		
	0.059	0.018	-0.002	-0.004		
47	48	49	50	51		
-0.24	-4.04	-2.28	-3.18	-3.11		
5	13	33	27	5		
-0.0500	0.0092	0.0231	0.0024	-0.0001		
-0.018	-0.019	-0.012	0.000	0.000		
52	53	54	55	56		
		-5.59	-0.30			
4	4	13	15	4		
		0.0026	0.0016			
		0.011	-0.001			
57	58	59	60	61		
	-1.21		-0.91			
1	8	3	6	1		
	0.0052		-0.0001			
	0.000		0.000			

FOLLOWING LAYER IS NUMBER 3 OF 4; MODEL= VELMOD-05

LEGEND:

BLOCK NUMBER
VELOCITY PERTURBATION
NUMBER OF HITS (RAYS)
COLUMN OF THE RESOLUTION MATRIX FOR BLOCK 38
COLUMN OF THE COVARIENCE MATRIX FOR BLOCK 38

LAYER IS TWO-DIMENSIONAL.

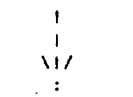

-UP=N OW-				
62	63	64	65	
	-1.04	-5.91	-0.04	
4	19	19	9	
	0.0185	0.0238	0.0011	
	-0.046	-0.014	0.001	
66	67	68	69	
7.36	-2.88	-0.96	-0.06	
9	21	23	6	
-0.0342	-0.0365	-0.0011	-0.0085	
0.036	0.027	-0.004	0.001	
70	71	72	73	
-0.19	-1.01	-1.12	-1.06	
15	30	15	7	
-0.0057	-0.0331	-0.0148	-0.0021	
0.006	0.014	-0.003	0.001	
74	75	76	77	
0.41	-4.71	1.09		
7	11	7	1	
-0.0031	-0.0060	-0.0038		
-0.003	-0.007	0.000		

FOLLOWING LAYER IS NUMBER 4 OF 4; MODEL= VELMOD-05

LEGEND:

BLOCK NUMBER
VELOCITY PERTURBATION
NUMBER OF HITS (RAYS)
COLUMN OF THE RESOLUTION MATRIX FOR BLOCK 38
COLUMN OF THE COVARIENCE MATRIX FOR BLOCK 38

LAYER IS TWO-DIMENSIONAL.

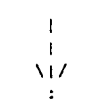

-UP=N OW-				
78	79	80	81	
-4.53	-1.26	4.16	0.12	
7	19	5	7	
0.0902	-0.0057	-0.0160	-0.0103	
-0.066	0.022	0.004	0.005	
82	83	84	85	
-5.12	1.16	4.07	1.62	
13	11	14	7	
0.0909	0.0049	-0.0028	0.0096	
-0.104	0.008	0.006	-0.003	
86	87	88	89	
4.76	5.09	-2.92	-0.23	
18	29	9	8	
0.0058	0.0083	-0.0006	-0.0018	
0.004	-0.004	0.003	-0.002	
90	91	92	93	
0.27	1.69	0.59		
8	9	5	1	
-0.0022	0.0006	0.0032		
0.003	0.002	0.000		

FOLLOWING LAYER IS NUMBER 1 OF 4; MODEL= VELMOD-05

LEGEND:

BLOCK NUMBER
VELOCITY PERTURBATION
NUMBER OF HITS (RAYS)
COLUMN OF THE RESOLUTION MATRIX FOR BLOCK 48
COLUMN OF THE COVARIENCE MATRIX FOR BLOCK 48

LAYER IS TWO-DIMENSIONAL.

-UP=N OW-						
1	2	3	4	5	6	
		-4.59	-0.28			
0	0	11	7	1	0	
		-0.0073	0.0175			
		0.013	0.001			
7	8	9	10	11	12	
		-1.01	0.88	-1.32		
0	0	11	23	10	0	
		0.0222	0.0060	0.0093		
		-0.018	0.002	0.008		
13	14	15	16	17	18	
		-0.10	1.42	0.11		
0	3	17	29	22	4	
		0.0652	0.0068	0.0024		
		-0.078	0.008	0.017		
19	20	21	22	23	24	
	2.92		-4.31	4.26	-0.70	
3	8	1	15	8	5	
	0.0126		-0.0048	0.0000	0.0084	
	-0.022		0.017	0.010	0.015	
25	26	27	28	29	30	
				0.05		
0	0	4	1	16	3	
				-0.0128		
				0.022		
31	32	33	34	35	36	
		-4.96				
0	1	13	0	0	0	
		-0.0038				
		0.005				

FOLLOWING LAYER IS NUMBER 2 OF 4; MODEL= VELMOD-05

LEGEND:

BLOCK NUMBER
VELOCITY PERTURBATION
NUMBER OF HITS (RAYS)
COLUMN OF THE RESOLUTION MATRIX FOR BLOCK 48
COLUMN OF THE COVARIENCE MATRIX FOR BLOCK 48

LAYER IS TWO-DIMENSIONAL.

-UP=N OW-						
37	38	39	40	41		
	14.90	5.98	4.65			
0	8	18	9	3		
	0.0092	-0.0392	-0.0022			
	-0.019	0.001	-0.021			
42	43	44	45	46		
	3.54	2.83	3.67	1.88		
2	13	26	21	5		
	-0.0678	-0.0134	-0.0270	-0.0126		
	0.043	-0.009	-0.016	-0.015		
47	48	49	50	51		
-0.24	-4.04	-2.28	-3.18	-3.11		
5	13	33	27	5		
-0.0570	0.7762	-0.0502	-0.0323	-0.0061		
0.014	0.306	0.028	-0.005	-0.017		
52	53	54	55	56		
		-5.56	-0.30			
4	4	13	15	4		
		-0.0049	-0.0167			
		-0.010	-0.006			
57	58	59	60	61		
	-1.21		-0.91			
1	8	3	6	1		
	-0.0085		0.0049			
	-0.001		-0.015			

FOLLOWING LAYER IS NUMBER 3 OF 4; MODEL= VELMOD-05

LEGEND:

BLOCK NUMBER
VELOCITY PERTURBATION
NUMBER OF HITS (RAYS)
COLUMN OF THE RESOLUTION MATRIX FOR BLOCK 48
COLUMN OF THE COVARIENCE MATRIX FOR BLOCK 48

LAYER IS TWO-DIMENSIONAL.

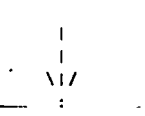

-UP=N OW-							
62	63	64	65				
	-1.04	-5.91	-0.04				
4	19	19	9				
	0.0047	-0.0130	0.0149				
	0.004	0.010	0.011				
66	67	68	69				
7.36	-2.88	-0.96	-0.06				
9	21	23	6				
0.0327	0.0277	-0.0274	0.0301				
0.006	-0.019	0.027	-0.009				
70	71	72	73				
-0.19	-1.01	-1.12	-1.06				
15	30	15	7				
0.1269	0.0135	0.0160	0.0047				
-0.156	-0.012	0.000	-0.015				
74	75	76	77				
0.41	-4.71	1.09					
7	11	7	1				
-0.0031	-0.0055	0.0057					
0.005	-0.002	-0.004					

FOLLOWING LAYER IS NUMBER 4 OF 4; MODEL= VELMOD-05

LEGEND:

BLOCK NUMBER
VELOCITY PERTURBATION
NUMBER OF HITS (RAYS)
COLUMN OF THE RESOLUTION MATRIX FOR BLOCK 48
COLUMN OF THE COVARIENCE MATRIX FOR BLOCK 48

LAYER IS TWO-DIMENSIONAL.

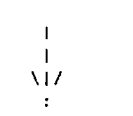

-UP=N OW-							
78	79	80	81				
-4.53	-1.26	4.16	0.12				
7	19	5	7				
-0.0110	0.0247	0.0257	-0.0080				
0.026	-0.004	0.000	0.016				
82	83	84	85				
-5.12	1.16	4.07	1.62				
13	11	14	7				
-0.0042	-0.0069	0.0744	-0.0163				
0.003	0.014	-0.059	0.028				
86	87	88	89				
4.76	5.09	-2.92	-0.23				
18	29	9	8				
0.0340	0.0270	0.0013	0.0232				
-0.053	-0.017	0.009	0.009				
90	91	92	93				
0.27	1.69	0.59					
8	9	5	1				
0.0184	0.0157	0.0032					
-0.007	-0.003	-0.002					

FOLLOWING LAYER IS NUMBER 1 OF 4; MODEL= VELMOD-05

LEGEND:

BLOCK NUMBER
VELOCITY PERTURBATION
NUMBER OF HITS (RAYS)
COLUMN OF THE RESOLUTION MATRIX FOR BLOCK 82
COLUMN OF THE COVARIENCE MATRIX FOR BLOCK 82

LAYER IS TWO-DIMENSIONAL.

-UP=N OW-						
1	2	3	4	5	6	
		-4.59	-0.28			
0	0	11	7	1	0	
		0.0002	0.0133			
		-0.027	-0.022			
7	8	9	10	11	12	
		-1.01	0.88	-1.32		
0	0	11	23	10	0	
		0.0210	0.0063	-0.0048		
		-0.039	-0.014	0.010		
13	14	15	16	17	18	
		-0.10	1.42	0.11		
0	3	17	29	22	4	
		0.0150	0.0086	0.0060		
		-0.011	-0.001	-0.004		
19	20	21	22	23	24	
	2.92		-4.31	4.26	-0.70	
3	8	1	15	8	5	
	-0.0136		0.0029	-0.0119	-0.0048	
	-0.008		0.005	0.002	-0.003	
25	26	27	28	29	30	
				0.05		
0	0	4	1	16	3	
				0.0030		
				-0.005		
31	32	33	34	35	36	
		-4.96				
0	1	13	0	0	0	
		0.0062				
		-0.007				

FOLLOWING LAYER IS NUMBER 2 OF 4; MODEL= VELMOD-05

LEGEND:

BLOCK NUMBER
VELOCITY PERTURBATION
NUMBER OF HITS (RAYS)
COLUMN OF THE RESOLUTION MATRIX FOR BLOCK 82
COLUMN OF THE COVARIENCE MATRIX FOR BLOCK 82

LAYER IS TWO-DIMENSIONAL.

-UP=N OW-						
37	38	39	40	41		
	14.90	5.98	4.65			
0	8	18	9	3		
	0.0909	0.0014	0.0044			
	-0.104	0.006	0.000			
42	43	44	45	46		
	3.54	2.83	3.67	1.88		
2	13	26	21	5		
	0.0132	0.0070	0.0000	-0.0004		
	-0.014	-0.023	-0.006	-0.004		
47	48	49	50	51		
-0.24	-4.04	-2.28	-3.18	-3.11		
5	13	33	27	5		
0.0550	-0.0042	-0.0363	0.0006	0.0028		
-0.011	0.003	0.026	-0.013	-0.003		
52	53	54	55	56		
		-5.59	-0.30			
4	4	13	15	4		
		-0.0025	0.0067			
		-0.019	-0.003			
57	58	59	60	61		
	-1.21		-0.91			
1	8	3	6	1		
	-0.0043		-0.0009			
	0.003		0.005			

FOLLOWING LAYER IS NUMBER 3 OF 4; MODEL= VELMOD-05

LEGEND:

BLOCK NUMBER
VELOCITY PERTURBATION
NUMBER OF HITS (RAYS)
COLUMN OF THE RESOLUTION MATRIX FOR BLOCK 82
COLUMN OF THE COVARIENCE MATRIX FOR BLOCK 82

LAYER IS TWO-DIMENSIONAL.

-UP=N OW-							
62	63	64	65				
	-1.04	-5.91	-0.04				
4	19	19	9				
	0.0116	-0.0012	-0.0031				
	0.003	0.009	0.004				
66	67	68	69				
7.36	-2.88	-0.96	-0.06				
9	21	23	6				
0.0565	0.0548	0.0018	0.0020				
-0.075	-0.057	0.012	0.005				
70	71	72	73				
-0.19	-1.01	-1.12	-1.06				
15	30	15	7				
-0.0080	0.0472	0.0193	-0.0019				
0.012	-0.042	0.000	0.003				
74	75	76	77				
0.41	-4.71	1.09					
7	11	7	1				
0.0009	0.0085	0.0012					
0.004	0.008	0.003					

FOLLOWING LAYER IS NUMBER 4 OF 4; MODEL= VELMOD-05

LEGEND:

BLOCK NUMBER
VELOCITY PERTURBATION
NUMBER OF HITS (RAYS)
COLUMN OF THE RESOLUTION MATRIX FOR BLOCK 82
COLUMN OF THE COVARIENCE MATRIX FOR BLOCK 82

LAYER IS TWO-DIMENSIONAL.

-UP=N OW-							
78	79	80	81				
-4.53	-1.26	4.16	0.12				
7	19	5	7				
-0.0594	-0.0149	-0.0015	-0.0102				
0.034	0.017	-0.006	0.014				
82	83	84	85				
-5.12	1.16	4.07	1.62				
13	11	14	7				
0.8704	-0.0141	-0.0091	-0.0115				
0.209	0.000	0.007	0.008				
86	87	88	89				
4.76	5.09	-2.92	-0.23				
18	29	9	8				
-0.0188	-0.0223	-0.0005	-0.0063				
0.018	0.023	-0.005	0.009				
90	91	92	93				
0.27	1.69	0.59					
8	9	5	1				
-0.0038	-0.0063	-0.0054					
0.001	-0.001	0.002					

FOLLOWING LAYER IS NUMBER 1 OF 4; MODEL= VELMOD-05

LEGEND:

BLOCK NUMBER
VELOCITY PERTURBATION
NUMBER OF HITS (RAYS)
COLUMN OF THE RESOLUTION MATRIX FOR BLOCK 90
COLUMN OF THE COVARIENCE MATRIX FOR BLOCK 90

LAYER IS TWO-DIMENSIONAL.

-UP=N OW-						
1	2	3	4	5	6	
		-4.59	-0.28			
0	0	11	7	1	0	
		0.0061	0.0023			
		-0.005	-0.004			
7	8	9	10	11	12	
		-1.01	0.88	-1.32		
0	0	11	23	10	0	
		0.0076	0.0077	0.0042		
		-0.014	-0.007	-0.001		
13	14	15	16	17	18	
		-0.10	1.42	0.11		
0	3	17	29	22	4	
		-0.0005	0.0110	0.0066		
		-0.004	-0.019	-0.005		
19	20	21	22	23	24	
	2.92		-4.31	4.26	-0.70	
3	8	1	15	8	5	
	-0.0018		-0.0036	0.0134	0.0014	
	-0.003		0.010	-0.012	0.000	
25	26	27	28	29	30	
				0.05		
0	0	4	1	16	3	
				0.0014		
				-0.005		
31	32	33	34	35	36	
		-4.96				
0	1	13	0	0	0	
		-0.0205				
		-0.059				

FOLLOWING LAYER IS NUMBER 2 OF 4; MODEL= VELMOD-05

LEGEND:

BLOCK NUMBER
VELOCITY PERTURBATION
NUMBER OF HITS (RAYS)
COLUMN OF THE RESOLUTION MATRIX FOR BLOCK 90
COLUMN OF THE COVARIENCE MATRIX FOR BLOCK 90

LAYER IS TWO-DIMENSIONAL.

-UP=N OW-						
37	38	39	40	41		
	14.90	5.98	4.65			
0	8	18	9	3		
	-0.0022	0.0049	-0.0004			
	0.003	0.000	0.000			
42	43	44	45	46		
	3.54	2.83	3.67	1.88		
2	13	26	21	5		
	0.0061	0.0049	0.0004	-0.0030		
	0.000	-0.004	0.003	0.001		
47	48	49	50	51		
-0.24	-4.04	-2.28	-3.18	-3.11		
5	13	33	27	5		
0.0041	0.0184	0.0182	0.0033	0.0011		
0.007	-0.007	-0.019	-0.002	0.001		
52	53	54	55	56		
		-5.59	-0.30			
4	4	13	15	4		
		-0.0036	0.0101			
		-0.010	0.004			
57	58	59	60	61		
	-1.21		-0.91			
1	8	3	6	1		
	0.1530		0.0160			
	-0.124		0.009			

FOLLOWING LAYER IS NUMBER 3 OF 4; MODEL= VELMOD-05

LEGEND:

BLOCK NUMBER
VELOCITY PERTURBATION
NUMBER OF HITS (RAYS)
COLUMN OF THE RESOLUTION MATRIX FOR BLOCK 90
COLUMN OF THE COVARIENCE MATRIX FOR BLOCK 90

LAYER IS TWO-DIMENSIONAL.

-UP=N OW-				
78	79	80	81	
-4.53	-1.26	4.16	0.12	
7	19	5	7	
-0.0025	-0.0110	-0.0007	-0.0032	
0.001	0.008	-0.010	0.001	
82	83	84	85	
-5.12	1.16	4.07	1.62	
13	11	14	7	
-0.0038	-0.0086	-0.0123	-0.0010	
0.001	0.004	-0.001	0.000	
86	87	88	89	
4.76	5.09	-2.92	-0.23	
18	29	9	8	
-0.0185	-0.0266	-0.0271	-0.0105	
0.011	0.016	0.002	0.000	
90	91	92	93	
0.27	1.69	0.59		
8	9	5	1	
0.7947	-0.0513	0.0091		
0.306	-0.005	0.038		

FOLLOWING LAYER IS NUMBER 4 OF 4; MODEL= VELMOD-05

LEGEND:

BLOCK NUMBER
VELOCITY PERTURBATION
NUMBER OF HITS (RAYS)
COLUMN OF THE RESOLUTION MATRIX FOR BLOCK 90
COLUMN OF THE COVARIENCE MATRIX FOR BLOCK 90

LAYER IS TWO-DIMENSIONAL.

-UP=N OW-				
62	63	64	65	
	-1.04	-5.91	-0.04	
4	19	19	9	
	-0.0018	-0.0041	-0.0068	
	0.003	0.011	0.005	
66	67	68	69	
7.36	-2.88	-0.96	-0.06	
9	21	23	6	
-0.0044	-0.0066	0.0050	-0.0043	
-0.001	0.016	0.004	0.000	
70	71	72	73	
-0.19	-1.01	-1.12	-1.06	
15	30	15	7	
-0.0012	0.0138	0.0088	-0.0003	
-0.001	-0.003	0.013	0.006	
74	75	76	77	
0.41	-4.71	1.09		
7	11	7	1	
0.0287	0.0913	0.0134		
-0.054	-0.045	-0.003		

Appendix E

USGS COMPUTER PROGRAM "THRLIST"; VERSION 2.001;
TECHNICAL CONTACT: JOHN R. EVANS.

THREED OUTPUT -- PRINTOUT OF BINARY FILE BY PROGRAM THRLIST

EXPERIMENT=** RESTE **, MODEL= FLATMOD-05, COMMENT=   = BLOCK BOUNDARIES STRIKING N

MODEL FILENAME=FLATMOD
THREED BINARY OUTPUT=BOUT

FOLLOWING LAYER IS NUMBER 1 OF 4;   MODEL= FLATMOD-05

LEGEND:

  BLOCK NUMBER
  VELOCITY PERTURBATION
  NUMBER OF HITS (RAYS)
  DIAGONAL OF THE RESOLUTION MATRIX
  STANDARD ERRORS

LAYER IS TWO-DIMENSIONAL.

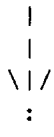

-UP-N OW-						
1	2	3	4	5	6	
		-4.39	-0.09			
0	0	11	7	1	0	
		0.9011	0.8368			
		0.41	0.53			
7	8	9	10	11	12	
		-2.82	1.25	-0.65		
0	0	11	23	10	0	
		0.8530	0.8695	0.7493		
		0.48	0.43	0.57		
13	14	15	16	17	18	
		-1.21	0.81	-0.01		
0	3	17	29	22	4	
		0.8777	0.8887	0.8835		
		0.42	0.40	0.39		
19	20	21	22	23	24	
	4.00		-4.11	4.17	-0.89	
3	8	1	15	8	5	
	0.8319		0.8571	0.6468	0.0431	
	0.48		0.46	0.65	0.27	
25	26	27	28	29	30	
				0.09		
0	0	4	1	16	3	
				0.8825		
				0.44		
31	32	33	34	35	36	
		-4.95				
0	1	13	0	0	0	
		0.8430				
		0.51				

FOLLOWING LAYER IS NUMBER 2 OF 4; MODEL= FLATMOD-05

LEGEND:

BLOCK NUMBER
VELOCITY PERTURBATION
NUMBER OF HITS (RAYS)
DIAGONAL OF THE RESOLUTION MATRIX
STANDARD ERRORS

LAYER IS TWO-DIMENSIONAL.

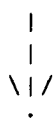

-UP=N OW-							
37	38	39	40	41			
	13.76	5.29	4.60				
0	8	18	9	3			
	0.7871	0.8561	0.7159				
	0.57	0.45	0.65				
42	43	44	45	46			
	3.76	1.91	4.12	1.77			
2	13	26	21	5			
	0.8262	0.8086	0.8199	0.7295			
	0.49	0.48	0.44	0.59			
47	48	49	50	51			
-1.79	-2.29	-1.93	-3.01	-2.71			
5	13	33	27	5			
0.4046	0.7563	0.8234	0.8198	0.7938			
0.66	0.54	0.47	0.44	0.57			
52	53	54	55	56			
		-4.64	-0.05				
4	4	13	15	4			
		0.6355	0.6570				
		0.63	0.61				
57	58	59	60	61			
	-0.93		-0.41				
1	8	3	6	1			
	0.7656		0.7116				
	0.59		0.66				

FOLLOWING LAYER IS NUMBER 3 OF 4; MODEL= FLATMOD-05

LEGEND:

BLOCK NUMBER
VELOCITY PERTURBATION
NUMBER OF HITS (RAYS)
DIAGONAL OF THE RESOLUTION MATRIX
STANDARD ERRORS

LAYER IS TWO-DIMENSIONAL.

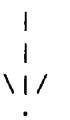

-UP=N OW-							
62	63	64	65				
	-1.58	-3.05	-0.71				
4	19	19	9				
	0.8869	0.8611	0.8259				
	0.44	0.45	0.53				
66	67	68	69				
7.68	-2.08	-0.74	0.52				
9	21	23	6				
0.7047	0.7932	0.7837	0.8401				
0.65	0.46	0.51	0.50				
70	71	72	73				
-0.13	-0.74	-1.05	-1.70				
15	30	15	7				
0.7457	0.8517	0.7905	0.7168				
0.58	0.43	0.49	0.53				
74	75	76	77				
-0.18	-4.88	1.82					
7	11	7	1				
0.7983	0.7151	0.7570					
0.60	0.61	0.58					

FOLLOWING LAYER IS NUMBER 4 OF 4; MODEL= FLATMOD-05

LEGEND:

BLOCK NUMBER
VELOCITY PERTURBATION
NUMBER OF HITS (RAYS)
DIAGONAL OF THE RESOLUTION MATRIX
STANDARD ERRORS

LAYER IS TWO-DIMENSIONAL.

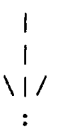

-UP=N OW-								
78	79	80	81					
-4.48	-1.08	0.41	1.06					
5	10	10	7					
0.7252	0.8388	0.7995	0.6954					
0.65	0.54	0.55	0.65					
82	83	84	85					
-4.23	1.21	4.15						
12	6	11	4					
0.8754	0.7302	0.7675						
0.47	0.59	0.58						
86	87	88	89					
3.76	4.89	-2.30	0.56					
16	22	8	8					
0.8557	0.8908	0.6757	0.6407					
0.50	0.42	0.66	0.64					
90	91	92	93					
4.41	2.38	-3.60						
9	15	7	3					
0.7980	0.8481	0.5613						
0.58	0.48	0.72						

USGS COMPUTER PROGRAM "THRLIST"; VERSION 2.001;
TECHNICAL CONTACT: JOHN R. EVANS.

THREED OUTPUT -- PRINTOUT OF BINARY FILE BY PROGRAM THRLIST

EXPERIMENT=** RESTE **, MODEL= FLATMOD-05, COMMENT=   = BLOCK BOUNDARIES STRIKING N6

MODEL FILENAME=FLATMOD
THREED BINARY OUTPUT=BOUT

FOLLOWING LAYER IS NUMBER 1 OF 4;   MODEL= FLATMOD-05

LEGEND:

  BLOCK NUMBER
  VELOCITY PERTURBATION
  NUMBER OF HITS (RAYS)
  DIAGONAL OF THE RESOLUTION MATRIX
  STANDARD ERRORS

LAYER IS TWO-DIMENSIONAL.

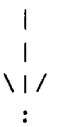

-UP=N30W-								
1	2	3	4	5	6			
			11.33	-7.07				
0	0	0	6	11	0			
			0.7142	0.9017				
			0.62	0.45				
7	8	9	10	11	12			
			2.74	2.93				
0	1	2	14	10	1			
			0.8933	0.8699				
			0.40	0.44				
13	14	15	16	17	18			
	0.79	-2.43	1.29	1.12				
2	7	14	20	21	2			
	0.9076	0.8588	0.8709	0.8698				
	0.43	0.45	0.45	0.41				
19	20	21	22	23	24			
			-4.21	-1.06				
0	0	2	18	23	0			
			0.8987	0.8837				
			0.40	0.40				
25	26	27	28	29	30			
	-5.06		-0.92	-3.40				
2	13	1	5	7	0			
	0.8802		0.6073	0.7312				
	0.43		0.64	0.59				
31	32	33	34	35	36			
			-0.20					
0	0	0	16	3	0			
			0.6830					
			0.43					

FOLLOWING LAYER IS NUMBER 2 OF 4; MODEL= FLATMOD-05

LEGEND:

BLOCK NUMBER
VELOCITY PERTURBATION
NUMBER OF HITS (RAYS)
DIAGONAL OF THE RESOLUTION MATRIX
STANDARD ERRORS

LAYER IS TWO-DIMENSIONAL.

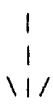

-UP=N30W-								
37	38	39	40	41				
		0.0	2.96					
0	2	10	9	2				
		0.7611	0.8541					
		0.56	0.48					
42	43	44	45	46				
	-2.00	-2.30	-0.12	5.19				
2	7	20	26	7				
	0.7125	0.8633	0.8569	0.6664				
	0.64	0.43	0.43	0.69				
47	48	49	50	51				
	1.59	0.79	-0.18	4.20				
2	14	30	32	8				
	0.8080	0.8536	0.8280	0.8342				
	0.52	0.45	0.46	0.55				
52	53	54	55	56				
-0.73	-6.17		0.33					
7	7	4	15	4				
0.8379	0.5980		0.8032					
0.52	0.70		0.45					
57	58	59	60	61				
		0.72	-0.32					
2	2	7	5	1				
		0.4722	0.6378					
		0.42	0.56					

FOLLOWING LAYER IS NUMBER 3 OF 4; MODEL= FLATMOD-05

LEGEND:

BLOCK NUMBER
VELOCITY PERTURBATION
NUMBER OF HITS (RAYS)
DIAGONAL OF THE RESOLUTION MATRIX
STANDARD ERRORS

LAYER IS TWO-DIMENSIONAL.

-UP=N30W-								
62	63	64	65					
	1.52	1.22	-2.88					
1	11	17	10					
	0.7972	0.7866	0.6964					
	0.52	0.51	0.58					
66	67	68	69					
2.79	0.67	3.27	1.60					
12	26	19	12					
0.7712	0.7395	0.8160	0.7746					
0.55	0.53	0.48	0.54					
70	71	72	73					
-2.46	-2.62	-0.45	-1.54					
6	23	18	6					
0.7913	0.7950	0.8845	0.8074					
0.56	0.46	0.44	0.57					
74	75	76	77					
	3.10							
4	8	3	4					
	0.6153							
	0.60							

FOLLOWING LAYER IS NUMBER 4 OF 4;   MODEL= FLATMOD-05

LEGEND:

  BLOCK NUMBER
  VELOCITY PERTURBATION
  NUMBER OF HITS (RAYS)
  DIAGONAL OF THE RESOLUTION MATRIX
  STANDARD ERRORS

LAYER IS TWO-DIMENSIONAL.

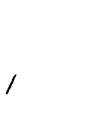

-UP=N30W-								
78	79	80	81					
-0.81	-1.78	-0.88	2.80					
6	8	13	6					
0.6951	0.7168	0.8182	0.6908					
0.68	0.66	0.52	0.64					
82	83	84	85					
-3.06	-0.93	1.88	2.57					
18	16	9	8					
0.8001	0.8265	0.7602	0.7910					
0.55	0.48	0.57	0.55					
86	87	88	89					
1.88	5.23	-3.50						
12	16	6	4					
0.7745	0.8525	0.7695						
0.60	0.46	0.61						
90	91	92	93					
-1.86	-0.85	-1.40						
9	8	5	3					
0.7159	0.6630	0.7937						
0.59	0.67	0.55						

USGS COMPUTER PROGRAM "THRLIST"; VERSION 2.001;
TECHNICAL CONTACT: JOHN R. EVANS.

THREED OUTPUT -- PRINTOUT OF BINARY FILE BY PROGRAM THRLIST

EXPERIMENT=** RESTE **, MODEL= FLATMOD-05, COMMENT=   = BLOCK BOUNDARIES STRIKING N3

MODEL FILENAME=FLATMOD
THREED BINARY OUTPUT=BOUT

FOLLOWING LAYER IS NUMBER 1 OF 4;   MODEL= FLATMOD-05

LEGEND:

  BLOCK NUMBER
  VELOCITY PERTURBATION
  NUMBER OF HITS (RAYS)
  DIAGONAL OF THE RESOLUTION MATRIX
  STANDARD ERRORS

LAYER IS TWO-DIMENSIONAL.

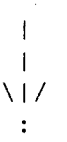

-UP=N60W-								
1	2	3	4	5	6			
0	0	0	0	0	0			
7	8	9	10	11	12			
0	3.22 7 0.7318 0.56	3	1	10.70 9 0.7731 0.58	-7.68 11 0.9039 0.45			
13	14	15	16	17	18			
0	1	-0.86 8 0.7002 0.49	-4.62 29 0.8662 0.44	1.23 21 0.8934 0.41	0.91 5 0.8292 0.53			
19	20	21	22	23	24			
-3.90 9 0.8552 0.49	4	2	-0.79 28 0.9062 0.36	-0.19 36 0.8867 0.35	0			
25	26	27	28	29	30			
1	0	2.23 6 0.3729 0.64	5.75 5 0.5632 0.65	0.25 7 0.6210 0.64	1			
31	32	33	34	35	36			
0	1	2.12 16 0.7778 0.41	3	0	0			

FOLLOWING LAYER IS NUMBER 2 OF 4; MODEL= FLATMOD-05

LEGEND:

BLOCK NUMBER
VELOCITY PERTURBATION
NUMBER OF HITS (RAYS)
DIAGONAL OF THE RESOLUTION MATRIX
STANDARD ERRORS

LAYER IS TWO-DIMENSIONAL.

-UP=N60W-								
37	38	39	40	41				
			0.71					
2	1	2	6	3				
			0.6414					
			0.69					
42	43	44	45	46				
	-0.71	2.72	4.16	4.51				
3	13	19	24	10				
	0.5172	0.8336	0.8023	0.8047				
	0.53	0.48	0.51	0.55				
47	48	49	50	51				
-2.27	-5.23	0.17	0.56	4.19				
7	11	29	33	10				
0.8157	0.8202	0.8365	0.8635	0.8382				
0.56	0.52	0.44	0.40	0.49				
52	53	54	55	56				
	-4.10	-1.74	0.80	1.87				
2	8	13	16	6				
	0.7491	0.8261	0.8130	0.7881				
	0.56	0.43	0.46	0.55				
57	58	59	60	61				
	-1.06	-1.37						
1	7	5	4	0				
	0.5226	0.5932						
	0.60	0.58						

FOLLOWING LAYER IS NUMBER 3 OF 4; MODEL= FLATMOD-05

LEGEND:

BLOCK NUMBER
VELOCITY PERTURBATION
NUMBER OF HITS (RAYS)
DIAGONAL OF THE RESOLUTION MATRIX
STANDARD ERRORS

LAYER IS TWO-DIMENSIONAL.

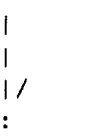

-UP=N60W-								
62	63	64	65					
-0.42	-0.68	0.27	0.54					
9	9	11	12					
0.7270	0.7784	0.8112	0.8381					
0.57	0.58	0.50	0.50					
66	67	68	69					
-0.90	0.58	-0.99	-0.89					
7	27	15	17					
0.7760	0.8369	0.8280	0.8467					
0.59	0.44	0.46	0.47					
70	71	72	73					
1.47	-4.46	0.45	2.76					
10	21	16	14					
0.7023	0.8267	0.7931	0.7374					
0.64	0.46	0.48	0.55					
74	75	76	77					
-0.64	-3.17	-3.21	-6.56					
6	7	9	6					
0.7494	0.7303	0.7185	0.6547					
0.61	0.65	0.59	0.70					

FOLLOWING LAYER IS NUMBER 4 OF 4; MODEL= FLATMOD-05

LEGEND:

BLOCK NUMBER
VELOCITY PERTURBATION
NUMBER OF HITS (RAYS)
DIAGONAL OF THE RESOLUTION MATRIX
STANDARD ERRORS

LAYER IS TWO-DIMENSIONAL.

-UP=N60W-								
78	79	80	81					
-0.15	-5.14	-1.19	-1.00					
10	12	7	14					
0.8168	0.8378	0.5087	0.8462					
0.54	0.51	0.72	0.50					
82	83	84	85					
1.29	2.12	5.16	-1.90					
14	23	8	17					
0.8596	0.8453	0.5735	0.8111					
0.47	0.50	0.66	0.52					
86	87	88	89					
2.73	-0.32	-0.54	4.02					
10	9	9	5					
0.8432	0.6972	0.8131	0.7175					
0.48	0.58	0.53	0.63					
90	91	92	93					
		-0.50						
2	3	7	2					
		0.7520						
		0.56